LOW-ENERGY ELECTRON DAMAGE IN DNA

CASTELLANI, MARIA,ELENA

CASTELLANI, MARIA,ELENA (2021) *LOW-ENERGY ELECTRON DAMAGE IN DNA*, Durham theses, Durham University. Available at Durham E-Theses Online: http://etheses.dur.ac.uk/14277/

LOW-ENERGY ELECTRON DAMAGE IN DNA

Thesis submitted in partial fulfilment of the requirements for the degree of Doctor of Philosophy.

MARIA ELENA CASTELLANI
DEPARTMENT OF CHEMISTRY, DURHAM UNIVERSITY, 2021
Supervisor: Prof. Dr. Jan R. R. Verlet

Declaration

The author declares that the material contained within this thesis has not previously been submitted for a degree at Durham University or any other institution. Unless indicated otherwise, the research presented in this thesis has been performed by the author.

Copyright Notice

Acknowledgements

Incredibly so, the end of my PhD has come. For this marvelous feat, I would like to thank my supervisor, Jan Verlet, for allowing me to work on this project and not kicking me out of the group despite: 1) offering my fingernails when asked for a nail 2) almost breaking the detector 3) forgetting I'm right-handed and trying to use a screwdriver with my left hand 4) my terrible puns and jokes at any time of day. The list would be longer, but I don't want to remind him of everything I've done so that he won't allow me to have my viva. A huge thank you also goes onto everyone else in the Verlet group, who had to listen to my never-ending, meaningless rants about literally anything, often preventing them from working. Thank you for being so patient and putting up with me for these three years! I would also like to thank everyone from LightDyNamics, particularly Dr. Davide Avagliano and Prof. Leticia González, for always providing entertainment and interesting topics of discussion (strictly for scientific purposes, even when loads of wine was involved).

I would also like to thank all the people who were so unlucky to cross my path at Durham, I'm sure I managed to embarrass myself and probably you as well during our encounter, no matter how brief. I'd also like to thank Irene Mazzei (21BV4EVA) and Lea Ibele (my favorite coconut person) for being so crazy to let me call them my friends. I could write something extremely thoughtful and sweet to express all the affection I have for you, but I'll just leave it to your imagination. I also want to thank all my other friends outside Durham, especially Giulia and her dog Scotch, who finally taught me after 28 years of life how to play fetch correctly.

It wouldn't be an acknowledgment section if I didn't thank my family. First, I'd like to thank my grandmother, to whom this thesis is dedicated, for always believing in me and showing her support by telling me "I knew you would've gotten a PhD since the day you were born". I don't know if this was a good or a bad omen, but surely it led me to this point. I'd also like to thank my cousins Adele and Andrea for always being there for me, especially after being bribed through sushi and/or pizza. I'm also very grateful to my parents for making me feel the thrills of being a teenager again when I found myself locked up with them during the Covid outbreak.

I could write a whole paragraph thanking all my other friends who have no idea what I do for a living, but just to name a few: B, Carlo, D, Gaia, Giulia, and Maddi, thank you for everything you've done for me, particularly taming my imposter syndrome, and befriending my inner demons. They really want to thank you as well.

Here is a list of other people, things, and places to whom/which I'd also like to show gratefulness. First, thank you Sense (the Chinese restaurant) and Sense Foods Asian Market for feeding me throughout these years, I wish you would've listened to me when I asked you if I could get a fidelity card, but I won't hold any grudges. Thank you to the lady from the Chem Café who always gave me double espresso even when I didn't have the heart to tell her that I don't tolerate caffein well. Also, big thanks to the one and only vegan hummus sandwich from the Palatine for being just mildly horrible.

I guess I'll also have to thank the madman who's agreed to marry me after truly getting to know me. We managed to withstand a pandemic, so I guess we're literally ready for a zombie apocalypse now.

Lastly, I'd like to thank two people, my organic chemistry 3 professor during my bachelor's and one of my supervisors from the master's, for respectively telling me "Less than one of you will become researchers" (speaking to the whole class) and "You don't have what it takes to become a scientist". Your words have kept me going through these years, probably more out of spite and pettiness than anything else, but it seems like it worked well in the end.

To my grandmother, Anna Maria, who still believes that
what I do will one day cure cancer.

Abstract

In this thesis, Photo-Electron Spectroscopy (PES) and Photo-Electron Imaging (PEI) have been exploited to study low-energy electron and photon-driven damage in DNA derivatives. After an introduction on photoelectron spectroscopy and DNA, an instrumental overview, together with a brief explanation of the theoretical methods used, is given.

The results section is divided according to the different chemical systems that have been considered. First, the viability of a dipole-bound state, which are electronic non-valence states that play an important role in electron transfer in DNA, has been studied in a model molecule: despite the presence of an alkyl chain directly poking into it, the dipole-bound state is retained in all cases. Secondly, the possibility of achieving intra-molecular charge transfer as probe for low-energy electron damage has been explored in a carboxylated adenosine analogue. Although no conclusive evidence of charge-transfer from the carboxylic acid to the nucleobase has been observed, this approach has then been applied to different DNA derivatives. The object of the third section of the results chapter is, in fact, the photophysics of the doubly-deprotonated dianion of adenosine-5'-triphosphate, which exhibits electron tunneling through the Repulsive Coulomb Barrier (RCB) upon irradiation at 266 nm; excited states calculation and RCB simulations have been performed to support these findings. Lastly, the photophysics of other doubly-deprotonated di- and tri-phosphorylated purine dianions have been explored in the last section: only one of them, adenosine diphosphate ($[ADP{-}H_2]^{2-}$), shows evidence of intra-molecular charge transfer, however further research is needed to corroborate this hypothesis.

Table of contents:

1. List of abbreviations....................7
2. Introduction....................9
   - 2.1. Motivation and overview....................10
   - 2.2. Photoelectron spectroscopy and imaging....................11
     - 2.2.1. Photoelectric effect....................11
     - 2.2.2. Franck-Condon principle....................12
     - 2.2.3. Time-dependent spectroscopy....................15
     - 2.2.4. The pump-probe principle....................17
     - 2.2.5. Photoelectron imaging and velocity-map imaging....................18
   - 2.3. Molecular relaxation processes....................22
       - 2.3.1.1. Radiative processes....................24
       - 2.3.1.2. Non-radiative processes....................24
       - 2.3.1.3. Conical intersections....................26
   - 2.4. Electron damage in DNA....................30
     - 2.4.1. DNA overview....................30
       - 2.4.1.1. Function and biological applications....................34
     - 2.4.2. DNA damage....................34
       - 2.4.2.1. Photon damage....................34
       - 2.4.2.2. Electron damage....................38
       - 2.4.2.3. Motivation of the project....................40
3. Experimental section....................42
   - 3.1. Experimental setup....................43
     - 3.1.1. Platinum plating and noise reduction....................44
   - 3.2. Theoretical methods....................46
   - 3.3. Data analysis....................47
4. Dipole-bound states in para-substituted phenolate anions....................48
   - 4.1. Motivation....................49
   - 4.2. Methods....................50
   - 4.3. Results....................51
   - 4.4. Discussion....................55
   - 4.5. Conclusions....................57

5. Photophysics of a carboxylated adenosine analogue……60
    5.1. Motivation……61
    5.2. Methods……62
    5.3. Results……62
    5.4. Discussion and conclusions……68
6. Photophysics of the doubly deprotonated ATP dianion……71
    6.1. Motivation……72
    6.2. Methods……74
    6.3. Computational details……75
    6.4. Results……75
    6.5. Discussion……84
    6.6. Conclusions……90
7. Photophysics of doubly deprotonated ADP, GDP and GTP dianions……92
    7.1. Motivation……93
    7.2. Methods……95
    7.3. Results……95
    7.4. Discussion……104
    7.5. Overall discussion and conclusions……107
8. Final remarks……109
9. References……113
10. Appendix: published research papers……135

1. List of abbreviations in alphabetical order

Abbreviation	**Full name**
(6-4)-PP	Pyrimidine-Pyrimidone-(6-4)-Photoproducts
9-oxo-7,8-dihydro-Guanine	9-oxoGua
A	Adenine
C	Cytosine
G	Guanine
T	Thymine
U	Uracil
ADC	Algebraic Diagrammatic Construction
ADE	Adiabatic Detachment Energy
Ade	Adenine
ADP	Adenosine Di-Phosphate
AMP	Adenosine Mono-Phosphate
ATP	Adenosine Tri-Phosphate
BO	Born-Oppenheimer
dAMP	Deoxy-Adenosine Mono-Phosphate
C-Ado	Carboxylated-5'-Adenosine
CI	Conical Intersection
CCD	Charged-Coupled Device
CMOS	Complementary Metal-Oxide Semiconductor
CPD	Cyclo-butane Pyrimidine Dimer
DBS	Dipole-Bound State
DEA	Dissociative Electron Attachment
DFT	Density Functional Theory
dGMP	Deoxy-Guanosine Mono-Phosphate
DNA	Deoxyribo-Nucleic Acid
DSB	Double-Strand Break
DVW	Dewar Valence Isomers
EA	Electron Affinity
EBE	Electron Binding Energy
EKE	Electron Kinetic Energy
ESI	Electro-Spray Ionization
FAD	Flavin Adenine Dinucleotide
FC	Franck-Condon
FR-PEI	Frequency-Resolved Photo-Electron Imaging
GMP	Guanosine Mono.Phosphate

Abbreviation	**Full name**
GDP	Guanosine Di-Phosphate
GTP	Guanosine Tri-Phosphate
Gua	Guanine
HOMO	Highest Occupied Molecular Orbital
I	Imidazole
IC	Internal Conversion
ISC	Inter-System Crossing
IR	Infra-Red
IVR	Intramolecular Vibrational Relaxation
KE	Kinetic Energy
LEE	Low Energy Electron
LUMO	Lowest Unoccupied Molecular Orbital
MCP	Multi-Channel Plate
MD	Molecular Dynamics
MS	Mass Spectrometry
NAD	Nicotinamide Adenine Dinucleotide
PAD	Photoelectron Angular Distributions
PE	Photo-Electron
PEI	Photo-Electron Imaging
PES	Photo-Electron Spectroscopy
PESs	Potential Energy Surfaces
POP	Polar Onion Peeling
R2PEI	Resonance-enhanced 2-photon Photo-Electron Imaging
RCB	Repulsive Coulomb Barrier
RMSD	Root Mean Squared Deviation
RNA	Ribo-Nucleic acid
SSB	Single-Strand Break
TD-DFT	Time-Dependent Density Functional Theory
TDM	Transition Dipole Moment
TNI	Transient Negative Ion
TOF	Time-Of-Flight
TR-PEI	Time-Resolved Photo-Electron Imaging
TR-PES	Time-Resolved Photo-Electron Spectroscopy
UV	Ultra-Violet
VMI	Velocity-Map Imaging

Introduction

2.1 Motivation and overview

Contrarily to popular belief, one of the greatest causes of lethal DNA damage is by electrons, rather than photons. In particular, so-called low-energy electrons (LEEs), with Electron Kinetic Energy (E_{ke}) < 3 eV, can impart damage on DNA and lead to severe biological processes, *e.g.* cell death and mutations.[1] LEE attachment can, in fact, cause double- and single-strand breakage in DNA, but also induce major disruptions of its smaller components, such as isolated bases, nucleosides, nucleotides, and small aggregates of the latter.[2]

The chemical mechanism of these processes, and more generally of the effect of ionizing radiation on living organisms is, up to this day, not entirely known. The high photo-stability of DNA and, consequently, its low quantum yield makes it hard to conduct fluorescence spectroscopy studies. The irradiation of DNA with UV light triggers the production of excited states, which decay rapidly to the ground electronic state. On the other hand, the interaction of DNA with LEEs below the excitation threshold entails the formation of transient anions that decay into reactive species, *e.g.* neutral radicals and stable anions.[3] The time-scale in which both photon and electron-driven events take place is ultra-fast, *i.e.* the femtosecond regime.

In order to shed light on these mechanisms, we have probed native and modified nucleotides through time and frequency-resolved photoelectron imaging, and photo-detachment action spectroscopy.[4] Anion photoelectron spectroscopy is particularly useful in studying biological systems, and more specifically DNA derivatives, as most systems of interest are naturally negatively charged. Moreover, the absence of selection rules in photoelectron spectroscopy allows for a broader pool of systems from which to choose. Although only smaller systems can be probed through photoelectron spectroscopy, a bottom-up approach can be incredibly useful for a deeper understanding of underlying biochemical mechanisms. In this thesis, such an approach was exploited to characterize electron-induced damage in DNA derivatives, using the idea of intra-molecular charge transfer as a probe for electron damage.

2.2 Photoelectron spectroscopy and imaging

2.2.1 *The photoelectric effect*

Photoelectron spectroscopy, also known as photoemission spectroscopy, is a technique that exploits the photoelectric effect to study electronic states and geometric structures of molecules. First reported by Heinrich Hertz in 1887, then subsequently explained by Albert Einstein in 1905, the photoelectric effect states that, if electromagnetic radiation of frequency ν is shone onto a material, an electron, also known as photoelectron, will be emitted from the material.[5] Therefore, the kinetic energy of the emitted electron, E_{ke}, is given by:

$$E_{\mathrm{ke}} = h\nu - \Phi, \tag{1}$$

where Φ is called the *work function* and is a value of the minimum energy required to produce photoemission from the given material. The work function is a representation of the Electron Binding Energy, E_{be}, of the material, also referred to as ionization potential.[6] The electron binding energy is subject to the following condition:

$$\Phi = E_{\mathrm{be}} = h\nu_0, \tag{2}$$

where ν_0 is the *threshold frequency* of the molecule. Therefore, to have photoemission, the kinetic energy must correspond to:

$$E_{\mathrm{ke}} > h(\nu - \nu_0). \tag{3}$$

This means that, to eject an electron from the molecule of interest, the frequency ν of photon must be higher than the threshold frequency ν_0 of the molecule. Typically, most ionization energies fall into the visible and ultraviolet ranges (between 1 and 15 eV).[6] Since photoelectrons are released from a specific orbital, either molecular or atomic, each photoelectron will have a different binding energy $E_{\mathrm{be},i}$. Thus, the kinetic energy of the ejected electron can be used as a probe of the original electronic state and Molecular (MO) or Atomic (AO) Orbital. Therefore, a photoelectron spectrum contains the probability of detaching an electron from a given orbital, and the energy necessary to do so.

When an electronic transition occurs, to re-establish equilibrium, the remaining core electrons undergo redistribution, while the nuclei experience vibrations. As a result, each electronic transition is also characterized by the presence of vibrational structure. The electron binding energy can be interpreted in terms of Koopmans' theorem:

$$E_{\mathrm{be},i} = -\varepsilon_i, \tag{4}$$

which states that the electron binding energy corresponds to the negative of the orbital energy of the Highest Occupied Molecular Orbital (HOMO).[7] However, Koopmans' theorem is only an approximation, as the reorganization of the remaining electrons after the ionization process is not taken into consideration. Therefore, Koopmans' theorem fails to estimate the ionization energies of open shell molecules and of cations that undergo changes in the ordering of MOs.[8]

2.2.2 The Franck-Condon principle

Due to the enormous difference in mass between nuclei and electrons, an electronic transition can be considered instantaneous with respect to nuclear motion timescales. This approximation, which states that the initial nuclear arrangement (geometry) is the same in the initial state and the final state, even if for the latter, that geometry is not the lowest energy geometry, is known as the Franck-Condon (FC) principle.[9] In terms of quantum mechanics, the FC principle essentially states that the probability of excitation to a final vibrational level f depends on the overlap of the vibrational wavefunctions between f and the initial state i; hence, electronic transitions are vertical (Figure 2.1).[10] Therefore, the most probable transition is the one that has the greatest overlap with the initial one.

Mathematically, this concept can be formulated as follows. Consider a transition of an electrical dipole from the initial vibrational state v of the electronic ground state ε, represented in bra-ket notation as $|\varepsilon v\rangle$, to another vibrational state v' of the electronic excited state ε', written as $|\varepsilon' v'\rangle$. Hence, the wavefunctions ψ and ψ' of the two states will be:

$$\psi = \psi_e \psi_v \psi_s \qquad \text{and} \qquad \psi' = {\psi'}_e {\psi'}_v {\psi'}_s, \tag{5}$$

with e, v and s standing for, respectively, electronic, vibrational and spin, as each overall state wavefunction is given by the product of an electronic, a vibrational and a spin wavefunction. Moreover, the transition dipole moment operator, μ, is known to be equal to:

$$\mu = \mu_e + \mu_N = -e\sum_i r_i + e\sum_j Z_j R_j\,, \tag{6}$$

where $-e$ and r_i are, respectively, charge and position of the electrons, and $+Z_je$ and R_j are charge and position of the nuclei. Additionally, the transition moment is defined as:

$$P = \langle \psi' | \mu | \psi \rangle. \tag{7}$$

If we apply the Born-Oppenheimer (BO) approximation, which states that the nuclei are static with respect to electronic motion, we can separately factorize the vibrational and the electronic wavefunctions. Consequently, the probability amplitude of the transition is given by:

$$\begin{aligned} P = \langle \psi' | \mu | \psi \rangle = \left\langle {\psi'}_e {\psi'}_v {\psi'}_s \middle| \mu \middle| \psi_e \psi_v \psi_s \right\rangle = \left\langle {\psi'}_e {\psi'}_v {\psi'}_s \middle| \mu_e + \mu_N \middle| \psi_e \psi_v \psi_s \right\rangle = \\ = \left\langle {\psi'}_e {\psi'}_v {\psi'}_s \middle| \mu_e \middle| \psi_e \psi_v \psi_s \right\rangle + \left\langle {\psi'}_e {\psi'}_v {\psi'}_s \middle| \mu_N \middle| \psi_e \psi_v \psi_s \right\rangle = \\ = \left\langle {\psi'}_v \middle| \psi_v \right\rangle * \left\langle {\psi'}_e \middle| \mu_e \middle| \psi_e \right\rangle * \left\langle {\psi'}_s \middle| \psi_s \right\rangle + \left\langle {\psi'}_v \middle| \psi_v \right\rangle * \left\langle {\psi'}_v \middle| \mu_N \middle| \psi_v \right\rangle * \left\langle {\psi'}_s \middle| \psi_s \right\rangle. \end{aligned} \tag{8}$$

The square of the first integral is the Franck-Condon Factor (FCF), whereas the second and third integrals represent, respectively, the orbital selection rule and the spin selection rule. The intensity of an absorption is known to be proportional to $|S(v'v)|^2$, which is the FCF for the transition:

$$|S(v'v)|^2 \propto \langle \psi'_v | \psi_v \rangle^2. \tag{9}$$

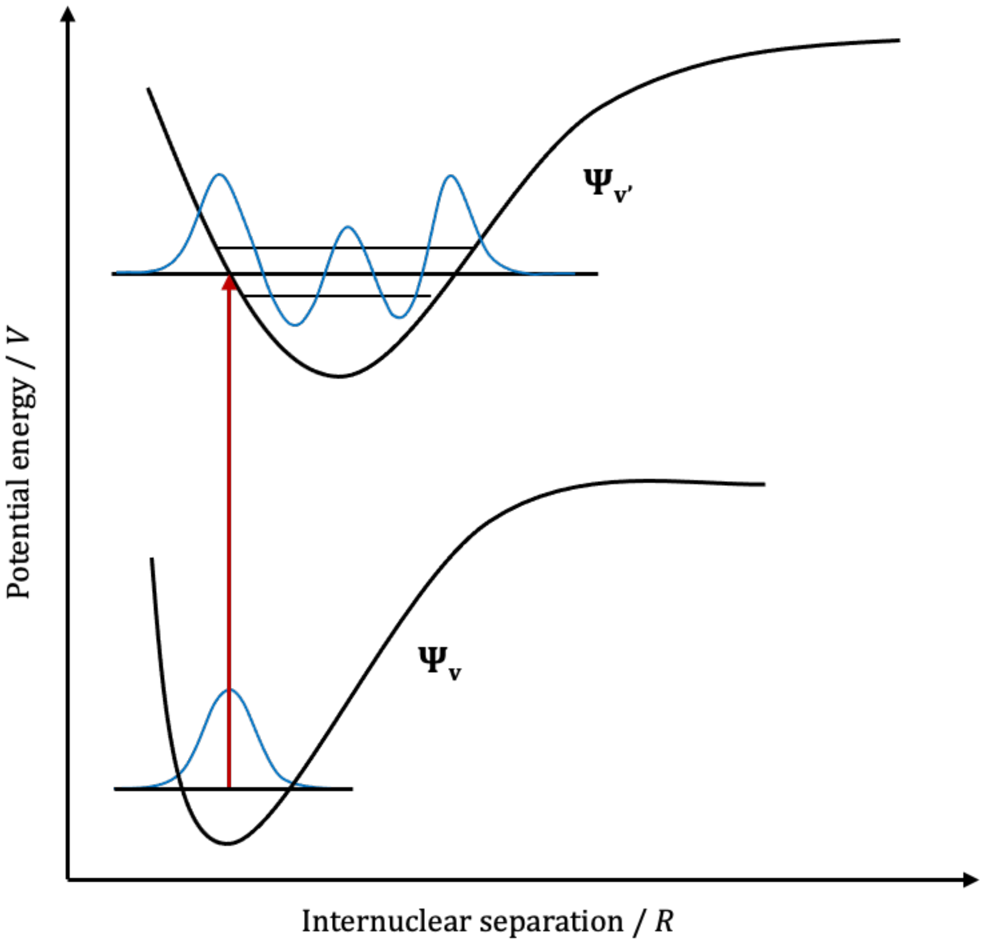

Figure 2.1: visual representation of the Franck-Condon principle.

Hence, the most favorable and intense transition is the one between the ground state of the molecule and the state with which the overlap integral is greatest. In the case of anions, the energy corresponding to this transition takes the name of Vertical Detachment Energy (VDE) and corresponds to the red vertical arrow in Figure 2.1, whereas the ionization potential of the molecule is called Adiabatic Detachment energy (ADE).

2.2.3 Time-dependent spectroscopy

To spectroscopically study the temporal evolution of a chemical system, time-dependency must be introduced. The theoretical basis can be found in the time-dependent Schrödinger equation:[11]

$$-\frac{\hbar^2}{2m}\frac{d^2\psi(x)}{dx^2} + V(x)\psi(x,t) = i\hbar\frac{\partial}{\partial t}\psi(x), \tag{10}$$

whose solutions, for a free particle with $V(x) = 0$, are simply the same ones as the time-independent Schrödinger equation, $\psi(x) = e^{ikx}$, multiplied by a time-dependent term, $e^{-i\omega t}$:

$$\psi(x,t) = \psi(x)e^{-i\omega t}, \tag{11}$$

in which k represents the wavevector. Yet, the probability of finding a particle in a specific quantum state with exact k is not time-dependent, as it is given by the square of the wavefunction:

$$|\psi(x,t)|^2 = |\psi(x,t)\psi(x,t)^*|^2 = \left|\psi(x,t)e^{-i\omega t}\psi(x)e^{+i\omega t}\right|^2 = |\psi(x)|^2. \tag{12}$$

This is due to the delocalization of the particle. In fact, the momentum of the particle p, since $k = 2\pi/\lambda$ and $p = h/\lambda$, is defined as $k = p/\hbar$. According to the Uncertainty Principle, the position of the particle and its motion cannot be both known at the same time; to satisfy this condition, a spread of p needs to be introduced to enable particle localization.

During a spectroscopic measurement, rather than a single particle, it is a wavepacket, which is a coherent superposition of time-dependent wavefunctions with quantum number n, that is taken into consideration:

$$\Psi(x,t) = \sum_n c_n\psi_n(x)e^{-i\omega_n t}, \tag{13}$$

where c_n is a weighing factor that defines the contribution of each wavefunction to the wavepacket, and ω_n describes the frequency of each level defined by quantum number

n. The motion of the wavepacket depends on the difference in energy between levels, meaning that the wavepacket depends on the quantum number n:

$$\Delta E_{\mathrm{av}} = \frac{\partial E}{dn}. \tag{14}$$

For vibrational levels, $\Delta E_{\mathrm{av}} = h\nu_e$ or $\Delta E_{\mathrm{av}} = h\nu_e - 2v\, h\nu_e x_e$, for, respectively, harmonic and anharmonic oscillators. The harmonic period of motion is defined as $T = 2\pi / \omega$ and is independent from n, while the anharmonic period of motion corresponds to $T = 2\pi\hbar/(E_{n+1} - E)$. Therefore, while in a harmonic wavepacket the energy difference between levels is constant, in an anharmonic wavepacket it varies. Specifically, a harmonic wavepacket will retain its shape, which is determined by the weighing factors, during motion; on the other hand, in an anharmonic wavepacket different parts will move at different speeds (Figure 2.2).

However, coherence is retained; in fact, after some time the faster components of the wavepacket will re-phase with the slower ones, according to the expression:

$$\Delta\Delta E_{\mathrm{av}} = \left|\frac{\partial^2 E}{\partial n^2}\right| = 2h\nu_e x_e. \tag{15}$$

Therefore, after a certain amount of time, the molecule resumes its usual vibration.

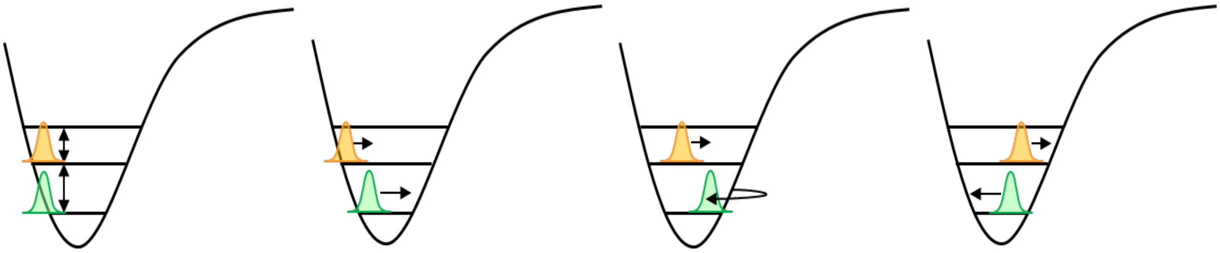

Figure 2.2: evolution of a wavepacket in an anharmonic oscillator.

2.2.4 The pump-probe principle

The most common arrangement for time-resolved spectroscopic measurements is the pump-probe setup.[12] First, a short laser pulse, named the pump, moves some population away from the ground state up to an excited state of the molecule. After a given time-delay, Δ*t*, a second laser pulse, called the probe, explores how the population has changed during this timeframe, therefore allowing the study of the temporal evolution of the system.[13] In the case of time-resolved photoelectron spectroscopy, the probe pulse exploits the photoelectric effect to further excite the molecule and remove an electron, spectroscopically probing the population in the excited state.[14]

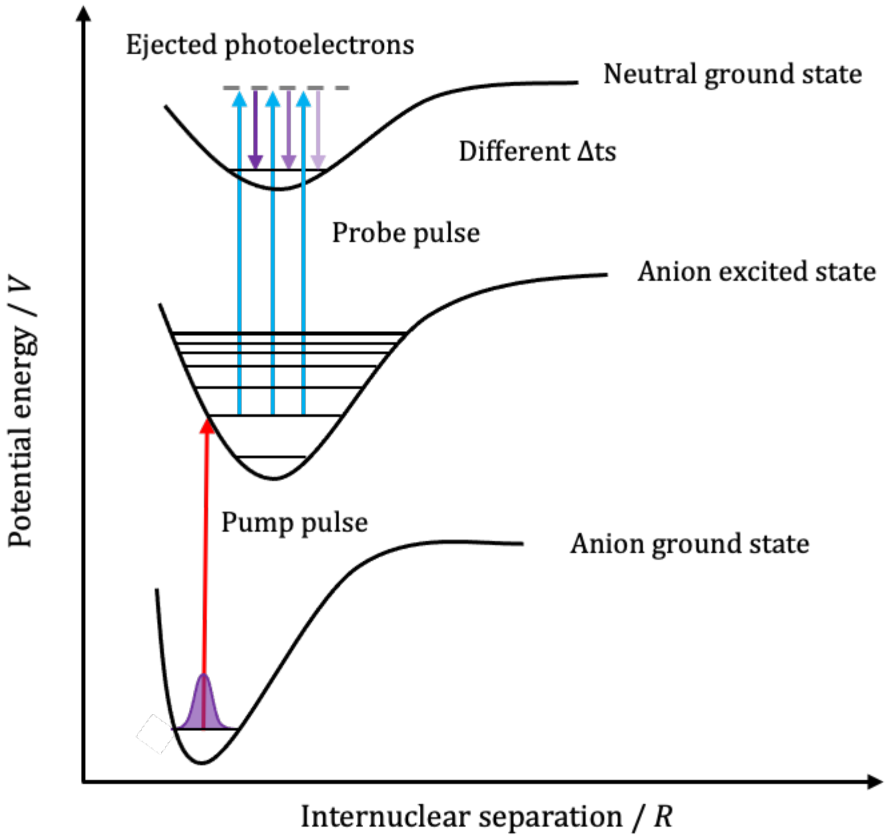

Figure 2.3: exemplification of a time-resolved photoelectron spectroscopy of an anionic species.

In a spectroscopic experiment, the delay between pump and probe is normally controlled through a movable optical delay line using a translation stage. The reference delay, $t = 0$, corresponds to the maximum overlap between the two laser pulses. Variations of the relative positions of the two pulses will hence produce negative or positive delays. A schematic representation of a pump-probe laser setup is shown in Figure 2.3.

As excited-state dynamic processes take place in the femtosecond regime, the laser pulses must be faster than molecular motion; this can only be achieved through a femtosecond-pulsed laser.[4]

2.2.5 Photoelectron imaging and velocity-map imaging

Photo-Electron Spectroscopy (PES) gives information on the probability of removing an electron from a molecule, and the energy necessary to do so. Photo-Electron Imaging (PEI), on the other hand, can provide additional information, particularly on the direction of the velocity vector of an electron. The distribution of these velocities is called Photoelectron Angular Distribution (PAD) and are defined as the angular component of the velocity vector of the emitted photoelectron. Due to the dependence on angular momentum, the PADs usually present anisotropy, which is defined as the quality of exhibiting different properties depending on directionality. Thanks to anisotropy, PADs can therefore provide precious structural and symmetrical information on the orbitals from which the photoelectron is ejected.[15, 16]

The PADs can be expressed through an anisotropy parameter, β_2, which, for a single-photon process, is defined as:

$$I(\theta) \propto 1 + \beta_2 P_2(\cos\theta), \tag{16}$$

where $P_2(\cos\theta) = \frac{1}{2}(3\cos^2\theta - 1)$ is the second-order Legendre polynomial, and θ is the angle between the velocity vector of the outgoing photoelectron and the polarization axis, $\vec{E}$. The value of β_2 can span from +2 to −1, with +2 corresponding to

PADs predominantly parallel to $\vec{E}$, hence with a $\cos^2\theta$ distribution, and −1 instead representing a $\sin^2\theta$ distribution, therefore mostly perpendicular to $\vec{E}$. Generally, a negative β_2 is associated with detachment from an orbital of either p- or π-character, whereas a positive β_2 value is attributed to detachment from orbitals with s- or σ-character.[17]

Moreover, PADs can also be defined as:

$$PAD = \vec{\mu} \cdot \vec{E} \tag{17}$$

which is the dot product between the polarization axis and the transition dipole moment. Therefore, to see the PADs, the two vectors must be parallel.

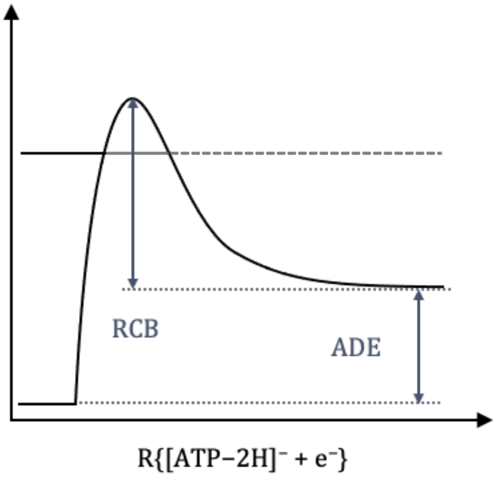

Figure 2.4: diagram of the Repulsive Coulomb Barrier for a model dianion.

Although this is true for monoanionic species, in the case of polyanions Equation 17 is not valid anymore. In fact, isolated polyanions present an additional energy barrier named the Repulsive Coulomb Barrier (RCB, Figure 2.4), [18-21] which arises from the short-range attraction, which stabilizes the dianion, and long-range repulsion, which instead destabilizes it, between an electron progressively moving away from the original dianion and the single negative charge that is left on the molecule. To detach an electron from the polyanion of interest, a total energy corresponding to the sum of the RCB and the ADE is required. [21, 22] PE spectroscopy and imaging are particularly useful as the outgoing electron is naturally sensitive to the RCB; this will appear in the PE spectrum as an E_{ke} cut-off below which no photoemission is observed.[18, 21, 23-25] However, if an excited state of the dianion lies below the RCB but higher than the ADE, this excited state will be a resonance, *i.e.* an excited state above the detachment threshold. Resonances are metastable to electron tunneling through the RCB and the tunneling lifetime can be directly measured through time-resolved PE spectroscopy.[26] One important characteristic of the RCB is its anisotropy, which depends on the relative location of the charged sites with respect to the departing electron. Provided that there is a connection between the laboratory frame and the molecular frame, the RCB's anisotropy can be probed through PADs.[27] This connection can be easily obtained through photo-excitation of a chromophore with a known transition dipole moment.[28] Therefore, as the RCB strongly affects the ejected photoelectron, Equation 17 is not sufficient to describe PADs in the case of a polyanionic species.

The most common photoelectron imaging setup is Velocity-Map Imaging (VMI). In a standard PE spectrometer setup, after undergoing ionization, the ions are mass-analyzed by a Time-Of-Flight (TOF) mass spectrometer, which culminates in a detector, in this case a VMI apparatus, which can be either vertically or perpendicularly arranged. In the detector region, the ion beam is parallel to the polarization axis and perpendicular to the laser pulse. The charged fragments, in this case photoelectrons, will pass through a set of ring electrodes that, by creating a static electric field, can project the image onto the detector. The detector is usually composed by a phosphor screen coupled with a Multi-Channel Plate (MCP), connected to a camera, either a Charge-Couple Device (CCD) or a Complementary Metal-Oxide Semiconductor (CMOS) device, that takes subsequent pictures of the phosphor screen, hence recording the image. A sketch of the general experimental setup, with a more detailed depiction of the imaging detector on the bottom, can be seen in Figure 2.5.

Contrarily to neutral and positively charged molecules, anions require considerably less energy to detach an electron from them. Specifically, most anionic species present ionization potentials that usually fall within the visible regime. The process of removing an electron from an anion is named photo-detachment, in opposition to photoionization of positively charged and neutral species.

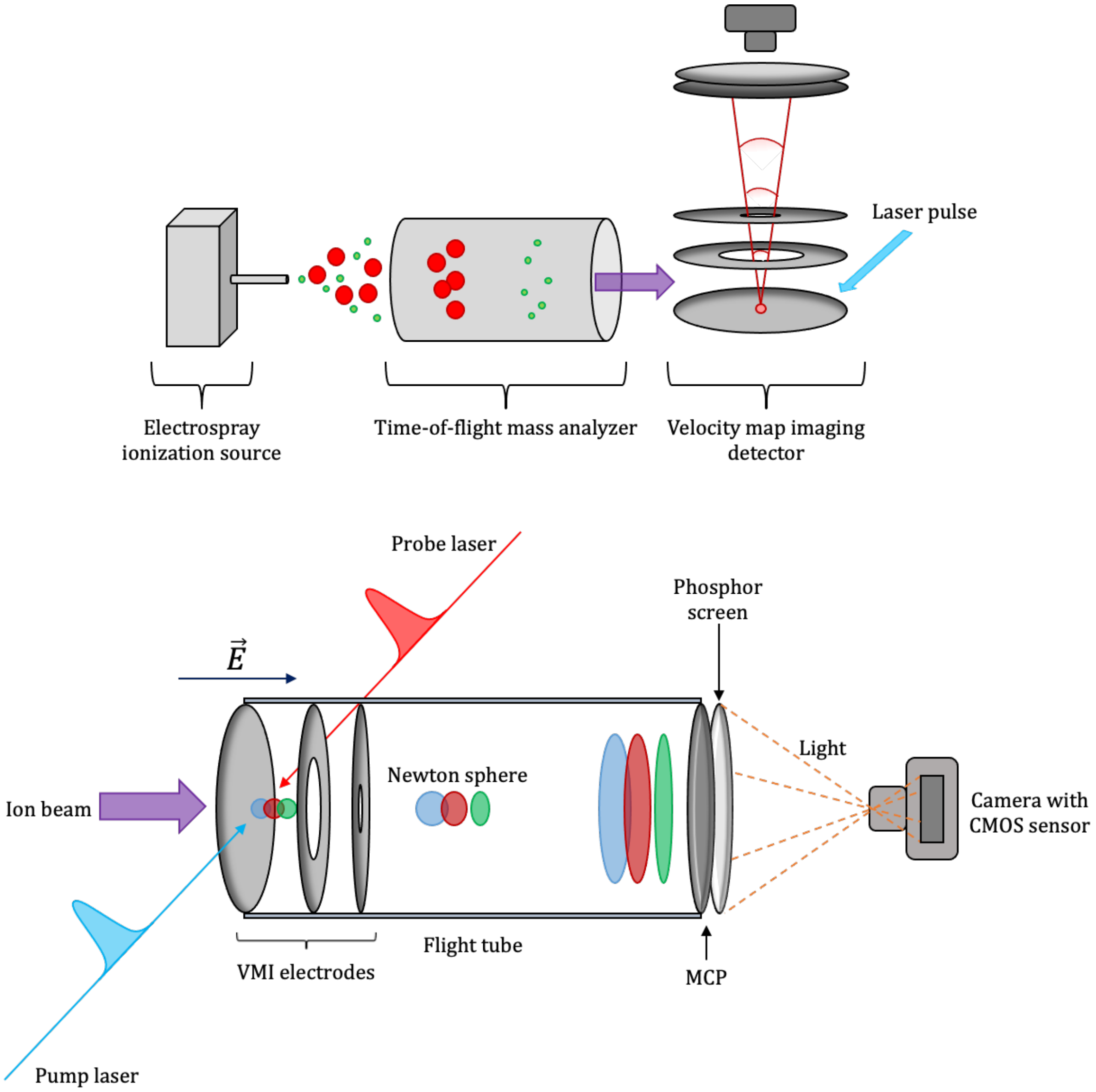

Figure 2.5: on the top is the general scheme of a photoelectron imaging experimental setup. The three principal components are the ion source, the TOF mass analyzer and the imaging detector. On the bottom is a detailed depiction of a photoelectron imaging detector. The VMI plates with the electrodes are represented in light blue and lie in the xy plate. The electric field vector (green arrow) and the ion beam (yellow arrow) are parallel to the plane in which the detector is contained, and perpendicular to the laser pulse (represented by a dark blue arrow). The photoelectron wavefront, in red, is projected onto the x axis. On the right is represented the top view of the detector portion in which the laser irradiates the molecule, and where the photoelectron is produced. The electric field and the ion beam are both parallel to the z axis, while the electrodes and the detector belong to the yz plane. The laser beam is, instead, parallel to the y axis.

In detail, photoelectrons produced at $t = 0$ at the source (hence with $r = 0$), which possess a kinetic energy of $E_{\mathrm{ke},0}$, are found at a later stage on the surface of a sphere with radius r_t, called a Newton sphere, which is expanding in time according to the equation:

$$r_t = \sqrt{\frac{2E_{\mathrm{ke},0}}{m}}\, t \tag{18}$$

The photoelectrons are generated in a region where the electric field is homogeneous and constant. Upon application of the static electric field produced by the VMI electrodes at $t = 0$, the sphere is projected onto the phosphor screen, which is position sensitive; hence, the thus-obtained bi-dimensional image contains information on both energy and position.[29] The photoelectron distributions are flattened in the plane of the detector and electrons with the same velocity will be mapped onto the same position. Normally, a photoelectron image is obtained by accumulating approximately 10^5 – 10^6 electrons, which are a representation of the probability of finding the photoelectrons on the detector's plane. The screen's phosphorescence is then picked up by the camera, thus yielding an image that contains both the information of a conventional photoelectron spectrum as well as the PADs.

2.3 Molecular relaxation processes

As previously mentioned, upon excitation with the pump pulse, the system is allowed to evolve for a given time delay t before the arrival of the probe pulse. During this timeframe, the system can undergo multiple molecular relaxation processes, which entail various ways of dispersing the energy that has been accumulated by the system. Molecular relaxation pathways in which the emission of a photon is involved are named radiative processes, whereas the ones in which only heat is produced are called non-radiative.[6]

Molecular relaxation processes are usually represented through *Jablonski* diagrams (Figure 2.6), which can show the electronic states of a molecule and the vibrational and electronic transitions between them. In the Jablonski diagram shown in Figure 2.6, the ground states of each electronic state are represented with thick, solid, horizontal lines, whereas vibrational levels are represented as black, thin, horizontal lines parallel to the electronic states. Radiative processes are represented by solid straight vertical arrows, while non-radiative processes are represented with a wiggly horizontal or vertical arrow.

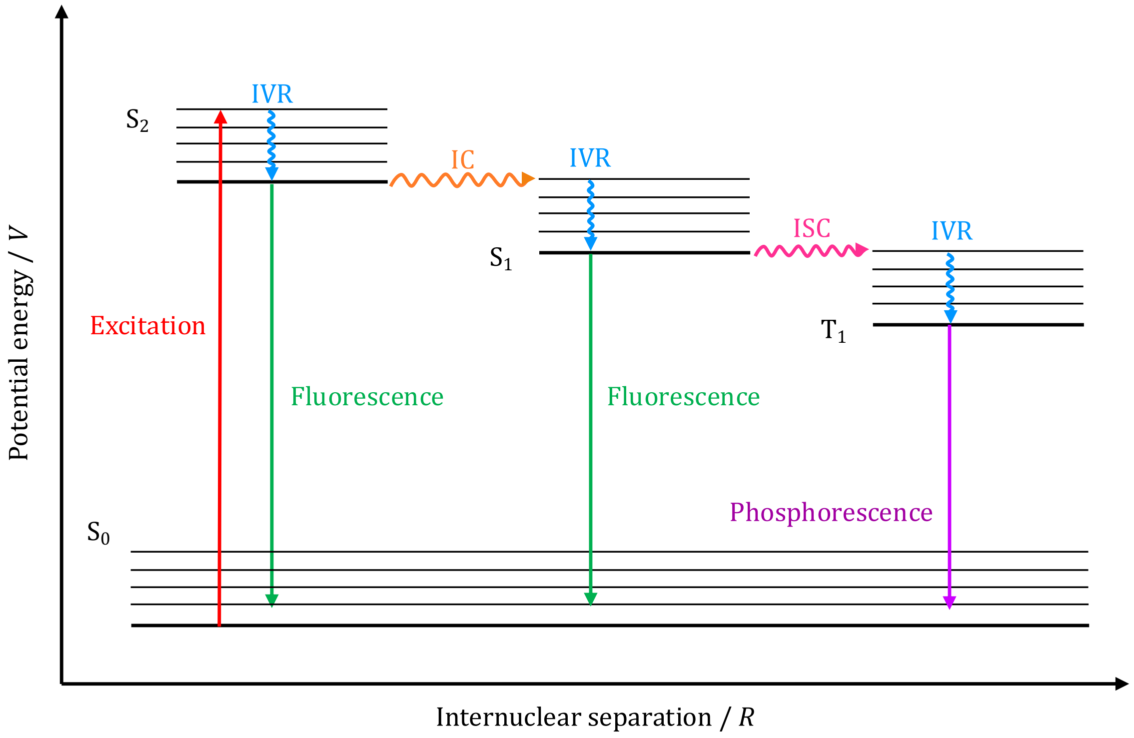

Figure 2.6: Jablonski diagram representing the different molecular relaxation pathways a molecule can undergo. The arrow in red represents excitation from the ground state S_0 to the S_2 state. The green and the purple arrows represent two different kinds of emission: respectively, fluorescence from a singlet to a singlet state, and phosphorescence from a triplet to a singlet state. The three wiggly lines represent non-radiative processes: internal conversion (IC, in orange) between the S_2 and S_1 states, intersystem crossing (ISC, in fuchsia) between the S_1 and T_1 states, and internal vibrational relaxation (IVR, in blue), intra each of the represented electronic states.

2.3.1 Radiative processes

Radiative processes are beyond the scope of this thesis, therefore only a brief description will be given. Emission from a higher to a lower state can be either spontaneous or induced by a photon. Depending on the spin multiplicity of the higher-lying state, *i.e.*, singlet or triplet, the spontaneous process will take the name of either *fluorescence* or *phosphorescence*.

Although phosphorescent transitions violate the spin-selection rule, with a sufficiently large spin-orbit coupling they can still take place. However, due to being kinetically disfavored, the time-scale of these relaxation processes is very long, and can span from μs to ms.[30]

2.3.2 Non-radiative processes: intramolecular vibrational relaxation or redistribution

Intramolecular Vibrational Relaxation (IVR) consists of a rearrangement of vibrational energy from the initially populated vibrational states to all the other degrees of freedom available. Hence, this process takes place inside the same electronic state, at a timescale within the picosecond regime.

The energy transfer occurs thanks to intrinsic molecular coupling, *e.g.,* anharmonic coupling, from the initial excited states to the adjacent ones. If the initial state is coupled to only one or a few other states, as in the case of gas-phase molecules, excitation will propagate coherently and, depending on the coupling matrix elements, quantum beats may arise. As no relaxation is involved, the process is called intramolecular vibrational redistribution. On the other hand, if the initial state is coupled to a high number of states, coherence is lost and dissipative IVR takes place. This is the case for large molecules, for which IVR is basically irreversible and incoherent.[31] While in the gas-phase the total energy remains the same, in the condensed phase the energy may dissipate into the surrounding environment; in this case, this process is referred to as internal vibrational relaxation.

IVR can be explained using *Fermi's golden rule*:

$$k = \frac{2\pi}{\hbar} V^2 \rho, \tag{19}$$

which shows that the rate coefficient k of an IVR between a higher vibrational state and one or more lower ones is proportional to the coupling strength V of the states multiplied by the density of the final vibrational states ρ.[32]

2.3.3 Non-radiative processes: internal conversion and intersystem crossing

Despite representing a violation of the Born-Oppenheimer approximation,[33] if multiple electronic states are close enough in energy and present sufficiently large state-to-state couplings, population transfer from one state to another may occur non-radiatively. Internal Conversion (IC) takes place when vibrational energy is transferred between two well-separated, adjacent electronic states with the same spin, thanks to the contribution of non-adiabatic coupling. If the states possess different spin, the process is forbidden by the spin selection rule (*Section 2.1.2*): nevertheless, as happens in the case of phosphorescence,[30] if the spin-orbit coupling term is large enough the conversion will occur anyway, giving rise to Inter-System Crossing (ISC).[34] As the final electronic state is typically lower in energy than the initial state, electronic energy is converted to vibrational energy in the final state.

IC and ISC can also be described using Fermi's golden rule, rearranging it for two different electronic states. Thus, the conversion rate coefficient k of an IC or an ISC between higher vibronic level l in an initial electronic state and lower vibronic levels m in the final electronic state is equal to:

$$k_{lm} = \frac{2\pi}{\hbar} V_{lm}^2 \rho_{mm}, \tag{20}$$

with V^2_{lm} being the intensity of the coupling interaction between the two electronic states, whereas ρ_{mm} represents the density of vibrational states in the final electronic state. The larger the electronic separation between the states, the smaller the coupling and consequently the conversion rate as well. Mathematically, this can be defined as the so-called *energy-gap law:*

$$k \propto e^{\left(-\frac{E}{\hbar\omega_\nu}\right)}, \tag{21}$$

which states that the IC or ISC rate coefficient is proportional to the minus exponential of the energy over the mode frequency. In general, IC and ISC processes range from hundreds of femtoseconds to many nanoseconds, sometimes even longer.[31]

2.3.4 Conical intersections

Potential Energy Surfaces (PESs) can be classified as either diabatic or adiabatic surfaces: while a diabatic surface retains its electronic character along a nuclear coordinate, an adiabatic surface can undergo changes. Adiabatic PESs arise from the BO approximation, in which the coupling between nuclear and electronic motion is overlooked.

Avoided crossings can take place when two PESs of the same symmetry try to cross in a diatomic molecule (Figure 2.7). For the crossing to occur, the energies E_1 and E_2 of the electronic states must be equal. Therefore, each electronic state ψ_n can be described as a linear combination of two diabatic states φ_n:

$$\begin{pmatrix}\psi_1\\ \psi_2\end{pmatrix} = \begin{pmatrix}c_{11} & c_{12}\\ c_{21} & c_{22}\end{pmatrix}\begin{pmatrix}\varphi_1\\ \varphi_2\end{pmatrix}. \tag{22}$$

The energies of the two states can be expressed in matrix terms: $H_{mn} = \langle\varphi_n|\hat{H}|\varphi_m\rangle$.

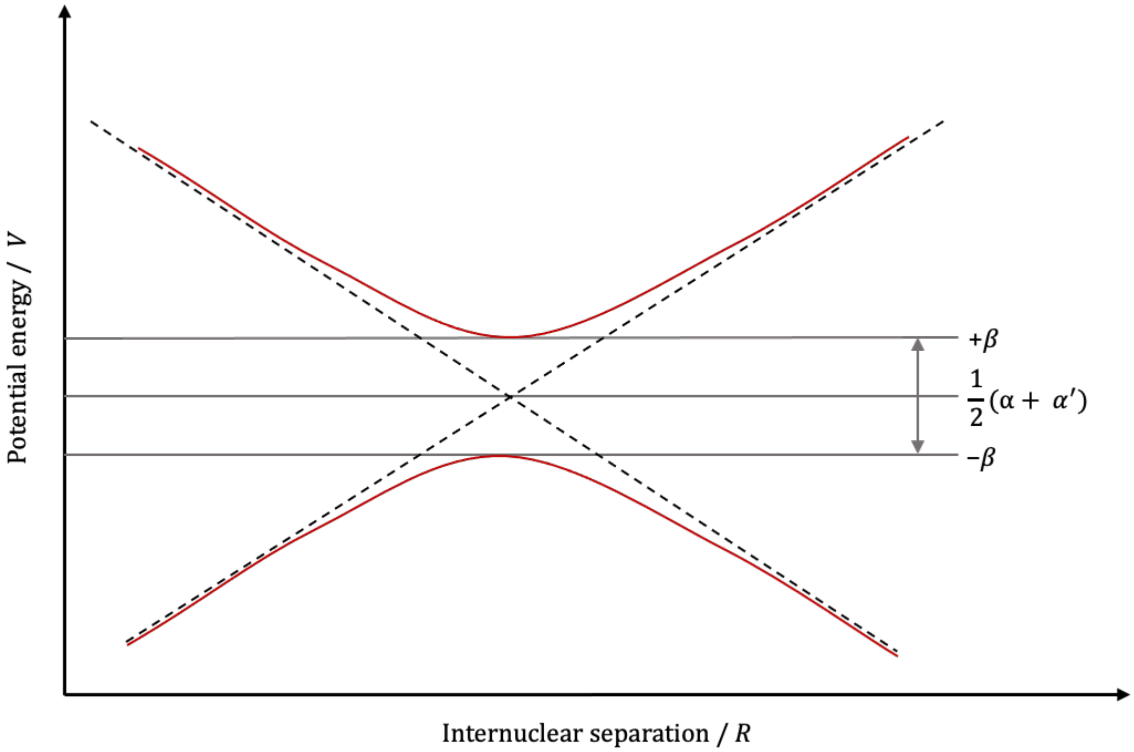

Figure 2.7: representation of an avoided crossing between two Potential Energy Surfaces (PESs).

If α is the energy of the first state (H_{11}) and α' is, instead, the energy of the second state (H_{22}), the interaction terms between the two states (H_{12} and H_{21}) will be equal (β). Accordingly, the secular determinant will be:

$$\begin{vmatrix} \alpha - E & \beta \\ \beta & \alpha' - E \end{vmatrix}, \tag{23}$$

with solutions:

$$E_{\pm} = \frac{1}{2}\left[(\alpha + \alpha') \pm \sqrt{(\alpha - \alpha')^2 + 4\beta^2}\right]. \tag{24}$$

Therefore, if $\alpha = \alpha'$ the energy will correspond to:

$$E_{\pm} = \frac{1}{2}(\alpha + \alpha') \pm \beta, \tag{25}$$

or, in other terms, the energy is equal to the average of both states, resulting in a spacing between the two PESs equal to 2β. If the two states present different symmetry or spin, and a coupling term $\beta = 0$, the two PESs can cross; their encounter is called *accidental crossing*.

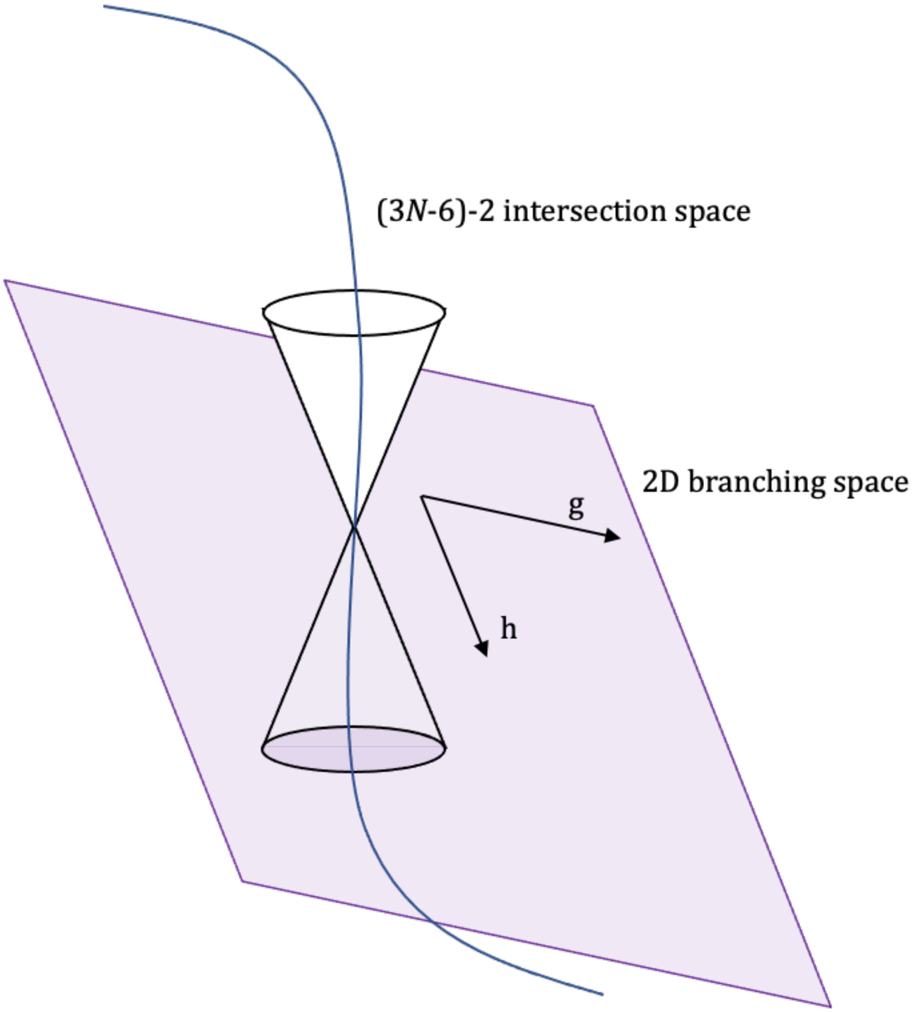

Figure 2.8: representation of the double-conical structure of a conical intersection (CI).

On the other hand, in the case of two states with the same spin and the same symmetry, the off-diagonals terms will be equal to zero only when the subspace comprises D – 2 dimensions, with D corresponding to the number of degrees of freedom of the system.[35] Since diatomic molecules present only one degree of freedom, this condition can never be satisfied, hence leading to the so-called *non-crossing rule*. Conversely, as non-linear polyatomic molecules have $D = 3N - 6$, with N

corresponding to the number of atoms, the crossing between PESs can occur. The region of degeneracy is called Conical Intersection (CI), as the crossing surface has the shape of a cone. Due to the strong coupling between nuclei and electrons, CIs represent a violation of the BO approximation, and the dynamics that take place through CIs are called non-adiabatic.[35]

The two dimensions that are not involved in the subspace and that can remove the degeneracy are named branching vectors, g and h:

$$g = \frac{\partial(E_1 - E_2)}{\partial q} \text{ and } h = \left\langle \varphi_1 \middle| \frac{\partial H}{\partial q} \middle| \varphi_2 \right\rangle, \tag{26}$$

also known as the gradient difference vector and the derivative coupling vector. These two vectors create a bi-dimensional subspace called branching space. The coordinate q represents nuclear displacement. A visual representation of the conical shape of a CI can be seen in Figure 2.8.

As population can very efficiently flow through CIs, the dynamics are only limited by the wavepacket motion on the PES towards the CI. Therefore, dynamics developing through CIs, usually take place in very short timescales (10^{-14} s).

2.4 Electron damage in DNA

2.4.1 DNA overview

Deoxyribo-Nucleic Acid (DNA) is a large biological macromolecule formed by two chains arranged in a double helical layout. DNA and Ribo-Nucleic Acid (RNA) are called nucleic acids, since their first discovery in the nucleus of cells. As DNA carries all the genetic information of all living organisms, as well as of some virus species, the understanding of its structure and function is one of the most researched biological topics.

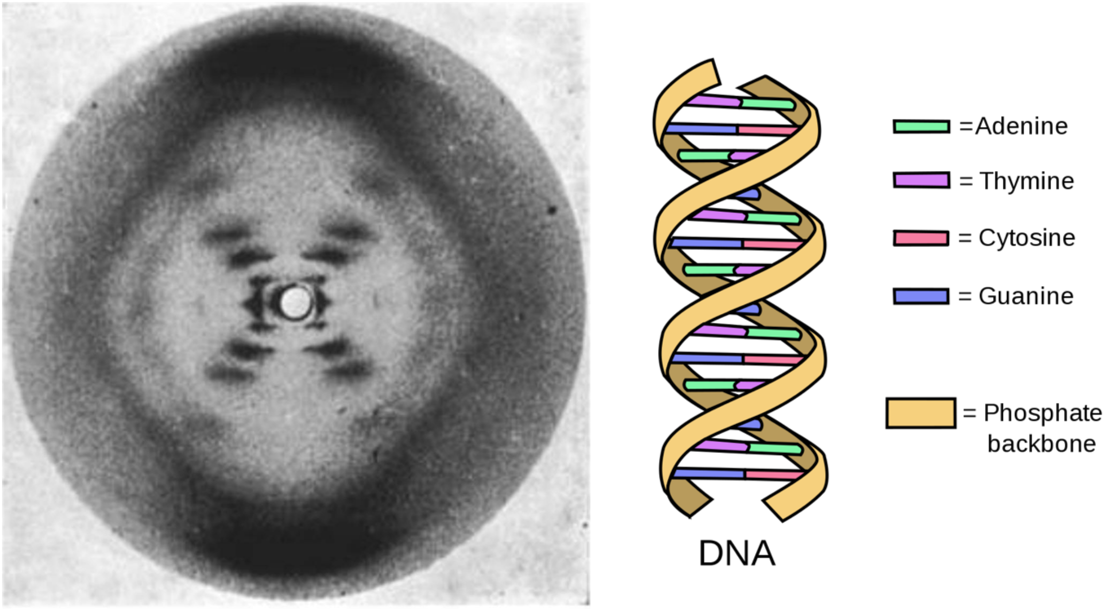

Figure 2.9: on the left is the first crystallographic image of the double helix of DNA. Credits to the respective owners.[36] *On the right is a graphical representation of the double helix. Source: wikicommons.*

The double helical structure of DNA was first discovered by Rosalind Franklin and coworkers in 1951, and subsequently published by Watson and Crick, through X-ray diffraction analysis of DNA crystal structures (Figure 2.10).[36] Each of the two DNA strands is composed of an elongated series of monomers, named nucleotides, linked one another. As can be seen in Figure 2.10, each nucleotide is formed by three components: a single-ringed or double-ringed nucleobase (blue), a pentose sugar called deoxyribose (green) and one or more phosphate groups (red), up to a maximum of three. In RNA, deoxyribose is substituted by ribose, which only differs from the former for the presence of an –OH functional group at the C2' terminus (Figure 2.11). The monomers are bound to each other through molecular interactions between bases, thus giving rise to the typical helical structure of nucleic acids.

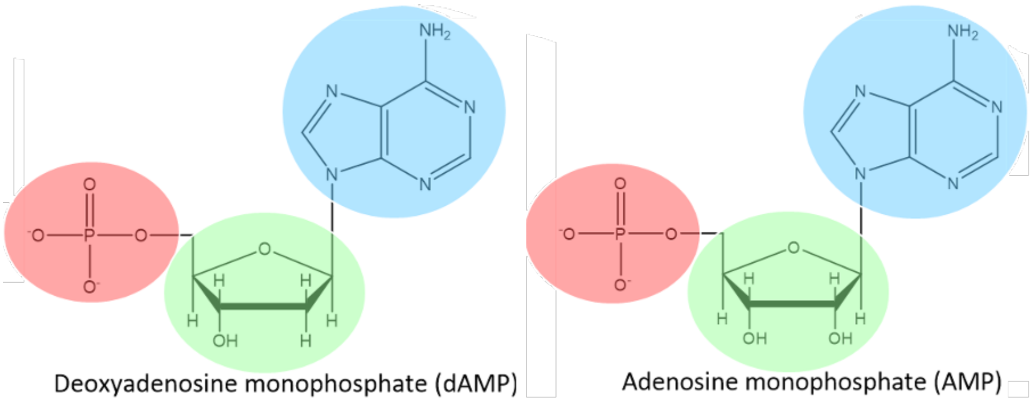

Figure 2.10: general structure of a nucleotide, using Deoxy-Adenosine Mono-Phosphate (dAMP) and Adenosine Mono-Phosphate (AMP) as an example. Each nucleotide comprises a nucleobase, a five-carbon monosaccharide and from one to three phosphate groups.

The precursors of the nucleobases are pyrimidine and purine, two nitrogen-containing aromatic compounds with, respectively, one and two rings. Depending on the precursor, nucleobases are classified as purines or pyrimidines. A purine always pairs with a pyrimidine through hydrogen bonding between the amino and carbonyl groups, and π-stacking between the electron densities of the π-orbitals of the aromatic rings. The purines are Adenine (A) and Guanine (G), whereas the pyrimidines are Thymine (T) and Cytosine (C). In RNA, T is substituted by Uracil (U), (Figure 2.11), which lacks the methyl group in the 5 position. The complementary purine-pyrimidine pairs are C-G and A-T in DNA, and C-G and A-U in doubly stranded RNA. Both DNA and RNA can also contain non-canonical bases, *e.g.*, 5-methyl cytosine and 7-methyl guanine, which arise from the modification of a primary base after the formation of the final strand.

In canonical base pairing (A-T or A-U, and C-G), also known as Watson-Crick base pairing, both bases are arranged in the preferred *anti* conformation.[37] In the *anti*-conformer, the smallest substituent (H-6 for the pyrimidine, H-8 for the purine) is placed above the sugar ring, while in the *syn* conformer it is the largest one (O-2 for the pyrimidine and N-3 for the purine). Therefore, A and T are held together by two hydrogen bridges, while G and C by three. High G-C concentration imparts stability to the DNA strand, although this is mainly due to π-stacking.[38]

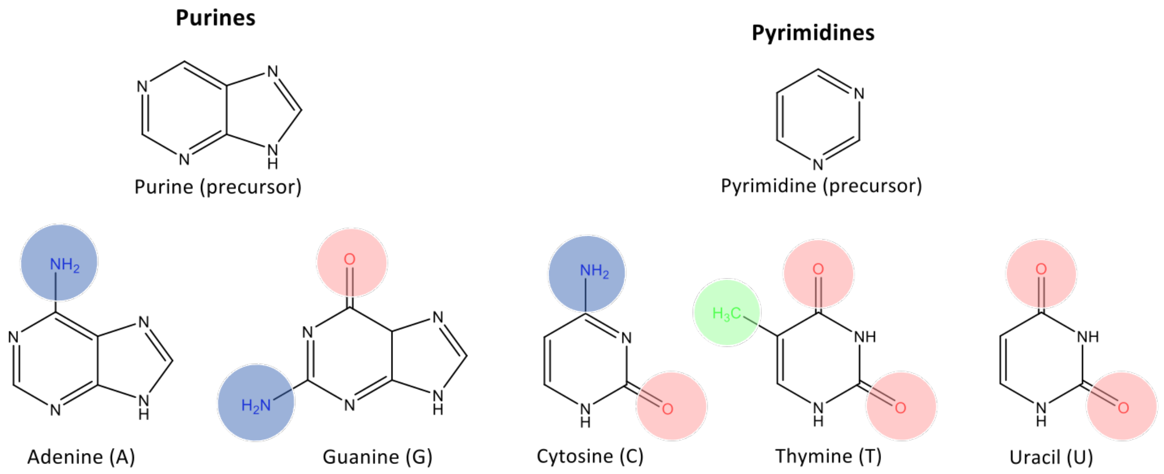

Figure 2.11: in the upper panel are represented the two double-ringed nucleobases that derive from purine, adenine (A) and guanine (G), with two heteroaromatic rings, together with the precursor. The functional groups (amino and carbonyl) that differentiate the nucleobases from the precursor are highlighted, respectively, in blue and red. Lower panel: the three pyrimidine nucleobases, cytosine (C), thymine, (T), and uracil (U), characterized by one heteroaromatic ring, and their precursor, pyrimidine. The functional groups (amino, methyl and carbonyl) that differentiate the nucleobases from the precursor are highlighted, respectively, in blue, green and red.

The most common form of DNA is B-DNA, which is a right-handed double-helix. B-DNA is characterized by a width of approximately 22-26 Å; the helix possesses an extension, named pitch, of roughly 34 Å, although it may vary depending on base stacking levels.[39] About every 10.5 base pairs, the double helix makes one complete turn around its axis. The total number of nucleotides in a double strand of DNA can reach the hundreds of millions, giving rise to very long polymers. Besides B-DNA, other double-helical DNA conformations, such as dehydrated A-DNA and methylated Z-DNA, can also occur, as witnessed both *in vitro* and *in vivo*.[40]

Nucleobases can sometimes form different combinations from the Watson-Crick pairs; these instances take the name of non-canonical pairings. Non-canonical pairings are responsible for less common tertiary structures, *e.g.,* triple or quadruple stranded DNA helices such as G-quadruplexes.[41] One of these less frequent base arrangements is the Hoogsteen hydrogen bonding pairing, in which the pyrimidine takes the *anti* configuration, while the purine is in the *syn* configuration (Figure 2.12).[42] One of the most common examples of Hoogsteen pairing is triple-stranded DNA, in which a third chain of nucleotides coils between the two original B-DNA strands, forming new Hoogsteen hydrogen bonds with the Watson-Crick pairs.[43] In RNA hypoxanthine, a non-canonical nucleoside, can sometimes bind to A, U or C; in this case G binds to U instead of C, thus giving rise to the so-called wobble base pair, which is responsible for a particular secondary RNA structure.[44]

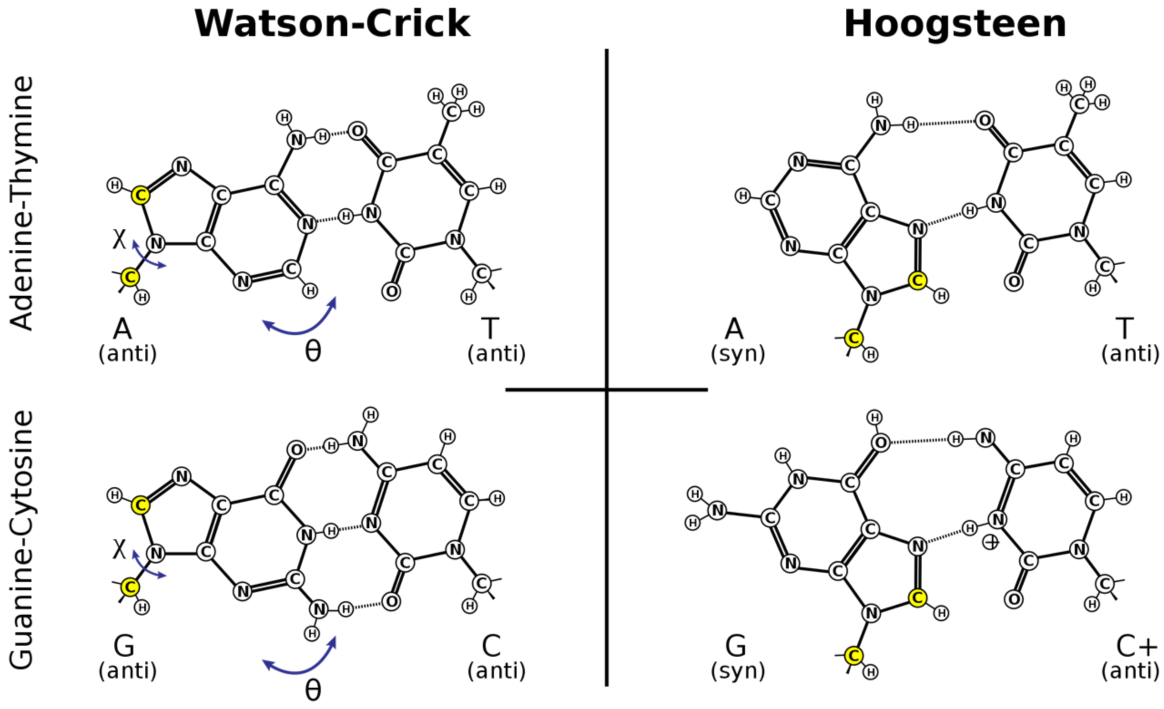

Figure 2.12: examples of Watson-Crick and Hogsteen base pairings in the cases of A-T and G-C. Note that C in the Hosgteen base-pairing is positively charged.

2.4.1.1 Function and biological applications

Inside cells, DNA appears as chromosomes, which are highly spiralized structures composed of DNA strands condensed together with binding proteins. Chromosomes can either be linear or circular, depending on whether the organism is eukaryotic or prokaryotic. In both cases, chromosomes are responsible for the storage of the genetic information of the organism. The complete set of chromosomes of a living organism is called the genome; in particular, the human genome contains a total number of 23 pairs of chromosomes. On the other hand, a gene is the specific and hereditary sequence of nucleotides that contains information about a given protein.[45] Information is copied from a DNA strand to its complementary RNA sequence through a process named transcription. This information is subsequently used by RNA for protein synthesis (translation); however, genetic information can also be transferred from one cell to another during cell division, in a process known as DNA replication.[46] Apart from these four major functions, DNA plays many other pivotal roles in the organism, *e.g.* interacting with other molecules and influencing their function.

As already mentioned, the study of DNA is crucial to fully grasp some of the most important biological functions of a living organism; specifically, understanding the underlying mechanisms of electron and photon-driven DNA damage can help explaining processes like molecular lesions, cell death, tumor development and growth.

2.4.2 DNA damage caused by photons and electrons

2.4.2.1 Photon damage

Thanks to the stabilizing effect of the hydrogen bonding and π-stacking interactions, which are responsible for the double helical structure of the polymer, DNA is chemically unreactive. However, potential damage can originate from ionizing radiation and oxidizing agents.[47, 48] This is because the nucleobases are characterized by the presence of optically bright $^1\pi\pi^*$ states, which can easily absorb Ultra-Violet (UV) light to form nucleobase excited states.[48] Nevertheless, most excitations do not lead to photochemical reactions, as confirmed by DNA's very low fluorescence quantum yield (less than 1%). This is due to the non-radiative decay mechanisms of the nucleobases, which impart photostability to the whole polymer.[49, 50]

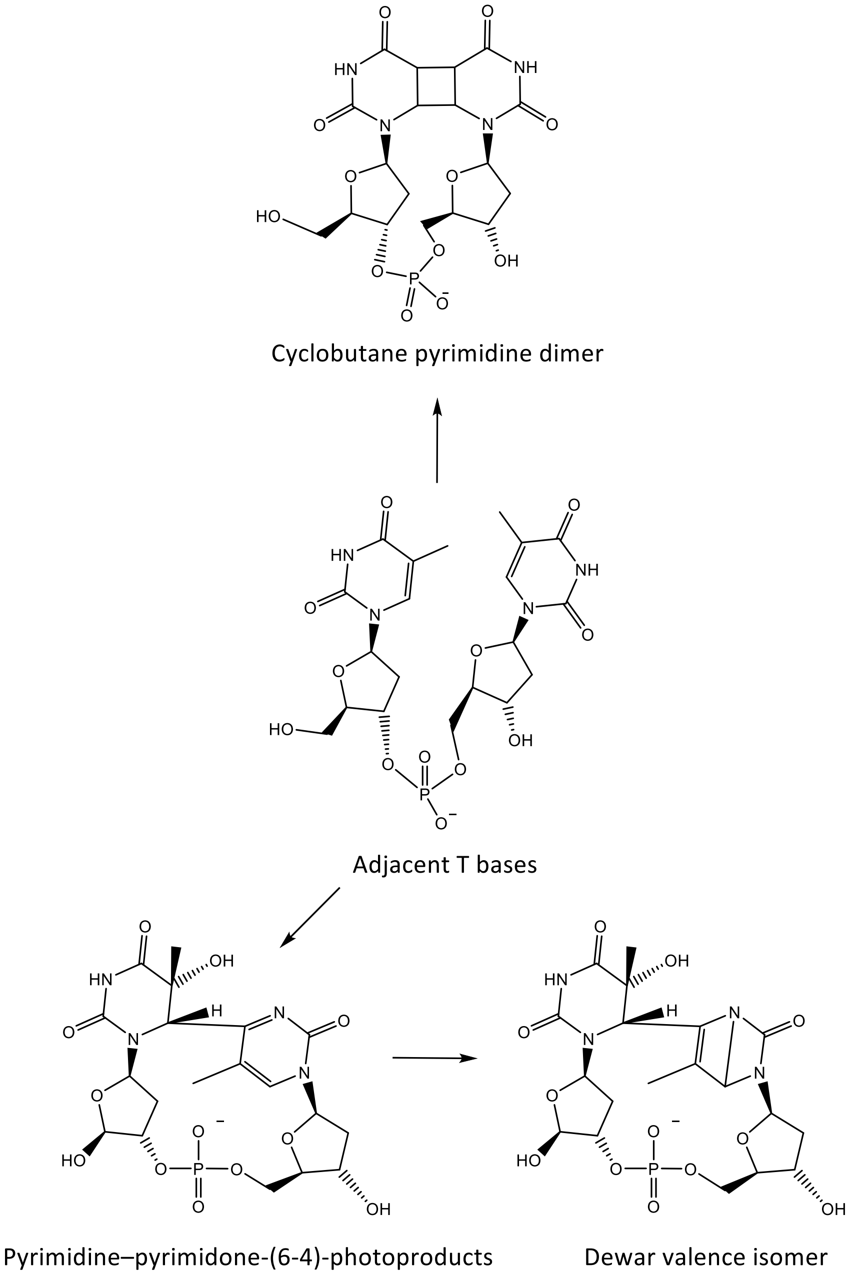

Figure 2.13: scheme of the different photoproducts that can derive from irradiation of DNA with ultraviolet light. Two adjacent pyrimidines can give a Cyclobutane Pyrimidine Dimer (CPD) or a Pyrimidine-Pyrimidone-(6-4)-Photo-Product [(6-4) PP], which can then evolve into a Dewar valence isomer, also known as Dewar lesion.

Despite the photostability of DNA, pyrimidine nucleobases can absorb the energy of the incoming photon and release it by a ring-opening reaction.[51] In particular, in the case of two neighboring pyrimidines, irradiation of the bases with ultraviolet light can induce a photo-isomerization reaction, which leads to the formation of two main photoproducts. These are, respectively, Cyclo-butane Pyrimidine Dimers (CPDs) and Pyrimidine-Pyrimidone-(6-4)-Photoproducts [(6-4)-PPs], which can as well convert into Dewar Valence Isomers (DEWs) (Figure 2.12).[52] These photoproducts are known to be responsible for malfunctions in nucleic acid replication.[53]

CPDs are caused by the formation of a four membered ring between the two pyrimidine nucleobases, which can either be T, C, or the non-canonical base 5-methylcytosine; additionally, the pyrimidines can be found in different conformations. Despite being stable in solution, CPDs degrade upon irradiation with UV-C (100-280 nm) photons, restoring the original nucleobases. Moreover, CPDs can undergo deamination to give a uracil moiety.[54] CPDs mostly arise due to photosensitized triplet-triplet energy transfer, although singlet states seem to play a role also.[55] CPD formation can also be prompted by UV-A light (315-400 nm), but with a much lower yield than UV-B (280-315 nm).

Upon interaction between DNA and UV photons, other less common photoproducts can also arise. Irradiation of DNA with UV-C wavelengths can produce dimeric photoproducts of A and T,[56] or two As,[57] as well as monomeric damage. UV-A light can also induce the formation of singlet oxygen ($^1O_2$) and hydroxyl radicals (OH·). $^1O_2$ can react with G and form 9-oxo-7,8-dihydro-Guanine (9-oxoGua), while OH· can cause single- and double-strand breakage.[55] Furthermore, two Ts can react to give the so-called spore photoproduct, an adduct that has been observed in bacterial spores.[55]

The study of the excited states dynamics of DNA components can shed light on the mechanisms of photodamage and photorepair of DNA. In fact, thanks to their femtosecond-timescale decays, the excited states of nucleobases are quite stable with respect to photochemical degradation.[50] Additionally, DNA derivatives exhibit substantially different behaviors whether they're isolated or in solution. Molecular interactions, like hydrogen bonding and quenching of internal excitation, make the role of the solvent crucial when it comes to decay mechanisms.[58, 59] As previously mentioned, the low fluorescence quantum yield of DNA is explained by their non-radiative decay mechanisms. Moreover, the lifetimes of nucleobase derivatives are considerably longer than the ones of the most common nucleobase tautomers. The sub-picosecond features in the lifetimes of the nucleobases seem to be due to Cis; IC is instead responsible for producing the vibrationally excited population in S_0, that moves away from the initial $^1\pi\pi^*$ state. On the other hand, the role of dark states is not yet completely understood; in particular, the $^1n\pi^*$ state is thought to play a role in the conversion from the $^1\pi\pi^*$ to S_0.[60]

Experimental[61] and computational[62] studies show evidence of photoinduced proton transfer in single base pairs. Watson-Crick pairs also exhibit evidence of electron-driven proton transfer, with a mechanism involving $^1\pi\pi^*$ states with inter-base charge-transfer character.[63] Transient absorption spectroscopy experiments on adenosine dimers yielded evidence of base stacking, showing that stacked structures have longer-lived excited states compared to isolated bases;[64] albeit controversial, the mechanism seem to involve exciplex and excimer states.[65]

Other important gas-phase work involves a molecule that bears the same chromophore as A, Imidazole (I). Like , the dynamics of I is characterized by an IC between $^1\pi\pi^*$ and $^1\pi\sigma^*$, and by a IC between $^1\pi\sigma^*$ and S_0.[66] Time-Resolved Photo-Electron Imaging (TR-PEI) has been used to study the decay mechanism of the deoxy-purine nucleotides, Deoxy-Adenosine-Mono-Phosphate ($dAMP^-$) and Deoxy-Guanine-Mono-Phosphate ($dGMP^-$): analogously to the corresponding isolated bases, $dAMP^-$ and $dGMP^-$ exhibit a biexponential decay composed by a fast (100 fs) and a slow (~1 ps) component. Interestingly, also the di- and tri-nucleotides of $dAMP^-$ show analogous decays.[67] As for the deoxy-pyrimidine nucleotides, while $dTMP^-$ shows a tri-exponential decay (100, 200 and >5000 fs), the decay of $dCMP^-$ can be fitted to a bi-exponential function, although low ionization and absorption cross sections make it difficult to draw any definitive conclusions.[68] Similarly to $dAMP^-$ and $dGMP^-$, also 9Me-Ade decays only through the $^1\pi\pi^*$ state; moreover, the mechanism, which involves a bi-exponential decay,[69] seems to be the same both in the gas and in the condensed phase.[63]

Gas-phase experiments on aqueous clusters of Ade give different results depending on the number of A and water molecules; however, the general observation is an increased activity of the $^1\pi\sigma^*$ states thanks to solvent stabilization.[70]

2.4.2.2 Electron damage

DNA damage can arise from different sources, *e.g.,* radiation or oxidizing agents.[47, 48] In the case of high-energy radiation such as X-rays, the highest amount of damage is produced via secondary reactions involving the species generated in the first instance. Ionization of water produces secondary electrons, typically with kinetic energy (E_{ke}) within the 0-20 eV range, called Low Energy Electrons (LEEs).[71, 72] LEEs are often the cause of fatal DNA lesions, *e.g.*, Single-Strand Break (SSB) and Double-Strand Break (DSB).[73] Additionally, LEEs can cause damage also in supercoiled DNA, even below the ionization threshold.[73]

LEEs can attach to any of the nucleotide's components, or even as a Dipole Bound State (DBS) outside the molecular framework.[74-78] The damage is, in fact, caused by the formation of Transient Negative Ions (TNIs), also known as resonances, of the various building blocks of DNA; resonances are known to induce mutagenesis in living organisms.[79, 80] The difference in electronic structure between the two main types of resonances, Feshbach and shape resonances, is shown in Figure 2.13. In particular, core-excited (Feshbach) resonances, which arise from electron attachment to the π* orbitals of the nucleobases, are responsible for single-strand breaks.[2] On the other hand, shape resonances are produced by LEEs with E_{ke} < 3 eV,[74, 81, 82] and can induce dehydrogenation as well as cleavage of the phosphodiester and glycosidic bonds.[71, 73, 83-85] After electron attachment and production of a shape resonance, no further excitation is prompted.[74] The mechanism of σ bond dissociation can be explained through a migration of the electron from the π* orbital of the base to the σ* orbital of the C-O, N_1-C or N-H bond. Electrons can attach to the π* orbital of a nucleobase, as these orbitals are capable of hosting an electron that falls in the energy range of 0.1-2 eV: this can then produce covalent bond breakage, particularly in the case of C and T nucleobases.[71] Dissociation of the σ bond is then elicited by the repulsive energy profile of the σ* anion state. The electron is transported to the antibonding σ* orbitals; hence, bond breakage occurs through three saturated bonds. [71, 80, 86, 87] It is also suggested by both experimental and computational works that electrons with energy > 2 eV can occupy the π* orbital of the phosphate group and contribute to SSB formation.[88] The phosphodiester bond and the N_1-C bond are the most sensitive to shape resonances, due to the low electron energy barrier and the high electron affinity that characterize the phosphate groups.[89] These bonds are highlighted in Figure 2.14. Moreover, the N_1-C glycosidic bond between sugar and base[73] can be disrupted at E_{ke}

~0 eV,[90] although the barrier to surmount in this case is higher than for the C-O bond.[71]

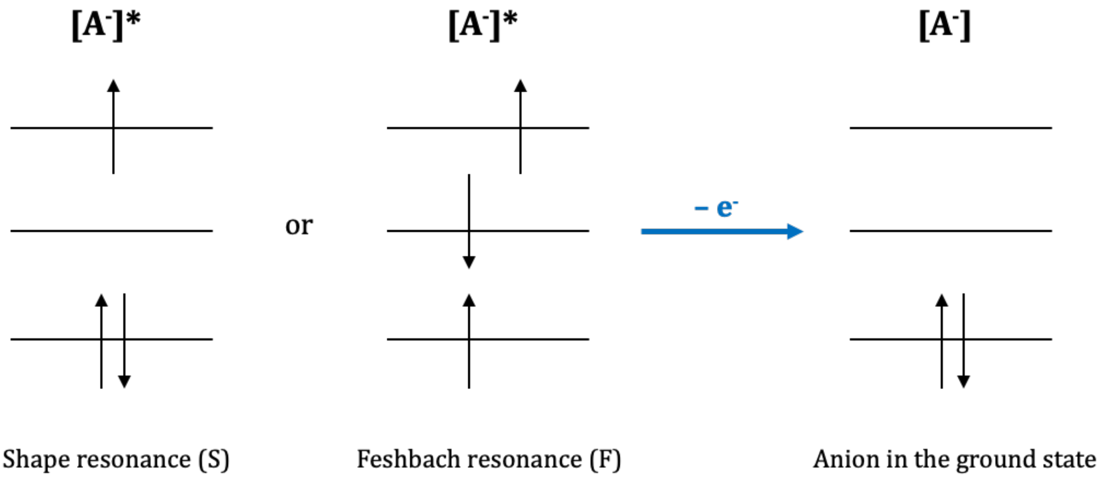

Figure 2.13: schematics of the electronic structure of a shape resonance and of a Feshbach resonance.

LEE-induced damage has been extensively studied by Sanche and co-workers through electron scattering measurements, in which the DNA sample is irradiated with an electron beam to generate the products, which are then subsequently probed.[2, 3, 73, 76, 79, 80, 87-89] Nevertheless, time-resolution is required to fully understand the underlying mechanisms of action, and this is not a simple feat. Molecules with positive electron affinity can be studied by time-resolved photoelectron spectroscopy, which allows the determination of the mechanisms by accessing the resonance states from anionic ground states.[91, 92] Johnson and co-workers have instead exploited iodide as a source of electrons, photoexciting iodide-molecule clusters to reach the dipole-bound state of the clustered molecule.[93-98] Time-resolved photoelectron imaging studies of such clusters, particularly $I^{-}\bullet N$ (N = nucleobase) clusters, have been extensively performed by the Neumark group.[99-103] Although efficient, issues may arise when probing charge-transfer in this way, namely due to the role of iodide, which is not yet well understood, and due to the photon energy used, which could correspond to nucleobase absorption bands.[104, 105]

Dehydrogenation has been classified as a predominant dissociative channel and takes place through Dissociative Electron Attachment (DEA). TNIs can undergo dissociation and prompt dehydrogenation of the nucleobases from cleavage of the N-

H bond, as seen by the decay of electronic states from the N sites of T and computational studies on other bases. The electron affinities of the dehydrogenated radicals span from 3.5 to 4 eV.[83]

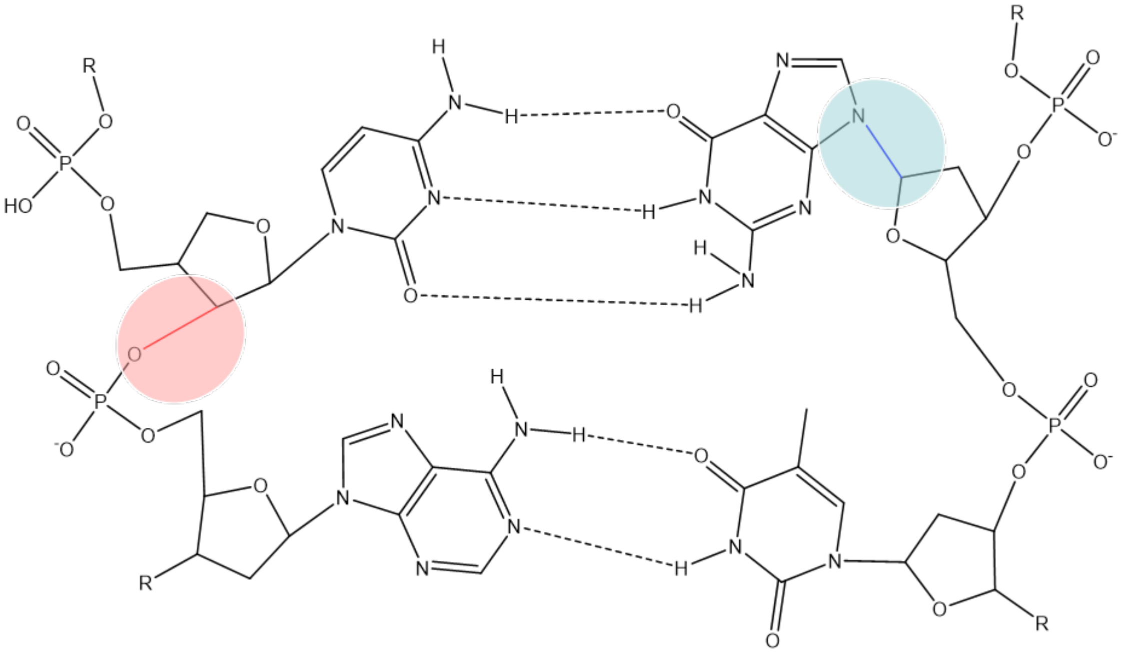

Figure 2.14: the four DNA bases in Watson-Crick pairings with highlighted the phosphodiester (red) and the glycosidic (blue) bonds, whose cleavage leads to SSB formation.

2.4.2.3 Motivation of the project

As explained in the previous sections of the Introduction, electron and photon-induced DNA damage represents one of the principal factors of several biological processes, *e.g.* cell death and mutations. [106] Specifically, the attachment of an LEE can cause breakage not only in complex structures, such as single and double-stranded DNA, but also in its smaller components, such as isolated bases, nucleosides, nucleotides, and small aggregates of the latter.[2]

This thesis explores the extent of LEE damage on DNA and its components, exploiting the concept of charge-transfer in an anionic species as a probe for electron damage. We applied one color and resonance-enhanced PE spectroscopy, as well as frequency and time-resolved photoelectron spectroscopy, to characterize several systems of interest, starting with a model molecule and moving on towards more complex systems, *i.e.*, nucleotide triphosphates. Although non-exhaustive, this study represents a stepping-stone in shedding light on the mechanisms of both electron and photon damage in DNA.

Experimental section

3.1 Experimental setup

The conception and the accurate details of the TR-PEI instrument can be found in the original publication by Lecointre *et al.*[107] A schematic representation is shown in Figure 3.1. The instrument is divided into eight distinct regions (R_0, R_1, R_2, R_{trap}, R_3, R_4, R_5 and R_6), characterized by gradually decreasing levels of pressure, from atmospheric pressure (760 Torr) to 10^{-9} Torr. The pressure in each region is kept constant by a set of six turbo pumps, aided by the action of four backing pumps, which can be opened and closed through pneumatic or manual valves. Four ion gauges and six thermocouples monitor the pressures in each differentially pressured region and in each backing pump.

A ~1 mM methanolic solution of the chosen analyte is inserted through a syringe in a Electro-Spray Ionization (ESI) capillary tube with a voltage of –5 kV at atmospheric pressure (R_0). Anions are produced by deprotonation and introduced by the capillary into a first vacuum region. The ions are then guided by a gradient of potential energy through a tube, formed by a series of ring-electrode ion guides divided in three regions (R_1, R_2 and R_{trap}), until the ions reach a pulsed ion trap.[108] The trap can be opened and closed and its action is governed by a microsecond-pulse generator, allowing the accumulation of the ions and providing a first separation in terms of time window. After exiting the trap, the ions are directed towards a collinear Wiley–McLaren Time-Of-Flight Mass-Spectrometer (TOF-MS),[109] formed by three TOF plates with different voltages, through an Einzel lens, which focuses the ion beam and aids the formation of the ion packets (R_3). This area is separated by the rest of the instrument through a pneumatic gate valve, which can be opened and closed to allow the flow of ions to pass through. The mass-selected ion packets are then guided through two different sets of deflectors and Einzel lenses (R_4 and R_5), which serve the purpose of focusing the beam further along. At the focus of the TOF, the ion packet is irradiated with either femtosecond or nanosecond laser pulses and mass-selection is achieved by timing the laser/ion packet overlap to excite only one *m/z*.

The laser pulses are obtained either with a tunable laser (an Nd:YAG pumped optical parametric oscillator, Continuum Surelite and Horizon) for frequency-resolved experiments, or with a commercial femtosecond laser (Ti:Sapphire oscillator and regenerative amplifier, Spectra Physics Tsunami and Spitfire XP), producing fundamental pulses centered at 1.55 eV (800 nm) and with ~50 fs duration, when doing time-resolved experiments. The photoelectrons are collected and imaged by a perpendicular VMI arrangement (R_6).

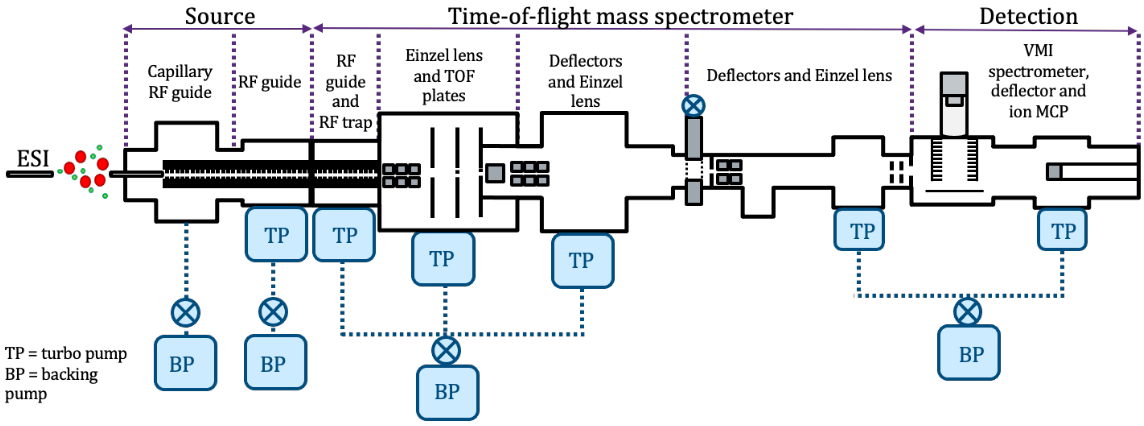

Figure 3.1: schematics of the in-house TR-PEI instrument.

3.1.1 Platinum plating and noise reduction

During the experiments performed with 4.66 eV light, intense Photo-Electron (PE) noise coming from photons striking the VMI electrodes was experienced. This is due to the fact that the work function of stainless steel is very close to this energy. High noise levels are incredibly detrimental to spectral quality, particularly in the case of time-resolved experiments. To solve this problem, two different approaches were tested. First, the bottom VMI plate was equipped with a fine mesh layer in stainless steel, which can retain these “unwanted” photoelectrons and prevent them from reaching the detector. The mechanism of the mesh is showed in Figure 3.2. The electric field lines of the mesh do not change the overall macroscopic electric field of the VMI setup; nevertheless, they can change the electric field at a microscopical level, as they are large enough to “trap” the photoelectrons coming from the bottom plate and reflect them back onto a electrode below the mesh. Unfortunately, this method did not yield the desired level of noise-reduction; for this reason, we resorted to platinum-plating of the VMI electrodes.

The second approach consisted in coating the top and bottom VMI electrodes with platinum, whose work function is higher than 5 eV, contrarily to stainless steel, which presents a work function of ~4.6 eV.[110] At $h\nu$ = 4.66 eV, the noise-reduction was approximately of an order of magnitude compared to the VMI assembly with the mesh. As an additional noise-subtraction method, the PE signal was collected both in the presence and absence of the ion beam. This was achieved through opening and closing the ion trap at ~1 Hz; the PE images without ions were then used as background and subtracted from the PE images with ions. Moreover, opening and closing the trap also leads to higher signal levels, as the loading rate of the trap is too low to fill the trap completely before it is emptied at 100 Hz. Consequently, if more ions can accumulate off-cycle, more ions can then be extracted from the trap.

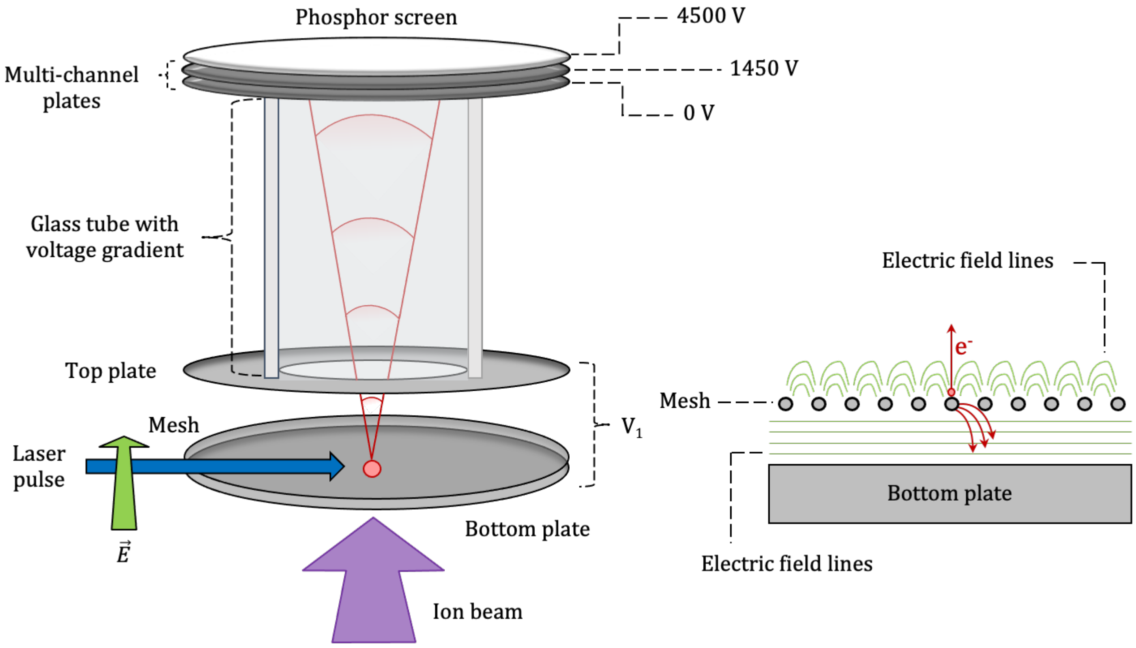

Figure 3.2: schematics of the Velocity Map Imaging (VMI) setup with the mesh layer on the bottom plate. A representation of the mechanism of action of the mesh is visible on the right side of the picture.

3.2 Theoretical methods

Density Functional Theory (DFT) calculations on C-Ado$^-$ were performed at the B3LYP (Becke three-parameter hybrid functional combined with Lee-Yang-Parr correlation functional) level of theory[111] with the 6-311G basis set, with addition of diffuse and polarization functions (6-311G++**), on the software Gaussian09, and the results visualized with GaussView. The Electron Affinity (EA) or Adiabatic Detachment Energy (ADE), and the Vertical Detachment Energy (VDE), the most intense FC feature, were calculated, respectively, as the difference in energy between the neutral in optimized geometry and the anion in optimized geometry, and as the difference in energy between the neutral in anion geometry and the anion in optimized geometry.

The theoretical study on $[ATP-H_2]^{2-}$ was performed by Dr. Davide Avagliano from Prof. Dr. Leticia Gonzalez's group at the University of Vienna. $[ATP-H_2]^{2-}$ was optimized using Møller-Plesset second-order perturbation theory with resolution of identity approximation (RI-MP2)[112] and the def2-TZVP basis set.[113] The ground state energy was then refined with the def2-QZVP[113] basis set. The first five excitation energies were obtained with the Algebraic Diagrammatic Construction scheme for the polarization propagator at the second order (ADC(2))[114] method and the same def2-QZVP[113] basis set. The RCB was calculated using the Local Static Approximation model,[115] in which the energy for the monoanion plus a point-charge electron (in the geometry of the $[ATP-H_2]^{2-}$) was calculated with an interval of 0.5 Å. Two planes (*xz* and *yz*) were considered, which pass through the transition dipole moment vector connecting the S_0 and S_2 state. RCB calculations were performed at MP2/def2-SVP level of theory. Ground state *ab initio* molecular dynamics were carried out at B3LYP[116, 117]/aug-cc-pVDZ[118] level of theory, starting from the $[ATP-H_2]^{2-}$ minimum energy geometry.

3.3 Data analysis

The Polar Onion Peeling (POP) algorithm developed by Roberts *et al.* [119] was used to extract the Photo-Electron (PE) spectra from the raw PE images. The method exploits onion peeling in polar coordinates. The well-known atomic spectrum of I^- was used as reference for spectral calibration; all the recorded spectra present spectral resolution of approximately 5%.

The VDE was taken as the highest point in the PE spectrum. The ADE was measured by making a linear fit to the steepest edge of the peak and extracting the value of the variable x from the equation of the corresponding straight line.

In the $[ATP–H_2]^{2-}$ study, as a second analysis method, a global fit to the time-resolved data was performed. The global fit is formulated as:

$$f(E_{\mathrm{ke}}, t) = \sum_i g(t) \otimes c_i(E_{\mathrm{ke}}) e^{-t/\tau_i}, \qquad (27)$$

where $c_i(E_{\mathrm{ke}})$ represent photoelectron spectra that are associated with specific decays with lifetime τ_i (so-called decay-associated spectra). These are convoluted with the instrument response function, $g(t)$ (the cross-correlation of pump and probe pulses, which is assumed to be a Gaussian function with full-width at half-maximum of 100 fs).

Dipole-bound states in para-substituted phenolate anions

4. Dipole bound states of para-substituted phenolate anions

The contents of this chapter are based on the following publication: Castellani, M. E.; Anstöter, C. S.; Verlet, J. R. R., On the stability of a dipole-bound state in the presence of a molecule. *Phys. Chem. Chem. Phys.* **2019,** *21* (44), 24286-24290.[120]

4.1 Motivation

First predicted by Fermi and Teller in 1947,[121] experimental evidence shows that, if a molecule presents a permanent dipole of more than ~2.5 D, a non-valence state known as Dipole-Bound State (DBSs) can be formed. [19, 122, 123] Due to the weak interaction that binds the electron to the neutral molecule, the DBS appears as a highly diffuse, atomic-like orbital, similarly to a Rydberg state in a neutral molecule.[124] DBSs can act as "door-way" states to electron attachment;[99, 125-129] moreover, the study of DBS is relevant to DNA as these resonance states are thought to be heavily involved in electron driven processes of its monomers and polymers.[102, 128, 130-134] For this reason, we decided to start our exploration of low-energy electron damage from the viability of a DBS in the presence of another molecule using a model anion.

Usually, DBSs are studied through photodetachment action spectroscopy,[135-141] photoelectron spectroscopy,[130, 138, 142-153] or, in some cases, also through by Rydberg electron-transfer spectroscopy, specifically when exploring their role in electron attachment dynamics.[154, 155] So far, dipole-bound anions have only been observed in the gas phase, both in isolated molecules and cluster experiments. However, there is currently no evidence of the subsistence of these states when something actively interacts with the DBS, or when the molecule is surrounded by an environment, *e.g.,* in solution. In this work, we study the stability of a DBS in presence of a second molecule by spectroscopically investigating a test molecule with Frequency-Resolved Photo-Electron Imaging (FR-PEI), resonance-enhanced two-photon photoelectron imaging (R2P-PEI) and electron yield (action) spectroscopy measurements. The test model exploits a molecule with known DBS, substituted with an alkyl chain that interacts with the DBS, “poking” into it. To avoid a significant alteration of the dipole moment, a saturated hydrocarbon chain was chosen as substituent. The phenolate anion ($C_6H_5O^-$) was selected as model: as already observed by the Wang group,[156, 157] phenolate presents a DBS as anionic excited state at a wavelength of approximately 553 nm. We then compared the stability of the DBS in five para-substituted phenolates with alkyl chains of different length. The model of the para-substituted phenolates with the hydrocarbon tail poking the DBS is exemplified in Figure 4.1. Calculations show that the increase in alkyl chain length has a minimal impact on the overall dipole moment of the neutral core.

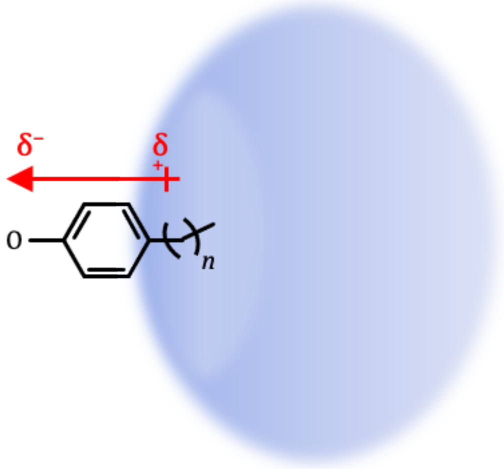

Figure 4.1: Representation of the dipole-bound state (DBS) of a para-substituted alkyl-phenolate anion with an alkyl chain of varying length, n-ph⁻.

4.2 Methods

The details of the experiment have been described in the dedicated section (page 41, Experimental Setup). Phenol (ph), 4-ethylphenol (2-ph), 4-propylphenol (3-ph), 4-pentylphenol (5-ph) and 4-octylphenol (8-ph) were purchased from Sigma Aldrich and 4-butylphenol (4-ph) from Tokyo Chemical Industry. The para-substituted phenolate anions, *n*-ph⁻, were produced by deprotonation of the methanolic solution

(~1 mM) through electrospray ionization. The details of the instrument can be found in the relevant chapter of this Thesis. The spectra were calibrated using the EA value of ph of 2.235(6) eV reported by the Lineberger group.[158]

4.3 Results

All the action spectroscopy experiments were performed at a VMI potential of 500 V. Figure 4.2, shows the action spectrum of ph⁻ (solid black line) compared to the results obtained by the Wang group (dashed vertical lines) with much higher resolution and at a temperature of 20 K.[156]

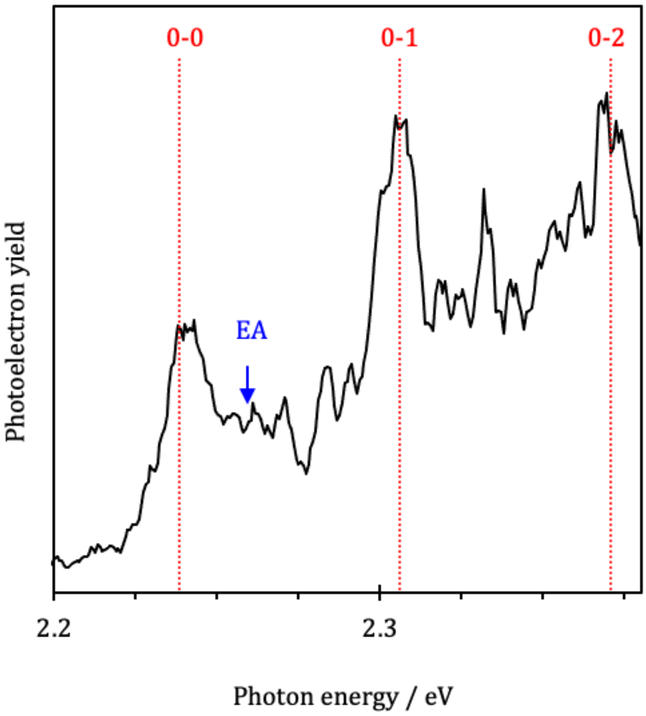

Figure 4.2: photodetachment action spectra for ph; the vertical lines indicate the transitions and the electron affinity (EA) observed by Liu et al.[156] The bands were assigned following the same annotation as the authors.

The considered wavelength range is 520-570 nm. The first band, at 553.22 nm, corresponds to the 0-0 transition of the DBS. The EA of the anion can be found at the beginning of the edge rise, at 550.27 nm. The other two bands, at 537.78 and 523.33

nm, correspond, respectively, to the 0-1 and 0-2 vibrational transitions, and correspond to the CCC bend.

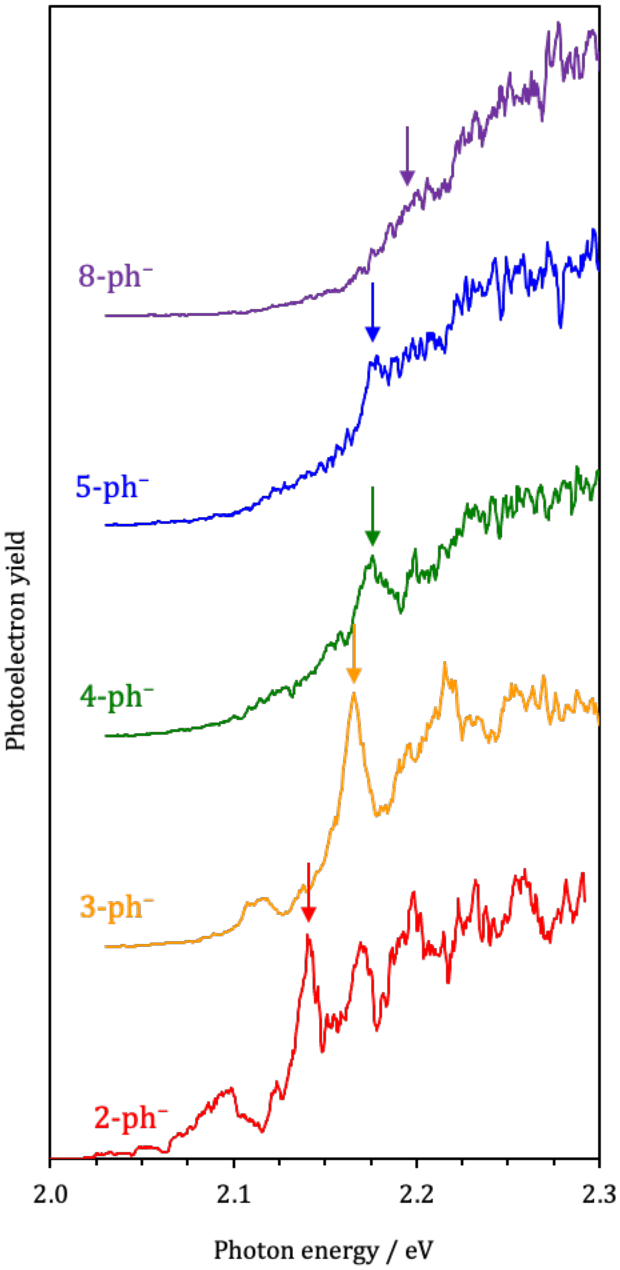

Figure 4.3: photodetachment action spectra for n-ph⁻ with n = 2-5 and 8, recorded near the photodetachment threshold; the vertical arrows highlight the excitation energy used for the resonance-enhanced photoelectron spectroscopy experiments, whose results are shown in Figure 4.4.

In Figure 4.3 are depicted the stacked action spectra of the five para-substituted phenolates between 2.0-2.3 eV. The energy of the 0-0 transition steadily shifts towards higher photon energy as more methylene bridges are added to the alkyl chain. In the cases of 2-ph⁻ and 3-ph⁻, the same bands that are present in the spectrum of ph⁻ can still be distinguished. Furthermore, as for ph⁻, a hot band can be seen just before the 0-0 transition peak. As the length of the chain increases, the peak resolution decreases dramatically, especially from 4-ph⁻ onwards. In 8-ph⁻, the 0-0 transition peak is almost impossible to assign. A plausible explanation for this drop in resolution could be that the DBS becomes highly unstable, to the point of being completely disrupted, when a sufficiently long chain is perturbing it. In that case, one would expect to see only the onset of direct detachment.

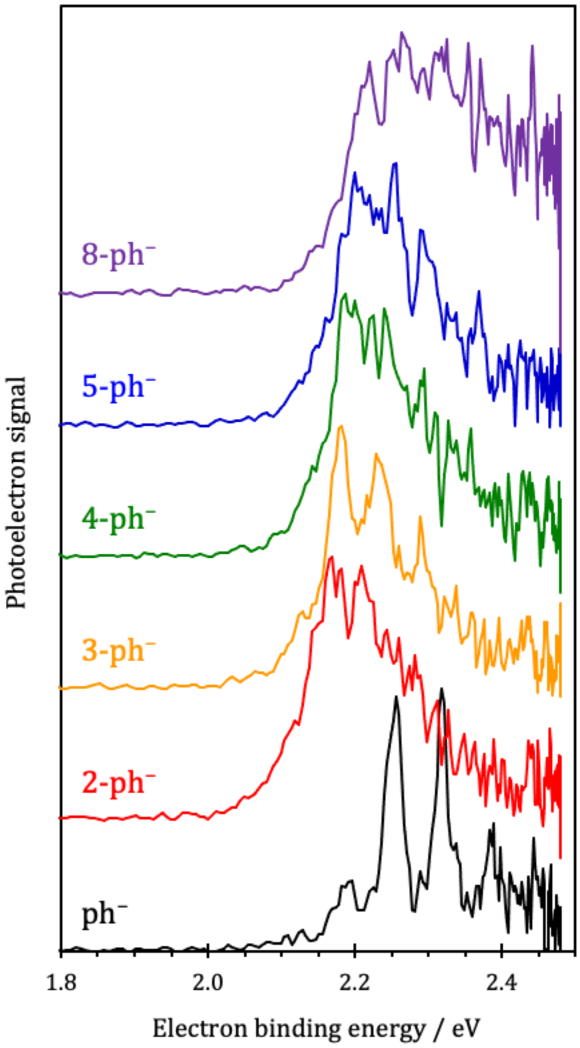

Figure 4.4: one-photon photoelectron spectra of phenolate and para-substituted alkyl-phenolate anions taken at hv = 2.48 eV (500 nm), with VMI = 250 V. Spectra have been vertically offset for clarity.

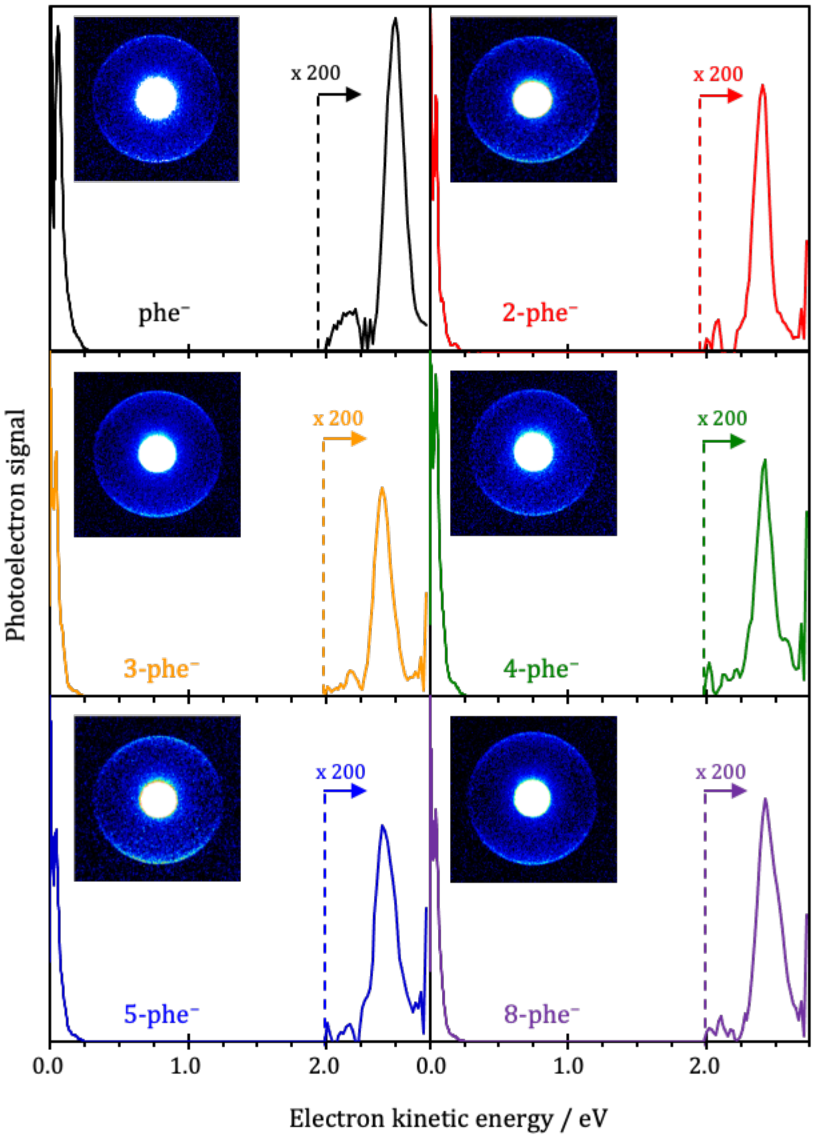

Figure 4.5: two-photon resonance-enhanced photoelectron spectra of phenolate and para-substituted alkyl-phenolate anions recorded at photon energies that are resonant with the DBS. The signal has been amplified at higher electron kinetic energies (>2.0 eV) to highlight the DBS peak. The respective raw photoelectron images are included as insets in each spectrum; the central feature has been intentionally saturated to visualize the outer narrow and anisotropic ring, which corresponds to the DBS peak in the spectrum.

The blue-shift of the DBS peak witnessed in the action spectra of para-substituted phenolates can be explained by the trend in EA shown in Figure 4.4. Figure 4.4 contains the stacked one-photon PE spectra of n-ph⁻, recorded at a wavelength of 500 nm (2.48 eV) with a VMI potential of 250 V. The EA values extracted from the spectra are 2.358 eV (552.23 nm) for ph⁻, 2.302 eV (578.00 nm) for 2-ph⁻, 2.321 eV (571.22 nm) for 3-ph⁻, 2.323 eV (569.40 nm) for 4-ph⁻, 2.326 eV for 5-ph⁻ (569.90 nm) and

2.330 eV (562.00 nm) for 8-ph$^-$. As a result, we can observe that when an alkyl substituent of given length is added in para position, the EA reduces, and then slowly rises again as the chain becomes longer. Therefore, para-substituted phenolates with longer alkyl groups show a higher 0-0 transition energy for the DBS peak as well.

To investigate the origin of the apparent progressive loss of the DBS (as implied by Figure 4.3), resonant-PE images of all compounds were recorded at the 0-0 transition energies attained from the action spectroscopy experiments. All the resonant-PE images and the corresponding PE spectra can be seen in Figure 4.5. The PE images shows two rings: the bright, inner feature arises from one-photon direct detachment and vibrational autodetachment, while the outer, faint, and narrow peak corresponds to the DBS. As the DBS ring is very dim, saturation of the one-photon detachment channel was necessary to visualize the DBS peak in the PE spectrum. In fact, although the extracted spectra seem to present only one feature, for every compound a smaller peak can be seen around $E_{\mathrm{ke}} \sim 2.5$ eV. Magnifications of the peak are included as insets in each spectrum; the peak is assigned as the two-photon resonant signal. As the PAD for these features in the PE images are parallel to the polarization axis, we can determine that the outgoing photoelectron is predominantly a p-wave. Since $h\nu$ is carrier of a single unit of angular momentum, the initial orbital is therefore an s-state, consistent with a DBS. Hence, despite the presence of the alkyl chain interacting with it, the DBS seems to exist in all cases.

4.4 Discussion

If the DBS is retained in each compound, then why do we lose resolution in the action spectra? As the alkyl substituents are not rigid, multiple conformers can be generated for each chain. We also performed DFT calculations on 5-ph$^-$, and have shown that the difference in energy between the optimized geometries of the fully extended and fully curled alkyl chain isomers is approximately ~0.12 eV.[120] The conformational change by the molecules will therefore cause a shift in the electron binding energy (E_{be}) of the DBS, resulting in a decrease in resolution. As the experiment is conducted at room temperature (300 K), many different conformers will be accessible for each chain. As every conformation will interact differently with the DBS, the DBS will present a range of varying electron binding energies, as shown schematically in Figure 4.6. Moreover, as the tail becomes longer the number of available conformers will increase, thus explaining why the loss of resolution is proportional to chain length.

Alternatively, the loss of resolution could be caused by different EA for different conformations, producing a change in excitation energy to the DBS. Nevertheless, as the PE spectra do not exhibit a change in gradient for the rising edge of the spectra, this does not seem to be the case. Moreover, the loss of resolution has already been observed for 2-ph in the past.[16, 159] Another explanation could be that only some conformers, *e.g.,* the ones in which the alkyl chain does not interact with the DBS, retain the DBS. However, if this were the case, only those conformers could be observed, causing a considerable loss of resonance-enhanced signal (Figure 4.4), which does not occur.

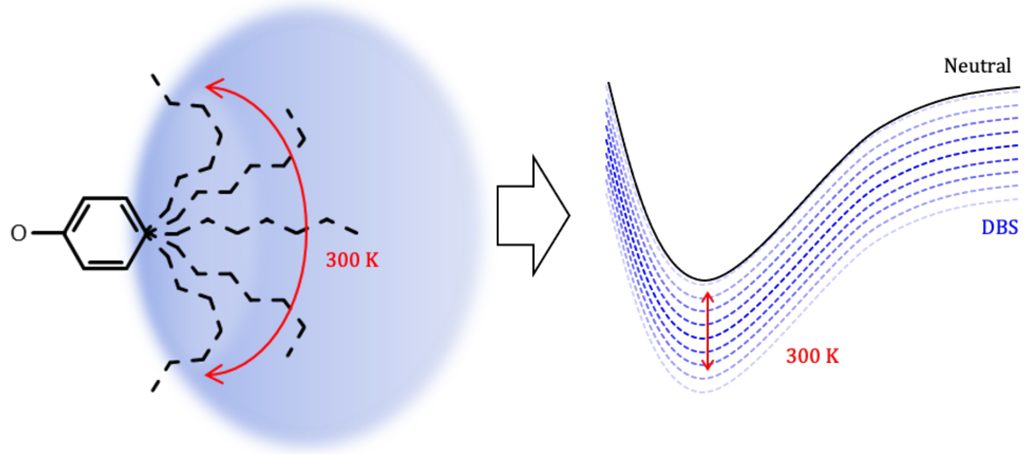

Figure 4.6: Schematic diagram of effect of temperature on the conformational freedom of alkyl chain and the corresponding effect on the binding energy of the dipole bound state.

The observation that the photoelectron angular distribution peaks parallel to the polarization axis ($\beta_2 \sim 1$) corroborates the thesis of photoemission from a DBS.[131, 132, 160] The alleged DBS PE peak is also spectrally narrow, suggesting that the potential energy surfaces of the intermediate and final states are very similar; moreover, the peak is very close in energy to the photon energy used in the experiment, therefore the state that produces resonance enhancement is weakly bound. For all these reasons, we can conclude that the DBS is retained in all the molecules observed, even if there is an alkyl chain of considerable length “invading” its space. It is interesting to notice how the β_2 parameter does not undergo significant changes with varying chain length.

Performing the experiments under cryogenic conditions, as in the case of Liu and co-workers,[156] and combining the experimental results with computational studies, would help in individuating the preferred conformer for each compound and studying the change in shape of the DBS in presence of the alkyl tail.

In the case of a molecule in aqueous solution, in which the solvent is dense and polar, it may be unlikely to find a DBS. However, dipolar stabilisation in polar solvents could arise directly from the solvent, similarly to charge-transfer-to-solvent (CTTS) states,[94, 161, 162] which could be considered DBSs. Moreover, some condensed phase environments, especially biological, exist as soft matter, thus presenting considerably lower density than, for example, the aqueous phase. For example, proteins present large, empty pockets and spaces where a DBS could be accommodated. It is also interesting to point out that the most stable conformation of tyrosine, one of the 20 fundamental amino acids, is the para-substituted phenolate anion rather than the carboxylic acid.[163]

4.5 Conclusions

In conclusion, we have provided solid evidence of the subsistence of the DBS despite the presence of an alkyl chain actively interacting with it. To achieve this study, we performed FR-PEI, R2P-PEI and action spectroscopy, using five differentially para-substituted phenolates as test models. The DBS peak can be clearly assigned in all the R2P-PE images and spectra. In the action spectra, a blue shift in the energy of the 0-0 transition and a dramatic loss of resolution can be observed as the alkyl chain in para position becomes longer. The blue shift in 0-0 transition energy can be explained through a specific trend in EA witnessed in the one-photon PE spectra. The loss of resolution can be attributed to a fluctuation in E_{be} of the DBS due to the conformational change that the molecule undergoes at 300 K, proportional to chain length. Additional research is required to understand how the DBS modifies its shape to welcome the alkyl chain, and whether it is possible to find DBSs in solution or in soft matter environments. Nonetheless, this study marks a first step towards the understanding of this issue and provides a useful model to investigate the behavior of DBSs in presence of other molecules.

Photophysics of a carboxylated adenosine analogue

5. Photophysics of a carboxylated adenosine analogue

The contents of this chapter are based on the following publication: Castellani, M. E.; Verlet, J. R. R., Intramolecular Photo-Oxidation as a Potential Source to Probe Biological Electron Damage: A Carboxylated Adenosine Analogue as Case Study. *Molecules* 2021, *26* (10), 2877.[164]

5.1 Motivation

As explained previously, all the components of a nucleotide can undergo LEE attachment; additionally, the LEE could also occupy a DBS.[74-78] The thus formed anionic resonances can lead to mutations and cell death.[79, 80] Feshbach resonances are responsible for single-strand breaks,[2] while shape resonances can lead to a number of different lesions.[71, 73, 74, 80-89]

LEE-induced DNA damage has been extensively studied by the Sanche group through electron scattering, [2, 3, 73, 76, 79, 80, 87-89] photoelectron spectroscopy[91, 92] of iodide-molecule clusters by the Johnson group,[93-98] and time-resolved photoelectron imaging of I^-•N (N = nucleobase) by the Neumark group.[99-103] However, this method has some setbacks, particularly because the role of iodide is not yet clear, and due to the photon energy used, which could correspond to nucleobase absorption bands.[104, 105]

In the present study, we tried using a nucleoside analog that could simultaneously serve as electron source and electron acceptor, exploiting an intramolecular anion moiety to then attach an electron to the nucleobase, therefore inducing intra-molecular charge transfer upon photoexcitation at 266 nm. Performing this experiment with a phosphorylated nucleotide, *e.g.*, deoxy-adenosine monophosphate ($dAMP^-$), is very challenging, due to the high (~5 eV) Electron Affinity (EA) of the phosphate group.[111, 165] Following the method created by Widlanski and Epp,[166] we synthesized an adenosine analog with a carboxylic group in 5' position (C-Ado). The –OH moieties of the sugar in position 2' and 3' are protected with an isopropyl function to prevent deprotonation; the chemical structure of the molecule can be seen in Figure 5.1. If the highest occupied molecular orbital (HOMO) is located on the carboxylic acid, one could envision a charge-transfer transition occurring from the carboxylic acid moiety to the π* state on the nucleobase. For this reason, we performed Time-Dependent Density Functional Theory (TD-DFT) calculations at the B3LYP-6311G level of theory and verified that the HOMO was located on the carboxylic acid, while the LUMO, which is also the π* state, was on the base. The energy associated with the charge-transfer transition from the carboxylic acid to the base was calculated to be 5.35 eV (236.19 nm), although it should be noted that this value is based on rather low level of theory and subject to large error. TR-PEI measurements have been performed with a pump energy of 4.66 eV (266 nm) and probe energies of, respectively, 3.10 eV (400 nm) and 1.55 eV (800 nm). Unfortunately, the excited-states dynamics of C-Ado$^-$ are dominated by the features typically associated with adenine, with no clear evidence of charge-transfer in the spectra. C-Ado exhibits a similar behavior to dAMP$^-$ and its di- and tri-nucleotide,[67] in which the main decay pathway is internal conversion of the $^1\pi\pi^*$ back to the ground-state.

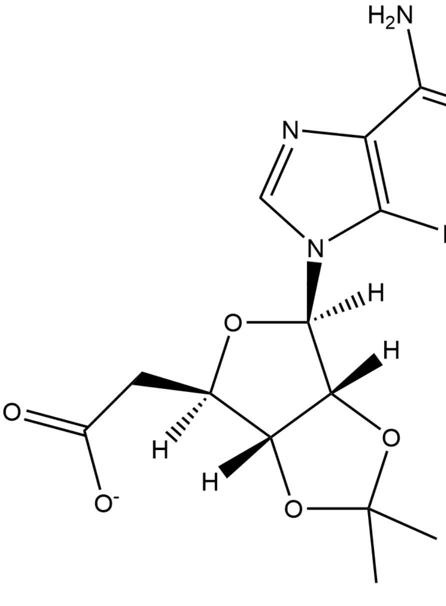

Figure 5.1: chemical structure of C-Ado$^-$.

5.2 Methods

A detailed description of the instrument can be found in the relevant chapter of this thesis (page 41, Experimental Setup) and in previous publications.[107, 108] Carboxylated-5'-Adenosine (C-Ado) was prepared following the protocol reported by Epp and Widlanski [166]. 1 mM of C-Ado was dissolved in methanol, adding few drops of NH_4 in MeOH to facilitate deprotonation.

Platinum plated VMI electrodes were used in order to ameliorate the signal-to-noise ratio, thanks to the higher work-function of platinum compared to stainless steel.[110] For background subtraction, as well as to increase PE signal, the PE images were collected with both the ion trap open and closed at ~1 Hz. A more detailed description of this procedure can be found in the Experimental chapter and in the relevant publication.

Time-resolved data were analyzed first by integration, then fitted to a given function to extract quantitative information. The model we use exploits exponentially modified Gaussian functions convoluted with the instrument response over time, which is given by the cross-correlation of the pump-probe signal. Details on the analytical expression of the fit can be found here.

Density functional theory (DFT) calculations have been performed with the software Gaussian09,[167] and the results visualized with GaussView 4. B3LYP (Becke three-parameter hybrid functional combined with Lee-Yang-Parr correlation functional) exchange correlation functional was used,[111] together with the 6-311G basis set.[168, 169] Diffuse and polarization functions were added. On the other hand, the corrected functional CAM-B3LYP was used for molecular orbital visualization.[170]

5.3 Results

The minimum energy structure of C-Ado$^-$, obtained with calculations at the B3LYP-6311G level of theory, is shown in Figure 5.2. As the hydroxyl groups on the ribose are inaccessible due to the protective group, the most likely deprotonation site is the carboxyl group, therefore the negative charge is located on this moiety. The calculated

Vertical Detachment Energy (VDE) and Adiabatic Detachment Energy (ADE) resulted, respectively, 4.48 eV and 4.29 eV.

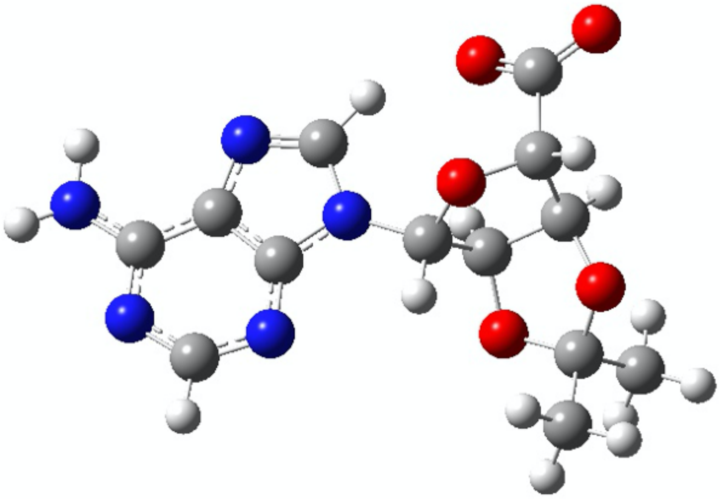

Figure 5.2: Minimum energy structure of C-Ado calculated at the B3LYP-6311G level of theory.

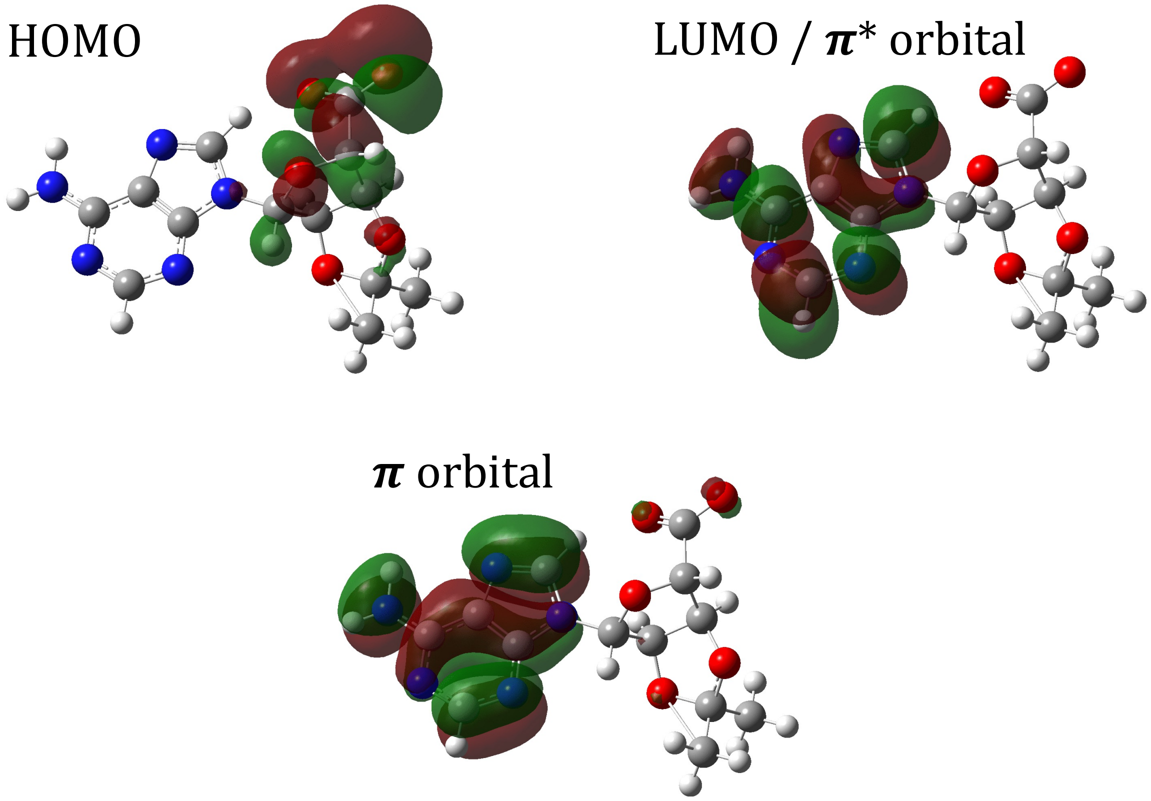

Figure 5.3: HOMO, π and π MOs of Carboxy-Ado.*

The Molecular Orbitals (MOs) were obtained through time-dependent DFT calculations (TD-DFT). The MOs can be seen in Figure 5.3, while the energetics can be seen in Figure 5.4. The Highest Occupied Molecular Orbital (HOMO) and the HOMO–1, which is the initial state for the charge-transfer transition, are both located on the carboxylic acid and almost degenerate. The Lowest Unoccupied Molecular Orbital (LUMO), which is also the lowest shape resonance state of the nucleobase, is a π* orbital and is involved in both the ππ* transition on the nucleobase (calculated at 5.18 eV (239 nm)), as well as in the lowest-energy charge-transfer transition (calculated at 5.25 eV (236 nm)). Therefore, although one could envision a similar mechanism to electron capture by a shape resonance when exciting the π* orbital during the charge-transfer transition, as the two transitions are predicted to be very close in energy it may be difficult to distinguish between them.

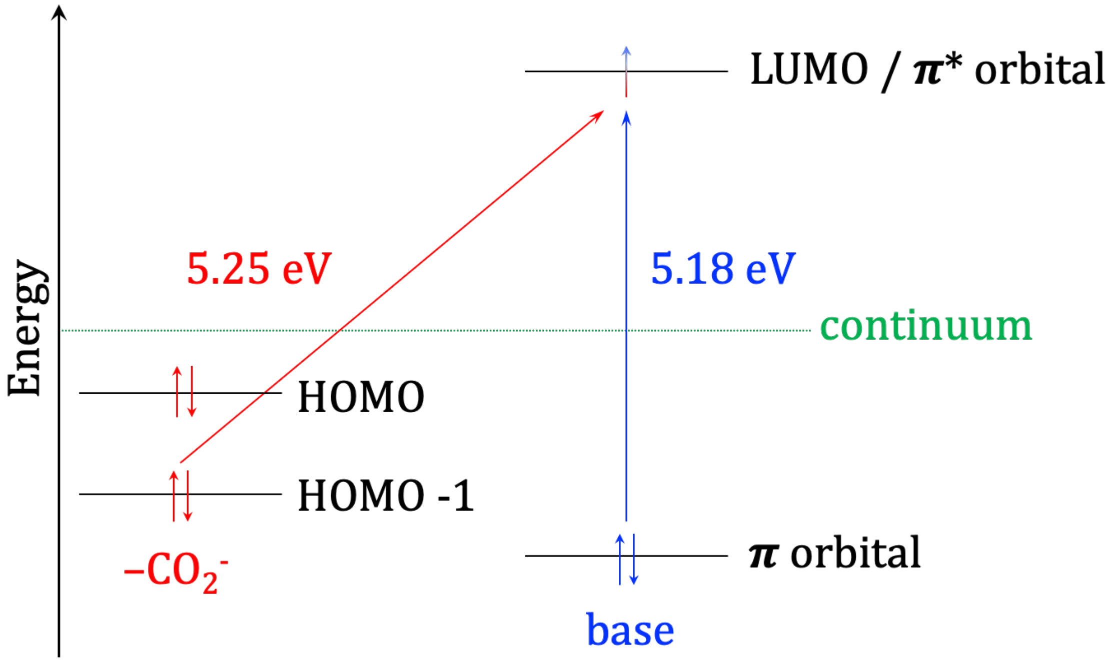

Figure 5.4: Energy level diagram and transitions for C-Ado⁻, showing the carboxy-localized molecular orbitals (HOMO and HOMO–1) as well as the nucleobase-localized molecular orbitals (π and π MOs). The two relevant transitions are shown with the charge-transfer (red) and the nucleobase-centered ππ* (blue).*

The two time-resolved PE spectra of C-Ado$^-$, taken with a 4.66 eV (266 nm) pump and either a 1.55 eV (800 nm) or 3.10 eV (400 nm) probe, can be respectively seen in panels (a) and (b) of Figure 5.5. The photoelectron signal from the pump only (*i.e.* before *t* = 0) has been subtracted from each time-resolved spectrum to leave only the temporally evolving dynamics.

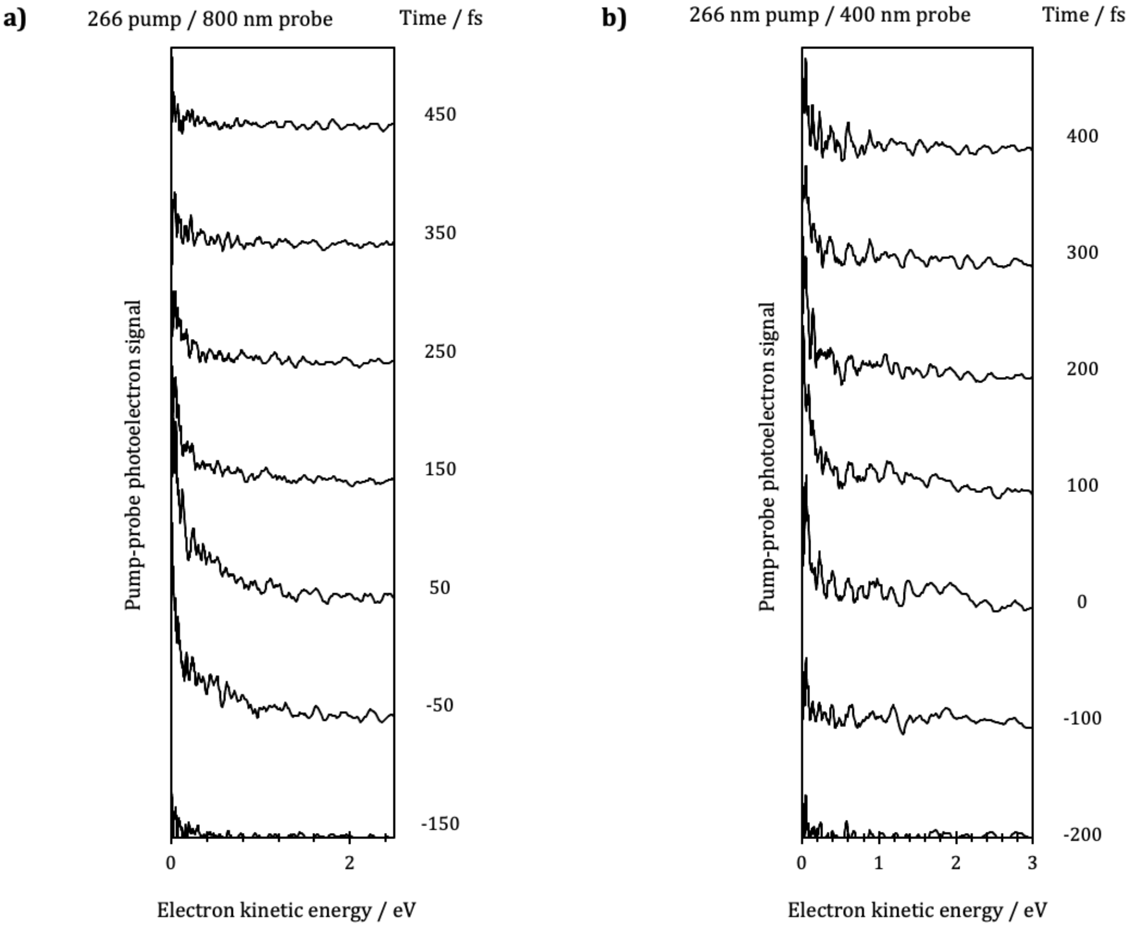

Figure 5.5: (a) Time-resolved photoelectron spectrum of C-Ado recorded with pump energy of 266 nm and probe energy of 800 nm between –150 and 450 fs; (b) Time-resolved photoelectron spectrum of C-Ado recorded with pump energy of 266 nm and probe energy of 400 nm between -200 and 400 fs. The maximum overlap between pump and probe pulse is taken as 0 fs reference.

In panel (a), two distinct features can be observed at different kinetic energies. The first peak, between 0 eV and 0.15 eV, and has a shoulder that extends almost until 1 eV. The low-energy feature is slightly visible at already –150 fs; it rapidly increases in intensity until 50 fs and then decays completely by ~350 fs. The high-energy peak is much harder to see due to its low intensity and has a shorter lifetime, as it appears approximately at –50 fs and has already disappeared by 250 fs. To probe a wider Franck-Condon window, the experiment with a pump energy of 3.10 eV was performed; however, the signal-to-noise ratio is lower. The spectrum in panel (b) can be instead roughly divided into three main features. The first feature, found between 0 eV and 0.2 eV, is the narrowest and most intense of the four, and, after appearing at already –200 fs, is still visible at 400 fs. The second peak (0.2-1 eV) arises at –100 fs and can still be slightly seen at 400 fs. The third and fourth feature, between 1 eV and 2 eV, is visible only around 0 fs, making it difficult to get an estimate of its lifetime. The average of three spectra at $t \sim 0$ fs has been used to extract an approximative value of the ADE for C-Ado$^-$. For the 800 nm probe experiment, the spectra at –50 fs, 50 fs and 100 fs were used; for the 400 nm probe experiment, –50 fs, 0 fs and 50 fs were instead used. The spectra exhibit, respectively, a peak at 0.98 eV and a peak at 2.50 eV, yielding an ADE of 5.22 eV for 800 nm (4.66 + 1.55 – 0.98 = 5.22), and of 5.26 eV for 400 nm (4.66 + 3.10 – 2.50 = 5.26), with an average value of ~5.24 eV. As the ADE value is obtained through a resonance-enhanced experiment, this ADE is associated with the initial excitation.

Figure 5.6 contains the integrated photoelectron signal for the time-resolved measurement with probe energies of 1.55 eV, with the total signal and the fit in panels (a), and the signal integrated over different energy ranges in panel (b). The total integrated PE signal of C-Ado$^-$ with the 1.55 eV probe pulse can be fitted with two exponential functions, convoluted with the instrument response function (which is a Gaussian), with lifetimes of, respectively, 102 fs and 326 fs. Considering the instrument response function, the first lifetime can be considered within the time-resolution of our experiment. The integrated photoelectron signal over 0-0.15 eV and 0.2-1.0 eV shows two features, corresponding to the two peaks that could be observed in Figure 5.5(a), which have been normalized to a maximum integrated intensity for clarity. The two features exhibit analogous lifetimes and very similar dynamics; hence, they are both a representation of the temporal evolution of the population of the same excited state. The total integrated dynamics can be described as a three-step process, A → B → C, in which, while the first two states A and B can be clearly observed, the final state C cannot be seen using the 1.55 eV probe pulse.

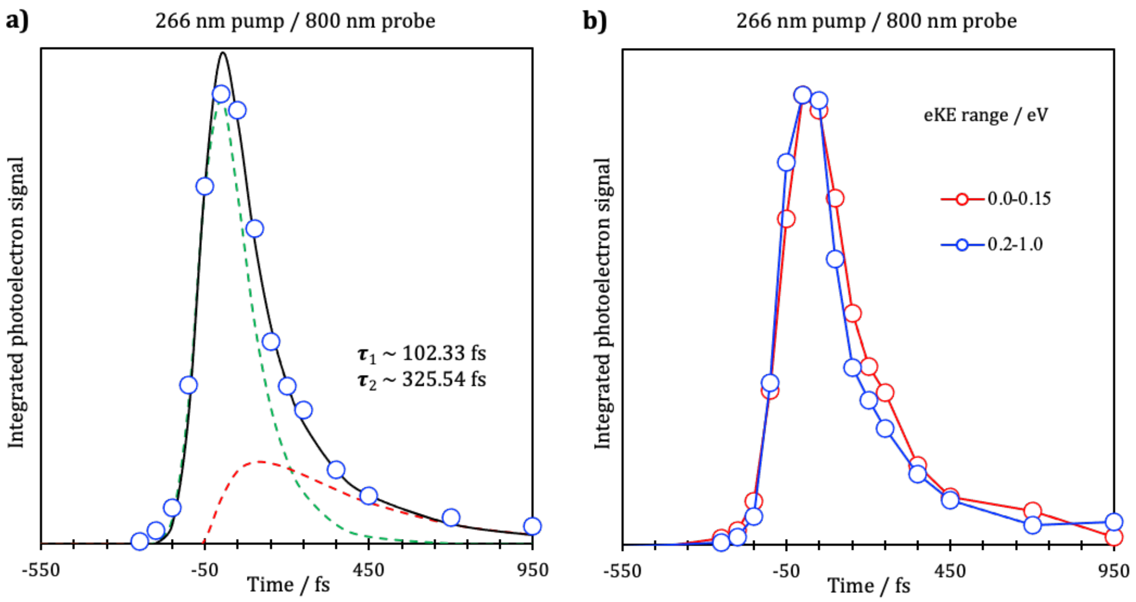

Figure 5.6: (a) Total integrated photoelectron signal with pump energy of 266 nm and probe energy of 800 nm (blue dots) plotted in function of time, with corresponding Gaussian fits; (b) Integrated photoelectron signal with pump energy of 266 nm and probe energy of 800 nm over different energy ranges.

Figure 5.7 contains the integrated photoelectron signal for the time-resolved measurement with probe energies of 3.10 eV; the total signal and the fit are in panels (a), while the signal integrated over different energy ranges is in panel (b). The total integrated PE signal taken with 400 nm probe (Figure 5.7(a)) can also be fitted as in Figure 5.6(a), with different lifetimes of 245 fs and 6.2 ps. Since we could not completely measure decay of the second exponential, the lifetime associated with it has a very large error. The photoelectron signal integrated over different energy ranges shows four distinct features. The one at lowest energy range rises slightly later compared to the other three but is also the last one to decay, still exhibiting signal at 2 ps. The other three features rise at approximately the same time and decay one after the other between 500 and 1000 fs. Moreover, since the features decay sequentially, the photoelectron signal seems to be effectively shifting to lower KE with time. Therefore, the fit which is based on a A → B → C model, does not fully represent the dynamics.

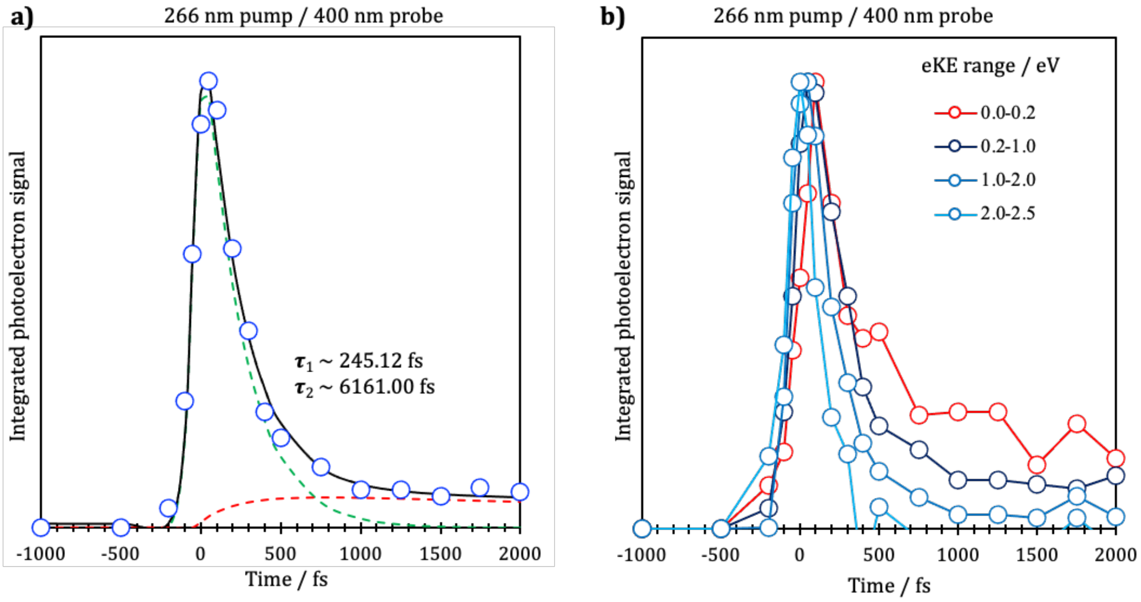

Figure 5.7: Total integrated photoelectron signal with pump energy of 266 nm and probe energy of 400 nm (blue dots) plotted in function of time, with corresponding Gaussian fits; (b) Integrated photoelectron signal with pump energy of 266 nm and probe energy of 400 nm over different energy ranges.

5.4 Discussion and conclusions

As expected, calculations show that the HOMO od C-Ado$^-$is on the carboxylic acid and the LUMO/ π* orbital on the base, with the charge-transfer transition lying at ~5.25 eV; this transition could in principle be used to induce electron injection onto the nucleobase. However, since the charge-transfer transition appears to be close in energy to the ππ*, it is likely that the latter will be the preferred transition. Nevertheless, the aim of the calculations was only to have an estimate of the relative position of the molecular orbitals and we note that much higher-level calculations have been used for analogous molecules in literature.[111] Moreover, it is known that calculations of transition energies may exhibit large associated errors. Although the computed ADE (4.29 eV) and the experimental value of ~5.2 eV are considerably different, it is important to underline that the two do not necessarily correspond to the same physical measure. While the calculations take the ADE associated with the removal of an electron from the carboxylic acid, the experimental value is taken from a resonance-enhanced experiment: if the initial excitation is localized on the nucleobase, then the ADE will correspond to the ionization energy of the nucleobase in C-Ado⁻. Moreover, the value of ~5.2 eV is not too far from the ionization energy of the nucleobase in dAMP⁻ (5.65 ± 0.15 eV).[111, 165]

As shown in Figure 5.4, due to the rapidity of the dynamics, the temporal evolution of the system cannot be fully described using the 1.55 eV probe. The 3.10 eV probe experiment shows that the initial excited state has a very short lifetime and that, within a few hundreds of fs, it shifts towards lower KE, much like dAMP⁻ under the same experimental conditions. [111, 165] In dAMP⁻, this was assigned to motion on the ππ* state away from the Franck-Condon region, with subsequent internal conversion to the ground state in approximately 290 fs, and no photoelectron signal after 1 ps. An analogous decay pathway has also been observed in isolated adenine, 9-methyl-adenine, adenine oligonucleotides and adenine triphosphate dianions.[67, 171-173] Although a fair comparison of the timescales cannot really be made, it is reasonable to note that C-Ado⁻ follows the same general decay mechanism of the other adenine derivatives at early times.

Although the overall mechanism is the same, some population seems to remain after 1 ps in C-Ado⁻, even if the peak is at very low KE and the noise levels make it difficult to confidently assign it. Considering that in C-Ado⁻, although close in energy to the ππ* transition, the charge-transfer transition is still, in theory, accessible, there is a chance that the signal at $t > 1$ ps corresponds to population arising from charge-transfer. In this way, the negative charge would be localized on the nucleobase, and the thus-produced excited state could have a longer lifetime. However, the quality of the data prevents us from assuredly drawing any conclusions in this regard.

Overall, C-Ado⁻ seems to follow a mechanism of excitation that primarily involves some population being promoted to the ππ* state of the nucleobase, which then decays analogously to the other adenine derivatives, while a smaller fraction could follow charge-transfer excitation. The small oscillator strength of the charge-transfer transition compared to the ππ* transition could explain why there is insufficient evidence to confidently differentiate the two excitations. Therefore, even if the substitution of the phosphate groups with a carboxylic acid lowers the electron affinity of the compound, the ππ* transition remains the principal form of excitation, as the charge-transfer transition is not sufficiently lower in energy compared to it.

Although this approach did not lead to the desired results, it can still be used as stepping-stone for future studies. Different substituents may reduce the EA further; for instance, substitution with hydroxyl groups seems to lower the EA in benzene derivatives.[174] Another approach could involve attaching a chromophore that has an excited state close in energy to the π* MO of the nucleobase, thus affecting the charge-transfer transition. Further research, both experimental and theoretical,[175-178] is necessary to understand how to exploit intra-molecular charge transfer as a probe for low-energy electron damage in DNA and its derivatives, but this study may already pave the way for interesting ways of probing electron-driven chemistry in DNA.

Photophysics of the doubly deprotonated ATP dianion

6. Photo-physics of the doubly-deprotonated adenosine-5’-triphosphate dianion

This chapter is based on the following publications: Castellani, M. E.; Avagliano, D.; González, L.; Verlet, J. R. R., Site-Specific Photo-oxidation of the Isolated Adenosine-5′-triphosphate Dianion Determined by Photoelectron Imaging. *J. Phys. Chem. Lett.* **2020,** *11* (19), 8195-8201, and Castellani, M. E.; Avagliano, D.; Verlet, J. R. R., Ultrafast Dynamics of the Isolated Adenosine-5′-triphosphate Dianion Probed by Time-Resolved Photoelectron Imaging. *J. Phys. Chem. A* **2021,** *125* (17), 3646-3652. [172, 179] All the calculations have been performed by Dr. Davide Avagliano.

6.1 Motivation

As previously mentioned in the introduction, DNA can undergo significant damage when exposed to radiation or oxidizing agents.[47, 48] In particular, photo-oxidation is responsible for some of the most severe lesions in DNA derivatives; this is due to the fact that nucleobases present optically bright $^1\pi\pi^*$ states that can readily absorb ultraviolet light.[48] Nevertheless, thanks to their non-radiative decay mechanisms, nucleobases present high intrinsic photostability, as confirmed by the low fluorescence quantum yield (less than 1%).[49, 50] Specifically, adenine is one of the most common nucleobases in nature, especially thanks to its important derivatives *e.g.*, Adenosine Triphosphate (ATP), Nicotinamide Adenine Dinucleotide (NAD), Flavin Adenine Dinucleotide (FAD) and Coenzyme A.[180, 181] Adenine has been the object of extensive studies, both experimental and theoretical, particularly through gas-phase spectroscopy and electronic structure calculations, respectively.[171, 182] Overall, both nucleobases[183-186] and nucleotides[67, 68, 111] have been often probed in gas-phase environments, together with their geometric structures;[187-191] and their photo-dissociation products.[192, 193]

Due to its pivotal role in intramolecular energy transfer, ATP is one of the most important adenine derivatives. The structure of ATP is characterized by three phosphate groups; therefore, it naturally presents multiple negative charges. The doubly-deprotonated form of ATP, $[ATP{-}H_2]^{2-}$, can be easily introduced in a gas-phase environment through electrospray ionization. Therefore, following the same idea as Carboxy-Ado, we decided to perform TR-PEI on $[ATP{-}H_2]^{2-}$ to see if intra-molecular charge transfer could occur between one of the excess charges on the phosphate groups and the adenine moiety.

As previously explained in the introduction, gas-phase polyanions present a Repulsive Coulomb Barrier (RCB), [18-21] an energy barrier given by the long-range attraction and short-range repulsion between the departing electron and the anionic core. The combination of these two interactions simultaneously gives both stability and instability to the molecule. The RCB has been the object of multiple theoretical[19, 20, 194] and experimental[21, 22] studies, among all, Photo-Electron Spectroscopy (PES) and, more specifically, Time-Resolved Photo-Electron imaging (TR-PEI), have emerged as useful tools to probe the photo-physics of di- and poly-anions,[18, 21, 23-25] and in particular of polyanionic DNA fragments.[192, 195-203]

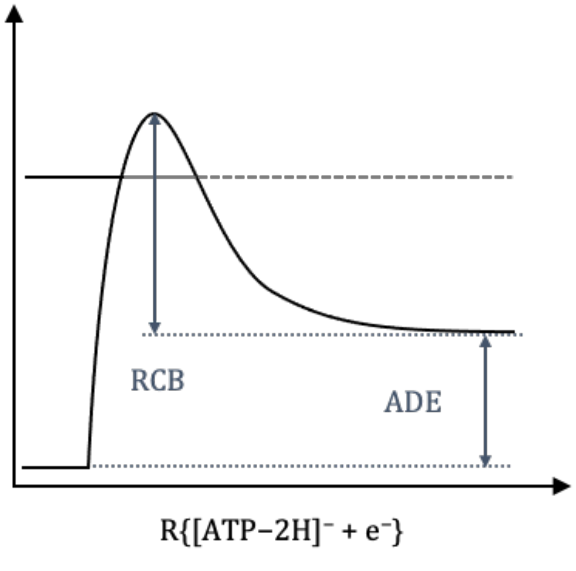

Figure 6.1: Schematic of repulsive Coulomb barrier indicating its height (RCB) as a function of the distance between $[ATP{-}H_2]^-$ and the free electron, and the adiabatic detachment energy (ADE).

The Kappes group[198] probed doubly-deprotonated Adenosine Diphosphate (ADP), $[ADP-H_2]^{2-}$, and $[ATP-H_2]^{2-}$ through PES. In the case of $[ATP-H_2]^{2-}$, they observed no PE emission upon excitation at 4.66 eV. On the other hand, the Dessent group[192] recorded a photo-detachment action spectrum where photoemission clearly seems to occur. For this study, we have exploited the unique properties of the RCB to determine the location of photo-oxidation in $[ATP-H_2]^{2-}$, and as a crude probe of its molecular structure. The schematics of the RCB for $[ATP-H_2]^{2-}$ can be seen in Figure 6.1. Following excitation of $[ATP-H_2]^{2-}$ with 4.66 eV (266 nm), we observed electron emission, showed that it arose from resonance tunneling through the RCB, and, with the aid of electronic structure calculations and bidimensional simulations of the RCB, revealed that photo-oxidation leads to directional electron emission from the $^1\pi\pi^*$ states on the nucleobase. We also provided further evidence of resonant tunneling by performing time-resolved photoelectron yield measurements, showing that the $^1\pi\pi^*$ state excited at 4.66 eV in $[ATP-H_2]^{2-}$ is a resonance. Moreover, we performed time-resolved PE spectroscopy experiments to distinguish between electron tunneling and nuclear dynamics on the excited $^1\pi\pi^*$ state, which ultimately leads to internal conversion back to the ground state, as reported by Cercola *et al.*[192] Exception made for tunneling through the RCB, $[ATP-H_2]^{2-}$ follows a comparable behavior to the decay dynamics of Deoxy-Adenosine Monophosphate ($dAMP^-$)[67, 68] and bare Adenine (Ade).[59, 183-185, 204-213]

6.2 Methods

The details of the instrument have been reported in the relevant section of this thesis (page 41, Experimental Setup).[107, 108] A ~1 mM methanolic solution of adenosine-5′-triphosphate disodium salt (Sigma Aldrich, UK) was electrosprayed. Photoelectron spectra were extracted from the raw images using onion peeling in polar coordinates.[119] The well-known photoelectron spectrum of I^- was used for calibration; the spectral resolution was approximately ~5% of the electron kinetic energy, E_{ke}.

6.3 Computational details

The structure of $[ATP–H_2]^{2-}$ was optimized using the Møller-Plesset second-order perturbation theory through the resolution of identity approximation (RI-MP2)[112] and the def2-TZVP basis set;[113] the ground state energy was then recalculated using the def2-QZVP[113] basis set. The Algebraic Diagrammatic Construction scheme for the polarization propagator at the second order (ADC(2))[114] method and the def2-QZVP[113] basis set were used to calculate the first five excitation energies. The 2D RCB map was obtained with the Local Static Approximation model;[115] in this model, an interval of 0.5 Å was used to calculate the energy of the monoanion and an electron, simplified as a negative point-charge, using the geometry of $[ATP–H_2]^{2-}$. The two planes containing the transition dipole moment vector connecting the S_0 and S_2 states, *xz* and *yz*, were taken into consideration. The RCB calculations were carried out at the MP2/def2-SVP level of theory; conversely, the ground state *ab initio* molecular dynamics were conducted at the B3LYP[116, 117]/aug-cc-pVDZ[118] level of theory, starting from the minimum energy structure of $[ATP–H_2]^{2-}$.

6.4 Results

The PE spectrum of $[ATP\text{-}2H]^{2-}$ was first recorded at 266 nm using the nanosecond laser (~5 ns pulse duration) and with the femtosecond laser (~80 fs pulse duration). The two PE spectra, plotted in terms of electron kinetic energy, do not exhibit any significant difference, and, in both cases, present a narrow peak centered at approximately 0.55 eV, with a small shoulder at higher E_{ke}. The PE image recorded with the femtosecond laser is shown in the left panel of Figure 6.2. The Photoelectron Angular Distribution (PAD) peaks appear to be strongly anisotropic, suggesting that the photoelectrons leave predominantly along the polarization axis, $\vec{E}$, which is vertical. For the dominant feature at E_{ke} = 0.55 eV, β_2 = +0.69±0.07. According to the reported ADE by Schinle *et al.*[198], the peak observed is below the RCB threshold; therefore, the peak most likely arises from electron tunneling through the barrier.

Moreover, 4.66 eV is resonant with the $^1\pi\pi^*$ state on adenine, thus the electron would tunnel from the nucleobase.

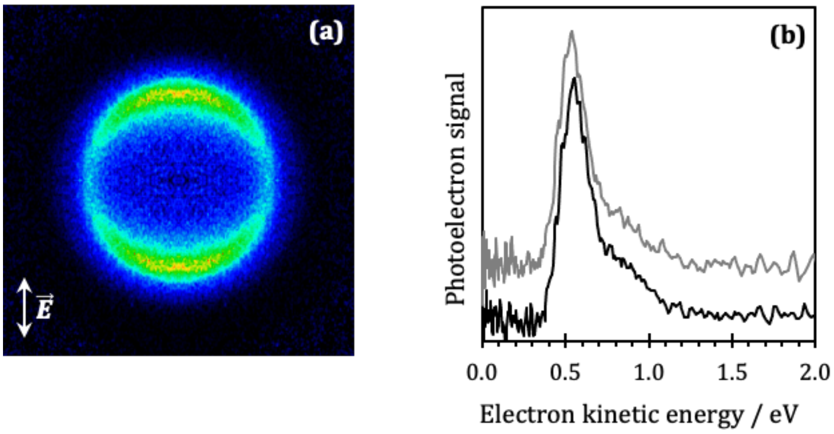

Figure 6.2: (a) Photoelectron image of [ATP–H_2]$^{2-}$ taken at 4.66 eV with nanosecond light pulses, with the polarization vector, $\vec{E}$, indicated. (b) Photoelectron spectra of [ATP–H_2]$^{2-}$ taken at 4.66 eV with femtosecond (grey) and nanosecond (black) light pulses.

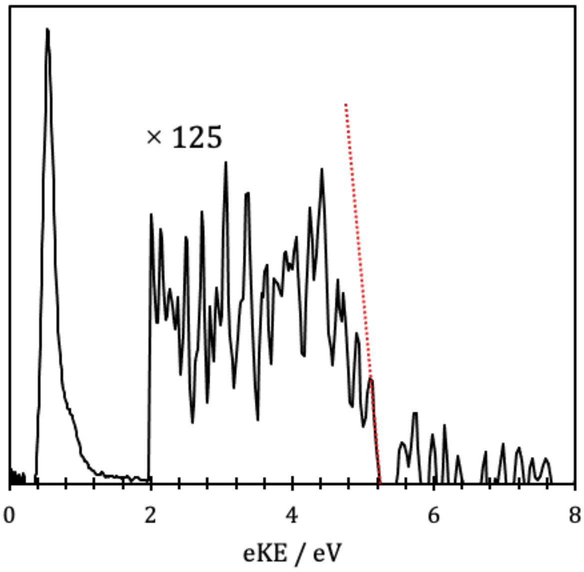

Figure 6.3: 2-photon resonant PE spectra of [ATP–H_2]$^{2-}$ taken with focused 4.66 eV femtosecond light. The red line shows the high E_{ke} edge of the photoelectron spectrum which intersects the 0 signal (dashed line) at ~5.2 eV.

To support the tunneling hypothesis, we performed a 2-photon resonance-enhancement experiment by focusing the femtosecond 4.66 eV light in the interaction region. The thus attained PE spectrum is shown in Figure 6.3; part of the spectrum has been magnified to highlight relevant features. A clear onset can be seen at E_{ke} ~5.2 eV: this corresponds to the ADE associated with the nucleobase: $\mathrm{ADE_A} = 2 \times 4.66 - 5.2 = 4.1$ eV. To consolidate the tunneling hypothesis further, we took single-photon PE spectra of $[\mathrm{ATP{-}H_2}]^{2-}$ at different wavelengths, from 280 to 260 nm (4.43 to 4.77 eV) (Figure 6.4). Despite the change in energy, the peak at 0.55 eV does not shift; therefore, this feature is inconsistent with a direct process and points instead to a tunneling process.

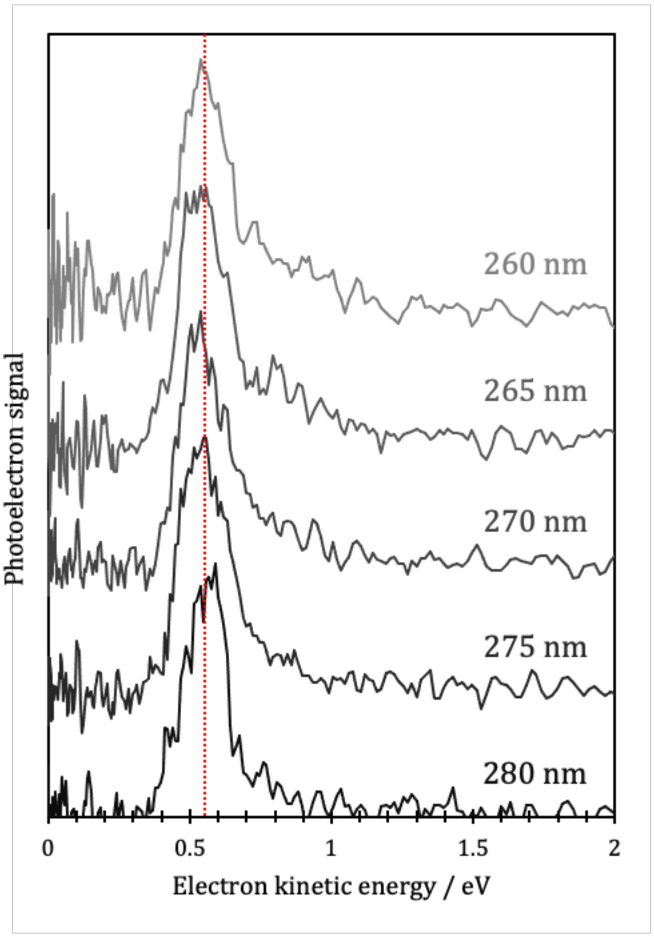

Figure 6.4: PE spectra of $[\mathrm{ATP{-}H_2}]^{2-}$ taken with tunable wavelength nanosecond light; the dashed red line shows that the tunneling peak does not shift in position but remains centered at E_{ke} = 0.55 eV despite the change in photon energy.

We have also performed a time-resolved PE spectroscopic study on $[ATP–H_2]^{2-}$ using a pump energy of 4.66 eV in combination with a 1.55 eV probe. Two pump-probe PE spectra, taken at delays of t = 200 fs and 0 fs, are shown in Figure 6.5. The two spectra look identical because the energy of the probe pulse is not sufficient to reach any excited states or the detachment threshold. On the other hand, at t = 0 fs, *i.e.*, at the maximum time overlap between pump and probe, the peak at E_{ke} = 0.55 eV becomes smaller, and at the same time a new feature rises between ~1 eV and 2 eV.

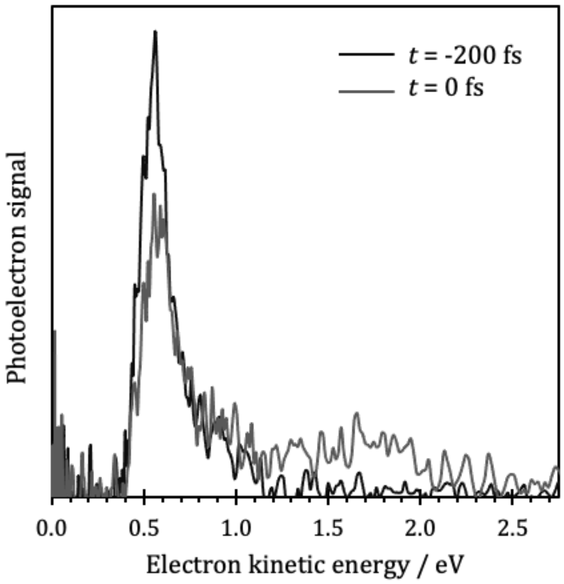

Figure 6.5: Time-resolved photoelectron spectra of $[ATP–H_2]^{2-}$ taken at t = −200 fs (black) and 0 fs (grey).

The time-resolved PE spectra of $[ATP–H_2]^{2-}$ between −200 fs and +300 fs are shown in Figure 6.6. The average of the spectra with $t \leq -200$ fs has been subtracted from each spectrum to highlight spectral changes; moreover, a 10-point moving average has been applied to compensate for high-frequency noise. Two distinct features can be seen in the spectra; each one of them is highlighted with a shading of different color. The first one, color-coded with a blue shading, has negative intensity, centered at approximately 0.55 eV in terms of E_{ke}. This depletion peak is slightly visible at already -150 fs; it increases in intensity until 0 fs, after which it rapidly recovers until almost no more signal is visible at +300 fs. At higher energy, there is a positive signal that decays as a function of pump-probe delay, but also appears to shift towards lower E_{ke}. Shifts in E_{ke} can arise from changing Franck-Condon factors associated with vibrational wavepacket dynamics along an excited state potential energy surface and/or from changes in electronic state following a nonadiabatic transition.

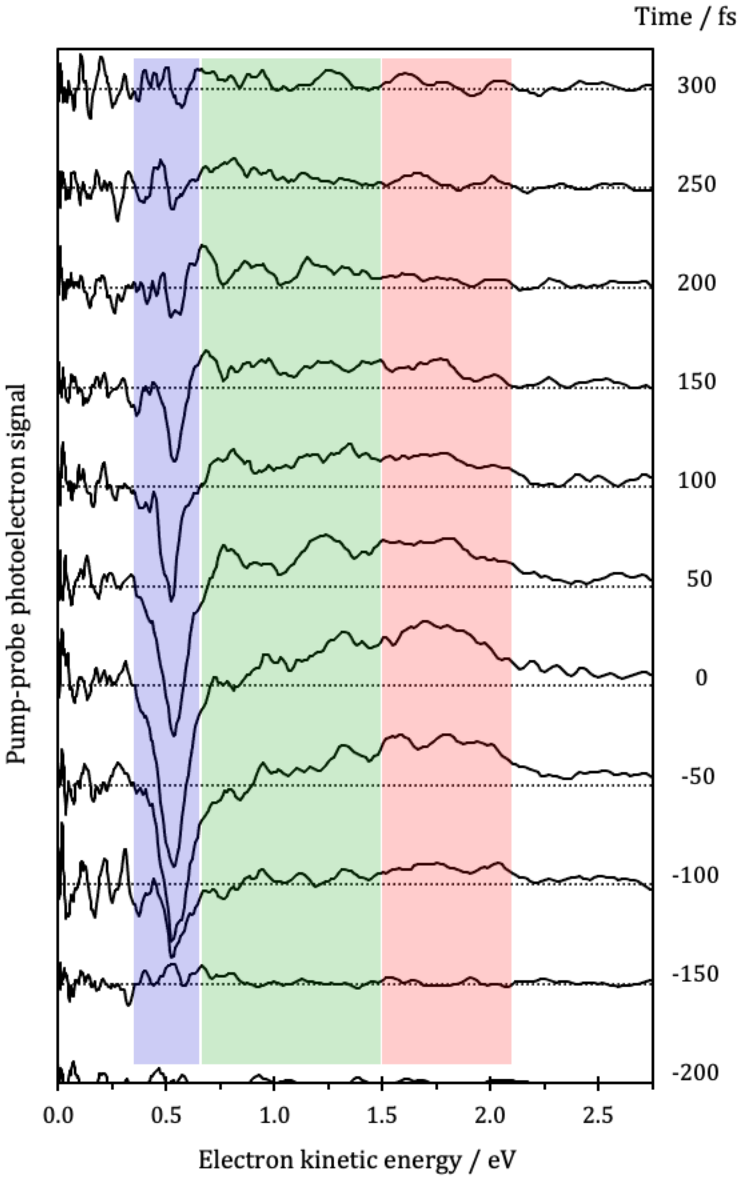

Figure 6.6: Time-resolved photoelectron spectra of [ATP–H_2]$^{2-}$ taken from −200 fs to +300 fs and plotted in terms of E_{ke}. An average of the spectra at $t \leq -200$ fs was used for background subtraction.

The positive signal can be roughly divided into two sections. Shaded with green, between approximately 0.75 eV and 1.25 eV, is a feature that appears at -100 fs and, after culminating at 0 fs, almost completely disappears by +250 fs. A second positive feature, highlighted with a red shading and much more intense than the second one, is registered between 1.25 and 2.25 eV. The feature starts peeking through at -100 fs, then rapidly increases in intensity until its peak at 0 fs and is already almost completely gone at +200 fs. The positive features roughly follow the timescale of the negative one, hence increasing and decreasing in absolute intensity accordingly to the depletion signal.

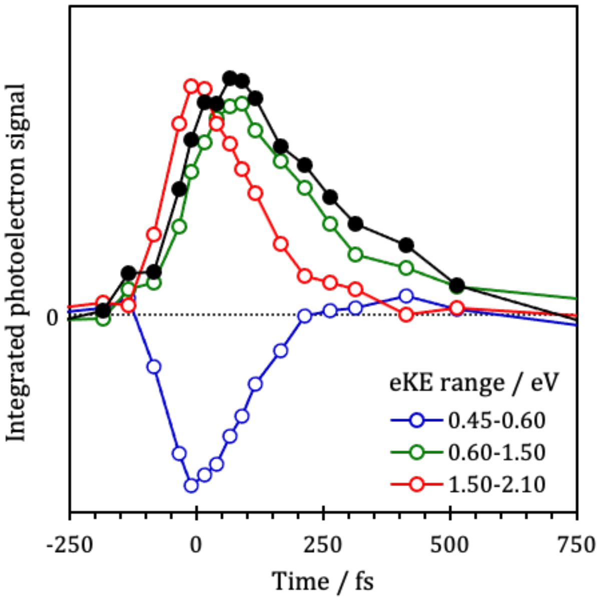

Figure 6.7: integrated photoelectron signal plotted as function of time over four different energy ranges. The black line represents the total integrated signal, the blue line represents the signal integrated over 0.45-0.60 eV, the green line between 0.60-1.50 eV, the red line between 1.50-2.10 eV.

The dynamics were analyzed using two approaches. Figure 6.7 contains the integrated pump-probe signal over three different energy ranges, corresponding to the energies individuated in the previous section.

Again, three features, with each corresponding to one of the three peaks in the time-resolved spectra and color-coded accordingly, are visible in the plot. All three features start rising around -150 fs, culminate at approximately 0 fs and terminate around +400 fs. The negative peak, represented in blue, corresponds to the depletion peak centered at 0.55 eV. This peak is almost perfectly mirrored by the second feature, in red. The second feature is slightly more intense in terms of absolute integrated intensity with respect to the first one. The third feature, shown by a green line, has positive intensity and is much less intense than the second feature. The first spectral window, $0.45 < E_{\mathrm{ke}} < 0.60$ eV, corresponds to the depletion peak in the time-resolved spectra, while the other two, $0.60 < E_{\mathrm{ke}} < 1.50$ eV, and $1.50 < E_{\mathrm{ke}} < 2.10$ eV, are representative of the dynamics associated with the two positive features, respectively at higher and lower E_{ke}.

These spectra provide another evidence of association between the depletion peak and the high E_{ke} feature, with a second feature rising and rapidly decaying within the $0.6 < E_{\mathrm{ke}} < 1.5$ eV spectral range. The high E_{ke} feature approximately decays within a timescale like the cross-correlation between pump and probe pulses, *i.e.,* <100 fs, and simultaneously to the depletion peak; conversely, the low E_{ke} positive feature decays to a value of $1/e$ at ~300 fs.

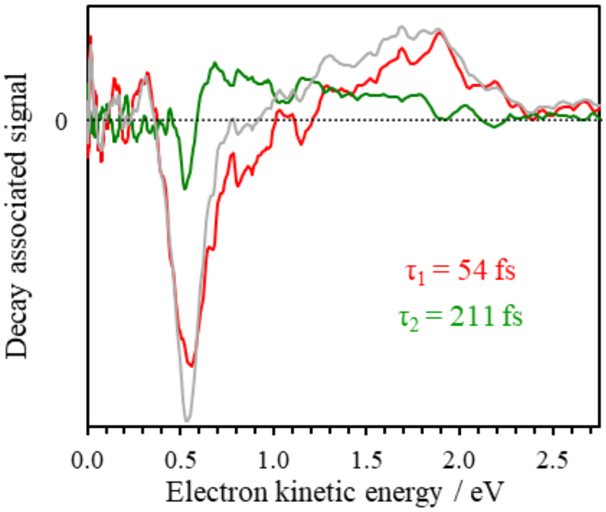

Figure 6.8: Decay associated spectra obtained from a global fit to the time-resolved photoelectron spectra, a selection of which was shown in Figure 6.6. The grey line represents the sum of the two decay associated spectra and corresponds to the PE spectrum associated with the initial excited state.

To gauge the individual contributions of each feature to the overall spectrum, a global fit to the time-resolved data was performed. The formulation of the fit is explained in the Experimental section. As the minimum number of decays to describe the spectrum was two, the global decay of the system can be described through a 3-state model 1 → 2 → 3, in which, while the first two states are observable, the third and last state cannot be observed with the current experimental setup.

Therefore, two decays, τ_1 = 54 fs and τ_2 = 211 fs, arise from this analysis. The corresponding decay-associated PE spectra can be seen in Figure 6.8. The first decay is within the time-resolution of the experiments, therefore corresponds to $\tau_1 < 100$ fs, and its kinetics are in line with what observed in Figure 6.7. The spectrum associated with τ_1 has positive signal between $1.2 < E_{\mathrm{ke}} < 2.3$ eV and negative signal between $0.4 < E_{\mathrm{ke}} < 1.2$ eV: while positive signal indicates decay, negative signal corresponds to population growth with the same lifetime. On the other hand, the τ_2-associated spectrum follows a simple decay as the final state cannot be observed.

The τ_1-associated spectrum contains a strong, negative peak at $E_{\mathrm{ke}} = 0.55$ eV and a positive peak, which instead reaches its maximum around $E_{\mathrm{ke}} \sim 1.9$ eV; moreover, the negative peak also extends between 0.6 eV and 1.2 eV, thus overlapping with the τ_2-associated spectrum. Therefore, while a portion of the signal leads to the recovery of the negative peak, another part at high E_{ke} instead produces the τ_2-associated spectrum. In the case of a three-state model global decay, the time-resolved PE spectrum associated with the initial excited state, also shown in Figure 6.8, corresponds to the sum of the τ_1- and τ_2-decay associated spectra.[214]

The computed RCB for $[\mathrm{ATP{-}H_2}]^- + e^-$ in the *xz* plane containing the adenine ring system is shown in Figure 6.9 (in the following page). Details of the calculation can be found in the supporting information of the relevant publication.[172] Electron emission from a π orbital on adenine produces an RCB that is highest in proximity of the three phosphate groups, where most of the negative charge is localized; conversely, the lowest saddle-point of the RCB, only 0.57 eV high, is located in proximity of the amino group of adenine (Figure 6.9). The calculations also reveal that the transition with the highest oscillator strength has ππ* character. Moreover, the TDM of this transition is parallel to the polarization axis; this is consistent with the PADs of the PE image of Figure 6.2.

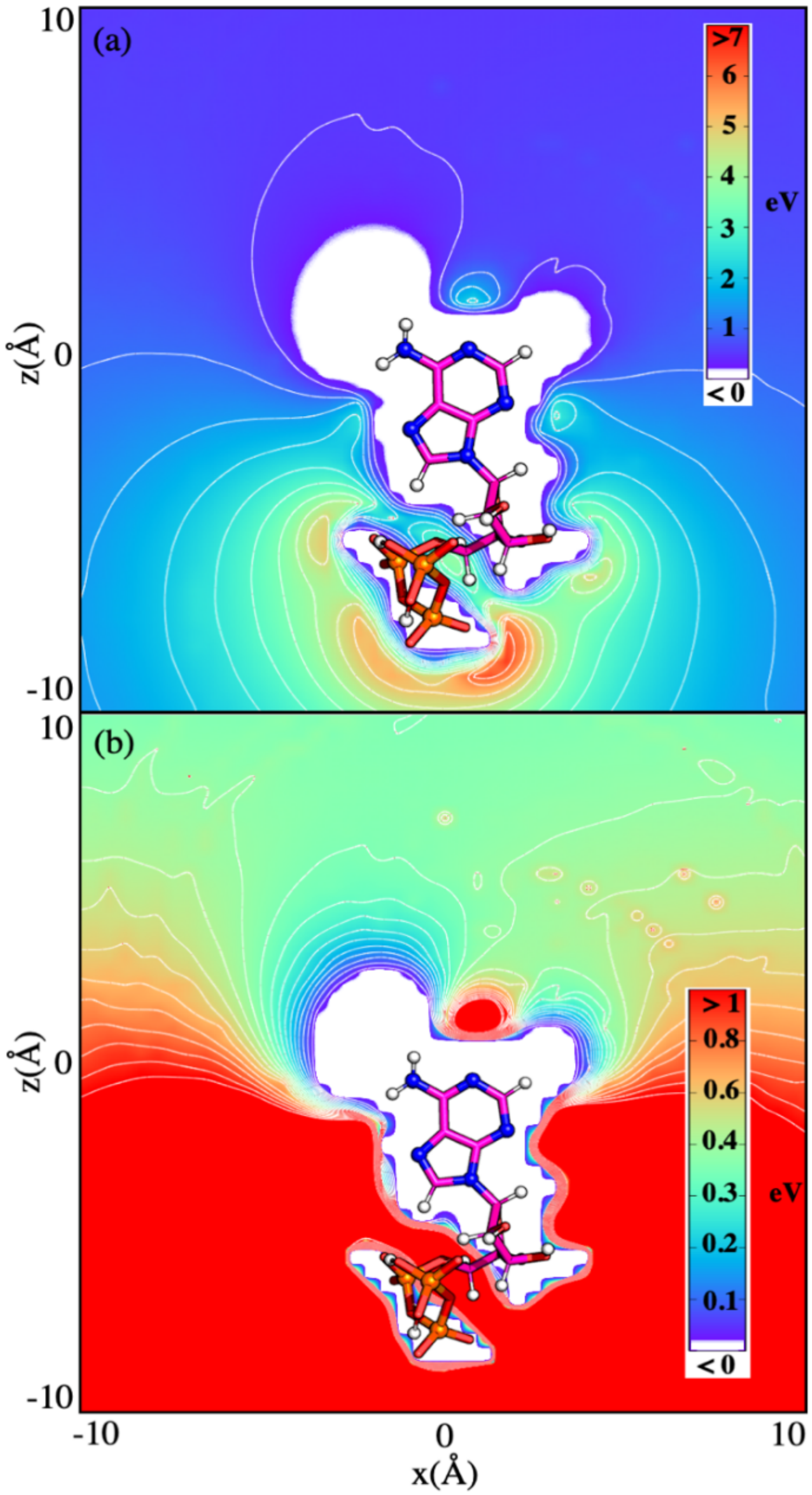

Figure 6.9: (a) Repulsive Coulomb barrier (RCB) for [ATP–H$_2$]$^-$ + e$^-$ in the plane passing through the calculated transition dipole moment of the excitation to the $^1\pi\pi^*$ state and including the adenine ring; each contour line represents an increment of 1 eV. (b) Map scaled to a maximum RCB of 1 eV; each contour line represents an increment of 0.05 eV. RCB maps are computed at MP2/def2-SVP level of theory.

The results of the ground state *ab initio* molecular dynamics simulation of $[ATP–H_2]^{2-}$ over 4 ps are shown in Figure 6.9, with an inset of the Root Mean Squared Deviation (RMSD) along the simulation time. This calculation gives an estimate of the conformational flexibility of $[ATP–H_2]^{2-}$ around the minimum energy structure. Although the phosphates move, their relative position with respect to adenine does not seem to change substantially.

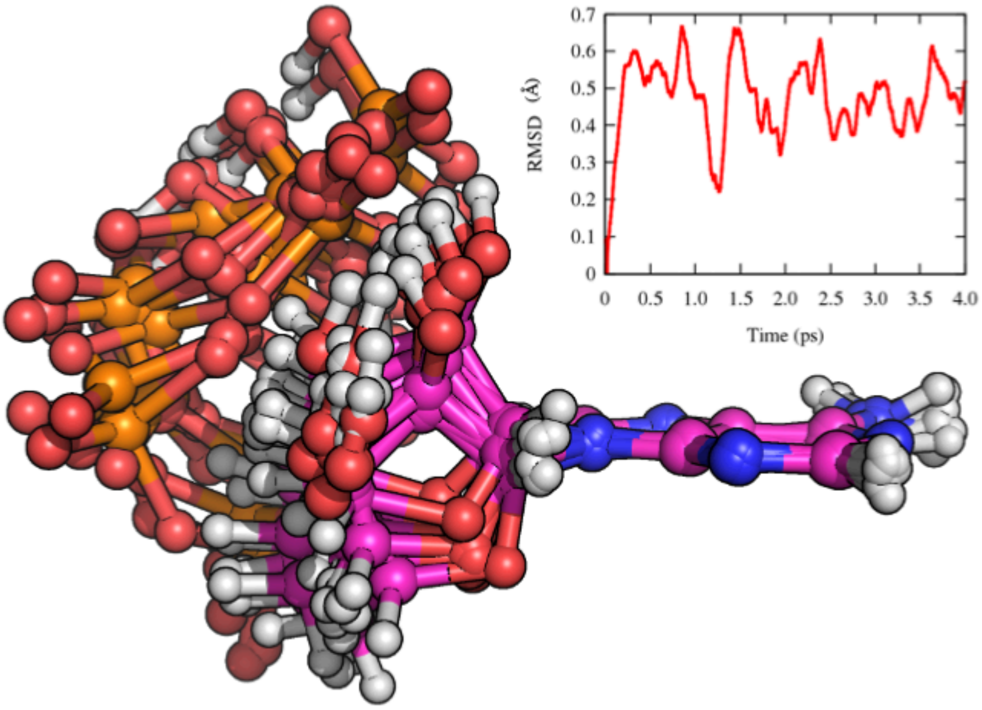

Figure 6.10: Superimposition of equidistant (every 100 fs) 10 $[ATP–H_2]^{2-}$ geometries along the first ps of the ab initio molecular dynamics simulation. Inset is the root mean squared deviation (RMSD) calculated along the 4 ps ground state dynamics.

6.5 Discussion

The single-photon PE spectrum of $[ATP\text{-}2H]^{2-}$, taken at 266 nm (4.66 eV), exhibits a peak centered at ~0.55 eV in terms of E_{ke} (Figure 6.2). Schinle *et al.*[198] reported an ADE of 3.35±0.11 eV and 4.01±0.08 eV, and an estimated RCB height of ~1.9 eV for $[ATP–H_2]^{2-}$; according to these results, the PE signal at 0.55 eV would arise from resonance tunneling through the RCB. The PADs can be quantified using the anisotropy parameter, β_2, as the photoelectron angular distribution corresponds to $I(\theta)\ \alpha\ 1 + \frac{1}{2}\beta_2(3\cos^2(\theta) - 1)$, where θ is the angle between $\vec{E}$ and the velocity vector of the emitted electron.[215-217] Additionally, the photon energy of 4.66 eV is only resonant with excited states localized on the nucleobase, therefore the electron can only be removed from the nucleobase.[165]

Additional evidence of electron tunneling from the nucleobase through the RCB is provided by the two-photon resonance enhanced experiment and the single-photon PE spectroscopy experiment using different wavelengths. However, if the highest occupied molecular orbital is also on the nucleobase, the $\mathrm{ADE_A}$ will correspond to the ADE of $[\mathrm{ATP{-}H_2}]^{2-}$. On the other hand, the single-photon experiment confirms that the peak at E_{ke} = 0.55 eV cannot arise from direct detachment; on the other hand, the possibility of autodetachment cannot be ruled out. If the ADE of $[\mathrm{ATP{-}H_2}]^{2-}$ is ~4.1 eV, the pump energy of 4.66 eV is above the adiabatic energy of the molecule. When irradiating the system only with this energy, a spectrum that looks like the 1-color PE spectra is produced (Figure 6.2), in which the photoelectron extends to $E_{\mathrm{ke}} \sim 2.1$ eV; however, according to the RCB estimate of Schinle *et al.*[198], 4.66 eV is still not high enough in energy to overcome the RCB. According to this reasoning, the peak would therefore arise from electron tunneling through the RCB, with the initial excitation being resonant with adenine's $^1\pi\pi^*$ states and the electron coming from there. At t = 0, when the 4.66 eV pump is in maximum overlap with the 1.55 eV probe, the latter brings the population that would have otherwise tunneled to a higher-lying excited state. Since the total energy is above the RCB ($h\nu_{\mathrm{pu}} + h\nu_{\mathrm{pr}} >$ ADE + RCB), this photoelectron feature is associated with direct detachment from the $^1\pi\pi^*$ states on adenine. Hence, less population can tunnel, and this appears in the TR-spectrum as a negative peak (bleach) centered at 0.55 eV. In correspondence of the bleach, the pump-probe signal can be seen at a higher energy (~2 eV). This positive signal is a measure of the population of the $^1\pi\pi^*$ state, and its kinetics mirror those of the negative feature. This can be clearly evidenced by Figure 6.8: the decay-associated spectrum of the initial process has both positive and negative components, therefore the high E_{ke} peak, which decays within $\tau_1 < 100$ fs, also leads to the recovery of the negative peak with the same time constant. In fact, as the system evolves with time, and hence the delay between pump and probe increases, the bleach peak recovers, as more population is tunneling through the RCB to form $[ATP–H_2]^-$ before the probe pulse's arrival. Once all the population has tunneled before the arrival of the probe pulse, the bleach disappears. Hence, we can conclude that the recovery dynamics of the peak at E_{ke} = 0.55 eV represents a direct measure of the tunneling lifetime.

However, another process takes place in parallel with tunneling. This can be evinced by the fact that the total integrated positive signal and negative transient signals do not cancel each other out (Figure 6.7).[91, 218] In the τ_1-decay associated spectrum (Figure 6.8), this coincides with the negative signal between $0.8 < E_{\mathrm{ke}} < 1.3$ eV, which shows that some motion on the initially excited $^1\pi\pi^*$ states is occurring. This motion is evidenced by the fact that the E_{ke} of the positive pump-probe signal is shifting to lower energy (green). The energy range in which this feature arises corresponds to the τ_2-associated spectrum; hence, population flows from the initial $^1\pi\pi^*$ states (with $\tau_1 < 100$ fs) to an intermediate state, whose PE spectrum is given by the τ_2-associated spectrum (Figure 6.8). Therefore, not all population decays through tunneling through the RCB. This conclusion is in line with the results obtained by Cercola *et al.*[192], in which photofragmentation, which is mostly a ground state process, was elicited upon excitation at 4.66 eV. Therefore, the τ_2-decay dynamics can be explained as internal conversion from the intermediate state to the ground state. Considering the shape of the peak at E_{ke} = 0.55 eV in the τ_2-associated spectrum, the 1.55 eV probe is not sufficiently high in energy to probe the entire population of the intermediate, with some signal being screened by an RCB at lower E_{ke}. Unfortunately, despite multiple attempts, probing the system with a probe pulse of 3.10 eV was unsuccessful.

The intermediate could arise from two distinct processes. The first would be vibrational motion of the wavepacket on the $^1\pi\pi^*$ states surface, which can remove population from the Franck-Condon region. The second would instead be initial motion on the $^1\pi\pi^*$ surface, which would then internally convert to a nearby $^1n\pi^*$ state through a conical intersection. The role and relative position of the optically dark $^1n\pi^*$ state is still controversial; nevertheless, as the gap between the $^1\pi\pi^*$ and $^1n\pi^*$ states is quite small for both Ade and $dAMP^-$, the involvement of the $^1n\pi^*$ cannot be ruled out.[67, 219, 220] Additionally, for both Ade and 9-Me-Ade, the relative position of the $^1n\pi^*$ with respect to the L_a and L_b states in solution is heavily dependent on the solvent of choice.[69, 221, 222]

$[ATP{-}H_2]^{2-}$ decays similarly to $dAMP^-$, whose dynamics at pump energy of 4.66 eV and probe energy of 3.10 eV also followed a 3-state model.[67] A schematic representation of the overall dynamics of $[ATP{-}H_2]^{2-}$ can be seen in Figure 6.11. The two lifetimes of $\tau_1 \sim 30$ fs and $\tau_2 = 290$ fs for $dAMP^-$ resemble the values of $[ATP{-}H_2]^{2-}$, in which τ_1 is less than the cross-correlation and $\tau_2 = 210$ fs. Moreover, the decay-associated spectra bear striking similarities. The two τ_1-associated spectra, exception made for the tunneling peak, are overall very close; moreover, the presence of negative signal in $dAMP^-$ also suggested the presence of an intermediate. Similarities can also be found between the two τ_2-associated spectra, suggesting the formation of the same intermediate and an analogous decay. Since the intermediate in $dAMP^-$ was positively assigned to nuclear motion on the $^1\pi\pi^*$ state, similarly to isolated Ade and 9Me-Ade, we suggest that this is also the case for $[ATP{-}H_2]^{2-}$.[67] Therefore, although the presence of the negative charge in $[ATP{-}H_2]^{2-}$ strongly affects the absolute energies of the π orbitals compared to Ade and 9-Me-Ade, the excitation energy of the $^1\pi\pi^*$ states does not change. Moreover, the dynamics of Ade, 9-Me-Ade and $[ATP{-}H_2]^{2-}$ remain overall very similar.

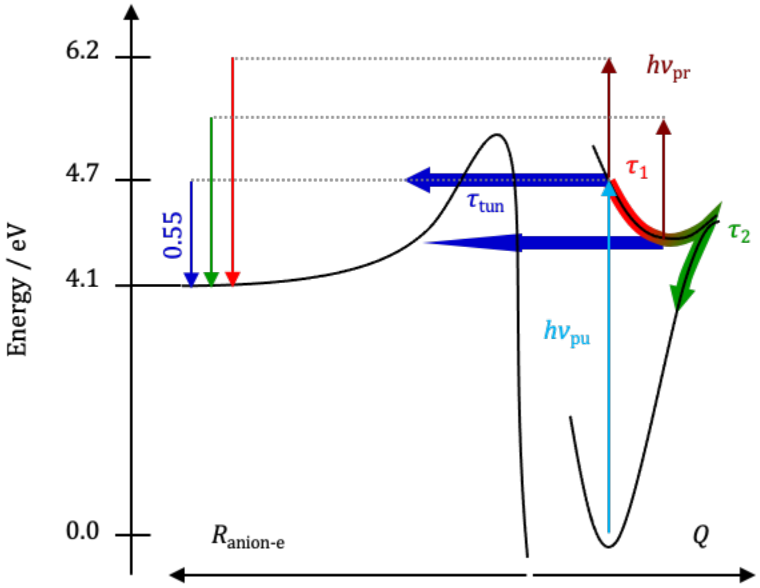

Figure 6.11: Schematic representation of the dynamics of $[ATP{-}H_2]^{2-}$ following excitation at 4.66 eV and probing at $h\nu_{pr}$ =1.55 eV. The lifetimes relate to the decays obtained from the global fit.

The bidimensional RCB map simulation for $[ATP–H_2]^-$ at the MP2/def2-SVP level of theory (Figure 6.9) yields a value of 0.57 eV for the lowest RCB saddle point. This number differs considerably from the RCB value of 1.9 eV reported by Schinle *et al.*[198]; therefore, one could argue that the pump energy of 4.66 eV is in fact above the RCB threshold. However, some observations need to be taken into consideration. Schinle *et al.* recorded the PE spectrum of $[ATP–H_2]^{2-}$ at a photon energy of 6.42 eV, which is probably resonant with other excited states located on the other moieties of the molecule. Resonances can notably hamper the assignation of RCB from a PE spectrum.[21] Additionally, upon irradiation of the system with a photon energy of 6.42 eV, multiple sites of $[ATP–H_2]^{2-}$ can undergo photoemission, without clear knowledge of the origin of the most intense signal.[111] In our case, 4.66 eV is only resonant with the $^1\pi\pi^*$ states on the nucleobase, therefore electron emission can only arise from this specific site.[165, 222-224] If linearly polarized light with polarization $\vec{E}$ is shone onto an ensemble of $[ATP–H_2]^{2-}$ molecules, excitation will occur only for those molecules within a $\cos^2\varphi$ distribution, where φ is the angle between $\boldsymbol{\varepsilon}$ and the transition TDM. As can be seen in Figure 6.10, these molecules are the ones for which the vertical axis z is parallel to the TDM of the brightest transition. Therefore, consistently with the PADs of the PE image in Figure 6.2 (a), electron emission will predominantly be parallel to $\vec{E}$.

Therefore, the computed RCB is generally consistent with what could be inferred by the experiments. Similarly to observations for the fluorescein dianion,[26] since $\tau_{\mathrm{tun}} < 1$ ps the resonance producing the $E_{\mathrm{ke}} = 0.55$ eV feature will be close to the lowest RCB saddle point at 0.57 eV. In the case of electron tunneling, the shape of the RCB will define the trajectory of the electron: specifically, the electron will avoid the high potential surrounding the phosphate groups (Figure 6.9). Such trajectory can be already inferred by the PE image in Figure 6.2 (a), as the electron appears to be ejected either along the amino or the methine groups.

Although classical molecular dynamics could be used to describe the behavior of an electron in presence of the RCB,[225] considering that the experiment is performed at ~300 K, rotational motion could blur the alignment.[28, 226] As seen by infrared multiphoton dissociation experiments and calculations, several isomers could be present, despite the αβ deprotonated isomer being the main form of $[ATP–H_2]^{2-}$.[190, [191, 198] Moreover, even if this were the case, the RCB could still be considerably affected by thermal motion of the phosphate groups.

The *ab initio* molecular dynamics simulation and RMSD calculation over 4 ps (Figure 6.10) show that, as the relative position of the phosphates with respect to the nucleobase does not change, we can expect little to no contribution of the phosphates to the overall shape of the RCB and, consequently, to the photoelectron angular distributions. For this reason, the nuclear dynamics will most likely not contribute to the RCB.[224, 227-229] On the other hand, the shoulder at higher E_{ke} on the 0.55 eV peak observed in Figure 6.2 could arise from dynamics of involving the ^{1}nπ* state. This shoulder peak also presents a slightly different β_2 parameter (+0.48±0.33, with the large error being due to reduced signal intensity). In this case, the electron would be removed from a different orbital, and the final states in $[\mathrm{ATP{-}H_2}]^-$ would also be different. To explore this, one could calculate the RCB for electron emission from the non-bonding orbital of the nitrogen on the amino group: in this case, the emitted electron would have different E_{ke}, as is the case of the shoulder. However, the experiment does not yield a different RCB and a different lifetime for the process, therefore we cannot draw any conclusions in this regard. Another explanation could be that the shoulder is produced by hot-bands and/or different isomers, or from direct- and/or autodetachment. The shoulder becomes more prominent with increasing photon energy: one explanation could be that, similarly to the fluorescein dianion, as the lowest saddle point in the RCB is surpassed, direct detachment starts contributing.[26]

Overall, limited insight would arise from MD simulations, which would anyway require a high level of approximation, yielding unreliable quantitative results. In any case, the simulation of the RCB map is consistent with resonance-tunneling and subsequent electron emission from the amino group of adenine upon excitation to the $^1\pi\pi^*$ states of $[\mathrm{ATP{-}H_2}]^{2-}$. Furthermore, the simulated map shows that the negative charges are localized on the phosphate groups around the sugar moiety, confirming previous findings[190, 191, 198] and thus representing a crude structural probe for $[\mathrm{ATP{-}H_2}]^{2-}$ in the gas-phase. Although tunneling detachment from the amino groups should yield a $\beta_2 \sim +2$, the smaller value seen in the experiment could be due to the position of the phosphate groups (Figure 6.10): as they lie out of the *xz* plane, a strong electric force is applied on the emitted electron along the *y* axis, hence decreasing the overall anisotropy.

Our results are in line with what reported by the Gabelica and Dugourd groups for larger DNA complexes, specifically, 6- and 20-mer single strands and 12-base pair double strands,[195, 196] as well as a 4-tetrad G-quadruplex,[197] where only the purine nucleobases exhibit enhanced electron emission compared to dissociation.[193, 195-197]

6.6 Conclusions

In this work, we have probed the doubly deprotonated dianion of ATP, $[\text{ATP–H}_2]^{2-}$, with single-photon and two-photon resonance enhanced photoelectron spectroscopy in the gas phase, as well as provided the first gas-phase time-resolved photoelectron imaging on this molecule. Excited-states calculations and ground- state optimization at the RI-MP2/def2-TZVP//def2-QZVP and ADC(2)/def2-QZVP levels of theory, as well as *ab-initio* molecular dynamics simulations over 4 ps, were performed to support the experimental findings.

Excitation of $[\text{ATP–H}_2]^{2-}$ with a photon energy of 4.66 eV produces a peak at E_{ke} = 0.55 eV, which is associated with tunneling through RCB. The corresponding PE image exhibits PAD peaks parallel to the laser polarization axis, therefore both electron emission and TDM are assumed to be in that direction. As 4.66 eV is resonant with the $^1\pi\pi^*$ state on the nucleobase, the electron is thought to come from adenine. A two-photon resonance enhanced experiment at 4.66 eV confirms that the electron originates from the nucleobase, and yields the electron affinity associated with the nucleobase, $\text{ADE}_\text{A} = 2 \times 4.66 - 5.2 = 4.1$ eV. A single-photon experiment conducted at different wavelengths, from 280 nm to 260 nm, confirms that the peak at 0.55 eV arises from an indirect process.

$[\text{ATP–H}_2]^{2-}$ is then probed using a 4.66 eV (266 nm) pump pulse and a 1.55 eV (800 nm) probe pulse. The population of the initially excited $^1\pi\pi^*$ state decays through a 3-step model; two competing processes, electron tunneling through the RCB and nuclear motion on the $^1\pi\pi^*$ state, can be observed. Nuclear motion occurs within a ~200 fs timescale. Upon application of a global analysis method, similarities are found between the dynamics of $[ATP–H_2]^{2–}$ and those of $dAMP^–$, in which the intermediate was assigned to population of the $^1\pi\pi^*$ moving away from the Franck-Condon region. As this population can no longer tunnel through the RCB, it internally converts back to the ground state, leading to photo-fragmentation as seen by Cercola *et al.*[192]

Excited states calculations confirm that only adenine is involved in photoemission upon irradiation with photon energy 4.66 eV, confirming that the electron affinity associated with the nucleobase also corresponds to the electron affinity of $[ATP–H_2]^{2–}$. The *ab initio* molecular dynamics simulation over 4 ps and RMSD calculation show that, since their relative position does not change, the phosphate groups' motion does not have significant effect on RCB. The simulation of the TDM confirm that the TDM vector lies in adenine's plane, as previously inferred by the PADs of the PE image at 4.66 eV; moreover, the bidimensional simulation of the RCB indicates that the lowest points of the barrier correspond to either the amino or the methine group of adenine, confirming what could be inferred by the experiments.

This approach provides a new way to study photo-oxidations in polyanions, as well as probing their structure. In the future, probing $[ATP–H_2]^{2–}$ within a cryogenic ion trap[230, 231] could provide quantitative information regarding electron emission; pairing these experiments with excited states dynamics calculations of the molecule could yield a more complete picture on the photo-oxidation of $[ATP–H_2]^{2–}$.

Photophysics of doubly deprotonated ADP, GDP and GTP dianions

7. Photophysics of doubly deprotonated ADP, GDP and GTP dianions

7.1 Motivation

Radiation and oxidation represent two of the major sources of damage for DNA,[47, 48] specifically through photo-oxidation, which is facilitated by the optically bright $^1\pi\pi^*$ states on the nucleobases. This makes DNA particularly sensitive to UV light;[48] however, the low quantum yield (less than 1%) of DNA shows that the molecule presents high intrinsic photostability.[49, 50]

Adenine (Ade) and Guanine (Gua), in particular, are two extremely important nucleobases, as they both derive from the same compound, purine, and are both present in DNA and RNA.[232] Despite being both purines, Ade and Gua differ in terms of position of the amino group, which is in the 6' position in Ade and in the 2' position in Gua; moreover, Gua presents a carboxyl group in 6' position, which allows it to establish three hydrogen bonds with cytosine.[232]

Ade and Gua, as well as their derivatives, have been the object of multiple experimental and computational spectroscopic studies, particularly in the gas-phase.[67, 68, 111, 120, 164, 165, 172, 179, 183, 184, 192, 208, 223, 233-237] It is known that Gua exhibits a lower ionization potential compared to the other nucleobases, which results in a lower adiabatic detachment energy for its deoxynucleotide, $[dGMP]^-$;[111, 165], this is due to the fact that, rather than occurring from the phosphate, electron detachment in $[dGMP]^-$ arises from the nucleobase; however, recent calculations controversially suggest that this is the case for all nucleotide monophosphates.[238-240] Moreover, $[dAMP]^-$ and $[dGMP]^-$ exhibit incredibly similar decay pathways,[67, 68] which are base-centered in both cases, suggesting that Ade and Gua derivatives could bear general similarities in terms of excited state dynamics.

For this reason, we decided to add to our previous study on $[ATP–H_2]^{2–}$[172, 179] and perform similar single-photon photoelectron imaging experiments on doubly deprotonated adenosine-5’-diphosphate, [ADP–H$_2$]$^{2-}$, doubly deprotonated guanosine-5’-diphosphate, [GDP–H$_2$]$^{2-}$, and doubly deprotonated guanosine-5’-triphosphate, [GTP–H$_2$]$^{2-}$ (Figure 7.1).

Contrary to our expectations, the behavior of the Ade derivatives is much different from that of the Gua derivatives: while both Ade derivatives, upon irradiation with 4.66 eV (266 nm) light, exhibit a peak at E_{ke} = 0.55 eV that is consistent with resonant tunneling through the RCB from the $^1\pi\pi^*$ state on the nucleobase, this feature is completely absent in the spectra of the two Gua nucleotides. Moreover, we also observed a sodium adduct of [GTP–H$_2$]$^{2-}$ in the mass spectrum, [GTP–H$_3$•Na]$^{2-}$, which behaves completely differently from [GTP–H$_2$]$^{2-}$: not only does [GTP–H$_3$•Na]$^{2-}$ show a peak at ~1 eV, which we assign to an indirect detachment process, but the energetics of the molecule change drastically when undergoing a sodium exchange.

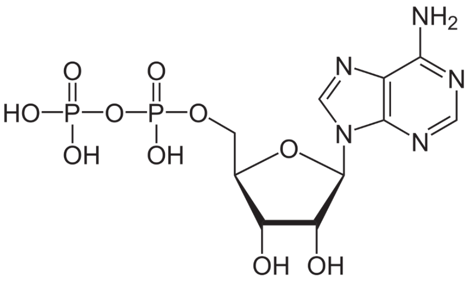

Adenosine diphosphate (ADP)

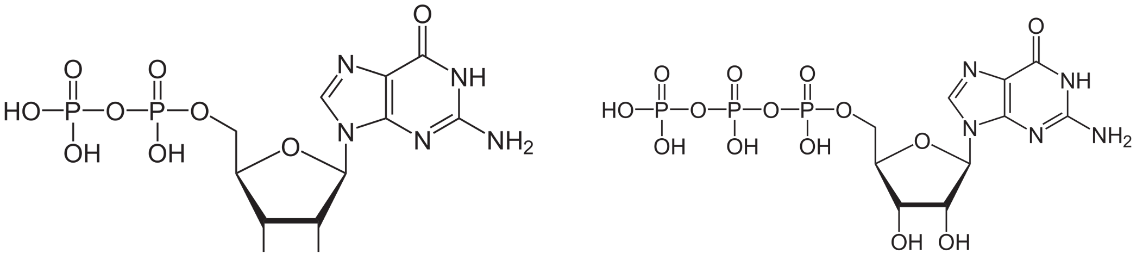

Guanosine diphosphate (GDP)

Guanosine triphosphate (GTP)

Figure 7.1: chemical structure of the nucleotides studied in this chapter.

7.2 Methods

The details of the TR-PEI instrument can be found in the Experimental Section, page 41. A ~1 mM methanolic solution of either adenosine-5'-diphosphate disodium salt, guanosine-5'-diphosphate disodium salt, or guanosine-5'-triphosphate disodium salt (Sigma Aldrich, UK), is electrosprayed via an ESI capillary with a negative voltage of -5 kV. All the PE images were recorded at a VMI voltage of 500 V, using the well-known PE image of I^- for calibration. The resolution of the corresponding PE spectra was approximately ~5%.

7.3 Results

ADP

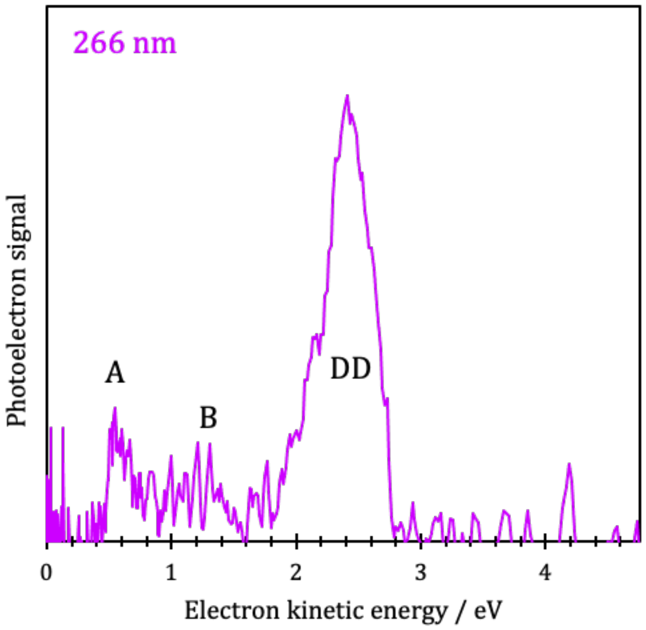

Figure 7.2: photoelectron spectrum of [ADP–2H]$^{2-}$ recorded at 266 nm (4.66 eV), plotted in terms of electron kinetic energy.

[ADP–H$_2$]$^{2-}$ was irradiated with a photon energy of 4.66 eV (266 nm), as previously done by Schinle *et al.*[241] The corresponding PE spectrum (Figure 7.2) presents an intense feature centered at 2.44 eV, which we assign to direct detachment (peak DD). Two other smaller features, centered at approximately E_{ke} = 0.55 eV and E_{ke} = 1.2 eV and labeled A and B, can be seen at lower kinetic energy compared to DD. Feature A is slightly more intense than feature B.

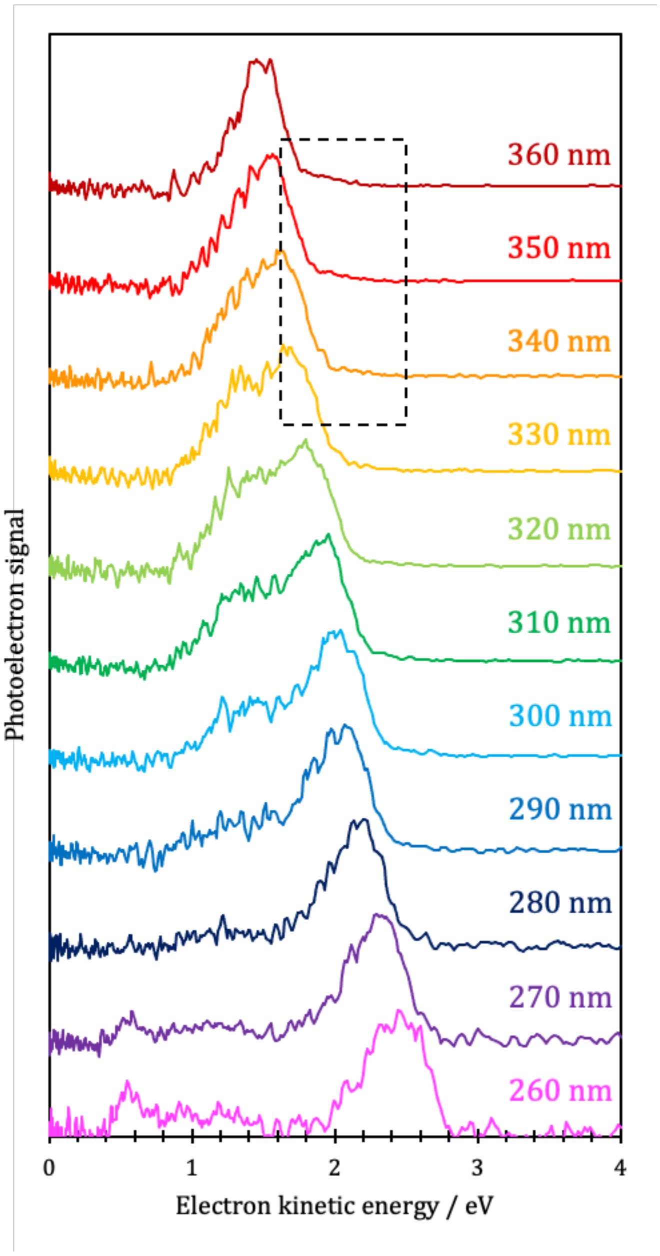

Figure 7.3: photoelectron spectra of [ADP-2H]$^{2-}$ recorded between 260 nm (4.76 eV) and 360 nm (3.44 eV), plotted in terms of electron kinetic energy.

Single-photon PE experiment were also performed on [ADP–H$_2$]$^{2-}$ using a wavelength range from 260 nm to 360 nm, with steps of 10 nm (Figure 7.3, in the previous page). Compared to the spectrum at 266 nm, peak A is present only in the spectra at 260 nm and 270 nm. Feature A then progressively disappears with increasing wavelength. Conversely, feature B gradually increases in intensity between 260 nm and 330 nm and merges with the DD feature, which red-shifts with longer wavelengths (as expected), until, from 340 nm onwards, the two peaks cannot be resolved anymore. It is important to notice that only DD shifts, while B roughly appear at the same kinetic energy. Additionally, a new feature seems to arise close to the high-energy tail of DD with decreasing photon energy. This new feature is labeled as C and is highlighted in Figure 7.3 by a dashed rectangle.

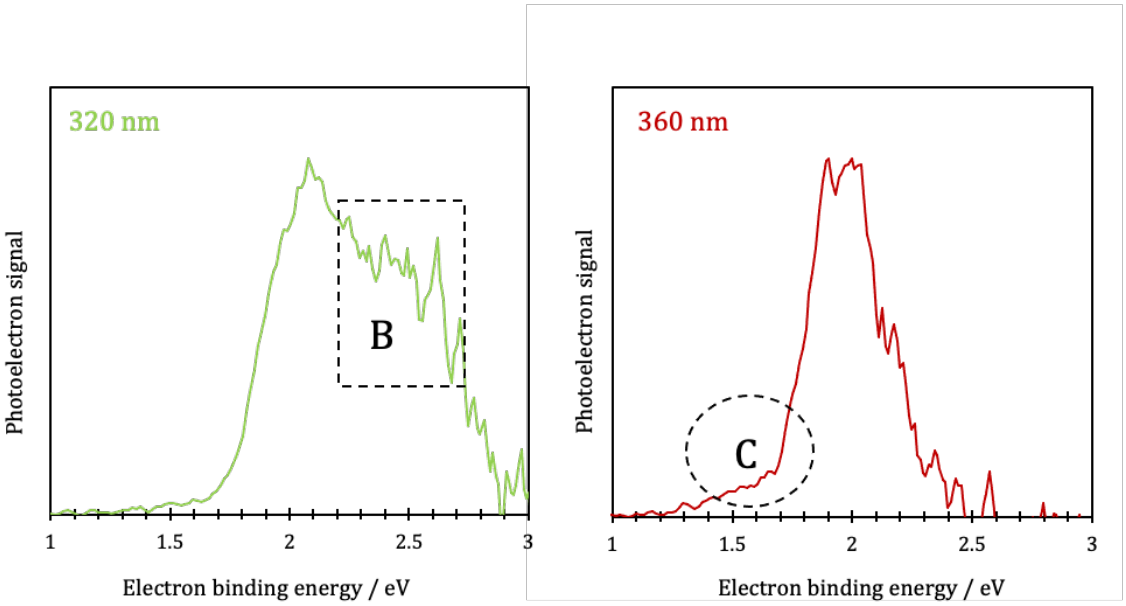

Figure 7.4: magnifications of photoelectron spectra of $[ADP\text{-}2H]^{2-}$ recorded at 320 nm (3.87 eV) and 360 nm (3.44 eV), plotted in terms of electron binding energy. Only the energy range between 1 and 3 eV is shown.

Magnifications of two single-photon PE spectra of $[ADP–H_2]^{2-}$, taken, respectively, at 320 nm (left panel) and at 360 nm (right panel), can be seen in Figure 7.4. The spectra are plotted in terms of Electron Binding Energy (E_{be}) and focus solely on 1 eV < E_{be} < 3 eV. The Vertical Detachment Energy (VDE) was extracted from the 320 nm spectrum, while the Adiabatic Detachment Energy (ADE) was derived from the 360 nm spectrum, resulting in ADE = 1.7 eV and VDE = 2.1 eV. The Repulsive Coulomb Barrier (RCB) was estimated to be around 1.0 eV. Moreover, the abovementioned spectral differences observed at different wavelengths can be more easily appreciated upon direct comparison of these two spectra. While feature B, highlighted by a dashed rectangle, is almost completely absorbed by DD at 320 nm, at 360 nm it is basically absent. On the other hand, feature C (circled with a dashed line in the 360 nm spectrum) exhibits an opposite behavior, hence is almost not present in the 320 nm spectrum.

GDP

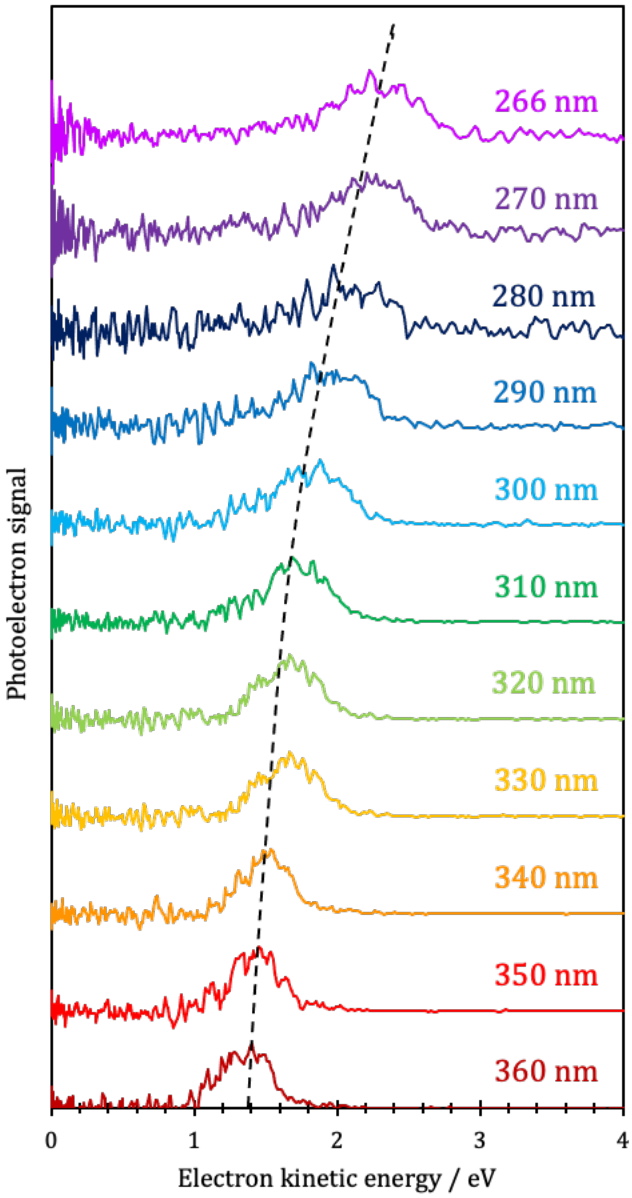

Figure 7.5: single-photon PE spectra of [GDP–H$_2$*]*$^{2-}$ *expressed in terms of E*$_{\mathrm{ke}}$ *taken at 270 nm < wavelength < 360 nm with steps of 10 nm, and at 266 nm.*

Single-photon PE spectra of $[GDP–H_2]^{2-}$ were taken at a wavelength range between 270 nm and 360 nm with steps of 10 nm, and at 266 nm (4.66 eV).

The spectra, plotted in terms of E_{ke}, can be seen in Figure 7.5. Only one feature can be seen in the spectra. The feature shifts towards higher E_{ke} as the wavelength decreases, suggesting that it arises from a direct process. Moreover, the peak does not exhibit shape changes with varying photon energy, although the signal-to-noise ratio decreases considerably as the photon energy increases.

The spectrum recorded at 320 nm (Figure 7.6) was used to extract the ADE and VDE values and to estimate the height of the RCB. The yielded values were, respectively, ADE = 1.8 eV, VDE = 2.2 eV, with errors of ±0.1 eV, and an RCB estimate of approximately ~1 eV.

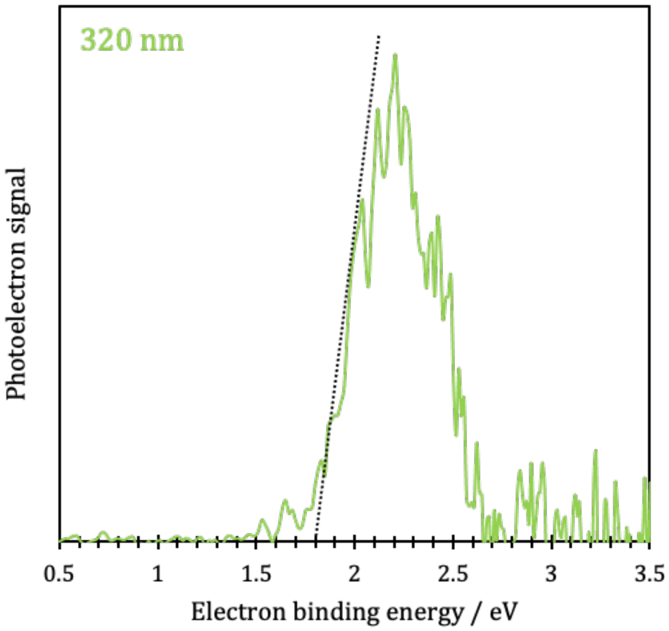

Figure 7.6: single-photon PE spectrum of $[GDP–H_2]^{2-}$ expressed in terms of E_{be} taken at 320 nm. The black oblique line indicates the adiabatic detachment energy.

GTP

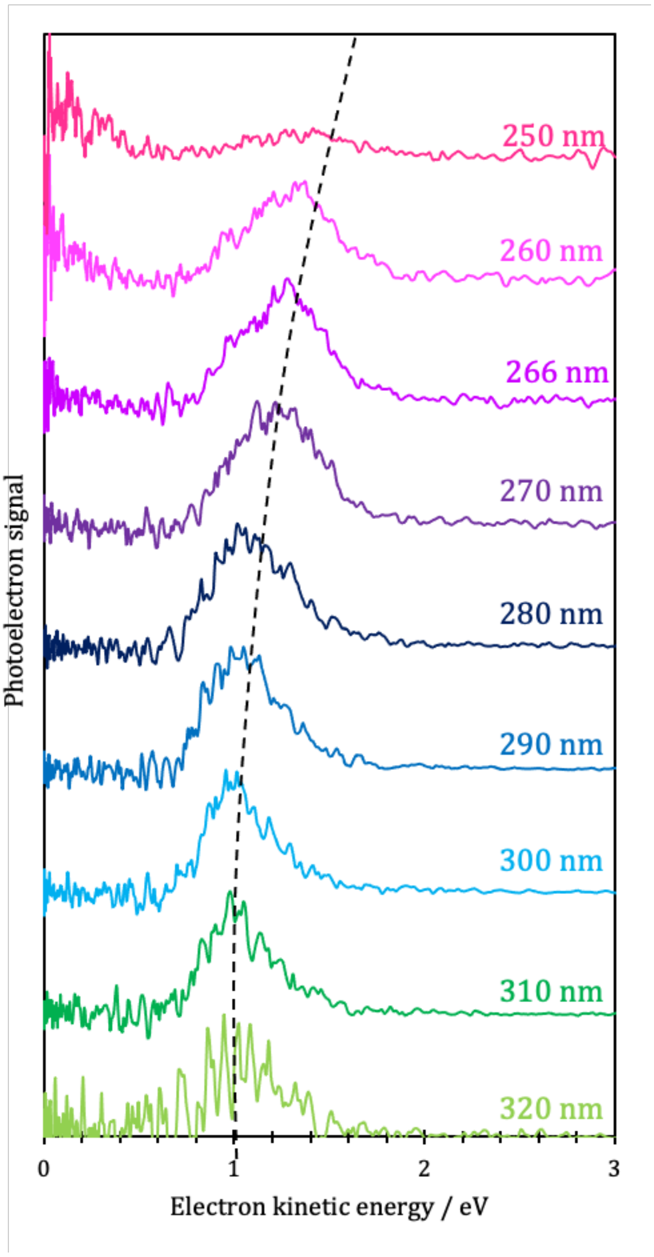

Figure 7.8: single-photon PE spectra of [GTP-H$_2$]$^{2-}$ expressed in terms of E_{ke} taken at 250 nm < wavelength < 320 nm with steps of 10 nm, and at 266 nm.

The single-photon PE spectra of [GTP–H$_2$]$^{2-}$ were taken at a wavelength range between 250 nm and 320 nm, with steps of 10 nm, and at 266 nm (Figure 7.8). Only one feature is observed in the spectra; this dominant feature most likely corresponds to direct detachment, as the peak steadily shifts towards high E_{ke} as the photon energy is increased. The spectrum at 266 nm (Figure 7.7) was used to extract ADE, VDE and RCB values, and yielded ADE = 3.0 eV, VDE = 3.4 eV and an RCB estimate of ~0.8 eV.

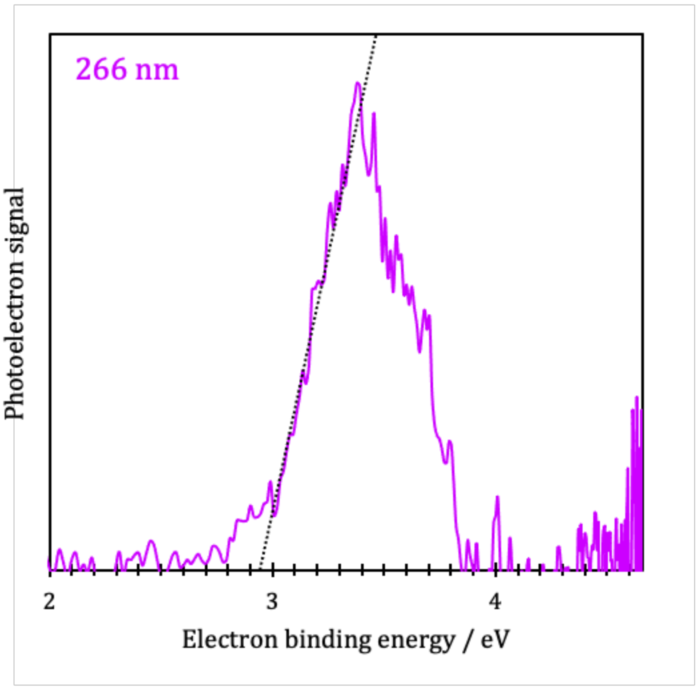

Figure 7.7: single-photon PE spectrum of [GTP-H$_2$*]*$^{2-}$ *expressed in terms of* $E_{\rm be}$ *taken at 266 nm. The red oblique line indicates the adiabatic detachment energy.*

Upon inspection of the mass spectrum of [GTP–H$_2$]$^{2-}$, a dianionic sodium adduct of the molecule, [GTP–H$_3$•Na]$^{2-}$, appeared to be present. Single-photon PE spectra of this adduct were also recorded, using a wavelength range between 270 nm and 320 nm, with steps of 10 nm, and taking an extra spectrum at 266 nm (Figure 7.9). The most intense feature in the 320 nm spectrum (highlighted in Figure 7.9 with a curved dashed line) shifts towards higher $E_{\rm ke}$ as photon energy is increased. On the other hand, a second feature at lower $E_{\rm ke}$ peak, centered at approximately 1 eV and highlighted in Figure 7.8 by a dashed rectangle, appears from 310 nm onwards and does not shift when changing photon energy. Moreover, this peak becomes dominant as the photon energy increases and, at 266 nm, completely covers the direct detachment peak. As the position of this feature does not change with changing photon energy, we assign it to an indirect process, most likely tunnelling trough the RCB.

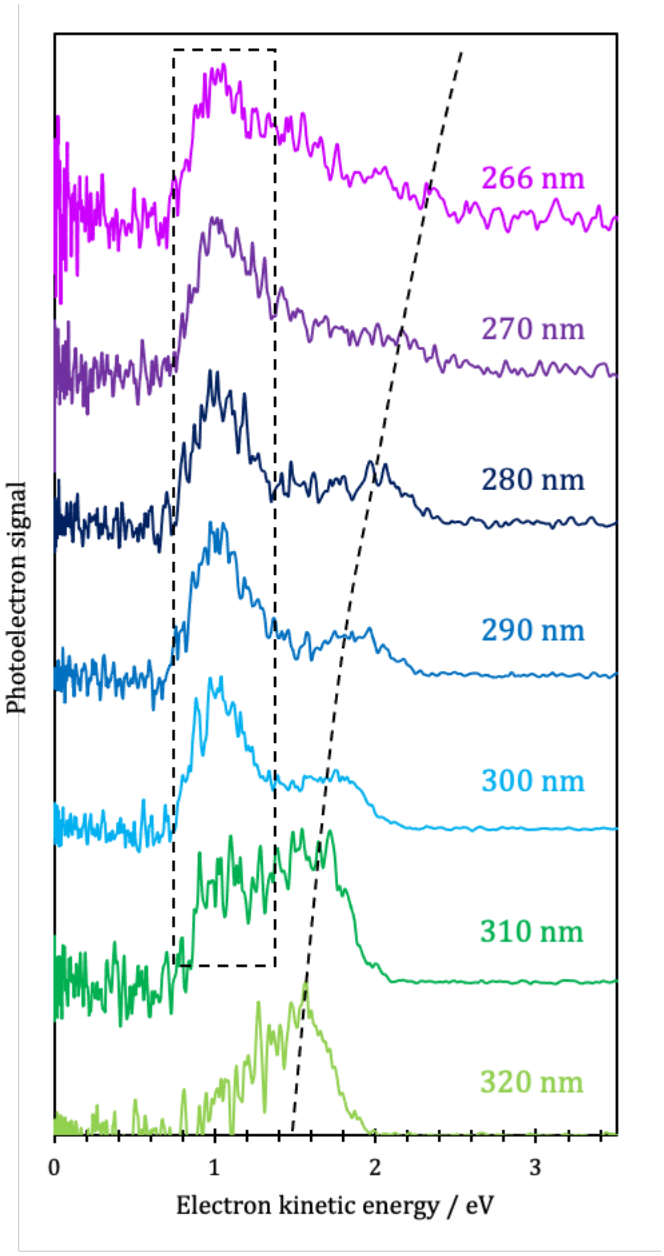

Figure 7.9: single-photon PE spectra of [GTP-H_3*•Na]*$^{2-}$ *expressed in terms of* E_{ke} *taken at 270 nm < wavelength < 320 nm with steps of 10 nm, and at 266 nm.*

The spectrum at 320 nm (Figure 7.10, in the following page) was used to attain ADE and VDE values and an estimate of the height of the RCB. The results were ADE = 2.0 eV, VDE = 2.3 eV, and RCB ~1.2 eV.

A summary of all the ADE and VDE values, together with the RCB estimates and, if present, the position of the tunneling peaks for all the doubly-deprotonated dianions of the purine nucleobases, $[\mathrm{ATP-H_2}]^{2-}$, $[\mathrm{ADP-H_2}]^{2-}$, $[\mathrm{GTP-H_2}]^{2-}$, $[\mathrm{GDP-H_2}]^{2-}$ and $[\mathrm{GTP-H_3{\bullet}Na}]^{2-}$ can be seen in Table 7.1 (in the following page).

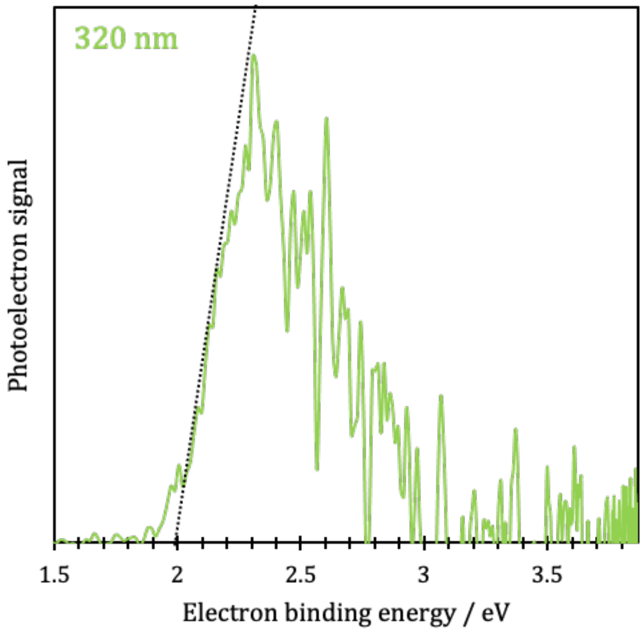

Figure 7.10: single-photon PE spectrum of [GTP-H$_3$•Na]$^{2-}$ expressed in terms of E_{be} taken at 320 nm. The red oblique line indicates the adiabatic detachment energy.

Table 7.1: energetics of the doubly deprotonated purine dianions, with RCB estimates and position of the tunneling peak (if present).

Species	**ADE (E_{be})**	**VDE (E_{be})**	**RCB (E_{ke})**	**Tunneling peak position (E_{ke})**
[ATP–H$_2$]$^{2-}$	~4.1 eV	N/A	0.57 eV (calculated)	0.55 eV
[ADP–H$_2$]$^{2-}$	1.7 eV	2.1 eV	~1 eV	0.55 eV
[GDP–H$_2$]$^{2-}$	1.8 eV	2.2 eV	~1 eV	N/A
[GTP–H$_2$]$^{2-}$	3.0 eV	3.4 eV	~0.8 eV	N/A
[GTP–H$_3$•Na]$^{2-}$	2.0 eV	2.3 eV	~1.2 eV	1 eV

7.4 Discussion

ADP

Our results on $[ADP–H_2]^{2-}$ are in contrast with the findings reported by Schinle *et al.*[241], but in accord with the results obtained by Cercola *et al.*[192]. Cercola and co-workers recorded a photodepletion spectrum of $[ADP–H_2]^{2-}$ that should be below the detachment continuum; additionally, the photofragment mass spectrum of $[ADP–H_2]^{2-}$ at 4.9 eV yields a peak that can be assigned to electron detachment.[192] On the other hand, the direct detachment peak of $[ADP–H_2]^{2-}$ in our PE spectra appears slightly blue-shifted when compared to the Kappes group's spectrum at the same energy (4.66 eV).[241] For this reason, the resulting ADE, VDE and RCB values are considerably different. While we observe ADE and VDE values of 1.7 eV and 2.1 eV, Schinle *et al.* [241] report ADE and VDE values that are, respectively, ~0.35 eV and ~0.2 eV lower. On the other hand, the RCB estimate reported by Schinle and co-workers[241] is greater than ours of approximately ~0.8-1.2 eV. The two experiments differ in terms of detector apparatus: while the Kappes group uses a magnetic bottle spectrometer,[242, 243] we perform our experiments with a VMI assembly. However, such differences should not have an impact on the estimation of the electron affinity of the molecule of study. Moreover, features A, B and C of Figure 7.2 are completely absent in the 266 nm PE spectrum recorded by Schinle and coworkers.[241] Peak A, which is clearly observable at 260 nm and 270 nm at approximately E_{ke} = 0.55 eV, can be assigned to electron tunneling through the RCB, similarly to what observed for $[ATP–H_2]^{2-}$.[172, 179] We also expect this electron to come from the $^1\pi\pi^*$ state on adenine, as it is at the same energy of the tunneling peak in $[ATP–H_2]^{2-}$.[172, 179] Peak B exhibits a very peculiar behavior. At these wavelengths, we should not be able to excite the individual components of $[ADP–H_2]^{2-}$. On the other hand, one could hypothesize that the peak arises from different isomers, although isomers should not result in such a shift. Another possibility could be the presence of different deprotomers, although this is not in accord with what observed both experimentally and theoretically by the Kappes group. The last option, and probably the most feasible, is that this peak arises from an interaction between different components of $[ADP–H_2]^{2–}$, specifically due to a charge-transfer transition from the diphosphate moiety to the adenine nucleobase. Peak C could instead be explained as a second conformer of $[ADP–H_2]^{2–}$. In fact Schinle *et al.* calculated two distinct conformers, ADP1 and ADP2, which differ in term of hydrogen bonding; nevertheless, both calculations and experiments do not suggest differential PE signal at 266 nm.[241] This is not necessarily in disagreement with our findings, as the feature does not appear in the PE spectra taken at $\lambda < 330$ nm.

We also tried performing a time-resolved measurement on $[ADP–H_2]^{2–}$ using a 266 nm pump pulse and a 800 nm probe pulse, but unfortunately these experiments were unsuccessful.

GDP

Contrary to $[ADP–H_2]^{2–}$, excitation of $[GDP–H_2]^{2–}$ at $260 \text{ nm} < \lambda < 360$ nm only yields one peak, which blue-shifts consistently as the photon energy is increased (Figure 7.5). Due to this behavior, this peak has been assigned to direct detachment. No other peaks are observed in the spectrum, although the poor quality of the lowest-energy spectra prevents us from drawing any conclusions. Nevertheless, the differences between the two molecules are quite unexpected, especially considering the similarities carried by mono-phosphorylated adenine and guanine nucleotides, $[dAMP]^-$ and $[dGMP]^-$, in terms of excited states dynamics.[67, 68]

Depsite these differences, the energetics of $[GDP–H_2]^{2–}$ are similar to those of $[ADP–H_2]^{2–}$, as shown in Table 7.1. Density functional theory calculations[111] and resonance enhanced two-photon detachment ionization[165] experiments, as well as excited states dynamics[222] and time-resolved photoelectron imaging experiments,[68] could help in better understanding our experimental findings.

GTP

Irradiation of $[GTP-H_2]^{2-}$ with $h\nu$ = 4.66 eV gives rise to a single, intense feature that shifts towards higher E_{ke} as the photon energy is increased. The ADE, VDE and RCB estimate of $[GTP-H_2]^{2-}$ are, respectively, 3.0 eV, 3.4 eV and an RCB estimate of ~0.8 eV, which is quite different from what observed for $[ATP-H_2]^{2-}$.[164] In particular, according to what we observed on our previous studies on $[ATP-H_2]^{2-}$, i.e., that the HOMO is located on the base, the lower ADE value (3.0 eV for $[GTP-H_2]^{2-}$ against 4.1 eV for $[ATP-H_2]^{2-}$) is in line with what previously observed for guanine and its derivatives, *i.e.,* the lower ionization potential compared to the other nucleobases.[68, 111, 165]

On the other hand, the behavior of the doubly deprotonated sodium adduct of GTP, $[GTP-H_3\bullet Na]^{2-}$, is rather interesting. $[GTP-H_3\bullet Na]^{2-}$ most likely arises from a sodium exchange with one of the hydrogens on the phosphate groups, as seen in the case of alkali metal-deoxynucleotide complexes[244] and Pb^{2+}•deprotonated 5'deoxyguanine adducts.[237] However, as the total charge remains –2, interaction between Na^+ and the nucleobase moiety cannot be excluded; in fact, chelation of Li^+ with the N7 and O6 positions of guanine has been observed for the isolated nucleobase.[236] Moreover, protonation at the N3 site has been observed to induce base rotation in both $[dAMP]^-$ and $[AMP]^-$.[245] Molecular dynamics simulations, Infrared Multi-Photon Dissociation (IR-MPD)[245] and ion mobility experiments[237] could help in identifying the position in which the sodium exchange occurs.

The PE spectrum of $[GTP-H_3\bullet Na]^{2-}$ exhibits a broad peak centered at approximately E_{ke} = 1 eV, and another smaller peak at higher energy, which is very hard to distinguish due to the poor spectral quality. Upon irradiation of $[GTP-H_3\bullet Na]^{2-}$ with laser pulses of wavelength 266 nm < λ < 320 nm, the 1 eV peak not only becomes more intense as the photon energy is increased, but also does not shift in its position. Hence, we can attribute this peak to an indirect process, *i.e.,* electron tunneling through the repulsive Coulomb barrier or autodetachment. However, we cannot say for sure whether this corresponds to electron ejection from the $\pi\pi^*$ states on the nucleobase, similarly to $[ATP-H_2]^{2-}$,[172, 179] as the position of the excited states of $[GTP-H_3\bullet Na]^{2-}$ is not known. This is particularly interesting, especially considering that $[dGMP]^-$ and $[dAMP]^-$ present striking similarities in terms of excited states dynamics, with both decays being base-centered.[67, 68] On the other hand, the high E_{ke} feature does not shift with varying photon energy, allowing us to explain it as direct detachment. While the direct detachment peak is dominant at 320 nm, with decreasing wavelength the ratio between the tunneling and direct detachment peaks is inverted. Already at 300 nm the tunneling peak is considerably more intense than the direct detachment feature; finally, at 266 nm the latter is almost completely covered by the tunneling peak.

The ADE, VDE and RCB estimates for $[\mathrm{GTP{-}H_3{\bullet}Na}]^{2-}$ are in stark contrast with what observed for $[\mathrm{GTP{-}H_2}]^{2-}$ (Table X). Overall, the presence of the sodium seems to significantly lower the energetics, particularly in the case of the ADE value, while the estimate of the RCB height increases of ~0.4 eV.

We tried performing time-resolved PE imaging experiments on $[\mathrm{GTP{-}H_2}]^{2-}$ using a 266 nm pump pulse and a 800 nm probe pulse, but unfortunately, due to the low quality of the spectra, interpreting the results with confidence was impossible.

7.5 Overall discussion and conclusions

The results obtained on $[\mathrm{ADP{-}H_2}]^{2-}$, $[\mathrm{GDP{-}H_2}]^{2-}$, $[\mathrm{GTP{-}H_2}]^{2-}$ and $[\mathrm{GTP{-}H_2{\bullet}Na}]^{2-}$ are very different from one another and of difficult interpretation. Evidence of intra-molecular charge-transfer has only been found in $[\mathrm{ADP{-}H_2}]^{2-}$; however, theoretical support is required to confirm these findings. Both $[\mathrm{ADP{-}H_2}]^{2-}$ and $[\mathrm{GTP{-}H_2}]^{2-}$ exhibit differences with our previous findings on $[\mathrm{ATP{-}H_2}]^{2-}$.[172, 179] Moreover, despite carrying the same number of phosphate groups, $[\mathrm{ADP{-}H_2}]^{2-}$ and $[\mathrm{GDP{-}H_2}]^{2-}$ give rise to completely different photoelectron spectra. It is clear that, although singly-charged purine-bearing nucleotides exhibit analogous behaviors,[68] this is not the case in presence of an extra negative charge.

The importance of counter-ions has also become apparent through these experiments: the same nucleotide, $[\mathrm{GTP{-}H_2}]^{2-}$, behaves in a completely different fashion if undergoing a sodium exchange. The effect of the $\mathrm{Na^+}$ has a huge impact on both the energetics and the dynamics of the molecule, raising interesting questions on the role of counter-ions in the decay pathways of biological molecules.

In conclusion, more experimental and theoretical support is necessary to fully understand our findings. A first step could be performing DFT calculations to attain the ADE and VDE values of the compounds,[111, 192] together with an estimation of the RCBs.[172] Conducting time-resolved PE imaging experiments would also be helpful in shedding light on our findings.[67, 68, 164, 172, 179] Lastly, molecular dynamics simulations, particularly ab initio calculations, combined with IR-MPD[245] and ion mobility-mass spectrometry,[237] would aid the understanding of the role of counter-ions in both the structure and the dynamics of nucleotides. Nevertheless, these results are a first step towards the understanding of the excited states dynamics of $[ADP{-}H_2]^{2-}$, $[GDP{-}H_2]^{2-}$, $[GTP{-}H_2]^{2-}$ and, more generally, of di-anionic nucleotides and other compounds of biological interest.

Final remarks

8. Final remarks

In this thesis, we have extensively explored the extremely challenging and broad topic of interactions of DNA with low-energy electrons and photons. To do so, we have exploited gas-phase photoelectron imaging of anions and spectroscopically probed the molecules of interest.

We have started our study by exploring the dipole-bound states (DBSs) of para-substituted phenolate anions.[120] Phenolate is a model molecule already studied by the Wang group[156]. DBSs have also been observed in DNA and its derivatives[149, 150, 152] and can act as a doorway to capture LEEs[74-78], hence potentially playing an important role in DNA damage and repair. We replicated Liu *et al.*'s[156] experiments with para-substituted phenolate anions with alkyl chains of increasing length and observed that, even though the alkyl chain interacts with the DBS, the latter is not disrupted. Instead, the DBS is retained in all cases, including the para-substituted phenolate with the longest alkyl chain, 4-octylphenolate: this makes us wonder if the DBS could survive in a condensed or soft-matter environment and, more specifically, in a biological environment.

We continued our study by choosing a model molecule, carboxy-5'-adenosine, to explore the possibility of intramolecular charge-transfer as a probe for electron damage in DNA.[164] We chose a model molecule, rather than a phosphorylated nucleotide like deoxy-adenosine monophosphate ($dAMP^-$), which presents a very high electron affinity due to the phosphate group.[111, 165] Following the method created by Widlanski and Epp,[166] we synthesized an adenosine analog with a carboxylic group in 5' position, and studied its dynamics upon irradiation with a 4.66 eV (266 nm) pump pulse and 1.55 eV (800 nm) and 3.10 eV (400 nm) probe pulses. Unfortunately, the carboxylated adenosine analog exhibits excited-states dynamics that are adenine-centered, and the charge-transfer transition appears to be disfavored. Specifically, the molecule's decay is similar to that of $dAMP^-$ and its di- and tri-nucleotide,[67] which is dominated by internal conversion of the $^1\pi\pi^*$ back to the ground-state.

We then tried to perform an analogous experiment on intra-molecular charge transfer using the doubly deprotonated dianion of adenosine-5'-triphosphate, $[ATP–H_2]^{2-}$, a molecule with great biological importance due to its involvement in cellular energy distribution and metabolism. The electron affinity of dianions is considerably lower than that of the corresponding anions, making the experiment with 266 nm light more accessible for our current experimental setup. $[ATP{-}H_2]^{2-}$ has already been studied by the Kappes group[198] and the Dessent group[192] in the past; contradicting results had emerged, as the photoelectron spectroscopy experiment by Schinle *et al.*[198] showed no photoemission upon irradiation with 4.66 eV light, while Cercola *et al.*'s[192] photodetachment action spectra suggested there should be. We reproduced the photoelectron spectroscopy experiment at 4.66 eV, showed that photoemission occurs in the form of tunneling through the repulsive Coulomb barrier (RCB) of the dianion resonant with the $^1\pi\pi^*$ state on adenine, and that from the photoelectron angular distribution (PAD) peaks of the photoelectron image we can deduce the site of electron ejection, the direction, and the transition dipole moment of $[ATP{-}H_2]^{2-}$. To confirm these findings, we performed additional single-photon experiments and a computational study to simulate the RCB of $[ATP{-}H_2]^{2-}$. Moreover, we performed a time-resolved photoelectron spectroscopy study on $[ATP{-}H_2]^{2-}$ with a 4.66 eV pump pulse and a 1.55 eV probe pulse. We showed that the dynamics of the molecule follow a three-step model, with competition between resonant tunneling and internal conversion back to the ground state, supporting what was previously observed by Cercola and co-workers.[192] Although we could not observe intra-molecular charge transfer, this study explores the interesting topic of electron tunneling in DNA derivatives and, more generally, in molecules of biological interest.

Lastly, we continued our study on nucleotide dianions by repeating the experiments previously performed with $[ATP{-}H_2]^{2-}$ on $[ADP{-}H_2]^{2-}$, $[GDP{-}H_2]^{2-}$ and $[GTP{-}H_2]^{2-}$. We discovered that adenine and guanine nucleotides exhibit completely different behaviors, *i.e.*, while electron tunneling resonant with the nucleobase is seen in both $[ATP{-}H_2]^{2-}$ and $[ADP{-}H_2]^{2-}$, irradiation of $[GDP{-}H_2]^{2-}$ and $[GTP{-}H_2]^{2-}$ with 4.66 eV only yields evidence of direct detachment. Evidence of intra-molecular charge transfer between the diphosphate moiety and the nucleobase is only observed in the case of $[ADP{-}H_2]^{2-}$. Interestingly, the photoelectron spectra at different wavelengths of the sodium adduct of $[GTP{-}H_2]^{2-}$, $[GTP{-}H_3{\bullet}Na]^{2-}$, suggest that an indirect process is taking place

To sum up, we have explored the role of low-energy electron and photon damage in DNA by studying progressively more complex systems, starting from the bare chromophore, and ending with di- and triphosphate nucleotides. Although some of the studies illustrated in this thesis are not conclusive, and further research, both computational and experimental, is necessary, it nevertheless represents an important steppingstone for understanding the underlying mechanisms of electron damage in DNA.

9. References

1. Yamazaki, R.; Matsuya, Y.; Ohtsubo, Y.; Tsutsumi, K.; Date, H.; Sasaki, K., Quantitative estimation of DNA damage by photon irradiation based on the microdosimetric-kinetic model. *J. Radiat. Res.* **2014,** *55* (3), 484-493.
2. Boudaiffa, B.; Cloutier, P.; Hunting, D.; Huels, M. A.; Sanche, L., Resonant formation of DNA strand breaks by low-energy (3 to 20 eV) electrons. *Science* **2000,** *287* (5458), 1658-60.
3. Li, Z.; Cloutier, P.; Sanche, L.; Wagner, J. R., Low-energy electron-induced DNA damage: effect of base sequence in oligonucleotide trimers. *J. Am. Chem. Soc.* **2010,** *132* (15), 5422-7.
4. Stolow, A.; Bragg, A. E.; Neumark, D. M., Femtosecond Time-Resolved Photoelectron Spectroscopy. *Chem. Rev.* **2004,** *104* (4), 1719-1758.
5. Einstein, A., Generation and conversion of light with regard to a heuristic point of view. *Annalen Der Physik* **1905,** *17* (6), 132-148.
6. Atkins, P. W.; De Paula, J., *Atkins' Physical chemistry*. Tenth edition. ed.; Oxford University Press: Oxford ; New York, 2014; p xxv, 1008 pages.
7. Koopmans, T., The classification of wave functions and eigen-values to the single electrons of an atom. *Physica* **1934,** *1*, 104-113.
8. Cockett, M. C. R., Photoelectron spectroscopy without photoelectrons: Twenty years of ZEKE spectroscopy. *Chem. Soc. Rev.* **2005,** *34* (11), 935-948.
9. Franck, J.; Dymond, E. G., Elementary processes of photochemical reactions. *J. Chem. Soc. Faraday Trans.* **1926,** *21* (February), 536-542.
10. Condon, E., A theory of intensity distribution in band systems. *Phys. Rev.* **1926,** *28* (6), 1182-1201.
11. Atkins, P. W.; Friedman, R., *Molecular quantum mechanics*. 5th ed.; Oxford University Press: Oxford ; New York, 2011; p xiv, 537 p.
12. Kraack, J. P.; Buckup, T., Introduction to State-of-the-Art Multidimensional Time-Resolved Spectroscopy Methods. *Topics in Current Chemistry* **2018,** *376* (4), 28.

13. Cabanillas-Gonzalez, J.; Grancini, G.; Lanzani, G., Pump-Probe Spectroscopy in Organic Semiconductors: Monitoring Fundamental Processes of Relevance in Optoelectronics. *Adv. Mater.* **2011,** *23* (46), 5468-5485.

14. Verlet, J. R. R., Femtosecond spectroscopy of cluster anions: insights into condensed-phase phenomena from the gas-phase. *Chem. Soc. Rev.* **2008,** *37* (3), 505-517.

15. Grumbling, E. R.; Pichugin, K.; Mabbs, R.; Sanov, A., Photoelectron Imaging as a Quantum Chemistry Visualization Tool. *J. Chem. Educ.* **2011,** *88* (11), 1515-1520.

16. Anstoter, C. S.; Dean, C. R.; Verlet, J. R. R., Sensitivity of Photoelectron Angular Distributions to Molecular Conformations of Anions. *J. Phys. Chem. Lett.* **2017,** *8* (10), 2268-2273.

17. Sanov, A., Laboratory-frame photoelectron angular distributions in anion photodetachment: insight into electronic structure and intermolecular interactions. *Annu. Rev. Phys. Chem.* **2014,** *65*, 341-63.

18. Wang, X.-B.; Ding, C.-F.; Wang, L.-S., Photodetachment Spectroscopy of a Doubly Charged Anion: Direct Observation of the Repulsive Coulomb Barrier. *Phys. Rev. Lett.* **1998,** *81*, 3351-3354.

19. Simons, J., Molecular anions. *J. Phys. Chem. A* **2008,** *112* (29), 6401-6511.

20. Dreuw, A.; Cederbaum, L. S., Multiply Charged Anions in the Gas Phase. *Chem. Rev.* **2002,** *102* (1), 181-200.

21. Verlet, J. R. R.; Horke, D. A.; Chatterley, A. S., Excited states of multiply-charged anions probed by photoelectron imaging: riding the repulsive Coulomb barrier. *Phys. Chem. Chem. Phys.* **2014,** *16* (29), 15043-15052.

22. Wang, L.-S.; Wang, X.-B., Probing Free Multiply Charged Anions Using Photodetachment Photoelectron Spectroscopy. *J. Phys. Chem. A* **2000,** *104* (10), 1978-1990.

23. Wang, X.-B.; Wang, L.-S., Observation of negative electron-binding energy in a molecule. *Nature* **1999,** *400* (6741), 245-248.

24. Wang, X.-B.; Woo, H.-K.; Huang, X.; Kappes, M. M.; Wang, L.-S., Direct Experimental Probe of the On-Site Coulomb Repulsion in the Doubly Charged Fullerene Anion $\mathrm{C}_{70}{}^{2\ensuremath{-}}$. *Phys. Rev. Lett.* **2006,** *96* (14), 143002.

25. Dau, P. D.; Liu, H.-T.; Yang, J.-P.; Winghart, M.-O.; Wolf, T. J. A.; Unterreiner, A.-N.; Weis, P.; Miao, Y.-R.; Ning, C.-G.; Kappes, M. M.; Wang, L.-S., Resonant tunneling through the repulsive Coulomb barrier of a quadruply charged molecular anion. *Phys. Rev. A* **2012,** *85* (6), 064503.

26. Horke, D. A.; Chatterley, A. S.; Verlet, J. R., Effect of internal energy on the repulsive Coulomb barrier of polyanions. *Phys. Rev. Lett.* **2012,** *108* (8), 083003.

27. Xing, X.-P.; Wang, X.-B.; Wang, L.-S., Photoelectron imaging of multiply charged anions: Effects of intramolecular Coulomb repulsion and photoelectron kinetic energies on photoelectron angular distributions. *J. Chem. Phys.* **2009,** *130* (7), 074301.

28. Horke, D. A.; Chatterley, A. S.; Verlet, J. R. R., Femtosecond Photoelectron Imaging of Aligned Polyanions: Probing Molecular Dynamics through the Electron–Anion Coulomb Repulsion. *J. Phys. Chem. Lett.* **2012,** *3* (7), 834-838.

29. Bordas, C.; Paulig, F.; Helm, H.; Huestis, D. L., Photoelectron imaging spectrometry: Principle and inversion method. *Rev. Sci. Instrum.* **1996,** *67* (6), 2257-2268.

30. Luminescent Materials. In *Ullmann's Encyclopedia of Industrial Chemistry*.

31. Hertel, I. V.; Radloff, W., Ultrafast dynamics in isolated molecules and molecular clusters. *Rep. Prog. Phys.* **2006,** *69* (6), 1897-2003.

32. Kuhlman, T. S.; Sauer, S. P. A.; Sølling, T. I.; Møller, K. B., Symmetry, vibrational energy redistribution and vibronic coupling: The internal conversion processes of cycloketones. **2012,** *137* (22), 22A522.

33. Mai, S.; Marquetand, P.; Gonzalez, L., Nonadiabatic dynamics: The SHARC approach. *Wiley Interdiscip. Rev. Comput. Mol. Sci.* **2018,** *8* (6), e1370.

34. Fang, W. H., Ab initio determination of dark structures in radiationless transitions for aromatic carbonyl compounds. *Acc. Chem. Res.* **2008,** *41* (3), 452-7.

35. Martinez, T. J., Seaming is believing. *Nature* **2010,** *467*, 412.

36. Watson, J. D.; Crick, F. H. C., Molecular Structure of Nucleic Acids: A Structure for Deoxyribose Nucleic Acid. *Nature* **1953,** *171* (4356), 737-738.

37. Miles, D. W.; Townsend, L. B.; Miles, D. L.; Eyring, H., Conformation of nucleosides: circular dichroism study on the syn-anti conformational equilibrium of 2-substituted benzimidazole nucleosides. *Proc. Natl. Acad. Sci. U.S.A.* **1979,** *76* (2), 553-6.

38. Yakovchuk, P.; Protozanova, E.; Frank-Kamenetskii, M. D., Base-stacking and base-pairing contributions into thermal stability of the DNA double helix. *Nucleic Acids Res.* **2006,** *34* (2), 564-74.

39. Richmond, T. J.; Davey, C. A., The structure of DNA in the nucleosome core. *Nature* **2003,** *423* (6936), 145-50.

40. DiMaio, F.; Yu, X.; Rensen, E.; Krupovic, M.; Prangishvili, D.; Egelman, E. H., Virology. A virus that infects a hyperthermophile encapsidates A-form DNA. *Science* **2015,** *348* (6237), 914-7.

41. Kwok, C. K.; Merrick, C. J., G-Quadruplexes: Prediction, Characterization, and Biological Application. *Trends Biotechnol.* **2017,** *35* (10), 997-1013.

42. Nikolova, E. N.; Kim, E.; Wise, A. A.; O'Brien, P. J.; Andricioaei, I.; Al-Hashimi, H. M., Transient Hoogsteen base pairs in canonical duplex DNA. *Nature* **2011,** *470* (7335), 498-502.

43. Frank-Kamenetskii, M. D.; Mirkin, S. M., Triplex DNA structures. *Annu. Rev. Biochem.* **1995,** *64*, 65-95.

44. Crick, F. H., Codon--anticodon pairing: the wobble hypothesis. *J. Mol. Biol.* **1966,** *19* (2), 548-55.

45. Pearson, H., Genetics: what is a gene? *Nature* **2006,** *441* (7092), 398-401.

46. Bruce Alberts, A. J., Julian Lewis, Martin Raff, Keith Roberts, and Peter Walter, *Molecular Biology of the Cell, 4th edition*. 4th ed.; Garland Science: New York, 2002.

47. Steenken, S., Purine bases, nucleosides, and nucleotides: aqueous solution redox chemistry and transformation reactions of their radical cations and e- and OH adducts. *Chem. Rev.* **1989,** *89* (3), 503-520.

48. Burrows, C. J.; Muller, J. G., Oxidative nucleobase modifications leading to strand scission. *Chem. Rev.* **1998,** *98* (3), 1109-1151.

49. Middleton, C. T.; Harpe, K. d. L.; Su, C.; Law, Y. K.; Crespo-Hernández, C. E.; Kohler, B., DNA Excited-State Dynamics: From Single Bases to the Double Helix. *Annu. Rev. Phys. Chem.* **2009,** *60* (1), 217-239.

50. Crespo-Hernández, C. E.; Cohen, B.; Hare, P. M.; Kohler, B., Ultrafast Excited-State Dynamics in Nucleic Acids. *Chem. Rev.* **2004,** *104* (4), 1977-2020.

51. Goodsell, D. S., The molecular perspective: ultraviolet light and pyrimidine dimers. *Oncologist* **2001,** *6* (3), 298-9.

52. Liu, Z.; Wang, L.; Zhong, D., Dynamics and mechanisms of DNA repair by photolyase. *Phys. Chem. Chem. Phys.* **2015,** *17* (18), 11933-49.

53. Heil, K.; Pearson, D.; Carell, T., Chemical investigation of light induced DNA bipyrimidine damage and repair. *Chem. Soc. Rev.* **2011,** *40* (8), 4271-8.

54. Labet, V.; Morell, C.; Douki, T.; Cadet, J.; Eriksson, L. A.; Grand, A., Hydrolytic deamination of 5,6-dihydrocytosine in a protic medium: a theoretical study. *J. Phys. Chem. A* **2010,** *114* (4), 1826-34.

55. Douki, T., The variety of UV-induced pyrimidine dimeric photoproducts in DNA as shown by chromatographic quantification methods. *Photochem. Photobiol. Sci.* **2013,** *12* (8), 1286-302.

56. Zhao, X.; Nadji, S.; Kao, J. L.; Taylor, J. S., The structure of d(TpA), the major photoproduct of thymidylyl-(3'5')-deoxyadenosine. *Nucleic Acids Res.* **1996,** *24* (8), 1554-60.

57. Sharma, N. D.; Davies, R. J., Extent of formation of a dimeric adenine photoproduct in polynucleotides and DNA. *J. Photochem. Photobiol. B* **1989,** *3* (2), 247-58.

58. Plasser, F.; Lischka, H., Electronic excitation and structural relaxation of the adenine dinucleotide in gas phase and solution. *Photochem. Photobiol. Sci.* **2013,** *12* (8), 1440-1452.

59. Kleinermanns, K.; Nachtigallová, D.; de Vries, M. S., Excited state dynamics of DNA bases. *Int. Rev. Phys. Chem.* **2013,** *32* (2), 308-342.

60. Middleton, C. T.; de La Harpe, K.; Su, C.; Law, Y. K.; Crespo-Hernandez, C. E.; Kohler, B., DNA Excited-State Dynamics: From Single Bases to the Double Helix. *Annual Review of Physical Chemistry* **2009,** *60*, 217-239.

61. Zhang, Y.; de La Harpe, K.; Beckstead, A. A.; Improta, R.; Kohler, B., UV-Induced Proton Transfer between DNA Strands. *J. Am. Chem. Soc.* **2015,** *137* (22), 7059-7062.

62. Perun, S.; Sobolewski, A. L.; Domcke, W., Role of Electron-Driven Proton-Transfer Processes in the Excited-State Deactivation of the Adenine−Thymine Base Pair. *J. Phys. Chem. A* **2006,** *110* (29), 9031-9038.

63. Ludwig, V.; da Costa, Z. M.; do Amaral, M. S.; Borin, A. C.; Canuto, S.; Serrano-Andrés, L., Photophysics and photostability of adenine in aqueous solution: A theoretical study. *Chem. Phys. Lett.* **2010,** *492* (1), 164-169.

64. Chen, J.; Kohler, B., Base stacking in adenosine dimers revealed by femtosecond transient absorption spectroscopy. *J. Am. Chem. Soc.* **2014,** *136* (17), 6362-72.

65. Crespo-Hernández, C. E.; Cohen, B.; Kohler, B., Base stacking controls excited-state dynamics in A·T DNA. *Nature* **2005,** *436* (7054), 1141-1144.

66. Montero, R.; Conde, Á. P.; Ovejas, V.; Castaño, F.; Longarte, A., Ultrafast Photophysics of the Isolated Indole Molecule. *J. Phys. Chem. A* **2012,** *116* (11), 2698-2703.

67. Chatterley, A. S.; West, C. W.; Roberts, G. M.; Stavros, V. G.; Verlet, J. R. R., Mapping the Ultrafast Dynamics of Adenine onto Its Nucleotide and Oligonucleotides by Time-Resolved Photoelectron Imaging. *J. Phys. Chem. Lett.* **2014,** *5* (5), 843-848.

68. Chatterley, A. S.; West, C. W.; Stavros, V. G.; Verlet, J. R. R., Time-resolved photoelectron imaging of the isolated deprotonated nucleotides. *Chem. Sci.* **2014,** *5* (10), 3963-3975.

69. Gustavsson, T.; Sarkar, N.; Vayá, I.; Jiménez, M. C.; Markovitsi, D.; Improta, R., A joint experimental/theoretical study of the ultrafast excited state deactivation of deoxyadenosine and 9-methyladenine in water and acetonitrile. *Photochem. Photobiol. Sci.* **2013,** *12* (8), 1375-1386.

70. Stavros, V. G.; Verlet, J. R. R., Gas-Phase Femtosecond Particle Spectroscopy: A Bottom-Up Approach to Nucleotide Dynamics. *Annu. Rev. Phys. Chem.* **2016,** *67*, 211-232.

71. Simons, J., How do low-energy (0.1-2 eV) electrons cause DNA-strand breaks? *Acc. Chem. Res.* **2006,** *39* (10), 772-9.

72. Kumar, A.; Becker, D.; Adhikary, A.; Sevilla, M. D., Reaction of Electrons with DNA: Radiation Damage to Radiosensitization. *Int. J. Mol. Sci.* **2019,** *20* (16), 3998.

73. Zheng, Y.; Cloutier, P.; Hunting, D. J.; Wagner, J. R.; Sanche, L., Glycosidic bond cleavage of thymidine by low-energy electrons. *J. Am. Chem. Soc.* **2004,** *126* (4), 1002-3.

74. Aflatooni, K.; Gallup, G. A.; Burrow, P. D., Electron attachment energies of the DNA bases. *J. Phys. Chem. A* **1998,** *102* (31), 6205-6207.

75. Ptasińska, S.; Denifl, S.; Scheier, P.; Märk, T. D., Inelastic electron interaction (attachment/ionization) with deoxyribose. *J. Chem. Phys.* **2004,** *120* (18), 8505-11.

76. Li, X.; Sevilla, M. D.; Sanche, L., Density functional theory studies of electron interaction with DNA: can zero eV electrons induce strand breaks? *J. Am. Chem. Soc.* **2003,** *125* (45), 13668-9.

77. Scheer, A. M.; Aflatooni, K.; Gallup, G. A.; Burrow, P. D., Bond Breaking and Temporary Anion States in Uracil and Halouracils: Implications for the DNA Bases. *Phys. Rev. Lett.* **2004,** *92* (6), 068102.

78. Baccarelli, I.; Bald, I.; Gianturco, F. A.; Illenberger, E.; Kopyra, J., Electron-induced damage of DNA and its components: Experiments and theoretical models. *Phys. Rep.* **2011,** *508* (1), 1-44.

79. Sanche, L., Role of secondary low energy electrons in radiobiology and chemoradiation therapy of cancer. *Chem. Phys. Lett.* **2009,** *474* (1), 1-6.

80. Sanche, L., Low energy electron-driven damage in biomolecules. *Eur. Phys. J. D* **2005,** *35* (2), 367-390.

81. Burrow, P. D.; Gallup, G. A.; Modelli, A., Are There π* Shape Resonances in Electron Scattering from Phosphate Groups? *J. Phys. Chem. A* **2008,** *112* (17), 4106-4113.

82. Fennimore, M. A.; Matsika, S., Core-excited and shape resonances of uracil. *Phys. Chem. Chem. Phys.* **2016,** *18* (44), 30536-30545.

83. Abdoul-Carime, H.; Gohlke, S.; Illenberger, E., Site-specific dissociation of DNA bases by slow electrons at early stages of irradiation. *Phys. Rev. Lett.* **2004,** *92* (16).

84. Barrios, R.; Skurski, P.; Simons, J., Mechanism for damage to DNA by low-energy electrons. *J. Phys. Chem. B* **2002,** *106* (33), 7991-7994.

85. Berdys, J.; Anusiewicz, I.; Skurski, P.; Simons, J., Damage to Model DNA Fragments from Very Low-Energy (<1 eV) Electrons. *J. Am. Chem. Soc.* **2004,** *126* (20), 6441-6447.

86. Bhaskaran, R.; Sarma, M., The role of the shape resonance state in low energy electron induced single strand break in 2′-deoxycytidine-5′-monophosphate. *Phys. Chem. Chem. Phys.* **2015,** *17* (23), 15250-15257.

87. Khorsandgolchin, G.; Sanche, L.; Cloutier, P.; Wagner, J. R., Strand Breaks Induced by Very Low Energy Electrons: Product Analysis and Mechanistic Insight into the Reaction with TpT. *J. Am. Chem. Soc.* **2019,** *141* (26), 10315-10323.

88. Martin, F.; Burrow, P. D.; Cai, Z. L.; Cloutier, P.; Hunting, D.; Sanche, L., DNA strand breaks induced by 0-4 eV electrons: The role of shape resonances. *Phys. Rev. Lett.* **2004,** *93* (6).

89. Zheng, Y.; Cloutier, P.; Hunting, D. J.; Wagner, J. R.; Sanche, L., Phosphodiester and N-glycosidic bond cleavage in DNA induced by 4-15 eV electrons. *J. Chem. Phys.* **2006,** *124* (6).

90. Abdoul-Carime, H.; Gohlke, S.; Fischbach, E.; Scheike, J.; Illenberger, E., Thymine excision from DNA by subexcitation electrons. *Chem. Phys. Lett.* **2004,** *387* (4-6), 267-270.

91. Horke, D. A.; Li, Q.; Blancafort, L.; Verlet, J. R., Ultrafast above-threshold dynamics of the radical anion of a prototypical quinone electron-acceptor. *Nat. Chem.* **2013,** *5* (8), 711-7.

92. West, C. W.; Bull, J. N.; Antonkov, E.; Verlet, J. R., Anion resonances of para-benzoquinone probed by frequency-resolved photoelectron imaging. *J. Phys. Chem. A* **2014,** *118* (48), 11346-54.

93. Dessent, C. E. H.; Kim, J.; Johnson, M. A., Photochemistry of Halide Ion−Molecule Clusters: Dipole-Bound Excited States and the Case for Asymmetric Solvation. *Acc. Chem. Res.* **1998,** *31* (9), 527-534.

94. Serxner, D.; Dessent, C. E. H.; Johnson, M. A., Precursor of the Iaq− charge-transfer-to-solvent (CTTS) band in I−·(H2O)n clusters. *J. Chem. Phys.* **1996,** *105* (16), 7231-7234.

95. Talbot, J. J.; Yang, N.; Huang, M.; Duong, C. H.; McCoy, A. B.; Steele, R. P.; Johnson, M. A., Spectroscopic Signatures of Mode-Dependent Tunnel Splitting in the Iodide–Water Binary Complex. *J. Phys. Chem. A* **2020,** *124* (15), 2991-3001.

96. Dessent, C. E. H.; Bailey, C. G.; Johnson, M. A., Dipole-bound excited states of the I−·CH3CN and I−·(CH3CN)2 ion–molecule complexes: Evidence for asymmetric solvation. *J. Chem. Phys.* **1995,** *103* (6), 2006-2015.

97. Dessent, C. E. H.; Kim, J.; Johnson, M. A., Spectroscopic observation of vibrational Feshbach resonances in near-threshold photoexcitation of X− ·CH3NO2 (X−=I− and Br−). *Faraday Discuss.* **2000,** *115* (0), 395-406.

98. Dessent, C. E. H.; Bailey, C. G.; Johnson, M. A., Observation of the dipole-bound excited state of the I−·acetone ion-molecule complex. *J. Chem. Phys.* **1995,** *102* (15), 6335-6338.

99. Kunin, A.; Neumark, D. M., Time-resolved radiation chemistry: femtosecond photoelectron spectroscopy of electron attachment and photodissociation dynamics in iodide-nucleobase clusters. *Phys. Chem. Chem. Phys.* **2019,** *21* (14), 7239-7255.

100. King, S. B.; Yandell, M. A.; Stephansen, A. B.; Neumark, D. M., Time-resolved radiation chemistry: Dynamics of electron attachment to uracil following UV excitation of iodide-uracil complexes. *J. Chem. Phys.* **2014,** *141* (22), 224310.

101. King, S. B.; Yandell, M. A.; Neumark, D. M., Time-resolved photoelectron imaging of the iodide–thymine and iodide–uracil binary cluster systems. *Faraday Discuss.* **2013,** *163* (0), 59-72.

102. Yandell, M. A.; King, S. B.; Neumark, D. M., Time-Resolved Radiation Chemistry: Photoelectron Imaging of Transient Negative Ions of Nucleobases. *J. Am. Chem. Soc.* **2013,** *135* (6), 2128-2131.

103. King, S. B.; Stephansen, A. B.; Yokoi, Y.; Yandell, M. A.; Kunin, A.; Takayanagi, T.; Neumark, D. M., Electron accommodation dynamics in the DNA base thymine. *J. Chem. Phys.* **2015,** *143* (2), 024312.

104. Stephansen, A. B.; King, S. B.; Yokoi, Y.; Minoshima, Y.; Li, W.-L.; Kunin, A.; Takayanagi, T.; Neumark, D. M., Dynamics of dipole- and valence bound anions in iodide-adenine binary complexes: A time-resolved photoelectron imaging and quantum mechanical investigation. *J. Chem. Phys.* **2015,** *143* (10), 104308.

105. Rogers, J. P.; Anstoter, C. S.; Verlet, J. R. R., Ultrafast dynamics of low-energy electron attachment via a non-valence correlation-bound state. *Nat. Chem.* **2018,** *10* (3), 341-346.

106. Yamazaki, R.; Matsuya, Y.; Ohtsubo, Y.; Tsutsumi, K.; Date, H.; Sasaki, K., Quantitative estimation of DNA damage by photon irradiation based on the microdosimetric-kinetic model. *Journal of Radiation Research* **2014,** *55* (3), 484-493.

107. Lecointre, J.; Roberts, G. M.; Horke, D. A.; Verlet, J. R. R., Ultrafast Relaxation Dynamics Observed Through Time-Resolved Photoelectron Angular Distributions. *J. Phys. Chem. A* **2010,** *114* (42), 11216-11224.

108. Stanley, L. H.; Anstöter, C. S.; Verlet, J. R. R., Resonances of the anthracenyl anion probed by frequency-resolved photoelectron imaging of collision-induced dissociated anthracene carboxylic acid. *Chem. Sci.* **2017,** *8* (4), 3054-3061.

109. Wiley, W. C.; McLaren, I. H., Time-of-Flight Mass Spectrometer with Improved Resolution. *Rev. Sci. Instrum.* **1955,** *26* (12), 1150-1157.

110. Fingerman, S., CRC handbook of chemistry and physics; a ready-reference book of chemical and physical data, 87th ed. *Sci-Tech News* **2007,** *61* (1), 38-38.

111. Yang, X.; Wang, X.-B.; Vorpagel, E. R.; Wang, L.-S., Direct experimental observation of the low ionization potentials of guanine in free oligonucleotides by using photoelectron spectroscopy. *Proc. Natl. Acad. Sci. U.S.A.* **2004,** *101* (51), 17588-17592.

112. Weigend, F.; Häser, M., RI-MP2: first derivatives and global consistency. *Theor. Chem. Acc.* **1997,** *97* (1), 331-340.

113. Weigend, F., Accurate Coulomb-fitting basis sets for H to Rn. *Phys. Chem. Chem. Phys.* **2006,** *8* (9), 1057-1065.

114. Dreuw, A.; Wormit, M., The algebraic diagrammatic construction scheme for the polarization propagator for the calculation of excited states. *Wiley Interdiscip. Rev. Comput. Mol. Sci.* **2015,** *5* (1), 82-95.

115. Dreuw, A.; Cederbaum, L. S., Erratum: Nature of the repulsive Coulomb barrier in multiply charged negative ions [Phys. Rev. A 63, 012501 (2000)]. *Phys. Rev. A* **2001,** *63* (4), 049904.

116. Becke, A. D., Density-functional thermochemistry. III. The role of exact exchange. *J. Chem. Phys.* **1993,** *98* (7), 5648-5652.

117. Lee, C.; Yang, W.; Parr, R. G., Development of the Colle-Salvetti correlation-energy formula into a functional of the electron density. *Phys. Rev. B* **1988,** *37* (2), 785-789.

118. Kendall, R. A.; Jr., T. H. D.; Harrison, R. J., Electron affinities of the first-row atoms revisited. Systematic basis sets and wave functions. *J. Chem. Phys.* **1992,** *96* (9), 6796-6806.

119. Roberts, G. M.; Nixon, J. L.; Lecointre, J.; Wrede, E.; Verlet, J. R. R., Toward real-time charged-particle image reconstruction using polar onion-peeling. *Rev. Sci. Instrum.* **2009,** *80* (5), 053104.

120. Castellani, M. E.; Anstöter, C. S.; Verlet, J. R. R., On the stability of a dipole-bound state in the presence of a molecule. *Phys. Chem. Chem. Phys.* **2019,** *21* (44), 24286-24290.

121. Fermi, E.; Teller, E., The Capture of Negative Mesotrons in Matter. *Phys. Rev.* **1947,** *72* (5), 399-408.

122. Jordan, K. D.; Wang, F., Theory of dipole-bound anions. *Annu. Rev. Phys. Chem.* **2003,** *54*, 367-96.

123. Crawford, O. H.; Garrett, W. R., Electron affinities of polar molecules. *J. Chem. Phys.* **1977,** *66* (11), 4968-4970.

124. Stebbings, R. F.; Dunning, F. B., *Rydberg states of atoms and molecules*. Cambridge University Press: Cambridge Cambridgeshire ; New York, 1983; p ix, 515 p.

125. Sommerfeld, T., Dipole-bound states as doorways in (dissociative) electron attachment. *J. Phys. Conf. Ser.* **2005,** *4*, 245-250.

126. Sarre, P. J., The diffuse interstellar bands: a dipole-bound state hypothesis. *Mon. Not. R. Astron. Soc.* **2000,** *313* (1), L14-L16.

127. Voora, V. K.; Jordan, K. D., Nonvalence Correlation-Bound Anion State of C6F6: Doorway to Low-Energy Electron Capture. *J. Phys. Chem. A* **2014,** *118* (35), 7201-7205.

128. Rogers, J. P.; Anstoter, C. S.; Verlet, J. R. R., Ultrafast dynamics of low-energy electron attachment via a non-valence correlation-bound state. *Nature Chem.* **2018,** *10* (3), 341-346.

129. Weber, J. M.; Ruf, M. W.; Hotop, H., Rydberg electron transfer to C-60 and C-70. *Z. Phys. D.* **1996,** *37* (4), 351-357.

130. Rogers, J. P.; Anstoter, C. S.; Verlet, J. R. R., Evidence of Electron Capture of an Outgoing Photoelectron Wave by a Nonvalence State in (C6F6)(n)(-). *J. Phys. Chem. Lett.* **2018,** *9* (10), 2504-2509.

131. Bull, J. N.; Verlet, J. R. R., Observation and ultrafast dynamics of a nonvalence correlation-bound state of an anion. *Sci. Adv.* **2017,** *3* (5).

132. Bull, J. N.; West, C. W.; Verlet, J. R. R., Ultrafast dynamics of formation and autodetachment of a dipole-bound state in an open-shell pi-stacked dimer anion. *Chem. Sci.* **2016,** *7* (8), 5352-5361.

133. Lecomte, F.; Carles, S.; Desfrancois, C.; Johnson, M. A., Dipole bound and valence state coupling in argon-solvated nitromethane anions. *J. Chem. Phys.* **2000,** *113* (24), 10973-10977.

134. Hendricks, J. H.; Lyapustina, S. A.; de Clercq, H. L.; Bowen, K. H., The dipole bound-to-covalent anion transformation in uracil. *J. Chem. Phys.* **1998,** *108* (1), 8-11.

135. Mead, R. D.; Lykke, K. R.; Lineberger, W. C.; Marks, J.; Brauman, J. I., Spectroscopy and Dynamics of the Dipole-Bound State of Acetaldehyde Enolate. *J. Chem. Phys.* **1984,** *81* (11), 4883-4892.

136. Brinkman, E. A.; Berger, S.; Marks, J.; Brauman, J. I., Molecular Rotation and the Observation of Dipole-Bound States of Anions. *J. Chem. Phys.* **1993,** *99* (10), 7586-7594.

137. Bull, J. N.; Buntine, J. T.; Scholz, M. S.; Carrascosa, E.; Giacomozzi, L.; Stockett, M. H.; Bieske, E. J., Photodetachment and photoreactions of substituted naphthalene anions in a tandem ion mobility spectrometer. *Faraday Discuss.* **2019,** *217* (0), 34-46.

138. Adams, C. L.; Schneider, H.; Ervin, K. M.; Weber, J. M., Low-energy photoelectron imaging spectroscopy of nitromethane anions: Electron affinity, vibrational features, anisotropies, and the dipole-bound state. *J. Chem. Phys.* **2009,** *130* (7).

139. Edwards, S. T.; Johnson, M. A.; Tully, J. C., Vibrational Fano resonances in dipole-bound anions. *J. Chem. Phys.* **2012,** *136* (15), 154305.

140. Gardenier, G. H.; Roscioli, J. R.; Johnson, M. A., Intermolecular Proton Binding in the Presence of a Large Electric Dipole: Ar-Tagged Vibrational Predissociation Spectroscopy of the CH3CN·H+·OH2 and CH3CN·D+·OD2 Complexes. *J. Phys. Chem. A* **2008,** *112* (47), 12022-12026.

141. Matthews, E.; Dessent, C. E. H., Observation of Near-Threshold Resonances in the Flavin Chromophore Anions Alloxazine and Lumichrome. *J. Phys. Chem. Lett.* **2018,** *9* (20), 6124-6130.

142. Bailey, C. G.; Dessent, C. E. H.; Johnson, M. A.; Jr., K. H. B., Vibronic effects in the photon energy-dependent photoelectron spectra of the CH3CN− dipole-bound anion. *J. Chem. Phys.* **1996,** *104* (18), 6976-6983.

143. Diken, E. G.; Hammer, N. I.; Johnson, M. A., Preparation and photoelectron spectrum of the glycine molecular anion: Assignment to a dipole-bound electron species with a high-dipole moment, non-zwitterionic form of the neutral core. *J. Chem. Phys.* **2004,** *120* (21), 9899-9902.

144. Belogolova, E. F.; Liu, G.; Doronina, E. P.; Ciborowski, S. M.; Sidorkin, V. F.; Bowen, K. H., Dipole-Bound Anions of Intramolecular Complexes. *J. Phys. Chem. Lett.* **2018,** *9* (6), 1284-1289.

145. Ciborowski, S. M.; Liu, G.; Graham, J. D.; Buytendyk, A. M.; Bowen, K. H., Dipole-bound anions: formed by Rydberg electron transfer (RET) and studied by velocity map imaging–anion photoelectron spectroscopy (VMI–aPES). *Eur. Phys. J. D* **2018,** *72* (8), 139.

146. Hendricks, J. H.; de Clercq, H. L.; Lyapustina, S. A.; Bowen, K. H., Negative ion photoelectron spectroscopy of the ground state, dipole-bound dimeric anion, (HF)(2)(-). *J. Chem. Phys.* **1997,** *107* (8), 2962-2967.

147. Hendricks, J. H.; Lyapustina, S. A.; Clercq, H. L. d.; Snodgrass, J. T.; Bowen, K. H., Dipole bound, nucleic acid base anions studied via negative ion photoelectron spectroscopy. *J. Chem. Phys.* **1996,** *104* (19), 7788-7791.

148. Huang, D. L.; Zhu, G. Z.; Wang, L. S., Communication: Observation of dipole-bound state and high-resolution photoelectron imaging of cold acetate anions. *J. Chem. Phys.* **2015,** *142* (9).

149. Huang, D. L.; Zhu, G. Z.; Liu, Y.; Wang, L. S., Photodetachment spectroscopy and resonant photoelectron imaging of cryogenically-cooled deprotonated 2-hydroxypyrimidine anions. *J. Mol. Spectrosc.* **2017,** *332*, 86-93.

150. Huang, D. L.; Liu, H. T.; Ning, C. G.; Dau, P. D.; Wang, L. S., Resonant photoelectron imaging of deprotonated uracil anion via vibrational levels of a dipole-bound excited state. *Chem. Phys.* **2017,** *482*, 374-383.

151. Czekner, J.; Cheung, L. F.; Kocheril, G. S.; Wang, L. S., Probing the coupling of a dipole-bound electron with a molecular core. *Chem. Sci.* **2019,** *10* (5), 1386-1391.

152. Liu, H. T.; Ning, C. G.; Huang, D. L.; Wang, L. S., Vibrational Spectroscopy of the Dehydrogenated Uracil Radical by Autodetachment of Dipole-Bound Excited States of Cold Anions. *Angew. Chem. Int. Ed.* **2014,** *53* (9), 2464-2468.

153. Zhu, G. Z.; Huang, D. L.; Wang, L. S., Conformation-selective resonant photoelectron imaging from dipole-bound states of cold 3-hydroxyphenoxide. *J. Chem. Phys.* **2017,** *147* (1).

154. Hammer, N. I.; Diri, K.; Jordan, K. D.; Desfrançois, C.; Compton, R. N., Dipole-bound anions of carbonyl, nitrile, and sulfoxide containing molecules. *J. Chem. Phys.* **2003,** *119* (7), 3650-3660.

155. Hammer, N. I.; Hinde, R. J.; Compton, R. N.; Diri, K.; Jordan, K. D.; Radisic, D.; Stokes, S. T.; Bowen, K. H., Dipole-bound anions of highly polar molecules: Ethylene carbonate and vinylene carbonate. *J. Chem. Phys.* **2004,** *120* (2), 685-690.

156. Liu, H. T.; Ning, C. G.; Huang, D. L.; Dau, P. D.; Wang, L. S., Observation of Mode-Specific Vibrational Autodetachment from Dipole-Bound States of Cold Anions. *Angew. Chem. Int. Ed.* **2013,** *52* (34), 8976-8979.

157. Zhu, G. Z.; Qian, C. H.; Wang, L. S., Dipole-bound excited states and resonant photoelectron imaging of phenoxide and thiophenoxide anions. *J. Chem. Phys.* **2018,** *149* (16).

158. Gunion, R. F.; Gilles, M. K.; Polak, M. L.; Lineberger, W. C., Ultraviolet Photoelectron-Spectroscopy of the Phenide, Benzyl and Phenoxide Anions, with Abinitio Calculations. *Int. J. Mass Spectrom. Ion Proc.* **1992,** *117* (1-3), 601-620.

159. Anstoter, C. S.; Dean, C. R.; Verlet, J. R. R., Chromophores of chromophores: a bottom-up Huckel picture of the excited states of photoactive proteins. *Phys. Chem. Chem. Phys.* **2017,** *19* (44), 29772-29779.

160. Rogers, J. P.; Anstoter, C. S.; Bull, J. N.; Curchod, B. F. E.; Verlet, J. R. R., Photoelectron Spectroscopy of the Hexafluorobenzene Cluster Anions: (C6F6)(n)(-) (n=1-5) and I-(C6F6). *J. Phys. Chem. A* **2019,** *123* (8), 1602-1612.

161. Nowakowski, P. J.; Woods, D. A.; Verlet, J. R. R., Charge Transfer to Solvent Dynamics at the Ambient Water/Air Interface. *J. Phys. Chem. Lett.* **2016,** *7* (20), 4079-4085.

162. Bradforth, S. E.; Jungwirth, P., Excited States of Iodide Anions in Water: A Comparison of the Electronic Structure in Clusters and in Bulk Solution. *J. Phys. Chem. A* **2002,** *106* (7), 1286-1298.

163. Tian, Z.; Wang, X. B.; Wang, L. S.; Kass, S. R., Are carboxyl groups the most acidic sites in amino acids? Gas-phase acidities, photoelectron spectra, and computations on tyrosine, p-hydroxybenzoic acid, and their conjugate bases. *J. Am. Chem. Soc.* **2009,** *131* (3), 1174-81.

164. Castellani, M. E.; Verlet, J. R. R., Intramolecular Photo-Oxidation as a Potential Source to Probe Biological Electron Damage: A Carboxylated Adenosine Analogue as Case Study. *Molecules* **2021,** *26* (10), 2877.

165. Chatterley, A. S.; Johns, A. S.; Stavros, V. G.; Verlet, J. R. R., Base-Specific Ionization of Deprotonated Nucleotides by Resonance Enhanced Two-Photon Detachment. *J. Phys. Chem. A* **2013,** *117* (25), 5299-5305.

166. Epp, J. B.; Widlanski, T. S., Facile Preparation of Nucleoside-5‘-carboxylic Acids. *J. Org. Chem.* **1999,** *64* (1), 293-295.

167. M. J. Frisch, G. W. T., H. B. Schlegel, G. E. Scuseria, M. A. Robb, J. R. Cheeseman, G. Scalmani, V. Barone, B. Mennucci, G. A. Petersson, H. Nakatsuji, M. Caricato, X. Li, H. P. Hratchian, A. F. Izmaylov, J. Bloino, G. Zheng, J. L. Sonnenberg, M. Hada, M. Ehara, K. Toyota, R. Fukuda, J. Hasegawa, M. Ishida, T. Nakajima, Y. Honda, O. Kitao, H. Nakai, T. Vreven, J. A. Montgomery, Jr., J. E. Peralta, F. Ogliaro, M. Bearpark, J. J. Heyd, E. Brothers, K. N. Kudin, V. N. Staroverov, R. Kobayashi, J. Normand, K. Raghavachari, A. Rendell, J. C. Burant, S. S. Iyengar, J. Tomasi, M. Cossi, N. Rega, J. M. Millam, M. Klene, J. E. Knox, J. B. Cross, V. Bakken, C. Adamo, J. Jaramillo, R. Gomperts, R. E. Stratmann, O. Yazyev, A. J. Austin, R. Cammi, C. Pomelli, J. W. Ochterski, R. L. Martin, K. Morokuma, V. G. Zakrzewski, G. A. Voth, P. Salvador, J. J. Dannenberg, S. Dapprich, A. D. Daniels, Ö. Farkas, J. B. Foresman, J. V. Ortiz, J. Cioslowski, and D. J. Fox. *Gaussian 09* Gaussian, Inc., Wallingford CT, 2009.

168. Krishnan, R.; Binkley, J. S.; Seeger, R.; Pople, J. A., Self-consistent molecular orbital methods. XX. A basis set for correlated wave functions. *J. Chem. Phys.* **1980,** *72* (1), 650-654.

169. McLean, A. D.; Chandler, G. S., Contracted Gaussian basis sets for molecular calculations. I. Second row atoms, Z=11–18. *J. Chem. Phys.* **1980,** *72* (10), 5639-5648.

170. Yanai, T.; Tew, D. P.; Handy, N. C., A new hybrid exchange–correlation functional using the Coulomb-attenuating method (CAM-B3LYP). *Chem. Phys. Lett.* **2004,** *393* (1), 51-57.

171. Stavros, V. G.; Verlet, J. R. R., Gas-Phase Femtosecond Particle Spectroscopy: A Bottom-Up Approach to Nucleotide Dynamics. *Annu. Rev. Phys. Chem.* **2016,** *67* (1), 211-232.

172. Castellani, M. E.; Avagliano, D.; González, L.; Verlet, J. R. R., Site-Specific Photo-oxidation of the Isolated Adenosine-5′-triphosphate Dianion Determined by Photoelectron Imaging. *J. Phys. Chem. Lett.* **2020,** *11* (19), 8195-8201.

173. Castellani, M. E.; Avagliano, D.; González, L.; Verlet, J. R. R., Probing the Ultrafast Dynamics of the Isolated Adenosine-5´-triphosphate Dianion through Time-Resolved Photoelectron Imaging. *Submitted* **2020**.

174. Vysotskii, Y. B., Effect of chemical substitution on the ionization potentials and electron affinity of systems with conjugated bonds. *Theor. Exp. Chem.* **1982,** *17* (4), 363-371.

175. Tully, J. C.; Preston, R. K., Trajectory Surface Hopping Approach to Nonadiabatic Molecular Collisions: The Reaction of H+ with D2. *J. Chem. Phys.* **1971,** *55* (2), 562-572.

176. Hammes-Schiffer, S.; Tully, J. C., Proton transfer in solution: Molecular dynamics with quantum transitions. *J. Chem. Phys.* **1994,** *101* (6), 4657-4667.

177. Mitrić, R.; Petersen, J.; Bonačić-Koutecký, V., Laser-field-induced surface-hopping method for the simulation and control of ultrafast photodynamics. *Phys. Rev. A* **2009,** *79* (5), 053416.

178. Mavri, J., Molecular Dynamics with Nonadiabatic Transitions: A Comparison of Methods. *Mol. Simul.* **2000,** *23* (6), 389-411.

179. Castellani, M. E.; Avagliano, D.; Verlet, J. R. R., Ultrafast Dynamics of the Isolated Adenosine-5′-triphosphate Dianion Probed by Time-Resolved Photoelectron Imaging. *J. Phys. Chem. A* **2021,** *125* (17), 3646-3652.

180. Bruice, P. Y., *Essential organic chemistry*. Third edition. ed.; Pearson: Upper Saddle River, New Jersey, 2016; p xxiv, 644 pages, 26 variously paged.

181. McMurry, J.; Begley, T. P., *The organic chemistry of biological pathways*. Second edition. ed.; Roberts and Company Publishers: Greenwood Village, Colorado, 2016; p pages cm.

182. Weber, J. M.; Marcum, J.; Nielsen, S. B., UV Photophysics of DNA and RNA Nucleotides In Vacuo: Dissociation Channels, Time Scales, and Electronic Spectra. In *Photophysics of Ionic Biochromophores*, Brøndsted Nielsen, S.; Wyer, J. A., Eds. Springer Berlin Heidelberg: Berlin, Heidelberg, 2013; pp 181-207.

183. Satzger, H.; Townsend, D.; Zgierski, M. Z.; Patchkovskii, S.; Ullrich, S.; Stolow, A., Primary processes underlying the photostability of isolated DNA bases: Adenine. *Proc. Natl. Acad. Sci. U.S.A.* **2006,** *103* (27), 10196-10201.

184. Bisgaard, C. Z.; Satzger, H.; Ullrich, S.; Stolow, A., Excited-State Dynamics of Isolated DNA Bases: A Case Study of Adenine. *ChemPhysChem* **2009,** *10* (1), 101-110.

185. Wells, K. L.; Hadden, D. J.; Nix, M. G. D.; Stavros, V. G., Competing πσ* States in the Photodissociation of Adenine. *J. Phys. Chem. Lett.* **2010,** *1* (6), 993-996.

186. Mai, S.; Richter, M.; Marquetand, P.; González, L., Excitation of Nucleobases from a Computational Perspective II: Dynamics. In *Photoinduced Phenomena in Nucleic Acids I: Nucleobases in the Gas Phase and in Solvents*, Barbatti, M.; Borin, A. C.; Ullrich, S., Eds. Springer International Publishing: Cham, 2015; pp 99-153.

187. Parker, A. W.; Quinn, S. J., Infrared Spectroscopy of DNA. In *Encyclopedia of Biophysics*, Roberts, G. C. K., Ed. Springer Berlin Heidelberg: Berlin, Heidelberg, 2013; pp 1065-1074.

188. Keane, P. M.; Baptista, F. R.; Gurung, S. P.; Devereux, S. J.; Sazanovich, I. V.; Towrie, M.; Brazier, J. A.; Cardin, C. J.; Kelly, J. M.; Quinn, S. J., Long-Lived Excited-State Dynamics of i-Motif Structures Probed by Time-Resolved Infrared Spectroscopy. *ChemPhysChem* **2016,** *17* (9), 1281-1287.

189. Hall, J. P.; Poynton, F. E.; Keane, P. M.; Gurung, S. P.; Brazier, J. A.; Cardin, D. J.; Winter, G.; Gunnlaugsson, T.; Sazanovich, I. V.; Towrie, M.; Cardin, C. J.; Kelly, J. M.; Quinn, S. J., Monitoring one-electron photo-oxidation of guanine in DNA crystals using ultrafast infrared spectroscopy. *Nature Chem.* **2015,** *7* (12), 961-967.

190. Ligare, M. R.; Rijs, A. M.; Berden, G.; Kabeláč, M.; Nachtigallova, D.; Oomens, J.; de Vries, M. S., Resonant Infrared Multiple Photon Dissociation Spectroscopy of Anionic Nucleotide Monophosphate Clusters. *J. Phys. Chem. B* **2015,** *119* (25), 7894-7901.

191. van Outersterp, R. E.; Martens, J.; Berden, G.; Steill, J. D.; Oomens, J.; Rijs, A. M., Structural characterization of nucleotide 5′-triphosphates by infrared ion spectroscopy and theoretical studies. *Phys. Chem. Chem. Phys.* **2018,** *20* (44), 28319-28330.

192. Cercola, R.; Matthews, E.; Dessent, C. E. H., Photoexcitation of Adenosine 5′-Triphosphate Anions in Vacuo: Probing the Influence of Charge State on the UV Photophysics of Adenine. *J. Phys. Chem. B* **2017,** *121* (22), 5553-5561.

193. Daly, S.; Porrini, M.; Rosu, F.; Gabelica, V., Electronic spectroscopy of isolated DNA polyanions. *Faraday Discuss.* **2019,** *217* (0), 361-382.

194. Scheller, M. K.; Compton, R. N.; Cederbaum, L. S., Gas-Phase Multiply Charged Anions. *Science* **1995,** *270* (5239), 1160-1166.

195. Gabelica, V.; Tabarin, T.; Antoine, R.; Rosu, F.; Compagnon, I.; Broyer, M.; De Pauw, E.; Dugourd, P., Electron photodetachment dissociation of DNA polyanions in a quadrupole ion trap mass spectrometer. *Anal. Chem.* **2006,** *78* (18), 6564-72.

196. Gabelica, V.; Rosu, F.; Tabarin, T.; Kinet, C.; Antoine, R.; Broyer, M.; De Pauw, E.; Dugourd, P., Base-dependent electron photodetachment from negatively charged DNA strands upon 260-nm laser irradiation. *J. Am. Chem. Soc.* **2007,** *129* (15), 4706-13.

197. Rosu, F.; Gabelica, V.; De Pauw, E.; Antoine, R.; Broyer, M.; Dugourd, P., UV spectroscopy of DNA duplex and quadruplex structures in the gas phase. *J. Phys. Chem. A* **2012,** *116* (22), 5383-91.

198. Schinle, F.; Crider, P. E.; Vonderach, M.; Weis, P.; Hampe, O.; Kappes, M. M., Spectroscopic and theoretical investigations of adenosine 5'-diphosphate and adenosine 5'-triphosphate dianions in the gas phase. *Phys. Chem. Chem. Phys.* **2013,** *15* (18), 6640-50.

199. Burke, R. M.; Dessent, C. E. H., Effect of Cation Complexation on the Structure of a Conformationally Flexible Multiply Charged Anion: Stabilization of Excess Charge in the Na+·Adenosine 5′-Triphosphate Dianion Ion-Pair Complex. *J. Phys. Chem. A* **2009,** *113* (12), 2683-2692.

200. Burke, R. M.; Pearce, J. K.; Boxford, W. E.; Bruckmann, A.; Dessent, C. E. H., Stabilization of Excess Charge in Isolated Adenosine 5‘-Triphosphate and Adenosine 5‘-Diphosphate Multiply and Singly Charged Anions. *J. Phys. Chem. A* **2005,** *109* (43), 9775-9785.

201. Vonderach, M.; Ehrler, O. T.; Matheis, K.; Weis, P.; Kappes, M. M., Isomer-Selected Photoelectron Spectroscopy of Isolated DNA Oligonucleotides: Phosphate and Nucleobase Deprotonation at High Negative Charge States. *J. Am. Chem. Soc.* **2012,** *134* (18), 7830-7841.

202. Weber, J. M.; Ioffe, I. N.; Berndt, K. M.; Löffler, D.; Friedrich, J.; Ehrler, O. T.; Danell, A. S.; Parks, J. H.; Kappes, M. M., Photoelectron Spectroscopy of Isolated Multiply Negatively Charged Oligonucleotides. *J. Am. Chem. Soc.* **2004,** *126* (27), 8585-8589.

203. Daly, S.; Rosu, F.; Gabelica, V., Mass-resolved electronic circular dichroism ion spectroscopy. *Science* **2020,** *368* (6498), 1465-1468.

204. Ullrich, S.; Schultz, T.; Zgierski, M. Z.; Stolow, A., Direct Observation of Electronic Relaxation Dynamics in Adenine via Time-Resolved Photoelectron Spectroscopy. *J. Am. Chem. Soc.* **2004,** *126* (8), 2262-2263.

205. Canuel, C.; Mons, M.; Piuzzi, F.; Tardivel, B.; Dimicoli, I.; Elhanine, M., Excited states dynamics of DNA and RNA bases: characterization of a stepwise deactivation pathway in the gas phase. *J. Chem. Phys.* **2005,** *122* (7), 074316.

206. Kang, H.; Lee, K. T.; Jung, B.; Ko, Y. J.; Kim, S. K., Intrinsic lifetimes of the excited state of DNA and RNA bases. *J. Am. Chem. Soc.* **2002,** *124* (44), 12958-9.

207. Nix, M. G. D.; Devine, A. L.; Cronin, B.; Ashfold, M. N. R., Ultraviolet photolysis of adenine: Dissociation via the π1σ* state. *J. Chem. Phys.* **2007,** *126* (12), 124312.

208. Serrano-Andrés, L.; Merchán, M.; Borin, A. C., Adenine and 2-aminopurine: paradigms of modern theoretical photochemistry. *Proc. Natl. Acad. Sci. U.S.A.* **2006,** *103* (23), 8691-8696.

209. Barbatti, M.; Aquino, A. J. A.; Szymczak, J. J.; Nachtigallová, D.; Hobza, P.; Lischka, H., Relaxation mechanisms of UV-photoexcited DNA and RNA nucleobases. *Proc. Natl. Acad. Sci. U.S.A.* **2010,** *107* (50), 21453-21458.

210. Barbatti, M.; Lischka, H., Nonadiabatic Deactivation of 9H-Adenine: A Comprehensive Picture Based on Mixed Quantum−Classical Dynamics. *J. Am. Chem. Soc.* **2008,** *130* (21), 6831-6839.

211. Barbatti, M.; Lan, Z.; Crespo-Otero, R.; Szymczak, J. J.; Lischka, H.; Thiel, W., Critical appraisal of excited state nonadiabatic dynamics simulations of 9H-adenine. *J. Chem. Phys.* **2012,** *137* (22), 22a503.

212. Serrano-Andrés, L.; Merchán, M., Are the five natural DNA/RNA base monomers a good choice from natural selection?: A photochemical perspective. *J. Photochem. Photobiol. C* **2009,** *10* (1), 21-32.

213. Improta, R.; Santoro, F.; Blancafort, L., Quantum Mechanical Studies on the Photophysics and the Photochemistry of Nucleic Acids and Nucleobases. *Chem. Rev.* **2016,** *116* (6), 3540-3593.

214. Mooney, C. R. S.; Horke, D. A.; Chatterley, A. S.; Simperler, A.; Fielding, H. H.; Verlet, J. R. R., Taking the green fluorescence out of the protein: dynamics of the isolated GFP chromophore anion. *Chem. Sci.* **2013,** *4* (3), 921-927.

215. Reid, K. L., Photoelectron angular distributions. *Annu. Rev. Phys. Chem.* **2003,** *54*, 397-424.

216. Cooper, J.; Zare, R. N., Angular Distribution of Photoelectrons. *J. Chem. Phys.* **1968,** *48* (2), 942-943.

217. Cooper, J.; Zare, R. N., Erratum: Angular Distribution of Photoelectrons. *J. Chem. Phys.* **1968,** *49* (9), 4252-4252.

218. Anstöter, C. S.; Bull, J. N.; Verlet, J. R. R., Ultrafast dynamics of temporary anions probed through the prism of photodetachment. *Int. Rev. Phys. Chem.* **2016,** *35* (4), 509-538.

219. Gustavsson, T.; Sharonov, A.; Onidas, D.; Markovitsi, D., Adenine, deoxyadenosine and deoxyadenosine 5′-monophosphate studied by femtosecond fluorescence upconversion spectroscopy. *Chem. Phys. Lett.* **2002,** *356* (1), 49-54.

220. Markovitsi, D., UV-induced DNA Damage: The Role of Electronic Excited States. *Photochem. Photobiol.* **2016,** *92* (1), 45-51.

221. Improta, R.; Barone, V., The excited states of adenine and thymine nucleoside and nucleotide in aqueous solution: a comparative study by time-dependent DFT calculations. *Theor. Chem. Acc.* **2008,** *120* (4), 491-497.

222. Santoro, F.; Improta, R.; Fahleson, T.; Kauczor, J.; Norman, P.; Coriani, S., Relative Stability of the La and Lb Excited States in Adenine and Guanine: Direct Evidence from TD-DFT Calculations of MCD Spectra. *J. Phys. Chem. Lett.* **2014,** *5* (11), 1806-1811.

223. Serrano-Andrés, L.; Merchán, M.; Borin, A. C., A Three-State Model for the Photophysics of Adenine. *Chem. Eur. J.* **2006,** *12* (25), 6559-6571.

224. Conti, I.; Garavelli, M.; Orlandi, G., Deciphering Low Energy Deactivation Channels in Adenine. *J. Am. Chem. Soc.* **2009,** *131* (44), 16108-16118.

225. West, C. W.; Bull, J. N.; Woods, D. A.; Verlet, J. R. R., Photoelectron imaging as a probe of the repulsive Coulomb barrier in the photodetachment of antimony tartrate dianions. *Chem. Phys. Lett.* **2016,** *645*, 138-143.

226. Blokhin, A. P.; Gelin, M. F.; Khoroshilov, E. V.; Kryukov, I. V.; Sharkov, A. V., Dynamics of optically induced anisotropy in an ensemble of asymmetric top molecules in the gas phase. *Opt. Spectrosc.* **2003,** *95* (3), 346-352.

227. Conti, I.; Nenov, A.; Höfinger, S.; Flavio Altavilla, S.; Rivalta, I.; Dumont, E.; Orlandi, G.; Garavelli, M., Excited state evolution of DNA stacked adenines resolved at the CASPT2//CASSCF/Amber level: from the bright to the excimer state and back. *Phys. Chem. Chem. Phys.* **2015,** *17* (11), 7291-7302.

228. Conti, I.; Di Donato, E.; Negri, F.; Orlandi, G., Revealing Excited State Interactions by Quantum-Chemical Modeling of Vibronic Activities: The R2PI Spectrum of Adenine. *J. Phys. Chem. A* **2009,** *113* (52), 15265-15275.

229. Picconi, D.; Avila Ferrer, F. J.; Improta, R.; Lami, A.; Santoro, F., Quantum-classical effective-modes dynamics of the $\pi\pi^* \rightarrow n\pi^*$ decay in 9H-adenine. A quadratic vibronic coupling model. *Faraday Discuss.* **2013,** *163* (0), 223-242.

230. Wang, X. B.; Wang, L. S., Development of a low-temperature photoelectron spectroscopy instrument using an electrospray ion source and a cryogenically controlled ion trap. *Rev. Sci. Instrum.* **2008,** *79* (7), 073108.

231. Garand, E., Spectroscopy of Reactive Complexes and Solvated Clusters: A Bottom-Up Approach Using Cryogenic Ion Traps. *J. Phys. Chem. A* **2018,** *122* (32), 6479-6490.

232. Alberts, B., *Molecular biology of the cell*. 5th ed.; Garland Science: New York, 2008.

233. Chin, W.; Mons, M.; Dimicoli, I.; Piuzzi, F.; Tardivel, B.; Elhanine, M., Tautomer contributions to the near UV spectrum of guanine: towards a refined picture for the spectroscopy of purine molecules. *Eur. Phys. J. D* **2002,** *20* (3), 347-355.

234. Langer, H.; Doltsinis, N. L., Nonradiative decay of photoexcited methylated guanine. *Phys. Chem. Chem. Phys.* **2004,** *6* (10), 2742-2748.

235. Mons, M.; Dimicoli, I.; Piuzzi, F.; Tardivel, B.; Elhanine, M., Tautomerism of the DNA Base Guanine and Its Methylated Derivatives as Studied by Gas-Phase Infrared and Ultraviolet Spectroscopy. *J. Phys. Chem. A* **2002,** *106* (20), 5088-5094.

236. Rodgers, M. T.; Campbell, S. A.; Beauchamp, J. L., Site-specific lithium ion attachment directs low-energy dissociation pathways of dinucleotides in the gas phase. Application to nucleic acid sequencing by mass spectrometry. *Int. J. Mass Spectrom. Ion Proc.* **1997,** *161* (1), 193-216.

237. Salpin, J.-Y.; MacAleese, L.; Chirot, F.; Dugourd, P., Structure of the Pb2+–deprotonated dGMP complex in the gas phase: a combined MS-MS/IRMPD spectroscopy/ion mobility study. *Phys. Chem. Chem. Phys.* **2014,** *16* (27), 14127-14138.

238. Close, D. M.; Øhman, K. T., Ionization Energies of the Nucleotides. *J. Phys. Chem. A* **2008,** *112* (44), 11207-11212.

239. Zakjevskii, V. V.; King, S. J.; Dolgounitcheva, O.; Zakrzewski, V. G.; Ortiz, J. V., Base and Phosphate Electron Detachment Energies of Deoxyribonucleotide Anions. *J. Am. Chem. Soc.* **2006,** *128* (41), 13350-13351.

240. Rubio, M.; Roca-Sanjuán, D.; Serrano-Andrés, L.; Merchán, M., Determination of the Electron-Detachment Energies of 2′-Deoxyguanosine 5′-Monophosphate Anion: Influence of the Conformation. *J. Phys. Chem. B* **2009,** *113* (8), 2451-2457.

241. Schinle, F.; Crider, P. E.; Vonderach, M.; Weis, P.; Hampe, O.; Kappes, M. M., Spectroscopic and theoretical investigations of adenosine 5'-diphosphate and adenosine 5'-triphosphate dianions in the gas phase. *Physical Chemistry Chemical Physics* **2013,** *15* (18), 6640-50.

242. Arnold, K.; Balaban, T. S.; Blom, M. N.; Ehrler, O. T.; Gilb, S.; Hampe, O.; van Lier, J. E.; Weber, J. M.; Kappes, M. M., Electron Autodetachment from Isolated Nickel and Copper Phthalocyanine−Tetrasulfonate Tetraanions: Isomer Specific Rates. *J. Phys. Chem. A* **2003,** *107* (6), 794-803.

243. Matheis, K. Karlsruher Institut für Technologie (KIT), 2013.

244. Xiang, Y.; Abliz, Z.; Takayama, M., Cleavage reactions of the complex ions derived from self-complementary deoxydinucleotides and alkali-metal ions using positive ion electrospray ionization with tandem mass spectrometry. *J. Am. Soc. Mass Spectrom.* **2004,** *15* (5), 689-696.

245. Wu, R. R.; He, C. C.; Hamlow, L. A.; Nei, Y. w.; Berden, G.; Oomens, J.; Rodgers, M. T., N3 Protonation Induces Base Rotation of 2′-Deoxyadenosine-5′-monophosphate and Adenosine-5′-monophosphate. *J. Phys. Chem. B* **2016,** *120* (20), 4616-4624.

Appendix: published research papers

PCCP

COMMUNICATION

View Article Online
View Journal | View Issue

Cite this: *Phys. Chem. Chem. Phys.*, 2019, **21**, 24286

Received 6th September 2019,
Accepted 24th October 2019

DOI: 10.1039/c9cp04942h

rsc.li/pccp

On the stability of a dipole-bound state in the presence of a molecule†

Maria Elena Castellani, Cate S. Anstöter and Jan R. R. Verlet*

Dipole-bound states (DBSs) are diffuse non-valence molecular orbitals of anions where the electron is bound by the permanent dipole moment of the neutral core. Here, an experimental study of the stability of such orbitals under the influence of a perturbing molecular alkyl chain is presented. Photodetachment action and photoelectron imaging spectroscopy of five *para*-substituted phenolate anions with progressively longer alkyl chains show that the DBS survives in all cases, suggesting that the perturbation of the orbital is not critical to the existence of the DBS.

First described by Fermi and Teller in 1947,[1] a dipole-bound state (DBS) is a non-valence electronic state of an anion in which the electron is bound by the permanent dipole moment of a neutral molecule, typically in excess of 2.5 D.[2–4] Because of the weak non-valence interaction, the DBS orbital is a highly diffuse atomic-like orbital, akin to a Rydberg state in a neutral molecule.[5] The DBS can be the ground state or an excited state of the anion. In addition to being a scientific curiosity, non-valence anionic states have been implicated as ''door-way'' states to electron attachment[6–11] and are involved in excited state dynamics of anions.[9,12–17] These studies have focussed exclusively on isolated anions as it is generally accepted that a DBS cannot survive in the condensed phase because of the excluded volume imposed by the surrounding molecules. Yet, to the best of our knowledge, there have been no experiments aimed at testing this accepted belief. Here, we probe the effect of an excluded volume imposed by an alkyl chain on the stability of a DBS and show that the DBS remains observable.

The spectroscopic observation of DBSs can be achieved through action and photoelectron (PE) spectroscopy. Early experiments by Brauman and colleagues uncovered their presence in photodetachment yield spectra,[18,19] and such features have been seen in many other action spectra[20–24] and in PE spectra.[21,25–30] More recently, Wang and co-workers have elegantly exploited resonant excitation to a DBS as a sensitive probe of the vibrational structure of the corresponding neutral, using both action and PE spectroscopy.[31–36] A DBS can also be accessed by Rydberg electron-transfer spectroscopy, which has been extensively used to probe their role in electron attachment dynamics.[26,37] While many experiments have assessed the effect of the overall permanent dipole moment and of rotational motion[19,38–42] of the neutral core on the binding energy of the DBS, there have been far fewer studies on the interaction of a DBS with molecular fragments. A recent study by Zhu *et al.*[43] showed how a small overlap between a valence system and a DBS can lead to non-radiative decay of the DBS.

Here we address how a ''non-interacting'' molecular fragment alters the binding of a DBS. Specifically, our test model uses *para*-substituted phenolates in which an alkyl chain of varying length can ''poke'' into the DBS orbital to a variable extent, as shown schematically in Fig. 1. As the saturated alkyl chain has no dipole moment of its own (see ESI† for calculated comparison), it can be viewed as non-interacting with the DBS, except through the excluded volume that the chain will impose on the orbital. The phenolate anion ($C_6H_5O^-$) was selected as it is known to support an excited DBS and because it has been extensively studied the Wang group.[44,45]

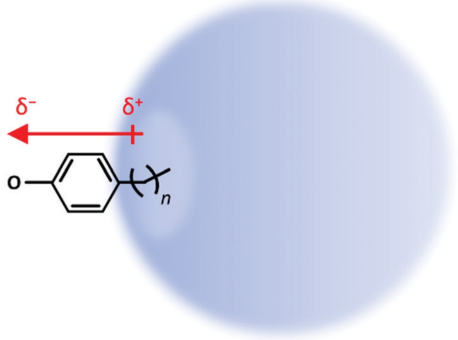

Fig. 1 Picture of dipole-bound state (DBS) of *para*-substituted alkyl-phenolate with varying chain length, *n*-ph⁻.

Department of Chemistry, Durham University, DH1 3LE, Durham, County of Durham, UK. E-mail: j.r.r.verlet@durham.ac.uk

† Electronic supplementary information (ESI) available: Supporting calculations. See DOI: 10.1039/c9cp04942h

The details of the experiment have been described previously.[46] Phenol (ph), 4-ethylphenol (2-ph), 4-propylphenol (3-ph), 4-pentylphenol (5-ph) and 4-octylphenol (8-ph) were purchased from Sigma Aldrich and 4-butylphenol (4-ph) from Tokyo Chemical Industry. The *para*-substituted phenolate anions, *n*-ph$^-$, were produced by deprotonation of their methanolic solution ($\sim$1 mM) through electrospray ionization. Ions were transferred by a capillary into a vacuum region, guided by a set of ring-electrode ion guides that also served as ion trap.[47] Ion packets were introduced in a collinear time-of-flight mass spectrometer[48] at 10 Hz and the mass-selected ion-packets were irradiated with laser pulses from a Nd:YAG pumped optical parametric oscillator. Ejected PEs were captured and imaged by a velocity-map imaging assembly.[49,50] Photodetachment action spectra were acquired by monitoring the total electron yield as a function of wavelength. PE spectra and angular distributions were derived from the raw images using Polar Onion Peeling.[51] The spectra were calibrated using phenolate, which has an electron affinity (EA) of 2.235(6) eV.[52] The PE spectral resolution was $\sim$5%.

Fig. 2(a) shows the photodetachment action spectrum of ph$^-$ and the five *para*-substituted phenolates around their respective thresholds. The spectrum of ph$^-$ includes transitions observed by the Wang group[44] at much higher resolution with cryogenically cooled ions. The 0–0, 0–1 and 0–2 transitions from the ground state to the DBS can be clearly identified as well as an offset starting just after the 0–0 transition, which corresponds to direct detachment into the continuum (*i.e.*, only the 0–0 transition is bound and all others are vibrational Feshbach resonances). Addition of a short alkyl-chain to form 2-ph$^-$ leads to a clear red-shift but the onset of signal steadily shifts towards higher photon energy as more –CH$_2$– units are added to the alkyl chain. With increasing *n*, the 0–0 transition becomes progressively less distinguishable as the chain length increases. Specifically, for 2-ph$^-$ and 3-ph$^-$, the 0–0 transition can be clearly discerned, while it is less so for 4-ph$^-$ and essentially becomes unresolved for 5-ph$^-$ and 8-ph$^-$. Note that hot bands can be seen on the red side of the 0–0 transition for all ions. These are expected because the ions are generated with an internal temperature of at least 300 K.

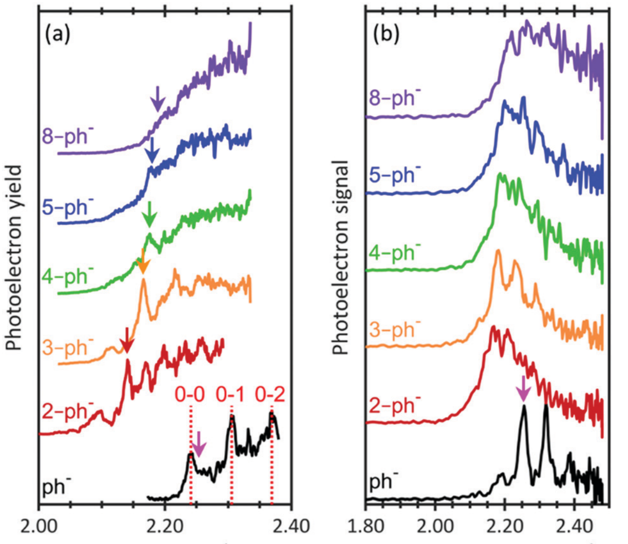

Fig. 2 (a) Photodetachment action spectra for n = 0, 2–5, and 8 near the photodetachment threshold. Vertical lines dashed lines indicate transitions measured by Liu *et al.*[44] Vertical arrows indicate excitation energy for resonance-enhanced photoelectron spectra in Fig. 3. (b) Photoelectron spectra of phenolate and *para*-substituted alkyl-phenolate anions at $h\nu$ =2.48 eV. All spectra have been vertically offset for clarity. The electron affinity (EA) is indicated by the vertical pink arrow.

The relative shifts of the 0–0 transition to the DBS arises from an increase in the EA as the chain length is increased. Fig. 2(b) shows PE spectra of the *n*-ph$^-$ species at $h\nu$ = 2.48 eV. The EA of ph sharply decreases upon *para*-substitution and then gradually increases as the chain becomes longer. Hence, assuming that the dipole-moment of *n*-ph remains constant, which is supported by our calculations (see ESI†), larger n (for $n \geq 2$) have a higher 0–0 transition energy for the DBS peak, consistent with the shift seen in Fig. 2(a).

The most striking observation of Fig. 2(a) is the loss of resolution of the 0–0 peak. We expect a signal rise near the 0–0 transition regardless of whether the DBS is excited because of the proximity of the opening of the direct detachment channel to the DBS. Hence, a possible explanation for the observed loss in resolution is that the DBS becomes completely disrupted as a sufficiently long chain perturbs its orbital.

To investigate whether the DBS still exists for larger *n*-ph$^-$, PE images were recorded at photon energies resonant with the 0–0 transition energies to the DBS (downward arrows in Fig. 2(a)). The resulting PE spectra are shown in Fig. 3 with raw PE images included as insets. The PE images exhibit two features. The bright inner feature has been intentionally saturated to enable a second larger ring to be visible. The corresponding PE spectra show the dominance of the low energy peak. This peak arises from direct detachment, which is the main detachment process. Although the extracted PE spectra seem to contain only this feature, a smaller peak can be seen around 2.5 eV. Magnifications of the kinetic energy range beyond 2.0 eV are included in Fig. 3 and shows the peak arising from the large radii features in the images. The kinetic energy of this peak indicates that two photons have been absorbed *via* an intermediate state.

There are a number of notable features associated with the two-photon peak. Firstly, the peak is very close to the photon energy. Hence, the state that is responsible for resonance-enhancement is weakly-bound. Secondly, the peak is spectrally narrow. This suggests that the potential energy surface of the intermediate state is very similar to the final neutral state. Thirdly, the PE angular distribution associated with the peak has maxima parallel to the polarization axis ($\beta_2 \sim 1$). Such emission anisotropy indicates that the outgoing PE is predominantly of p-wave character, so that the initial orbital is an s- or d-like state. Taken together, these observations are consistent with photodetachment from a non-valence state, *i.e.*, the DBS of *n*-ph$^-$. Indeed, our data are fully consistent with the much higher-resolution work from the Wang group on ph$^-$.[44] Given that the same resonance enhancement *via* a DBS is seen

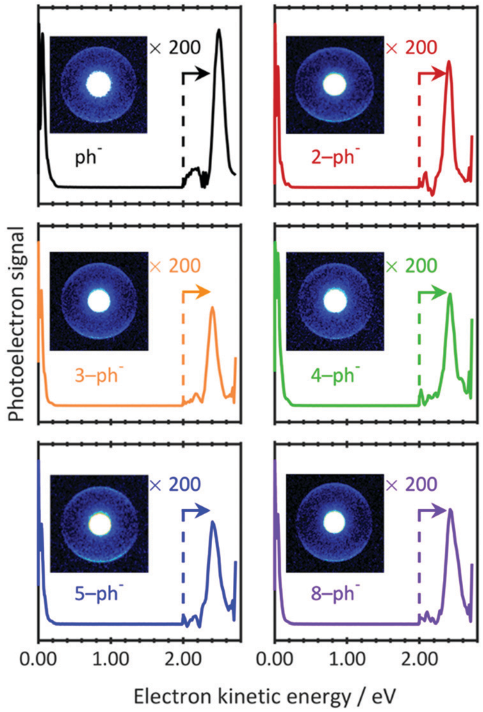

Fig. 3 Two-photon resonance-enhanced photoelectron spectra of phenolate and *para*-substituted alkyl-phenolate anions recorded at photon energies that are resonant with a DBS (see Fig. 2(a)). The signal has been amplified at higher electron kinetic energies (>2.0 eV) for clarity. Inset are the raw photoelectron images from which the spectra have been extracted. The central feature has been intentionally saturated to emphasise the outer narrow and anisotropic ring.

for all *n*-ph$^-$, we can conclude that the DBS remains intact, despite the presence of the alkyl chain.

Considering that the DBS is retained in each compound, why is a loss in resolution observed in the action spectra? The alkyl groups are conformationally flexible, especially at 300 K. For 5-ph, DFT calculations suggest that the energy difference between geometries optimised from a fully extended and fully curled alkyl chain is only $\sim$0.12 eV (see ESI†). Moreover, we have calculated the barrier for rotation of 2-ph$^-$ to be $<$80 meV and this will only be smaller for longer chains.[53] Hence, we anticipate that at 300 K there are many conformations ranging from ones with an extended chain to ones with a compact shape. Each conformation is likely to interact differently with the DBS, leading to a range of electron binding energies of the DBS, as shown schematically in Fig. 4. The consequence of this is a decrease in resolution for excitation to the DBS. As the tail becomes longer, the number of available conformers increases and the more the chain can interact with the DBS orbital, thus explaining the loss of resolution with increased chain length.

An alternative explanation for the loss of resolution of the 0–0 transition is that the EA differs for different conformations, which would lead to a change in excitation energy to the DBS. However, the PE spectra in Fig. 2(b) do not appear to support this. A variation in EA with conformational flexibility would lead to a reduction in the gradient of the PE signal's rising edge. This is not quite observed, although there is a clear loss in resolution also of the PE spectra, starting with the smallest chains. This loss of resolution has previously been noted also for ethyl-phenolate.[54] Finally, it is also possible that the experiment only samples a sub-set of conformers. Specifically, if only certain conformers support a DBS, then only those would be observable. For instance, one might envisage that an alkyl chain that points into the DBS might be disruptive to the orbital and, hence, these conformers are not observed. However, one would expect that such a selectivity would also lead to a noticeable reduction in the relative signal of resonance-enhanced signal in Fig. 3, which is not observed.

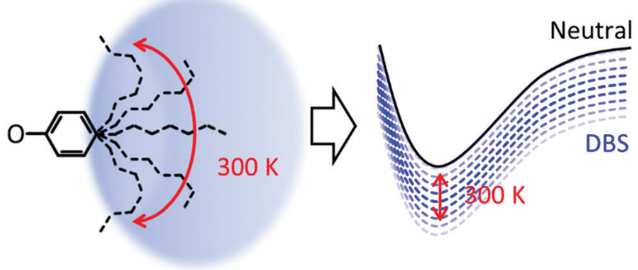

Fig. 4 Schematic diagram of effect of temperature on the conformational freedom of alkyl chain and the corresponding effect on the binding energy of the dipole-bound state.

Loss of DBS resonances in photodetachment spectra have previously been noted by Brauman and co-workers.[19,38,39] The loss was attributed to the rotational motion of the neutral core; when the dipole moment rotates then the DBS electron lags behind and the effective dipole moment is reduced. If sufficiently fast, the reduction in dipole moment renders the DBS unbound. In the present case, an increase in *n* is expected to reduce the rotational speed of the dipole moment. Hence, it seems unlikely that rotational motion is the cause of the reduced resolution. Interestingly, Walthall *et al.* also noticed a loss of resolution in the photodetachment spectra of 4-X cyclohex-1-enolate when X = methyl was replaced by X = ethyl.[39] This was considered to be a consequence of the coupling of the ethyl twisting to the rotational motion of the molecule, making the DBS unstable. However, we have shown here that such loss of resolution does not necessarily mean that the DBS is not present. It would be of interest to revisit some of these previous studies using resonance-enhanced PE spectroscopy.

The observation of a PE angular distribution with maxima parallel to the polarisation axis is consistent with photoemission from a DBS.[14,15,55] Perhaps surprisingly, however, there is no qualitative change in the β_2 parameter as a function of chain length. We had suspected that perhaps an alkyl chain "poking" a hole into a DBS orbital might alter the PE angular distribution, but this appears not to be the case, although we stress that our experiments measure an average of all conformations and so we might not be sensitive to such small effects.

While our 300 K experiments are of much reduced resolution compared to the experiments by the Wang group,[44] there may be some advantages. Under cryogenic conditions, only a few conformations will be present, and these may be the ones that avoid the DBS orbital. Nevertheless, such cold experiments will be valuable, especially when combined with computational studies which are much more difficult at 300 K.

We have shown that a DBS is not destroyed by the presence of an alkyl chain, but can it survive in the bulk? In an apolar solvent, the density of molecules is too large and the excluded volume will not allow a DBS to exist. In polar solvents, the solvent itself can provide a dipolar stabilisation as is the case for charge-transfer-to-solvent (CTTS) states,[56–58] which may be viewed as a DBS. However, much of biology exists as soft-matter, for which the molecular density can be much lower. For example, proteins contain large vacant pockets, which could accommodate a DBS that may have small molecular fragments poking into it. It is also noteworthy that the most stable conformation of tyrosine is the *para*-substituted phenolate anion rather than the carboxylic acid.[59]

Conflicts of interest

There are no conflicts to declare.

Acknowledgements

This project has received funding from the European Union's Horizon 2020 research and innovation programme under grant agreement no. 765266.

Notes and references

1 E. Fermi and E. Teller, *Phys. Rev.*, 1947, **72**, 399–408.
2 K. D. Jordan and F. Wang, *Annu. Rev. Phys. Chem.*, 2003, **54**, 367–396.
3 J. Simons, *J. Phys. Chem. A*, 2008, **112**, 6401–6511.
4 O. H. Crawford and W. R. Garrett, *J. Chem. Phys.*, 1977, **66**, 4968–4970.
5 R. F. Stebbings and F. B. Dunning, *Rydberg states of atoms and molecules*, Cambridge University Press, Cambridge Cambridgeshire, New York, 1983.
6 T. Sommerfeld, *J. Phys.: Conf. Ser.*, 2005, **4**, 245–250.
7 P. J. Sarre, *Mon. Not. R. Astron. Soc.*, 2000, **313**, L14–L16.
8 V. K. Voora and K. D. Jordan, *J. Phys. Chem. A*, 2014, **118**, 7201–7205.
9 J. P. Rogers, C. S. Anstöter and J. R. R. Verlet, *Nat. Chem.*, 2018, **10**, 341–346.
10 J. M. Weber, M. W. Ruf and H. Hotop, *Z. Phys. D: At., Mol. Clusters*, 1996, **37**, 351–357.
11 A. Kunin and D. M. Neumark, *Phys. Chem. Chem. Phys.*, 2019, **21**, 7239–7255.
12 M. A. Yandell, S. B. King and D. M. Neumark, *J. Am. Chem. Soc.*, 2013, **135**, 2128–2131.
13 J. P. Rogers, C. S. Anstöter and J. R. R. Verlet, *J. Phys. Chem. Lett.*, 2018, **9**, 2504–2509.
14 J. N. Bull and J. R. R. Verlet, *Sci. Adv.*, 2017, **3**, e1603106.
15 J. N. Bull, C. W. West and J. R. R. Verlet, *Chem. Sci.*, 2016, **7**, 5352–5361.
16 F. Lecomte, S. Carles, C. Desfrancois and M. A. Johnson, *J. Chem. Phys.*, 2000, **113**, 10973–10977.
17 J. H. Hendricks, S. A. Lyapustina, H. L. de Clercq and K. H. Bowen, *J. Chem. Phys.*, 1998, **108**, 8–11.
18 R. D. Mead, K. R. Lykke, W. C. Lineberger, J. Marks and J. I. Brauman, *J. Chem. Phys.*, 1984, **81**, 4883–4892.
19 E. A. Brinkman, S. Berger, J. Marks and J. I. Brauman, *J. Chem. Phys.*, 1993, **99**, 7586–7594.
20 J. N. Bull, J. T. Buntine, M. S. Scholz, E. Carrascosa, L. Giacomozzi, M. H. Stockett and E. J. Bieske, *Faraday Discuss.*, 2019, **217**, 34–46.
21 C. L. Adams, H. Schneider, K. M. Ervin and J. M. Weber, *J. Chem. Phys.*, 2009, **130**, 074307.
22 S. T. Edwards, M. A. Johnson and J. C. Tully, *J. Chem. Phys.*, 2012, **136**, 154305.
23 G. H. Gardenier, J. R. Roscioli and M. A. Johnson, *J. Phys. Chem. A*, 2008, **112**, 12022–12026.
24 E. Matthews and C. E. H. Dessent, *J. Phys. Chem. Lett.*, 2018, **9**, 6124–6130.
25 C. G. Bailey, C. E. H. Dessent, M. A. Johnson and K. H. Bowen, *J. Chem. Phys.*, 1996, **104**, 6976–6983.
26 E. G. Diken, N. I. Hammer and M. A. Johnson, *J. Chem. Phys.*, 2004, **120**, 9899–9902.
27 E. F. Belogolova, G. Liu, E. P. Doronina, S. M. Ciborowski, V. F. Sidorkin and K. H. Bowen, *J. Phys. Chem. Lett.*, 2018, **9**, 1284–1289.
28 S. M. Ciborowski, G. Liu, J. D. Graham, A. M. Buytendyk and K. H. Bowen, *Eur. Phys. J. D*, 2018, **72**, 139.
29 J. H. Hendricks, H. L. de Clercq, S. A. Lyapustina and K. H. Bowen, *J. Chem. Phys.*, 1997, **107**, 2962–2967.
30 J. H. Hendricks, S. A. Lyapustina, H. L. d. Clercq, J. T. Snodgrass and K. H. Bowen, *J. Chem. Phys.*, 1996, **104**, 7788–7791.
31 D. L. Huang, G. Z. Zhu and L. S. Wang, *J. Chem. Phys.*, 2015, **142**, 091103.
32 D. L. Huang, G. Z. Zhu, Y. Liu and L. S. Wang, *J. Mol. Spectrosc.*, 2017, **332**, 86–93.
33 D. L. Huang, H. T. Liu, C. G. Ning, P. D. Dau and L. S. Wang, *Chem. Phys.*, 2017, **482**, 374–383.
34 J. Czekner, L. F. Cheung, G. S. Kocheril and L. S. Wang, *Chem. Sci.*, 2019, **10**, 1386–1391.
35 H. T. Liu, C. G. Ning, D. L. Huang and L. S. Wang, *Angew. Chem., Int. Ed.*, 2014, **53**, 2464–2468.
36 G. Z. Zhu, D. L. Huang and L. S. Wang, *J. Chem. Phys.*, 2017, **147**, 013910.
37 N. I. Hammer, K. Diri, K. D. Jordan, C. Desfrançois and R. N. Compton, *J. Chem. Phys.*, 2003, **119**, 3650–3660.
38 D. A. Walthall, J. M. Karty and J. I. Brauman, *J. Phys. Chem. A*, 2005, **109**, 8794–8799.
39 D. A. Walthall, J. M. Karty, B. Romer, O. Ursini and J. I. Brauman, *J. Phys. Chem. A*, 2005, **109**, 8785–8793.
40 J. Simons, *J. Chem. Phys.*, 1989, **91**, 6858–6865.
41 A. S. Mullin, K. K. Murray, C. P. Schulz, D. M. Szaflarski and W. C. Lineberger, *Chem. Phys.*, 1992, **166**, 207–213.
42 W. R. Garrett, *Phys. Rev. A: At., Mol., Opt. Phys.*, 1971, **3**, 961–972.
43 G.-Z. Zhu, L. F. Cheung, Y. Liu, C.-H. Qian and L.-S. Wang, *J. Phys. Chem. Lett.*, 2019, 4339–4344.

44 H. T. Liu, C. G. Ning, D. L. Huang, P. D. Dau and L. S. Wang, *Angew. Chem., Int. Ed.*, 2013, **52**, 8976–8979.

45 G. Z. Zhu, C. H. Qian and L. S. Wang, *J. Chem. Phys.*, 2018, **149**, 164301.

46 J. Lecointre, G. M. Roberts, D. A. Horke and J. R. R. Verlet, *J. Phys. Chem. A*, 2010, **114**, 11216–11224.

47 L. H. Stanley, C. S. Anstöter and J. R. R. Verlet, *Chem. Sci.*, 2017, **8**, 3054–3061.

48 W. C. Wiley and I. H. Mclaren, *Rev. Sci. Instrum.*, 1955, **26**, 1150–1157.

49 A. T. J. B. Eppink and D. H. Parker, *Rev. Sci. Instrum.*, 1997, **68**, 3477–3484.

50 D. A. Horke, G. M. Roberts, J. Lecointre and J. R. R. Verlet, *Rev. Sci. Instrum.*, 2012, **83**, 063101.

51 G. M. Roberts, J. L. Nixon, J. Lecointre, E. Wrede and J. R. R. Verlet, *Rev. Sci. Instrum.*, 2009, **80**, 053104.

52 R. F. Gunion, M. K. Gilles, M. L. Polak and W. C. Lineberger, *Int. J. Mass Spectrom.*, 1992, **117**, 601–620.

53 C. S. Anstöter, C. R. Dean and J. R. R. Verlet, *J. Phys. Chem. Lett.*, 2017, **8**, 2268–2273.

54 C. S. Anstöter, C. R. Dean and J. R. R. Verlet, *Phys. Chem. Chem. Phys.*, 2017, **19**, 29772–29779.

55 J. P. Rogers, C. S. Anstöter, J. N. Bull, B. F. E. Curchod and J. R. R. Verlet, *J. Phys. Chem. A*, 2019, **123**, 1602–1612.

56 P. J. Nowakowski, D. A. Woods and J. R. R. Verlet, *J. Phys. Chem. Lett.*, 2016, **7**, 4079–4085.

57 S. E. Bradforth and P. Jungwirth, *J. Phys. Chem. A*, 2002, **106**, 1286–1298.

58 D. Serxner, C. E. H. Dessent and M. A. Johnson, *J. Chem. Phys.*, 1996, **105**, 7231–7234.

59 Z. Tian, X. B. Wang, L. S. Wang and S. R. Kass, *J. Am. Chem. Soc.*, 2009, **131**, 1174–1181.

molecules

MDPI

Article

Intramolecular Photo-Oxidation as a Potential Source to Probe Biological Electron Damage: A Carboxylated Adenosine Analogue as Case Study

Maria Elena Castellani and **Jan R. R. Verlet** *

Department of Chemistry, Durham University, Durham DH1 3LE, UK; maria.e.castellani@durham.ac.uk
* Correspondence: j.r.r.verlet@durham.ac.uk

Abstract: A carboxylated adenosine analog (C-Ado$^-$) has been synthesized and probed via time-resolved photoelectron spectroscopy in order to induce intra-molecular charge transfer from the carboxylic acid moiety to the nucleobase. Intra-molecular charge transfer can be exploited as starting point to probe low-energy electron (LEE) damage in DNA and its derivatives. Time-dependent density functional theory (TD-DFT) calculations at the B3LYP-6311G level of theory have been performed to verify that the highest occupied molecular orbital (HOMO) was located on carboxylic acid and that the lowest occupied molecular orbital (LUMO) was on the nucleobase. Hence, the carboxylic acid could work as electron source, whilst the nucleobase could serve the purpose of electron acceptor. The dynamics following excitation at 4.66 eV (266 nm) were probed using time-resolved photoelectron spectroscopy using probes at 1.55 eV (800 nm) and 3.10 eV (400 nm). The data show rapid decay of the excited state population and, based on the similarity of the overall dynamics to deoxy-adenosine monophosphate (dAMP$^-$), it appears that the dominant decay mechanism is internal conversion following $^1\pi\pi^*$ excitation of the nucleobase, rather than charge-transfer from the carboxylic acid to the nucleobase.

Keywords: photoelectron spectroscopy; low energy electron damage in DNA; charge transfer

check for updates

Citation: Castellani, M.E.; Verlet, J.R.R. Intramolecular Photo-Oxidation as a Potential Source to Probe Biological Electron Damage: A Carboxylated Adenosine Analogue as Case Study. *Molecules* **2021**, *26*, 2877. https://doi.org/10.3390/molecules26102877

Academic Editors: Fatwa Firdaus Abdi and Danilo Roccatano

Received: 7 April 2021
Accepted: 10 May 2021
Published: 13 May 2021

1. Introduction

DNA is one of the most important biomolecules, as it contains genetic information that is essential to most forms of life. DNA can suffer damage from different sources, for example radiation or oxidizing agents [1–3]. For high-energy radiation such as X-rays used in radiography or beta-radiation emitted in the Chernobyl disaster 35 years ago, it is the secondary products rather than the primary radiation that causes the largest disruptions [4,5]. The high-energy radiation ionizes predominantly water to form secondary electrons with a kinetic energy (eKE) between 0 and 20 eV. These so-called low energy electrons (LEEs) are responsible for severe DNA lesions, such as single- and double-strand breakages, which can ultimately lead to cell death and disease [6].

LEEs can attach to any of the nucleotide's components, i.e., the nucleobase, sugar and phosphate [7–9]. At very low energy, LEEs can attach as a dipole bound state (DBS) outside the molecular framework [10,11]. LEE attachment can lead to the formation of metastable anionic states known as temporary negative ions or resonances, which are responsible for inducing mutagenesis in living organisms [12,13]. Boudaiffa et al. [14] showed that single-strand breaks are caused by core-excited (Feshbach) resonances, which are produced by electron attachment to the π^* orbitals of the nucleobases. Conversely, electrons with eKE < 3 eV cause the formation of shape resonances [7,15,16], in which dissociative channels, involving mainly dehydrogenation, but also cleavage of the phosphodiester and glycosidic bonds, are active [4,6,17–19]. The mechanism comprises electron migration from the π^* orbital on the nucleobase to the σ^* orbital of either the C-O, N_1-C or N-H bond, with subsequent dissociation of the σ bond [4,20–22]. Computational and experimental evidence [23] suggests that electrons with energy > 2 eV can occupy the π* orbital of the phosphate group and contribute to single-bond breaks. Moreover, due to its low energy barrier and the high electron affinity (EA) of the phosphate group, the phosphodiester bond, together with the N_1-C bond, is the most probable to undergo cleavage caused by shape resonances [24].

LEE-induced damage has been extensively studied by Sanche and co-workers through electron scattering measurements, in which whole DNA samples are irradiated with an electron beam, and then the products, formed across a spectrum of incoming electron energies, are probed [6,9,12–14,21–25]. However, in order to probe the dynamics of the processes and thus offer a direct experimental window into the mechanisms at play, time-resolved spectroscopy is required. Probing LEE-driven chemistry in the time-domain remains challenging. One approach is to access the resonances from an anionic ground state and subsequently probe the dynamics using time-resolved photoelectron spectroscopy [26,27]. We have developed and exploited such methods—however, they are limited to molecules that have a positive electron affinity. An alternative method involves the use of iodide as a source of LEEs. Specifically, the Johnson group showed how photoexcitation of iodide-molecule clusters accesses the dipole-bound state of the clustered molecule [28–33]. The Neumark group [34–38] has elegantly extended this method to the time-domain using time-resolved photoelectron imaging, including on I^-•N (N = nucleobase) clusters. However, these methods are limited by two main factors: (1) the iodine remains present and may be more than a mere spectator and (2) the excitation energy of the charge-transfer transition from iodide is at relatively high photon energies that often coincide with absorption bands on the nucleobase. Still, this is an excellent approach to probing the role of non-valence states in electron capture [39,40].

In the present study, we explore the feasibility of a new approach based on the use of an intra-molecular electron source using photo-induced charge-transfer. In principle, a nucleotide would be an ideal candidate, given that the phosphate is negatively charged: one might envisage the possibility of performing a charge-transfer transition to the nucleobase, then subsequently probing the dynamics using time-resolved photoelectron spectroscopy. However, the electron affinity of the phosphate group is very large and would require *hv* > 5 eV [41,42]. Instead, here we explore the use of a different source of electrons based on a carboxylic acid. Specifically, following the method by Widlanski and Epp [43], we synthesized an adenosine analog with a carboxylic group in 5′ position (C-Ado). The –OH moieties of the sugar in position 2′ and 3′ are protected with an isopropyl function, in order to prevent deprotonation. If the highest occupied molecular orbital (HOMO) is located on the carboxylic acid, one could envision a charge-transfer transition occurring from the carboxylic acid moiety to the π* state on the nucleobase.

2. Results

To assess whether the electronic structure of C-Ado is suitable, density function theory (DFT) calculations were performed. The minimum energy structure of C-Ado$^-$ was obtained at the B3LYP-6311G level of theory and is shown in Figure 1. As the hydroxyl groups on the ribose are inaccessible due to the protective group, the only deprotonation site is the carboxyl group, and this is where the negative charge is hosted. The calculated vertical detachment energy (VDE) and adiabatic detachment energy (ADE) resulted, respectively, 4.48 eV and 4.29 eV.

Time-dependent DFT calculations were used to compute the molecular orbitals (MOs). The highest occupied MO (HOMO), lowest unoccupied MO (LUMO), and relevant π MOs of C-Ado$^-$ are shown in Figure 2 along with the relevant energetics. The HOMO, as expected, is predominantly located on the carboxylic acid moiety, with some charge density extending onto the ribose sugar. The initial state for the charge-transfer transition and is also hosted by the carboxyl group and is the HOMO-1 but it is essentially degenerate to the HOMO. The LUMO is an anti-bonding π* orbital of the nucleobase, as can be seen in Figure 2. This is the lowest resonance of the nucleobase (shape resonance). The lowest energy charge-transfer transition from the carboxylic acid to the nucleobase excites this π* orbital and so, in principle, such an excitation can directly mimic electron capture via the shape resonance. However, the π^* orbital is also involved in the $\pi\pi^*$ transition localized on the nucleobase. The $\pi\pi^*$ transition is calculated at 5.18 eV (239 nm), while the charge transfer transition is higher, at 5.25 eV (236 nm). Hence, both transitions are very close in energy according to the calculations. We stress however that the calculations are not intended to offer quantitative insight and rather to obtain some qualitative information on the relevant transitions and their relative energies.

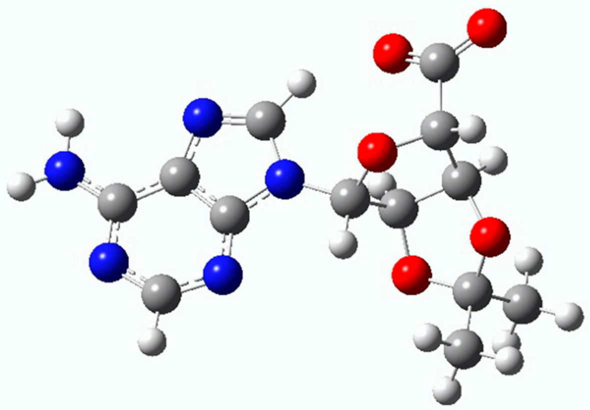

Figure 1. Minimum energy structure of C-Ado$^-$ calculated at the B3LYP-6311G level of theory. The hydrogen atom is white, carbon is grey, nitrogen is blue, and oxygen is red.

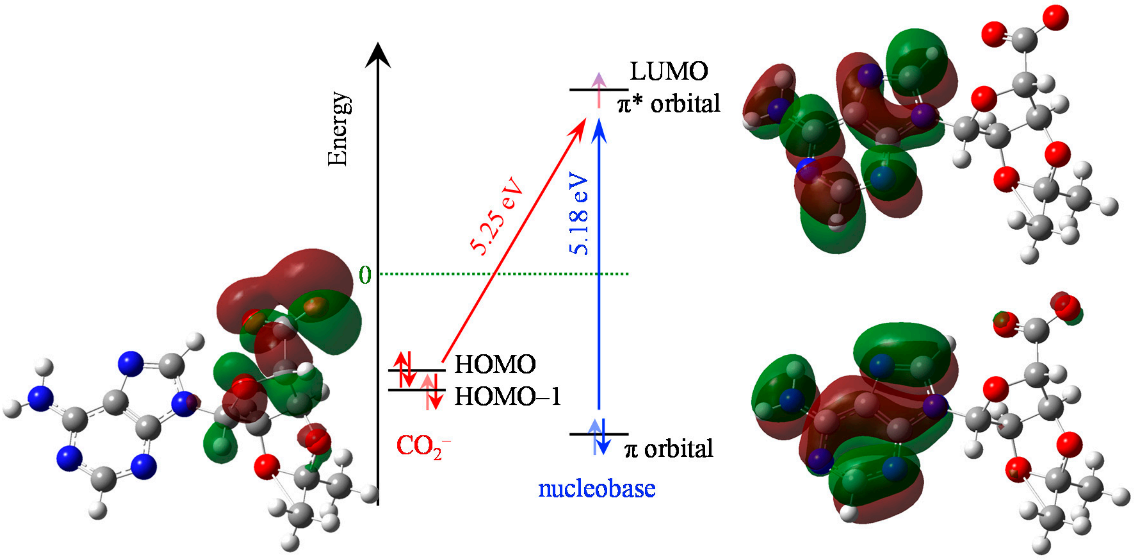

Figure 2. Energy level diagram and transitions for C-Ado$^-$, showing the carboxy-localized molecular orbitals (red/green transparent shading, HOMO and HOMO–1) as well as the nucleobase-localized molecular orbitals (π and π^* MOs). The two relevant transitions are shown with the charge-transfer (red diagonal arrow) and the nucleobase-centered $\pi\pi^*$ (blue vertical arrow). Atoms have same colours as in Figure 1.

The excited state dynamics following excitation of C-Ado$^-$ at 4.66 eV (266 nm) were probed using time-resolved photoelectron imaging using both a 1.55 eV (800 nm) probe or a 3.10 eV (400 nm) probe. The results from these experiments are shown in Figure 3a,b, respectively. In Figure 3, the photoelectron signal from the pump only (i.e., before $t = 0$) has been subtracted from each time-resolved spectrum to leave only the temporally evolving dynamics.

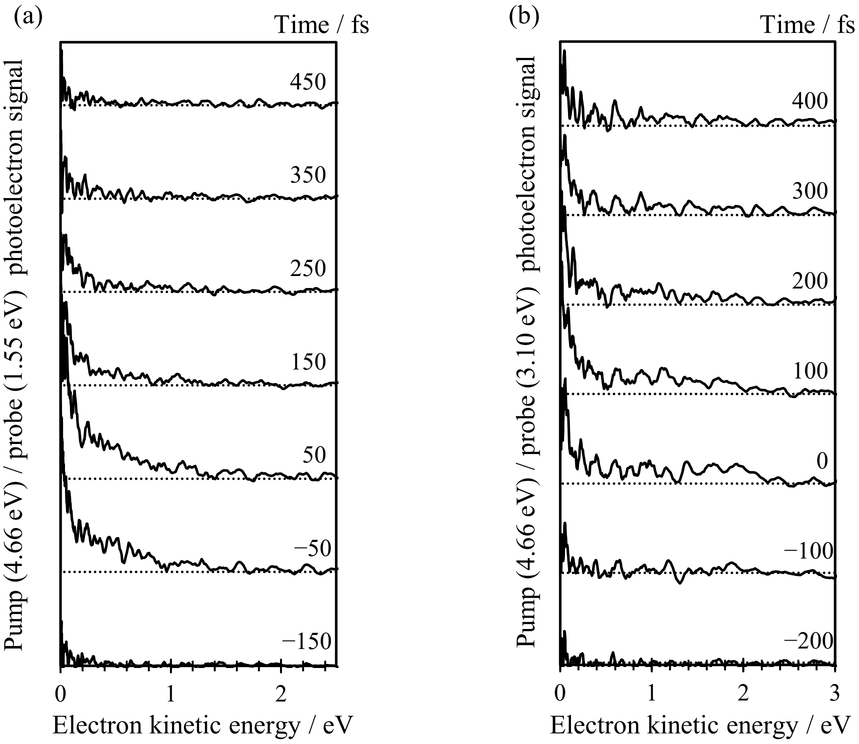

Figure 3. (**a**) Time-resolved photoelectron spectrum of C-Ado$^-$ recorded with pump energy of 266 nm and probe energy of 800 nm between −150 and 450 fs; (**b**) Time-resolved photoelectron spectrum of C-Ado$^-$ recorded with pump energy of 266 nm and probe energy of 400 nm between −200 and 400 fs. The maximum overlap between pump and probe pulse is taken as 0 fs reference.

In Figure 3a, two distinct photoelectron features can be observed at different kinetic energies. At very low KE (<0.15 eV), a narrow peak is seen near $t = 0$, which appears to have a shoulder extending out to ~1 eV. The dynamics of the higher KE feature appear to be faster than the low KE peak. In an attempt to probe a slightly larger Franck–Condon window, we also probed the same dynamics with a 3.10 eV probe as shown in Figure 3b. Unfortunately, these data are of slightly poorer signal-to-noise compared to the spectra with the 1.55 eV probe.

The time-resolved spectra in Figure 3b can be roughly divided into a number of distinct features. The first at low KE is similar to that observed with the 1.55 eV probe. It is a narrow peak with KE < 0.2 eV. There is also a feature between 0.2 < KE < 1.0 eV that seems to decay at a similar timescale to the low KE peak. At higher energy still, 1.0 < KE < 2.5 eV, a third feature can be discerned, but only near $t = 0$.

The time-resolved photoelectron spectrum at t~0 can be used to extract an approximate value of the ADE for C-Ado$^-$. To improve the signal to noise, we have taken the average of three spectra at t~0 fs and from the maximum KE of these, we conclude that the ADE~5.2 eV for both the experiment with a 1.55 eV and the one with a 3.10 eV probe pulse. Note that the ADE determined in this manner is that associated with the initial excitation because it is determined using a resonance-enhanced scheme.

To analyze the decay dynamics of the spectral features identified in Figure 3, we consider the integrated photoelectron signal over specific spectral ranges. These are shown in Figure 4 for the data taken with a 1.55 eV probe in (a) and a 3.10 eV (b). In Figure 4a, the total integrated signal is shown along with the dynamics associated with the two features—the peak at low KE and the shoulder at 0.2 < KE < 1.0 eV. The latter have been normalized to a common maximum integrated intensity to allow for easy comparison of the dynamics of the individual features. Both features decay very rapidly and with essentially identical dynamics, suggesting that both peaks are a measure of the same excited state population dynamics. The total integrated dynamics are best fit to a sequential decay process, A→B→C, where both A and B are observable, and C is some final state that is not observable with the 1.55 eV probe pulse. The fit is included in Figure 4a and shows that the two decay lifetimes are τ_{AB} = 100 fs and τ_{BC} = 330 fs. Given that the instrument response function (cross-correlation of pump and probe) is ~100 fs, τ_{AB} is effectively within our time-resolution.

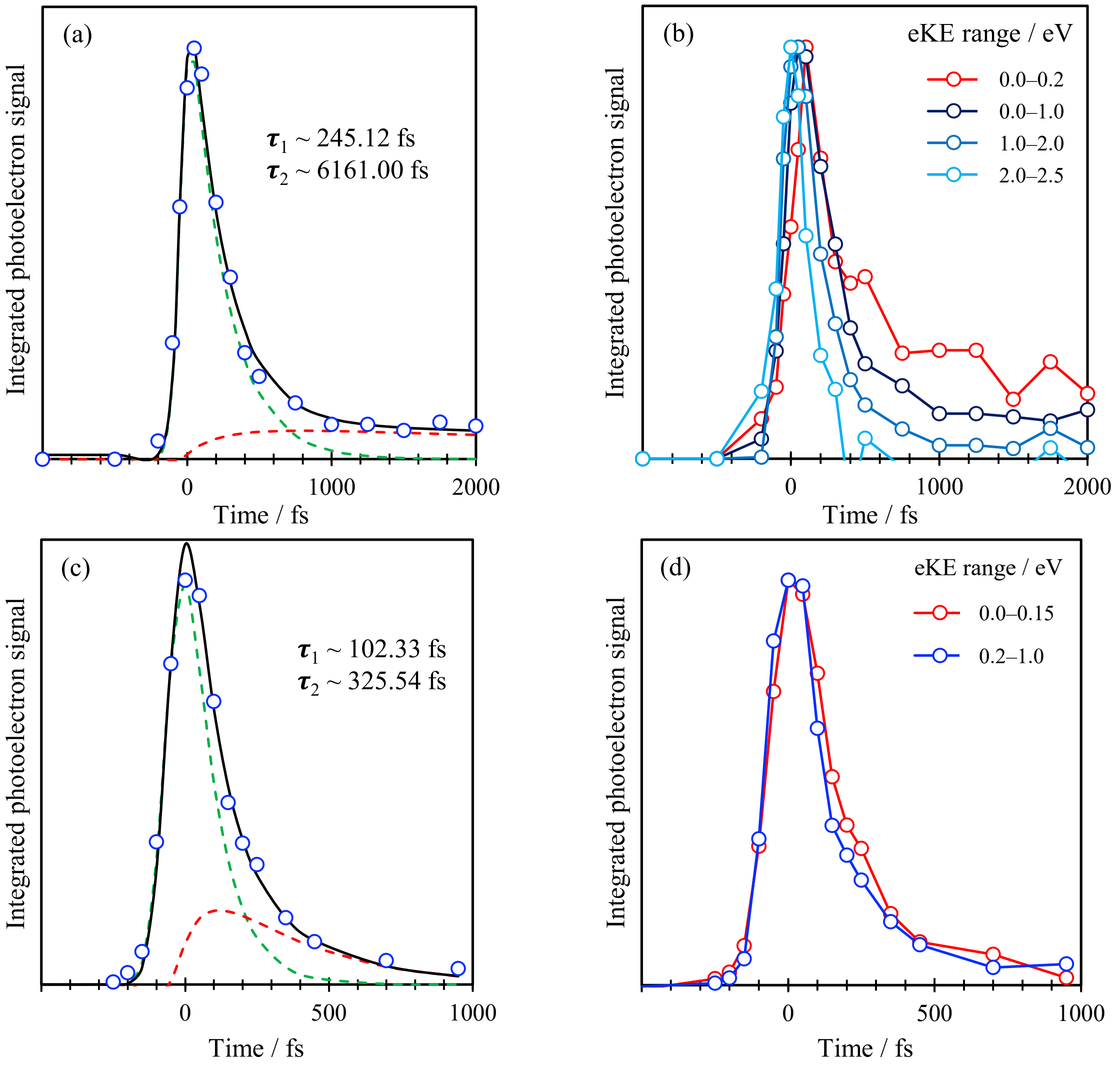

Figure 4. (**a**) Total integrated photoelectron signal with pump energy of 266 nm and probe energy of 400 nm (blue dots) plotted in function of time, with corresponding fits; (**b**) Integrated photoelectron signal with pump energy of 266 nm and probe energy of 800 nm over different energy ranges. (**c**) Same as (**a**) with pump energy of 266 nm and probe energy of 800 nm; (**d**) Same as (**b**) with pump energy of 266 nm and probe energy of 400 nm. Black lines in (**a**,**c**) are fit to total signal; dashed green and red lines are fits to kinetic model for the fast and slow component, respectively.

Performing a similar analysis for the data using a 3.10 eV probe is shown in Figure 4b. The total integrated photoelectron signal can similarly be fitted to a sequential decay as shown, which yields decay lifetimes of τ_{AB} = 250 fs and τ_{BC} ~ 6.2 ps (although the latter has a very large error as we have not measured the complete decay of this signal). However, dividing up the spectral ranges into representative slices, as shown in Figure 4b, reveals that the decay lifetime scales inversely with the KE of the photoelectron signal. Specifically, for 2.0 < KE < 2.5 eV, the signal decays very fast and essentially appears as the Gaussian instrument response function. The decay for 1.0 < KE < 2.0 eV is slightly slower with a small offset at longer times which becomes even slower for 0.2 < KE < 1.0 eV and with a larger long-time offset and again for the 0.0 < KE < 0.2 eV range. Additionally, it is clear that the rise of the signal is delayed at lower KE, suggesting that the photoelectron signal is effectively shifting to lower KE as time progresses. Hence, even though the fit to the sequential decay is good, it does not capture the true dynamics taking place.

3. Discussion

In line with our design aims, calculations show that the HOMO of C-Ado$^-$ is predominantly localized on the carboxylic acid and the LUMO/π* orbital on the nucleobase. Moreover, a charge-transfer transition calculated to lie at ~5.25 eV is accessible and can, in principle, be used to drive an intramolecular charge injection onto the nucleobase. However, it is also clear that the $\pi\pi$* transition on the nucleobase alone is also near to this computed energy and would provide an alternative to the intended charge-transfer. Nevertheless, our computations were used predominantly as a guide of the electronic structure rather than an absolute indicator and we note that much higher-level calculations have been used in literature [41]. In particular, calculations of transition energies may be expected to have large associated errors. Perhaps surprising is the poor agreement between the computed ADE (4.29 eV) and that measured at ~5.2 eV. However, it is important to underline that the experimental value does not necessarily correspond to the computed ADE. As the HOMO is localized predominantly on the carboxylic acid, the computed ADE corresponds to the removal of an electron from this site. The experimental ADE is derived from a resonance-enhanced measurement. If the initial excitation is localized on the nucleobase, then the measured ADE will correspond to the ionization energy of the nucleobase in C-Ado$^-$. Note that the measured ~5.2 eV is not that dissimilar to the ionization of adenine in the phosphorylated nucleotide, dAMP$^-$, measured to be 5.65 ± 0.15 eV [41,42]. Hence, it is important to know where the initial excitation takes place, for which the time-resolved measurements may provide some insight.

The time-resolved measurements in Figure 4 show that the dynamics are rapid and that the 1.55 eV probe is probing only a small fraction of the excited state evolution. We therefore focus the discussion on the dynamics observed with the 3.10 eV probe. This shows that the initially excited is very short lived and appears to shift towards lower KE on a timescale of a few 100s fs. Overall, these dynamics are similar to those observed for dAMP$^-$ [41,42] following excitation and probing at the same energies. While it is difficult to correlate the exact timescales, the overall shifting towards lower KE also occurs in dAMP$^-$ and this was assigned to motion on the $\pi\pi$* state away from the Franck–Condon region. That population then decays on a 290 fs timescale by internal conversion leaving no excited state photoelectron signal beyond ~1 ps. The same population dynamics are also seen in bare adenine, 9-methyl-adenine, adenine oligonucleotides and adenine triphosphate dianions [42,44–47]. Hence, it is not wholly unsurprising that similar overall dynamics are observed in C-Ado$^-$.

While the initial dynamics are similar, it is apparent from Figure 4b that some population remains after 1 ps. It should be noted that this signal is at very low KE, where noise is most severe and, therefore, there is some uncertainty in this signal and certainly in its subsequent decay. Nevertheless, it does appear that there are differences between the observed dynamics in dAMP$^-$ and C-Ado$^-$ at longer times. The main difference between the two systems is the availability of the charge-transfer transition that is predicted at a very similar excitation energy as the $\pi\pi$* state in C-Ado$^-$. Hence, the low KE signal seen in C-Ado$^-$ for $t > 1$ ps could, in principle, be associated with population arising from charge-transfer. The excited state produced following such an excitation would leave the negative charge localized on the nucleobase and appears to have a longer lifetime. However, our data are of insufficient quality to analyze the evolution nor to be certain that the charge-transfer transition is excited.

Taking the above observations together, it appears that the majority of the excitation energy excites population into the nucleobase-centered $\pi\pi$* state. This then decays in a similar manner as other adenine and purine derivatives [44,45,48]. The lack of very clear evidence for differing dynamics may be due to the oscillator strength for direct charge-transfer excitation from the carboxylate to the nucleobase being much smaller than that for the $\pi\pi^*$ transition. Hence, despite lowering the electron affinity of the compound, substitution of the phosphate group with a carboxylic acid does not red-shift the charge-transfer transition sufficiently to avoid the $\pi\pi^*$ transition. Nevertheless, we believe that the principle remains valid, and that the present study offers valuable lessons moving forward in the design of nucleotide-derivatives with different substituents. Specifically, one should aim to reduce the EA further for the anion group and to reduce the transition energy of the charge-transfer state. Possible modification could include the incorporation of hydroxyl groups that have been observed to lower the EA in substituted benzene derivatives [49]. Alternatively, on might consider attaching a nearby chromophore whose excited state has a similar energy to the π^* MO on the nucleobase to affect charge-transfer. The current preliminary study is intended to serve as a stepping-stone for future work, which will aim to understand how to exploit intra-molecular charge transfer as a probe for low-energy electron damage in DNA and its derivatives, but it may open up exciting opportunities to probe electron-driven chemistry in DNA. Coupling this experimental approach with quantum dynamics calculations, particularly surface hopping, could help in better understanding the extent of charge-transfer in DNA. [50–53]

4. Materials and Methods

A detailed description of the instrument can be found in previous publications [54,55]. Carboxylated-5′-adenosine (C-Ado) was prepared following the protocol reported by Epp and Widlanski [43]. 1 mM of C-Ado was dissolved in methanol, adding few drops of NH_4 in MeOH to facilitate deprotonation. The solution was pushed through a syringe into the first vacuum region of the apparatus, in which the anions were produced by electrospray ionization (ESI). Sets of ring-electrode ion guides guided the ions through a potential gradient towards a pulsed ion trap, then focused collinearly into a Wiley–McLaren time-of-flight mass spectrometer [56]. The mass-selected ion packet was irradiated with laser pulses obtained from a commercial Ti:Sapphire laser. The fundamental at 1.55 eV and the second harmonic at 3.10 eV were used as probe pulses for different experiments. The third harmonic was instead used as a pump pulse, with ~100 fs temporal resolution. The thus-produced photoelectrons were collected and imaged using a perpendicular velocity-map imaging (VMI) arrangement [57]. Onion peeling in polar coordinates was exploited for spectral extraction [58]. The well-known PE image of I^- was chosen as calibrant. Spectral resolution resulted in $\sim$5% of the kinetic energy.

Platinum plated VMI electrodes were used in order to ameliorate the signal-to-noise ratio, thanks to the higher work-function of platinum compared to stainless steel [59]. For background subtraction, as well as to increase PE signal, the PE images were collected with both the ion trap open and closed at ~1 Hz. A more detailed description of this procedure can be found here [46].

Time-resolved data were analyzed first by integration, then fitted to a given function to extract quantitative information. The model we use exploits exponentially modified Gaussian functions convoluted with the instrument response over time, which is given by the cross-correlation of the pump-probe signal. Details on the analytical expression of the fit can be found here [60].

Density functional theory (DFT) calculations have been performed with the software Gaussian09 [61], and the results visualized with GaussView 4. B3LYP (Becke three-parameter hybrid functional combined with Lee-Yang-Parr correlation functional) exchange correlation functional was used [41] together with the 6-311G basis set [62,63]. Diffuse and polarization functions were added. For molecular orbital visualization, the corrected functional CAM-B3LYP was instead used [64].

Author Contributions: Conceptualization, J.R.R.V.; methodology, M.E.C.; formal analysis M.E.C. and J.R.R.V.; writing, reviewing and editing, M.E.C. and J.R.R.V.; supervision J.R.R.V.; funding acquisition, J.R.R.V. All authors have read and agreed to the published version of the manuscript.

Funding: This work was supported by funding from the European Union's Horizon 2020 research and innovation program under the Marie Sklodowska-Curie grant agreement No.765266 (LightDyNAmics).

Institutional Review Board Statement: Not applicable.

Informed Consent Statement: Not applicable.

Data Availability Statement: Data is available from the authors upon reasonable request.

Conflicts of Interest: The authors declare no conflict of interest.

References

1. Alberts, B. *Molecular Biology of the Cell*, 5th ed.; Garland Science: New York, NY, USA, 2008.
2. Steenken, S. Purine bases, nucleosides, and nucleotides: Aqueous solution redox chemistry and transformation reactions of their radical cations and e- and OH adducts. *Chem. Rev.* **1989**, *89*, 503–520. [CrossRef]
3. Burrows, C.J.; Muller, J.G. Oxidative nucleobase modifications leading to strand scission. *Chem. Rev.* **1998**, *98*, 1109–1151. [CrossRef]
4. Simons, J. How do low-energy (0.1–2 eV) electrons cause DNA-strand breaks? *Acc. Chem. Res.* **2006**, *39*, 772–779. [CrossRef]
5. Kumar, A.; Becker, D.; Adhikary, A.; Sevilla, M.D. Reaction of Electrons with DNA: Radiation Damage to Radiosensitization. *Int. J. Mol. Sci.* **2019**, *20*, 3998. [CrossRef]
6. Zheng, Y.; Cloutier, P.; Hunting, D.J.; Wagner, J.R.; Sanche, L. Glycosidic bond cleavage of thymidine by low-energy electrons. *J. Am. Chem. Soc.* **2004**, *126*, 1002–1003. [CrossRef]
7. Aflatooni, K.; Gallup, G.A.; Burrow, P.D. Electron attachment energies of the DNA bases. *J. Phys. Chem. A* **1998**, *102*, 6205–6207. [CrossRef]
8. Ptasińska, S.; Denifl, S.; Scheier, P.; Märk, T.D. Inelastic electron interaction (attachment/ionization) with deoxyribose. *J. Chem. Phys.* **2004**, *120*, 8505–8511. [CrossRef]
9. Li, X.; Sevilla, M.D.; Sanche, L. Density functional theory studies of electron interaction with DNA: Can zero eV electrons induce strand breaks? *J. Am. Chem. Soc.* **2003**, *125*, 13668–13669. [CrossRef]
10. Scheer, A.M.; Aflatooni, K.; Gallup, G.A.; Burrow, P.D. Bond Breaking and Temporary Anion States in Uracil and Halouracils: Implications for the DNA Bases. *Phys. Rev. Lett.* **2004**, *92*, 068102. [CrossRef]
11. Baccarelli, I.; Bald, I.; Gianturco, F.A.; Illenberger, E.; Kopyra, J. Electron-induced damage of DNA and its components: Experiments and theoretical models. *Phys. Rep.* **2011**, *508*, 1–44. [CrossRef]
12. Sanche, L. Role of secondary low energy electrons in radiobiology and chemoradiation therapy of cancer. *Chem. Phys. Lett.* **2009**, *474*, 1–6. [CrossRef]
13. Sanche, L. Low energy electron-driven damage in biomolecules. *Eur. Phys. J. D* **2005**, *35*, 367–390. [CrossRef]
14. Boudaiffa, B.; Cloutier, P.; Hunting, D.; Huels, M.A.; Sanche, L. Resonant formation of DNA strand breaks by low-energy (3 to 20 eV) electrons. *Science* **2000**, *287*, 1658–1660.
15. Burrow, P.D.; Gallup, G.A.; Modelli, A. Are There π^* Shape Resonances in Electron Scattering from Phosphate Groups? *J. Phys. Chem. A* **2008**, *112*, 4106–4113. [CrossRef]
16. Fennimore, M.A.; Matsika, S. Core-excited and shape resonances of uracil. *Phys. Chem. Chem. Phys.* **2016**, *18*, 30536–30545. [CrossRef]
17. Abdoul-Carime, H.; Gohlke, S.; Illenberger, E. Site-specific dissociation of DNA bases by slow electrons at early stages of irradiation. *Phys. Rev. Lett.* **2004**, *92*, 168103. [CrossRef]
18. Barrios, R.; Skurski, P.; Simons, J. Mechanism for damage to DNA by low-energy electrons. *J. Phys. Chem. B* **2002**, *106*, 7991–7994. [CrossRef]
19. Berdys, J.; Anusiewicz, I.; Skurski, P.; Simons, J. Damage to Model DNA Fragments from Very Low-Energy (<1 eV) Electrons. *J. Am. Chem. Soc.* **2004**, *126*, 6441–6447. [CrossRef]
20. Bhaskaran, R.; Sarma, M. The role of the shape resonance state in low energy electron induced single strand break in 2′-deoxycytidine-5′-monophosphate. *Phys. Chem. Chem. Phys.* **2015**, *17*, 15250–15257. [CrossRef] [PubMed]
21. Khorsandgolchin, G.; Sanche, L.; Cloutier, P.; Wagner, J.R. Strand Breaks Induced by Very Low Energy Electrons: Product Analysis and Mechanistic Insight into the Reaction with TpT. *J. Am. Chem. Soc.* **2019**, *141*, 10315–10323. [CrossRef] [PubMed]
22. Pan, X.; Cloutier, P.; Hunting, D.; Sanche, L. Dissociative Electron Attachment to DNA. *Phys. Rev. Lett.* **2003**, *90*, 208102. [CrossRef] [PubMed]
23. Martin, F.; Burrow, P.D.; Cai, Z.L.; Cloutier, P.; Hunting, D.; Sanche, L. DNA strand breaks induced by 0-4 eV electrons: The role of shape resonances. *Phys. Rev. Lett.* **2004**, *93*, 068101. [CrossRef]
24. Zheng, Y.; Cloutier, P.; Hunting, D.J.; Wagner, J.R.; Sanche, L. Phosphodiester and N-glycosidic bond cleavage in DNA induced by 4-15 eV electrons. *J. Chem. Phys.* **2006**, *124*, 064710. [CrossRef]
25. Li, Z.; Cloutier, P.; Sanche, L.; Wagner, J.R. Low-energy electron-induced DNA damage: Effect of base sequence in oligonucleotide trimers. *J. Am. Chem. Soc.* **2010**, *132*, 5422–5427. [CrossRef]
26. Horke, D.A.; Li, Q.; Blancafort, L.; Verlet, J.R. Ultrafast above-threshold dynamics of the radical anion of a prototypical quinone electron-acceptor. *Nat. Chem.* **2013**, *5*, 711–717. [CrossRef] [PubMed]

27. West, C.W.; Bull, J.N.; Antonkov, E.; Verlet, J.R. Anion resonances of para-benzoquinone probed by frequency-resolved photoelectron imaging. *J. Phys. Chem. A* **2014**, *118*, 11346–11354. [CrossRef]
28. Dessent, C.E.H.; Kim, J.; Johnson, M.A. Photochemistry of Halide Ion−Molecule Clusters: Dipole-Bound Excited States and the Case for Asymmetric Solvation. *Acc. Chem. Res.* **1998**, *31*, 527–534. [CrossRef]
29. Serxner, D.; Dessent, C.E.H.; Johnson, M.A. Precursor of the Iaq− charge-transfer-to-solvent (CTTS) band in I—(H_2O)n clusters. *J. Chem. Phys.* **1996**, *105*, 7231–7234. [CrossRef]
30. Talbot, J.J.; Yang, N.; Huang, M.; Duong, C.H.; McCoy, A.B.; Steele, R.P.; Johnson, M.A. Spectroscopic Signatures of Mode-Dependent Tunnel Splitting in the Iodide–Water Binary Complex. *J. Phys. Chem. A* **2020**, *124*, 2991–3001. [CrossRef]
31. Dessent, C.E.H.; Bailey, C.G.; Johnson, M.A. Dipole-bound excited states of the I^-CH_3CN and $I^-(CH_3CN)_2$ ion–molecule complexes: Evidence for asymmetric solvation. *J. Chem. Phys.* **1995**, *103*, 2006–2015. [CrossRef]
32. Dessent, C.E.H.; Kim, J.; Johnson, M.A. Spectroscopic observation of vibrational Feshbach resonances in near-threshold photoexcitation of $X^-\cdot CH_3NO_2$ ($X^- = I^-$ and Br^-). *Faraday Discuss.* **2000**, *115*, 395–406. [CrossRef]
33. Dessent, C.E.H.; Bailey, C.G.; Johnson, M.A. Observation of the dipole-bound excited state of the I^-·acetone ion-molecule complex. *J. Chem. Phys.* **1995**, *102*, 6335–6338. [CrossRef]
34. Kunin, A.; Neumark, D.M. Time-resolved radiation chemistry: Femtosecond photoelectron spectroscopy of electron attachment and photodissociation dynamics in iodide-nucleobase clusters. *Phys. Chem. Chem. Phys.* **2019**, *21*, 7239–7255. [CrossRef] [PubMed]
35. King, S.B.; Yandell, M.A.; Stephansen, A.B.; Neumark, D.M. Time-resolved radiation chemistry: Dynamics of electron attachment to uracil following UV excitation of iodide-uracil complexes. *J. Chem. Phys.* **2014**, *141*, 224310. [CrossRef] [PubMed]
36. King, S.B.; Yandell, M.A.; Neumark, D.M. Time-resolved photoelectron imaging of the iodide–thymine and iodide–uracil binary cluster systems. *Faraday Discuss.* **2013**, *163*, 59–72. [CrossRef] [PubMed]
37. Yandell, M.A.; King, S.B.; Neumark, D.M. Time-Resolved Radiation Chemistry: Photoelectron Imaging of Transient Negative Ions of Nucleobases. *J. Am. Chem. Soc.* **2013**, *135*, 2128–2131. [CrossRef]
38. King, S.B.; Stephansen, A.B.; Yokoi, Y.; Yandell, M.A.; Kunin, A.; Takayanagi, T.; Neumark, D.M. Electron accommodation dynamics in the DNA base thymine. *J. Chem. Phys.* **2015**, *143*, 024312. [CrossRef]
39. Stephansen, A.B.; King, S.B.; Yokoi, Y.; Minoshima, Y.; Li, W.-L.; Kunin, A.; Takayanagi, T.; Neumark, D.M. Dynamics of dipole- and valence bound anions in iodide-adenine binary complexes: A time-resolved photoelectron imaging and quantum mechanical investigation. *J. Chem. Phys.* **2015**, *143*, 104308. [CrossRef]
40. Rogers, J.P.; Anstoter, C.S.; Verlet, J.R.R. Ultrafast dynamics of low-energy electron attachment via a non-valence correlation-bound state. *Nat. Chem.* **2018**, *10*, 341–346. [CrossRef]
41. Yang, X.; Wang, X.-B.; Vorpagel, E.R.; Wang, L.-S. Direct experimental observation of the low ionization potentials of guanine in free oligonucleotides by using photoelectron spectroscopy. *Proc. Natl. Acad. Sci. USA* **2004**, *101*, 17588–17592. [CrossRef]
42. Chatterley, A.S.; Johns, A.S.; Stavros, V.G.; Verlet, J.R.R. Base-Specific Ionization of Deprotonated Nucleotides by Resonance Enhanced Two-Photon Detachment. *J. Phys. Chem. A* **2013**, *117*, 5299–5305. [CrossRef]
43. Epp, J.B.; Widlanski, T.S. Facile Preparation of Nucleoside-5′-carboxylic Acids. *J. Org. Chem.* **1999**, *64*, 293–295. [CrossRef] [PubMed]
44. Chatterley, A.S.; West, C.W.; Roberts, G.M.; Stavros, V.G.; Verlet, J.R.R. Mapping the Ultrafast Dynamics of Adenine onto Its Nucleotide and Oligonucleotides by Time-Resolved Photoelectron Imaging. *J. Phys. Chem. Lett.* **2014**, *5*, 843–848. [CrossRef] [PubMed]
45. Stavros, V.G.; Verlet, J.R.R. Gas-Phase Femtosecond Particle Spectroscopy: A Bottom-Up Approach to Nucleotide Dynamics. *Annu. Rev. Phys. Chem.* **2016**, *67*, 211–232. [CrossRef]
46. Castellani, M.E.; Avagliano, D.; Verlet, J.R.R. Ultrafast Dynamics of the Isolated Adenosine-5′-triphosphate Dianion Probed by Time-Resolved Photoelectron Imaging. *J. Phys. Chem. A* **2021**. [CrossRef]
47. Castellani, M.E.; Avagliano, D.; González, L.; Verlet, J.R.R. Site-Specific Photo-oxidation of the Isolated Adenosine-5′-triphosphate Dianion Determined by Photoelectron Imaging. *J. Phys. Chem. Lett.* **2020**, *11*, 8195–8201. [CrossRef]
48. Chatterley, A.S.; West, C.W.; Stavros, V.G.; Verlet, J.R.R. Time-resolved photoelectron imaging of the isolated deprotonated nucleotides. *Chem. Sci.* **2014**, *5*, 3963–3975. [CrossRef]
49. Vysotskii, Y.B. Effect of chemical substitution on the ionization potentials and electron affinity of systems with conjugated bonds. *Theor. Exp. Chem.* **1982**, *17*, 363–371. [CrossRef]
50. Tully, J.C.; Preston, R.K. Trajectory Surface Hopping Approach to Nonadiabatic Molecular Collisions: The Reaction of H+ with D2. *J. Chem. Phys.* **1971**, *55*, 562–572. [CrossRef]
51. Hammes-Schiffer, S.; Tully, J.C. Proton transfer in solution: Molecular dynamics with quantum transitions. *J. Chem. Phys.* **1994**, *101*, 4657–4667. [CrossRef]
52. Mitrić, R.; Petersen, J.; Bonačić-Koutecký, V. Laser-field-induced surface-hopping method for the simulation and control of ultrafast photodynamics. *Phys. Rev. A* **2009**, *79*, 053416. [CrossRef]
53. Mavri, J. Molecular Dynamics with Nonadiabatic Transitions: A Comparison of Methods. *Mol. Simul.* **2000**, *23*, 389–411. [CrossRef]
54. Lecointre, J.; Roberts, G.M.; Horke, D.A.; Verlet, J.R.R. Ultrafast Relaxation Dynamics Observed Through Time-Resolved Photoelectron Angular Distributions. *J. Phys. Chem. A* **2010**, *114*, 11216–11224. [CrossRef]

55. Stanley, L.H.; Anstöter, C.S.; Verlet, J.R.R. Resonances of the anthracenyl anion probed by frequency-resolved photoelectron imaging of collision-induced dissociated anthracene carboxylic acid. *Chem. Sci.* **2017**, *8*, 3054–3061. [CrossRef]
56. Wiley, W.C.; McLaren, I.H. Time-of-Flight Mass Spectrometer with Improved Resolution. *Rev. Sci. Instrum.* **1955**, *26*, 1150–1157. [CrossRef]
57. Horke, D.A.; Roberts, G.M.; Lecointre, J.; Verlet, J.R.R. Velocity-map imaging at low extraction fields. *Rev. Sci. Instrum.* **2012**, *83*, 063101. [CrossRef] [PubMed]
58. Roberts, G.M.; Nixon, J.L.; Lecointre, J.; Wrede, E.; Verlet, J.R.R. Toward real-time charged-particle image reconstruction using polar onion-peeling. *Rev. Sci. Instrum.* **2009**, *80*, 053104. [CrossRef]
59. Fingerman, S. *CRC Handbook of Chemistry and Physics: A Ready-Reference Book of Chemical and Physical Data*, 87th ed.; Sci-Tech News; CRC Press: Boca Raton, FL, USA, 2007; Volume 61, p. 38.
60. Horke, D.A. *Femtosecond Photoelectron Imaging of Anions*; Durham University: Durham, UK, 2012.
61. Frisch, M.J.; Schlegel, H.B.; Scuseria, G.E.; Robb, M.A.; Cheeseman, J.R.; Scalmani, G.; Barone, V.; Mennucci, B.; Petersson, G.A.; Nakatsuji, H.; et al. *Gaussian 09*; Gaussian, Inc.: Wallingford, CT, USA, 2009.
62. Krishnan, R.; Binkley, J.S.; Seeger, R.; Pople, J.A. Self-consistent molecular orbital methods. XX. A basis set for correlated wave functions. *J. Chem. Phys.* **1980**, *72*, 650–654. [CrossRef]
63. McLean, A.D.; Chandler, G.S. Contracted Gaussian basis sets for molecular calculations. I. Second row atoms, Z = 11–18. *J. Chem. Phys.* **1980**, *72*, 5639–5648. [CrossRef]
64. Yanai, T.; Tew, D.P.; Handy, N.C. A new hybrid exchange–correlation functional using the Coulomb-attenuating method (CAM-B3LYP). *Chem. Phys. Lett.* **2004**, *393*, 51–57. [CrossRef]

The Journal of Physical Chemistry Letters

pubs.acs.org/JPCL Letter

Site-Specific Photo-oxidation of the Isolated Adenosine-5′-triphosphate Dianion Determined by Photoelectron Imaging

Maria Elena Castellani,[§] Davide Avagliano,[§] Leticia González,* and Jan R. R. Verlet*

Cite This: *J. Phys. Chem. Lett.* 2020, 11, 8195–8201 Read Online

ACCESS | Metrics & More | Article Recommendations | Supporting Information

ABSTRACT: Photoelectron imaging of the isolated adenosine-5′-triphosphate dianion excited to the $^1\pi\pi^*$ states reveals that electron emission is predominantly parallel to the polarization axis of the light and arises from subpicosecond electron tunneling through the repulsive Coulomb barrier (RCB). The computed RCB shows that the most probable electron emission site is on the amino group of adenine. This is consistent with the photoelectron imaging: excitation to the $^1\pi\pi^*$ states leads to an aligned ensemble distributed predominantly parallel to the long axis of adenine; the subsequent electron tunneling site is along this axis; and the negatively charged phosphate groups guide the outgoing electron mostly along this axis at long range. Imaging of electron tunneling from polyanions combined with computational chemistry may offer a general route for probing the intrinsic photo-oxidation site and dynamics as well as the overall structure of complex isolated species.

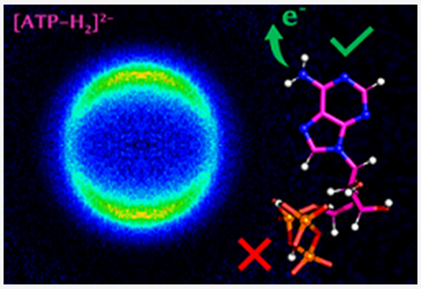

Photo-oxidation is an important source of biological damage, especially in DNA and its derivatives. All of the nucleobases possess bright $^1\pi\pi^*$ states that can readily absorb ultraviolet light. Adenine in particular is a common nucleobase, as it is present not only as one of the four DNA bases but also in adenosine triphosphate (ATP) and nicotinamide adenine dinucleotide, which are central to cell energy distribution and metabolism, respectively.[1,2] To gain an understanding of the intrinsic photoresponse of such molecules, gas-phase spectroscopy in conjunction with electronic structure theory has played an important role.[3,4] For example, gas-phase environments have been used to probe the decay dynamics of photoexcited nucleobases,[5−8] nucleotides[9] and oligonucleotides;[10] the ionization potentials of the nucleobases in nucleotides;[9,11] their geometric structures;[12−16] and their photodissociation products.[17,18] The phosphate groups render most nucleotide derivatives negatively charged, and therefore, multiple phosphates lead to polyanions. While ubiquitous in the condensed phase, a polyanion of charge Q can also exist in the gas phase, but with the unique property that oxidation leads to a repulsive Coulomb barrier (RCB) between the departing electron and the remaining molecule with overall charge Q + 1.[19−22] Here we exploit the unique properties of the RCB to determine the location of photo-oxidation in isolated doubly deprotonated adenosine-5′-triphosphate dianions, $[ATP-H_2]^{2-}$, and as a crude probe of its molecular structure.

The electronic RCB arises from a balance between short-range attraction and long-range repulsion and has been extensively studied both theoretically[20,21,23] and experimentally.[22,24] The latter has been conveniently enabled by photoelectron (PE) spectroscopy of the polyanion.[19,22,25−27] Consider a dianion, as in the case of $[ATP-H_2]^{2-}$. In the absence of photoexcited states, the RCB height shown in Figure 1a can be directly measured from an electron kinetic energy (eKE) cutoff in the PE spectrum below which a PE cannot be emitted. If an excited state of the dianion lies below the RCB but higher than the adiabatic detachment energy (ADE) of the dianion, then the excited state will be a resonance and will be metastable with respect to electron tunneling through the RCB. This scenario is shown in Figure 1a. The tunneling lifetime can be directly measured using time-resolved PE spectroscopy.[28] Moreover, the RCB is not isotropic and depends on the relative location of the charged sites with respect to the departing electron. This anisotropy can be clearly seen in the computation of the RCB and in principle can be probed experimentally through PE imaging.[29] However, to do so requires a connection between the laboratory and molecular frames of reference, as the experiment probes only the laboratory-frame PE angular distribution. Such a connection can be most conveniently attained through photoexcitation of a chromophore with a known transition dipole moment, as has been shown for a model dianion.[30] While PE spectroscopy of polyanions has been predominantly an academic curiosity, there have been some PE spectroscopic measurements on polyanionic DNA fragments.[17,31−39] In

Received: July 8, 2020
Accepted: September 4, 2020
Published: September 4, 2020

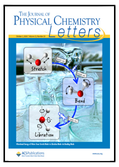

https://dx.doi.org/10.1021/acs.jpclett.0c02089
J. Phys. Chem. Lett. 2020, 11, 8195−8201

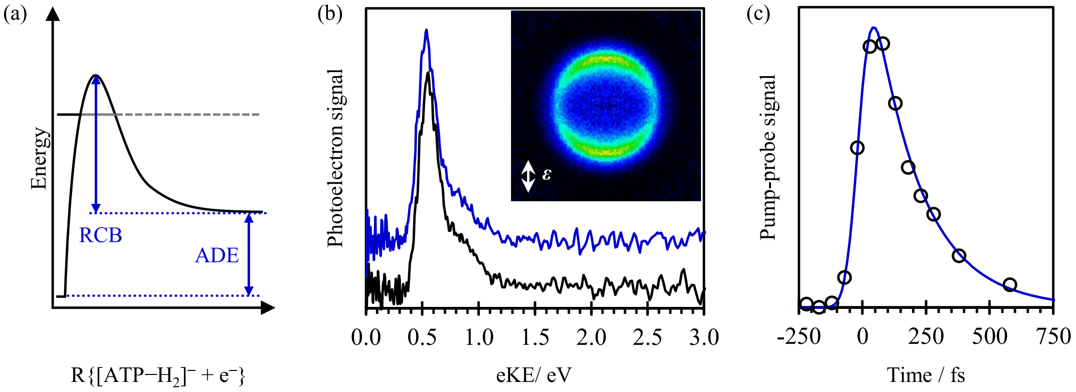

Figure 1. (a) Schematic of the repulsive Coulomb barrier (RCB), indicating its height as a function of the distance between $[ATP-H_2]^-$ and the free electron, and the adiabatic detachment energy (ADE). (b) Photoelectron spectra of $[ATP-H_2]^{2-}$ taken at 4.66 eV with femtosecond (blue) and nanosecond (black) light pulses. The inset is a photoelectron image of $[ATP-H_2]^{2-}$ taken at 4.66 eV with nanosecond light pulses, with the polarization vector, $\boldsymbol{\varepsilon}$, indicated. (c) Integrated pump−probe photoelectron signal following excitation to $^1\pi\pi^*$ states.

particular, Schinle et al.[34] performed a study of adenosine diphosphate, $[ADP-H_2]^{2-}$, and $[ATP-H_2]^{2-}$. For the latter, they observed no PE emission for excitation at 4.66 eV, although the photodetachment action spectrum by Cercola et al.[17] clearly suggests that such emission should be present. Here we observe this emission, show that it arises from resonance tunneling, and, with the aid of electronic structure calculations, reveal that photo-oxidation leads to electron emission from the amino group of adenine.

Figure 1b shows the PE spectrum of mass-selected $[ATP-H_2]^{2-}$ taken with 4.66 eV light pulses derived from either a nanosecond laser (~5 ns pulse duration) or a femtosecond laser (~80 fs pulse duration). The PE spectra using the different light sources are essentially indistinguishable and show a dominant detachment feature that peaks at eKE = 0.55 eV with a slight shoulder at higher eKE. The PE spectra were obtained from their respective PE images, an example of which is shown in the Figure 1b inset. The PE feature at eKE = 0.55 eV is correlated with the intense anisotropic inner ring. The anisotropy of this feature peaks parallel to the polarization axis of the light, $\boldsymbol{\varepsilon}$. The PE angular distribution, $I(\theta) \propto 1 + {}^1/_2\beta_2[3\cos^2(\theta) - 1]$, where θ is the angle between $\boldsymbol{\varepsilon}$ and the velocity vector of the emitted electron, can be quantified using the anisotropy parameter β_2.[40−42] For the dominant feature at eKE = 0.55 eV, $\beta_2 = +0.69 \pm 0.07$.

Schinle et al.[34] determined the adiabatic and vertical detachment energies of $[ATP-H_2]^{2-}$ to be 3.35 ± 0.11 and 4.01 ± 0.08 eV, respectively, and estimated the RCB to have a height of ~1.9 eV. Accordingly, the PE spectra in Figure 1b would arise from resonance tunneling. We verified this using time-resolved PE spectroscopy, which probed the initially excited state pumped at 4.66 eV with a 1.55 eV probe photon. The probe detaches a fraction of the excited-state population generating the electron signal at higher eKE. Concomitantly, the peak at 0.55 eV is depleted as less population is available to tunnel. The integrated time-resolved PE signal over the energy range $0.9 < \text{eKE} < 2.0$ eV, which probes the excited-state population as a function of the pump−probe delay time, t, is shown in Figure 1c, together with a fit to the data. The measured excited state lifetime is 190 ± 30 fs. This decay depends on the electron tunneling lifetime, τ_{tun}, as well as any other decay processes that may compete, such as internal conversion, which is known to be fast in adenine following excitation to the $^1\pi\pi^*$ states.[5,6] Unfortunately, the signal-to-noise ratio in the time-resolved PE spectra was insufficient to allow further data analysis. However, Cercola et al.[17] measured the relative quantum yields of electron emission and photodissociation. Assuming a simple competitive first-order kinetic model might then suggest that τ_{tun} is ~2.5 times the observed lifetime, allowing us to estimate τ_{tun} as ~475 fs.

Figure 2 shows the computed RCB for $[ATP-H_2]^- + e^-$ in the xz plane containing the adenine ring system, as shown. Details of the calculation of the RCB are given in section S1.2 in the Supporting Information, as well as a larger region of the plane (Figure S2). The loss of a π electron from adenine results in an RCB that is highest near the phosphate groups, where most of the negative charge resides. However, the potential energy is also highly structured on adenine itself. The lowest-energy saddle point of the RCB can be found at the amino group, as is more clearly shown in Figure 2b, and has a computed barrier height of 0.57 eV. Although this is different from the 1.9 eV RCB estimated by Schinle et al.,[34] caution should be applied regarding the previous PE spectrum. First, the PE spectrum by Schinle et al. was taken at a photon energy of 6.42 eV, which is likely to be resonant with excited states of not just the nucleobase but also the sugar and phosphate. It has been shown that the presence of resonances can lead to significant complications in terms of assigning the RCB from the PE spectrum.[22] Second, at a photon energy of 6.42 eV, electron emission (direct or by tunneling) can arise from several sites of $[ATP-H_2]^{2-}$, and it is not known a priori which one results in the strongest signal.[11] In the present experiment, the photon energy of 4.66 eV is resonant only with excited states localized on the nucleobase, ensuring that the electron is removed exclusively from the nucleobase.[43] In a separate experiment, we focused the femtosecond 4.66 eV light in the interaction region to obtain the two-photon resonance-enhanced PE spectrum shown in Figure 3a. This shows an onset of the eKE signal at ~5.2 eV, which yields the ADE associated with the nucleobase: $\text{ADE}_A = 2 \times 4.66 - 5.2 = 4.1$ eV. However, the highest occupied molecular orbital is also on the nucleobase, so this measured ADE_A is probably equivalent to the ADE of $[ATP-H_2]^{2-}$. The computed RCB is consistent with our measurements. Given $\tau_{tun} < 1$ ps, the resonance leading to the peak at eKE = 0.55 eV will be near the lowest RCB saddle point (as previously seen for the fluorescein dianion),[28] which is energetically close to the calculated RCB height of 0.57 eV. The RCB for a plane perpendicular to the

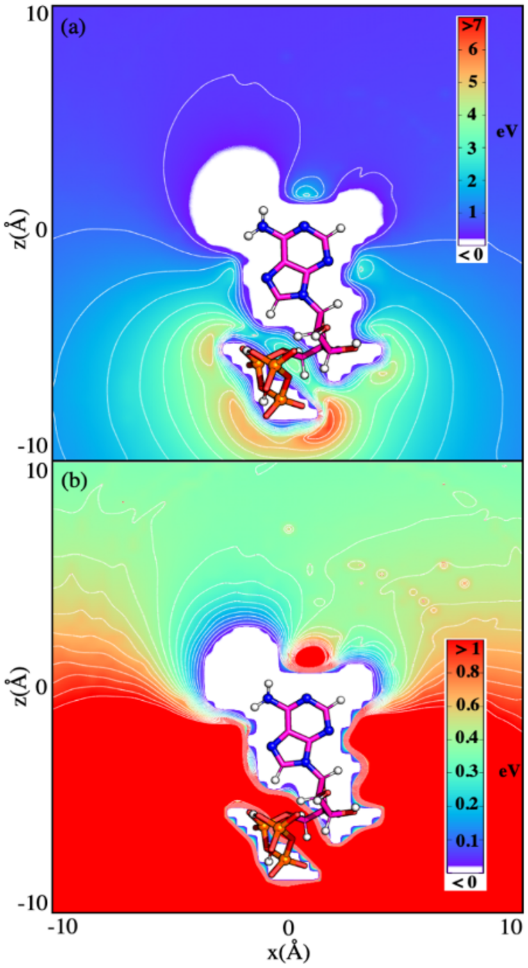

Figure 2. (a) Repulsive Coulomb barrier (RCB) for $[ATP-H_2]^- + e^-$ in the plane passing through the calculated transition dipole moment of the excitation to the $^1\pi\pi^*$ state and including the adenine ring; each contour line represents an increment of 1 eV. (b) Map scaled to a maximum RCB of 1 eV; each contour line represents an increment of 0.05 eV. The RCB maps were computed at the MP2/def2-SVP level of theory.

nucleobase was also computed (see Figure S3), but the emission barrier along the *yz* plane was found to be higher than that along the *xz* plane. While the signal at 0.55 eV is consistent with tunneling through the RCB, it may also arise from direct detachment or autodetachment from the $^1\pi\pi^*$ states. We explored these possibilities by measuring the PE spectra over a range of photon energies from 4.43 to 4.77 eV (280 to 260 nm) as shown in Figure 3b. The PE peak at eKE = 0.55 eV does not shift despite the change in $h\nu$ by 0.34 eV, which should be readily observable. This observation excludes direct detachment. Autodetachment could still be consistent, but in that case, the electron simply tunnels through a different potential barrier and does not affect the following arguments concerning the angular distributions. Finally, we briefly comment on the possibility that the peak at 0.55 eV arises from thermionic emission (i.e., statistical electron emission from the ground state of the dianion following internal conversion from the $^1\pi\pi^*$ states). After all, some ground-state recovery does take place, as shown by Cercola et al.[17] By delaying an electronic gate on the detector, we showed that all of the electron emission takes place within 100 ns, thus excluding thermionic emission, which proceeds on a much longer time scale. Moreover, the photoelectron spectrum and angular distribution would be inconsistent with such a process.

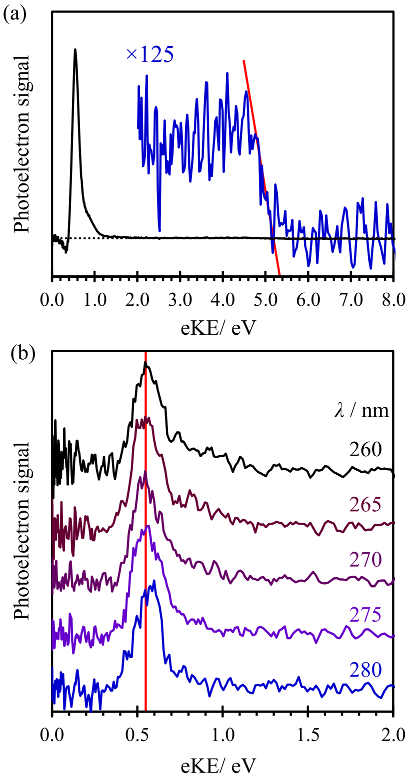

Figure 3. PE spectra of $[ATP-H_2]^{2-}$ taken with (a) focused 4.66 eV femtosecond light pulses and (b) variable-wavelength nanosecond light pulses. In (a), a resonance-enhanced two-photon photoelectron spectrum is obtained. The red line shows the high-eKE edge of the photoelectron spectrum, which intersects the zero signal (dashed line) at ~5.2 eV. In (b) the red line shows the position of 0.55 eV and highlights that the change in wavelength does not lead to a change in photoelectron spectrum of the tunneling peak.

An electron produced by tunneling will subsequently move along a trajectory determined by the RCB. Given the RCB in Figure 2a, intuition suggests that such a trajectory will avoid the high potential associated with the phosphate groups. The PE image inset in Figure 1b in principle contains this directional information. The resonance initially excited on the nucleobase involves the optically bright states of adenine, the $^1\pi\pi^*$ states.[44−46] Our calculations show that the transition with the highest oscillator strength is of this character (for details, see the Supporting Information). Upon excitation with linearly polarized light of polarization $\boldsymbol{\varepsilon}$, only those $[ATP-H_2]^{2-}$ molecules within a $\cos^2 \varphi$ distribution will be excited, where φ is the angle between $\boldsymbol{\varepsilon}$ and the transition dipole moment (TDM). In Figure 2, $[ATP-H_2]^{2-}$ has been aligned in such a way that the vertical axis (z) is aligned with the TDM of the brightest transition. Hence, from Figure 2 we anticipate that the PE will be emitted predominantly parallel to $\boldsymbol{\varepsilon}$. This is consistent with the PE image in Figure 1b and its positive β_2 value.

In principle, one could simulate the emission using classical molecular dynamics (MD) of an electron under the influence of the RCB.[47] However, we refrained from performing such a simulation here because there are several factors that would undermine such a quantitative prediction and potentially even the qualitative reasoning provided thus far. First, the ions are

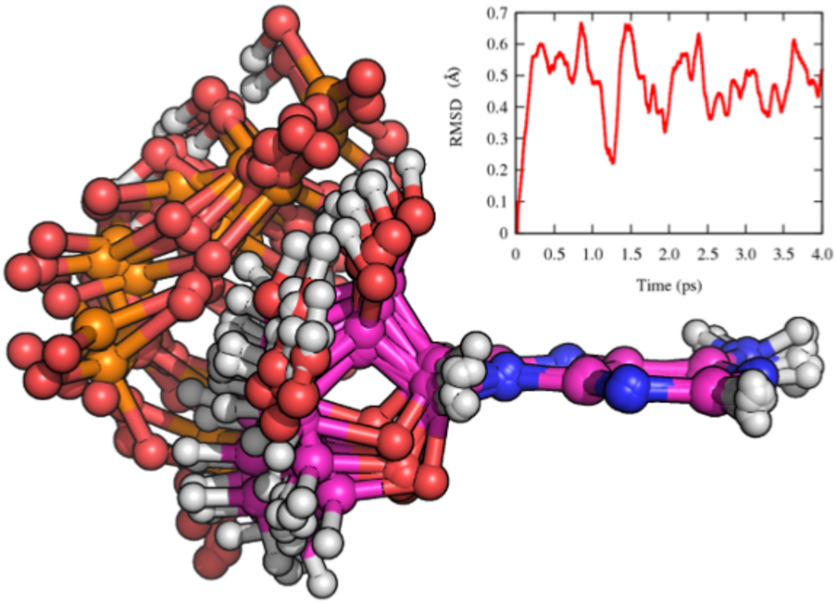

Figure 4. Superimposition of 10 equidistant (every 100 fs) $[ATP-H_2]^{2-}$ geometries along the first picosecond of the ab initio molecular dynamics simulation. The inset shows the root-mean-square deviation (RMSD) calculated along the 4 ps ground-state dynamical trajectory.

thermalized at ~300 K, and therefore, rotational motion of $[ATP-H_2]^{2-}$ could blur the alignment.[30] On the basis of the computed rotational constants, the rotational dephasing time[48] of $[ATP-H_2]^{2-}$ at 300 K is 5 ps, which exceeds τ_{tun} by at least 1 order of magnitude. Hence, rotational motion will not be a significant factor. Second, at ~300 K a number of isomers could be present in the gas-phase sample. Infrared multiphoton dissociation experiments and calculations show that $[ATP-H_2]^{2-}$ is predominantly $\alpha\beta$ deprotonated and that it forms an intramolecular hydrogen bond between the β phosphate and a neighboring oxygen atom.[15,16,34] Third, even if a single dominant isomer were present, significant thermal motion could be associated with the phosphates, which could lead to dramatic changes in the RCB. Figure 4 presents the results of a ground-state ab initio molecular dynamics simulation over 4 ps (for details, see section S1.3). This shows the conformational flexibility of $[ATP-H_2]^{2-}$ around the minimum-energy structure. The inset shows the root-mean-square deviation (RMSD) calculated along the simulation time. While the phosphates clearly move, their locations relative to the adenine remain quite similar, and therefore, this motion does not qualitatively affect the RCB or the angular distribution of the emitted electrons. Fourth, as demonstrated by the results of Cercola et al.,[17] excited-state dynamics competes with tunneling. On the ground-state potential energy surface, $[ATP-H_2]^{2-}$ dissociates rather than losing an electron,[17] so this cannot contribute to the PE signal. However, substantial nuclear motion clearly takes place in the $^1\pi\pi^*$ states, and $^1n\pi^*$ states may also be involved in the decay mechanism.[46,49−51] The nuclear dynamics likely does not have a major impact on the photoelectron angular distribution because the positions of the phosphates relative to the nucleobase do not change significantly over the time scale of the dynamics (the lifetime is 190 fs). The electronic dynamics, on the other hand, will alter the relevant molecular orbitals that should be considered. For example, in the case of a $^1n\pi^*$ state, the orbital from which the electron is removed will differ, as will the final states in $[ATP-H_2]^{-}$. The former could be taken into account by calculating the RCB for loss of an electron from the nonbonded orbital located on the amino nitrogen atom. The consequence of this should be reflected in a different final eKE of the emitted electron. It should be noted that Figures 1b and 3b show a shoulder to higher eKE, which also has a slightly reduced anisotropy (β_2 = +0.48 ± 0.33, where the much larger error reflects the reduced signal intensity). This feature could be consistent with emission from the $^1n\pi^*$ state, although there would also be a different RCB associated with such a process and thus a different lifetime, which was not seen in the experiment; we stress that the data are not of sufficient quality at present to be assertive on this conclusion. Alternatively, the shoulder could also arise from hot bands and/or different isomers or from direct and/or autodetachment. It is interesting to notice that in Figure 3b, the shoulder appears to become more prominent as $h\nu$ increases. This observation is very reminiscent of the behavior in the fluorescein dianion,[28] where direct detachment contributes once the lowest saddle point of the RCB is surpassed.

The above discussion shows that MD simulations would provide only limited added insight. In any case, such simulations would only be feasible if a high level of approximation (e.g., no conformational space investigation, low-dimensional analytical potentials, low accuracy) were considered, which in turn would lower the significance of any quantitative results. Despite the complications highlighted above, we can conclude that following photoexcitation to the $^1\pi\pi^*$ states, resonance tunneling in $[ATP-H_2]^{2-}$ is qualitatively consistent with emission from the amino group of adenine. Moreover, it provides a crude structural measure of isolated $[ATP-H_2]^{2-}$ by showing that the negative charges are located on phosphate groups and that these are located around the sugar. This latter observation is in agreement with IR multiphoton dissociation spectra of $[ATP-H_2]^{2-}$ and computational work.[15,16,34] Tunneling detachment from the amino groups is expected to result in a β_2 that approaches +2. The reduced value observed here likely arises from the fact that the phosphate lies out of the *xz* plane (Figure 4), which imposes a Coulombic force on the outgoing electron along the y axis, thus reducing the overall anisotropy observed experimentally.

The above observations of electron tunneling following photoexcitation of adenine in a polyanionic system potentially offer some insight into the photoemission observed in larger DNA complexes studied by the Gabelica and Dugourd groups.[18,31−33] Specifically, they studied polyanions of 6- and 20-mer single strands and 12 base pair double strands[31,32] as well as a four-tetrad G-quadruplex.[33] A general conclusion of their work is that only the purine nucleobases (adenine and guanine) appear to show enhanced electron emission compared with dissociation: for a homobase 6-mer single strand, this was observed over the $^1\pi\pi^*$ absorption band regardless of charge state (from −2 to −4).[18] The Kappes group also measured the PE spectra at 4.66 eV for the −3 charge state of the homobase 6-mer single strands.[37] However, these are difficult to interpret without knowledge of which features arise from direct detachment and which arise from tunneling. It should be noted that even if a resonance is above the RCB saddle point, it may still be subject to emission by tunneling, as shown for the fluorescein dianion[28] and the bisdisulizole tetraanion.[27] Very recently, Daly et al. showed that electron circular dichroism can be observed for chiral DNA strands.[39] Here we have shown that tunneling may be efficient in DNA fragments and that PE imaging may offer some insight into the emission process.

Our method provides a new route to understanding the photo-oxidation sites and overall structures of polyanions. Looking ahead, reducing the internal temperature of $[\mathrm{ATP{-}H_2}]^{2-}$ using cryogenic ion traps will provide a more controlled environment[52,53] and may enable quantitative determination of the emission process. A computational perspective on the excited-state dynamics of the molecule may in the end allow a complete picture of the photo-oxidation of this molecule to be obtained.

EXPERIMENTAL AND COMPUTATIONAL DETAILS

The details of the TR-PEI instrument can be found elsewhere.[54,55] An ∼1 mM methanolic solution of adenosine-5′-triphosphate disodium salt (Sigma-Aldrich), was pushed through a syringe and introduced into the first vacuum region through a capillary. A potential gradient led the ions through a series of ring-electrode ion guides until they reached a pulsed ion trap. Ions were ejected and focused into a collinear Wiley−McLaren time-of-flight mass spectrometer[56] at 10 Hz. At the focus of the mass spectrometer, a mass-selected ion packet was irradiated with laser pulses either from a commercial Ti:sapphire laser (producing femtosecond pulses) or a Nd:YAG-pumped optical parametric oscillator (producing nanosecond pulses). For time-resolved measurements, the third harmonic of the fundamental at 1.55 eV was used as a pump pulse and the fundamental as a probe pulse. The time resolution of the experiment was ∼100 fs. Following the interaction of the light with the ion packet, emitted photoelectrons were collected and imaged by a perpendicular velocity map imaging arrangement.[57] A 300 ns electronic gate was applied to the microchannel plates so that only signal over this window was collected. PE spectra were obtained from the PE images using polar onion peeling.[58] The PE images were calibrated using the well-known PE image of $\mathrm{I^-}$. The spectral resolution was approximately ∼5% of the kinetic energy.

$[\mathrm{ATP{-}H_2}]^{2-}$ was optimized with Møller−Plesset second-order perturbation theory using the resolution of identity approximation (RI-MP2)[59] and the def2-TZVP basis set.[60] The ground-state energy was then refined with the def2-QZVP[60] basis set. The first five excitation energies were obtained with the algebraic diagrammatic construction scheme for the polarization propagator at second order (ADC(2))[61] method and the same def2-QZVP[60] basis set. The RCB was calculated using the local static approximation model,[62] in which the energy of the monoanion plus a point-charge electron (in the geometry of $[\mathrm{ATP{-}H_2}]^{2-}$) was calculated with an interval of 0.5 Å. Two planes (xz and yz) that pass through the transition dipole moment vector connecting the S_0 and S_2 states were considered. RCB calculations were performed at the MP2/def2-SVP level of theory. Ground-state ab initio molecular dynamics calculations were carried out at the B3LYP[63,64]/aug-cc-pVDZ[65] level of theory starting from the $[\mathrm{ATP{-}H_2}]^{2-}$ minimum-energy geometry. Further computational details are given in the Supporting Information.

ASSOCIATED CONTENT

Supporting Information

The Supporting Information is available free of charge at https://pubs.acs.org/doi/10.1021/acs.jpclett.0c02089.

> Computational details and results of calculations on ground-state optimized structure and excited states, the repulsive Coulomb barrier, and ab initio molecular dynamics (PDF)

AUTHOR INFORMATION

Corresponding Authors

Leticia González − *Institute of Theoretical Chemistry, Faculty of Chemistry, University of Vienna, 1090 Vienna, Austria;* orcid.org/0000-0001-5112-794X; Email: leticia.gonzalez@univie.ac.at

Jan R. R. Verlet − *Department of Chemistry, Durham University, Durham DH1 3LE, United Kingdom;* orcid.org/0000-0002-9480-432X; Email: j.r.r.verlet@durham.ac.uk

Authors

Maria Elena Castellani − *Department of Chemistry, Durham University, Durham DH1 3LE, United Kingdom*

Davide Avagliano − *Institute of Theoretical Chemistry, Faculty of Chemistry, University of Vienna, 1090 Vienna, Austria*

Complete contact information is available at: https://pubs.acs.org/10.1021/acs.jpclett.0c02089

Author Contributions

[§]M.E.C. and D.A. contributed equally.

Notes

The authors declare no competing financial interest.

ACKNOWLEDGMENTS

This project has received funding from the European Union's Horizon 2020 Research and Innovation Programme under the Marie Skłodowska-Curie Grant Agreement 765266 (LightDyNAmics). D.A. and L.G. thank the University of Vienna and the Vienna Scientific Cluster (VSC) for allocation of computational resources.

REFERENCES

(1) Bruice, P. Y. *Essential Organic Chemistry*, 3rd ed.; Pearson: Upper Saddle River, NJ, 2016.

(2) McMurry, J.; Begley, T. P. *The Organic Chemistry of Biological Pathways*, 2nd ed.; Roberts and Company Publishers: Greenwood Village, CO, 2016.

(3) Stavros, V. G.; Verlet, J. R. R. Gas-Phase Femtosecond Particle Spectroscopy: A Bottom-Up Approach to Nucleotide Dynamics. *Annu. Rev. Phys. Chem.* **2016**, *67* (1), 211−232.

(4) Weber, J. M.; Marcum, J.; Nielsen, S. B. UV Photophysics of DNA and RNA Nucleotides In Vacuo: Dissociation Channels, Time Scales, and Electronic Spectra. In *Photophysics of Ionic Biochromophores*; Brøndsted Nielsen, S., Wyer, J. A., Eds.; Springer: Berlin, 2013; pp 181−207.

(5) Satzger, H.; Townsend, D.; Zgierski, M. Z.; Patchkovskii, S.; Ullrich, S.; Stolow, A. Primary processes underlying the photostability of isolated DNA bases: Adenine. *Proc. Natl. Acad. Sci. U. S. A.* **2006**, *103* (27), 10196−10201.

(6) Bisgaard, C. Z.; Satzger, H.; Ullrich, S.; Stolow, A. Excited-State Dynamics of Isolated DNA Bases: A Case Study of Adenine. *ChemPhysChem* **2009**, *10* (1), 101−110.

(7) Wells, K. L.; Hadden, D. J.; Nix, M. G. D.; Stavros, V. G. Competing $\pi\sigma^*$ States in the Photodissociation of Adenine. *J. Phys. Chem. Lett.* **2010**, *1* (6), 993−996.

(8) Mai, S.; Richter, M.; Marquetand, P.; González, L. Excitation of Nucleobases from a Computational Perspective II: Dynamics. In *Photoinduced Phenomena in Nucleic Acids I: Nucleobases in the Gas Phase and in Solvents*; Barbatti, M., Borin, A. C., Ullrich, S., Eds.; Springer: Cham, Switzerland, 2015; pp 99−153.

(9) Chatterley, A. S.; West, C. W.; Stavros, V. G.; Verlet, J. R. R. Time-resolved photoelectron imaging of the isolated deprotonated nucleotides. *Chem. Sci.* **2014**, *5* (10), 3963−3975.

(10) Chatterley, A. S.; West, C. W.; Roberts, G. M.; Stavros, V. G.; Verlet, J. R. R. Mapping the Ultrafast Dynamics of Adenine onto Its Nucleotide and Oligonucleotides by Time-Resolved Photoelectron Imaging. *J. Phys. Chem. Lett.* **2014**, *5* (5), 843−848.

(11) Yang, X.; Wang, X.-B.; Vorpagel, E. R.; Wang, L.-S. Direct experimental observation of the low ionization potentials of guanine in free oligonucleotides by using photoelectron spectroscopy. *Proc. Natl. Acad. Sci. U. S. A.* **2004**, *101* (51), 17588−17592.

(12) Parker, A. W.; Quinn, S. J. Infrared Spectroscopy of DNA. In *Encyclopedia of Biophysics*; Roberts, G. C. K., Ed.; Springer: Berlin, 2013; pp 1065−1074.

(13) Keane, P. M.; Baptista, F. R.; Gurung, S. P.; Devereux, S. J.; Sazanovich, I. V.; Towrie, M.; Brazier, J. A.; Cardin, C. J.; Kelly, J. M.; Quinn, S. J. Long-Lived Excited-State Dynamics of i-Motif Structures Probed by Time-Resolved Infrared Spectroscopy. *ChemPhysChem* **2016**, *17* (9), 1281−1287.

(14) Hall, J. P.; Poynton, F. E.; Keane, P. M.; Gurung, S. P.; Brazier, J. A.; Cardin, D. J.; Winter, G.; Gunnlaugsson, T.; Sazanovich, I. V.; Towrie, M.; Cardin, C. J.; Kelly, J. M.; Quinn, S. J. Monitoring one-electron photo-oxidation of guanine in DNA crystals using ultrafast infrared spectroscopy. *Nat. Chem.* **2015**, *7* (12), 961−967.

(15) Ligare, M. R.; Rijs, A. M.; Berden, G.; Kabeláč, M.; Nachtigallova, D.; Oomens, J.; de Vries, M. S. Resonant Infrared Multiple Photon Dissociation Spectroscopy of Anionic Nucleotide Monophosphate Clusters. *J. Phys. Chem. B* **2015**, *119* (25), 7894−7901.

(16) van Outersterp, R. E.; Martens, J.; Berden, G.; Steill, J. D.; Oomens, J.; Rijs, A. M. Structural characterization of nucleotide 5′-triphosphates by infrared ion spectroscopy and theoretical studies. *Phys. Chem. Chem. Phys.* **2018**, *20* (44), 28319−28330.

(17) Cercola, R.; Matthews, E.; Dessent, C. E. H. Photoexcitation of Adenosine 5′-Triphosphate Anions in Vacuo: Probing the Influence of Charge State on the UV Photophysics of Adenine. *J. Phys. Chem. B* **2017**, *121* (22), 5553−5561.

(18) Daly, S.; Porrini, M.; Rosu, F.; Gabelica, V. Electronic spectroscopy of isolated DNA polyanions. *Faraday Discuss.* **2019**, *217* (0), 361−382.

(19) Wang, X.-B.; Ding, C.-F.; Wang, L.-S. Photodetachment Spectroscopy of a Doubly Charged Anion: Direct Observation of the Repulsive Coulomb Barrier. *Phys. Rev. Lett.* **1998**, *81*, 3351−3354.

(20) Simons, J. Molecular Anions. *J. Phys. Chem. A* **2008**, *112* (29), 6401−6511.

(21) Dreuw, A.; Cederbaum, L. S. Multiply Charged Anions in the Gas Phase. *Chem. Rev.* **2002**, *102* (1), 181−200.

(22) Verlet, J. R. R.; Horke, D. A.; Chatterley, A. S. Excited states of multiply-charged anions probed by photoelectron imaging: riding the repulsive Coulomb barrier. *Phys. Chem. Chem. Phys.* **2014**, *16* (29), 15043−15052.

(23) Scheller, M. K.; Compton, R. N.; Cederbaum, L. S. Gas-Phase Multiply Charged Anions. *Science* **1995**, *270* (5239), 1160−1166.

(24) Wang, L.-S.; Wang, X.-B. Probing Free Multiply Charged Anions Using Photodetachment Photoelectron Spectroscopy. *J. Phys. Chem. A* **2000**, *104* (10), 1978−1990.

(25) Wang, X.-B.; Wang, L.-S. Observation of negative electron-binding energy in a molecule. *Nature* **1999**, *400* (6741), 245−248.

(26) Wang, X.-B.; Woo, H.-K.; Huang, X.; Kappes, M. M.; Wang, L.-S. Direct Experimental Probe of the On-Site Coulomb Repulsion in the Doubly Charged Fullerene Anion C_{70}^{2-}. *Phys. Rev. Lett.* **2006**, *96* (14), 143002.

(27) Dau, P. D.; Liu, H.-T.; Yang, J.-P.; Winghart, M.-O.; Wolf, T. J. A.; Unterreiner, A.-N.; Weis, P.; Miao, Y.-R.; Ning, C.-G.; Kappes, M. M.; Wang, L.-S. Resonant tunneling through the repulsive Coulomb barrier of a quadruply charged molecular anion. *Phys. Rev. A: At., Mol., Opt. Phys.* **2012**, *85* (6), No. 064503.

(28) Horke, D. A.; Chatterley, A. S.; Verlet, J. R. Effect of internal energy on the repulsive Coulomb barrier of polyanions. *Phys. Rev. Lett.* **2012**, *108* (8), No. 083003.

(29) Xing, X.-P.; Wang, X.-B.; Wang, L.-S. Photoelectron imaging of multiply charged anions: Effects of intramolecular Coulomb repulsion and photoelectron kinetic energies on photoelectron angular distributions. *J. Chem. Phys.* **2009**, *130* (7), No. 074301.

(30) Horke, D. A.; Chatterley, A. S.; Verlet, J. R. R. Femtosecond Photoelectron Imaging of Aligned Polyanions: Probing Molecular Dynamics through the Electron−Anion Coulomb Repulsion. *J. Phys. Chem. Lett.* **2012**, *3* (7), 834−838.

(31) Gabelica, V.; Tabarin, T.; Antoine, R.; Rosu, F.; Compagnon, I.; Broyer, M.; De Pauw, E.; Dugourd, P. Electron photodetachment dissociation of DNA polyanions in a quadrupole ion trap mass spectrometer. *Anal. Chem.* **2006**, *78* (18), 6564−72.

(32) Gabelica, V.; Rosu, F.; Tabarin, T.; Kinet, C.; Antoine, R.; Broyer, M.; De Pauw, E.; Dugourd, P. Base-dependent electron photodetachment from negatively charged DNA strands upon 260-nm laser irradiation. *J. Am. Chem. Soc.* **2007**, *129* (15), 4706−13.

(33) Rosu, F.; Gabelica, V.; De Pauw, E.; Antoine, R.; Broyer, M.; Dugourd, P. UV spectroscopy of DNA duplex and quadruplex structures in the gas phase. *J. Phys. Chem. A* **2012**, *116* (22), 5383−91.

(34) Schinle, F.; Crider, P. E.; Vonderach, M.; Weis, P.; Hampe, O.; Kappes, M. M. Spectroscopic and theoretical investigations of adenosine 5′-diphosphate and adenosine 5′-triphosphate dianions in the gas phase. *Phys. Chem. Chem. Phys.* **2013**, *15* (18), 6640−50.

(35) Burke, R. M.; Dessent, C. E. H. Effect of Cation Complexation on the Structure of a Conformationally Flexible Multiply Charged Anion: Stabilization of Excess Charge in the Na+·Adenosine 5′-Triphosphate Dianion Ion-Pair Complex. *J. Phys. Chem. A* **2009**, *113* (12), 2683−2692.

(36) Burke, R. M.; Pearce, J. K.; Boxford, W. E.; Bruckmann, A.; Dessent, C. E. H. Stabilization of Excess Charge in Isolated Adenosine 5‘-Triphosphate and Adenosine 5‘-Diphosphate Multiply and Singly Charged Anions. *J. Phys. Chem. A* **2005**, *109* (43), 9775−9785.

(37) Vonderach, M.; Ehrler, O. T.; Matheis, K.; Weis, P.; Kappes, M. M. Isomer-Selected Photoelectron Spectroscopy of Isolated DNA Oligonucleotides: Phosphate and Nucleobase Deprotonation at High Negative Charge States. *J. Am. Chem. Soc.* **2012**, *134* (18), 7830−7841.

(38) Weber, J. M.; Ioffe, I. N.; Berndt, K. M.; Löffler, D.; Friedrich, J.; Ehrler, O. T.; Danell, A. S.; Parks, J. H.; Kappes, M. M. Photoelectron Spectroscopy of Isolated Multiply Negatively Charged Oligonucleotides. *J. Am. Chem. Soc.* **2004**, *126* (27), 8585−8589.

(39) Daly, S.; Rosu, F.; Gabelica, V. Mass-resolved electronic circular dichroism ion spectroscopy. *Science* **2020**, *368* (6498), 1465−1468.

(40) Reid, K. L. Photoelectron angular distributions. *Annu. Rev. Phys. Chem.* **2003**, *54*, 397−424.

(41) Cooper, J.; Zare, R. N. Angular Distribution of Photoelectrons. *J. Chem. Phys.* **1968**, *48* (2), 942−943.

(42) Cooper, J.; Zare, R. N. Erratum: Angular Distribution of Photoelectrons. *J. Chem. Phys.* **1968**, *49* (9), 4252−4252.

(43) Chatterley, A. S.; Johns, A. S.; Stavros, V. G.; Verlet, J. R. R. Base-Specific Ionization of Deprotonated Nucleotides by Resonance Enhanced Two-Photon Detachment. *J. Phys. Chem. A* **2013**, *117* (25), 5299−5305.

(44) Santoro, F.; Improta, R.; Fahleson, T.; Kauczor, J.; Norman, P.; Coriani, S. Relative Stability of the La and Lb Excited States in Adenine and Guanine: Direct Evidence from TD-DFT Calculations of MCD Spectra. *J. Phys. Chem. Lett.* **2014**, *5* (11), 1806−1811.

(45) Serrano-Andrés, L.; Merchán, M.; Borin, A. C. A Three-State Model for the Photophysics of Adenine. *Chem. - Eur. J.* **2006**, *12* (25), 6559−6571.

(46) Conti, I.; Garavelli, M.; Orlandi, G. Deciphering Low Energy Deactivation Channels in Adenine. *J. Am. Chem. Soc.* **2009**, *131* (44), 16108−16118.

(47) West, C. W.; Bull, J. N.; Woods, D. A.; Verlet, J. R. R. Photoelectron imaging as a probe of the repulsive Coulomb barrier in the photodetachment of antimony tartrate dianions. *Chem. Phys. Lett.* **2016**, *645*, 138−143.

(48) Blokhin, A. P.; Gelin, M. F.; Khoroshilov, E. V.; Kryukov, I. V.; Sharkov, A. V. Dynamics of optically induced anisotropy in an ensemble of asymmetric top molecules in the gas phase. *Opt. Spectrosc.* **2003**, *95* (3), 346−352.

(49) Conti, I.; Nenov, A.; Höfinger, S.; Flavio Altavilla, S.; Rivalta, I.; Dumont, E.; Orlandi, G.; Garavelli, M. Excited state evolution of DNA stacked adenines resolved at the CASPT2//CASSCF/Amber level: from the bright to the excimer state and back. *Phys. Chem. Chem. Phys.* **2015**, *17* (11), 7291−7302.

(50) Conti, I.; Di Donato, E.; Negri, F.; Orlandi, G. Revealing Excited State Interactions by Quantum-Chemical Modeling of Vibronic Activities: The R2PI Spectrum of Adenine. *J. Phys. Chem. A* **2009**, *113* (52), 15265−15275.

(51) Picconi, D.; Avila Ferrer, F. J.; Improta, R.; Lami, A.; Santoro, F. Quantum-classical effective-modes dynamics of the $\pi\pi^* \rightarrow n\pi^*$ decay in 9H-adenine. A quadratic vibronic coupling model. *Faraday Discuss.* **2013**, *163* (0), 223−242.

(52) Wang, X. B.; Wang, L. S. Development of a low-temperature photoelectron spectroscopy instrument using an electrospray ion source and a cryogenically controlled ion trap. *Rev. Sci. Instrum.* **2008**, *79* (7), No. 073108.

(53) Garand, E. Spectroscopy of Reactive Complexes and Solvated Clusters: A Bottom-Up Approach Using Cryogenic Ion Traps. *J. Phys. Chem. A* **2018**, *122* (32), 6479−6490.

(54) Lecointre, J.; Roberts, G. M.; Horke, D. A.; Verlet, J. R. R. Ultrafast Relaxation Dynamics Observed Through Time-Resolved Photoelectron Angular Distributions. *J. Phys. Chem. A* **2010**, *114* (42), 11216−11224.

(55) Stanley, L. H.; Anstöter, C. S.; Verlet, J. R. R. Resonances of the anthracenyl anion probed by frequency-resolved photoelectron imaging of collision-induced dissociated anthracene carboxylic acid. *Chem. Sci.* **2017**, *8* (4), 3054−3061.

(56) Wiley, W. C.; McLaren, I. H. Time-of-Flight Mass Spectrometer with Improved Resolution. *Rev. Sci. Instrum.* **1955**, *26* (12), 1150−1157.

(57) Horke, D. A.; Roberts, G. M.; Lecointre, J.; Verlet, J. R. R. Velocity-map imaging at low extraction fields. *Rev. Sci. Instrum.* **2012**, *83* (6), No. 063101.

(58) Roberts, G. M.; Nixon, J. L.; Lecointre, J.; Wrede, E.; Verlet, J. R. R. Toward real-time charged-particle image reconstruction using polar onion-peeling. *Rev. Sci. Instrum.* **2009**, *80* (5), No. 053104.

(59) Weigend, F.; Häser, M. RI-MP2: first derivatives and global consistency. *Theor. Chem. Acc.* **1997**, *97* (1), 331−340.

(60) Weigend, F. Accurate Coulomb-fitting basis sets for H to Rn. *Phys. Chem. Chem. Phys.* **2006**, *8* (9), 1057−1065.

(61) Dreuw, A.; Wormit, M. The algebraic diagrammatic construction scheme for the polarization propagator for the calculation of excited states. *Wiley Interdiscip. Rev. Comput. Mol. Sci.* **2015**, *5* (1), 82−95.

(62) Dreuw, A.; Cederbaum, L. S. Erratum: Nature of the repulsive Coulomb barrier in multiply charged negative ions [Phys. Rev. A 63, 012501 (2000)]. *Phys. Rev. A: At., Mol., Opt. Phys.* **2001**, *63* (4), No. 049904.

(63) Becke, A. D. Density-functional thermochemistry. III. The role of exact exchange. *J. Chem. Phys.* **1993**, *98* (7), 5648−5652.

(64) Lee, C.; Yang, W.; Parr, R. G. Development of the Colle-Salvetti correlation-energy formula into a functional of the electron density. *Phys. Rev. B: Condens. Matter Mater. Phys.* **1988**, *37* (2), 785−789.

(65) Kendall, R. A.; Dunning, T. H., Jr.; Harrison, R. J. Electron affinities of the first-row atoms revisited. Systematic basis sets and wave functions. *J. Chem. Phys.* **1992**, *96* (9), 6796−6806.

THE JOURNAL OF PHYSICAL CHEMISTRY A
A JOURNAL OF THE AMERICAN CHEMICAL SOCIETY

pubs.acs.org/JPCA Article

Ultrafast Dynamics of the Isolated Adenosine-5′-triphosphate Dianion Probed by Time-Resolved Photoelectron Imaging

Published as part of The Journal of Physical Chemistry virtual special issue "Daniel Neumark Festschrift".

Maria Elena Castellani, Davide Avagliano, and Jan R. R. Verlet*

Cite This: *J. Phys. Chem. A* 2021, 125, 3646−3652 Read Online

ACCESS | Metrics & More | Article Recommendations

ABSTRACT: The excited state dynamics of the doubly deprotonated dianion of adenosine-5′-triphosphate, $[ATP{-}H_2]^{2-}$, has been spectroscopically explored by time-resolved photoelectron spectroscopy following excitation at 4.66 eV. Time-resolved photoelectron spectra show that two competing processes occur for the initially populated $^1\pi\pi^*$ state. The first is rapid electron emission by tunneling through a repulsive Coulomb barrier as the $^1\pi\pi^*$ state is a resonance. The second is nuclear motion on the $^1\pi\pi^*$ state surface leading to an intermediate that no longer tunnels and subsequently decays by internal conversion to the ground electronic state. The spectral signatures of the features are similar to those observed for other adenine-derivatives, suggesting that this nucleobase is quite insensitive to the nearby negative charges localized on the phosphates, except of course for the appearance of the additional electron tunneling channel, which is open in the dianion.

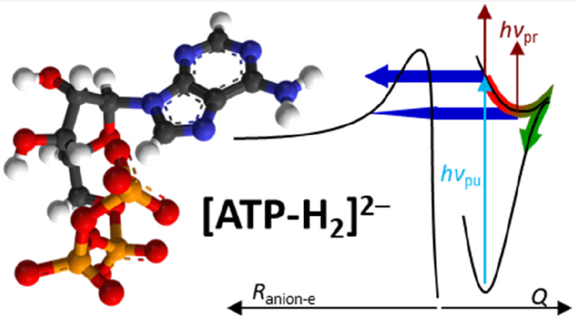

■ INTRODUCTION

DNA, together with its building-blocks and derivatives, represents one of the most important molecules of biological interest.[1] DNA has a high stability imparted by hydrogen bonding and π-stacking such that it is chemically unreactive. However, DNA can undergo significant damage when exposed to radiation or oxidizing agents.[2,3] Specifically, photo-oxidative damage represents one of the major causes of stress for the nucleobases, which can easily absorb ultraviolet light via their optically bright $^1\pi\pi^*$ states.[3] Despite this, the photoinduced damage quantum yield of DNA is less than 1%. This intrinsic photostability of the nucleobases arises from their nonradiative decay mechanisms.[4,5] Consequently, there has been extensive experimental as well as theoretical work aimed at understanding the relaxation pathways of nucleobases following UV excitation. Adenine in particular has been the focus of much research, especially through gas-phase spectroscopy,[6,7] where it has been studied as an isolated nucleobase,[8−11] but also as part of more complex structures, such as nucleotides and oligonucleotides.[12−15]

Adenosine-5′-triphosphate (ATP) is one of the most important adenine derivatives because of its pivotal role in intramolecular energy transfer. Due to the presence of three phosphate groups, ATP is generally negatively charged, which can in principle affect its photophysics. In the gas-phase, for example, the doubly deprotonated form of ATP, $[ATP{-}H_2]^{2-}$, is most readily generated by electrospray ionization. Isolated dianions like $[ATP{-}H_2]^{2-}$ (and polyanions more generally) have a repulsive Coulomb barrier (RCB)[16−19] that comes about from a balance between the long-range repulsive interaction between an electron and the monoanion and the short-range attraction that forms the dianion. The RCB can be conveniently studied using photoelectron spectroscopy as the outgoing electron is naturally sensitive to the RCB and represents a barrier that needs to be overcome in order to successfully detach an electron from the molecule. From an electronic structure perspective, excited states of the dianion can lie above the adiabatic detachment energy (ADE) but below the RCB threshold. This therefore renders the excited state a resonance that is metastable toward electron tunneling through the RCB. The RCB has been the focus of multiple theoretical[17,18,20] and experimental studies.[19,21] In particular, photoelectron spectroscopy and, more specifically, photoelectron imaging, have emerged as useful tools to probe the photophysics of multiply charged anionic species.[16,19,22−27]

Anionic DNA fragments and derivatives have been the subject of multiple spectroscopy studies in the past.[12−15,25,28−38] Specifically, $[ATP{-}H_2]^{2-}$ has been probed

Received: February 23, 2021
Revised: April 12, 2021
Published: April 22, 2021

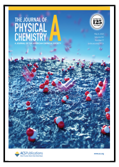

https://doi.org/10.1021/acs.jpca.1c01646

by the Kappes group[31] and the Dessent group,[34] using photoelectron and photodetachment action spectroscopy, respectively. We recently added to this work[13] using photoelectron imaging. Following excitation of $[ATP-H_2]^{2-}$ with 4.66 eV light, we observed electron emission from the $^1\pi\pi^*$ states on the nucleobase. The emission was directional and, in combination with theory, we could correlate this directionality to the shape of the RCB, which peaks strongly around the negatively charged phosphates. We also provided evidence that the emission arose from electron tunneling through the RCB. That is to say that the $^1\pi\pi^*$ state excited at 4.66 eV in $[ATP-H_2]^{2-}$ is a resonance. Part of this evidence was produced using time-resolved photoelectron yield measurements. Here, we add to our previous study, and we report on the time-resolved photoelectron spectra. This allows us to spectroscopically distinguish between electron tunneling and nuclear dynamics on the excited $^1\pi\pi^*$ state, which ultimately leads to internal conversion back to the ground electronic state of $[ATP-H_2]^{2-}$. It also serves as a comparison between the $^1\pi\pi^*$ state dynamics in $[ATP-H_2]^{2-}$ and in deoxyadenosine monophosphate ($dAMP^-$)[12,39] and bare adenine (Ade).[8−10,38,40−49]

METHODS

The details of the anion photoelectron imaging instrument are reported elsewhere.[50,51] $[ATP-H_2]^{2-}$ anions were generated by electrospray ionization (ESI) of a ∼ 1 mM methanolic solution of adenosine-5′-triphosphate disodium salt (Sigma-Aldrich, U.K.) and introduced in the first vacuum region of the instrument. The negative ions were subsequently guided by a potential gradient through a series of ring-electrode ion guides, which culminated in a pulsed ion trap. Ions were ejected and focused into a colinear Wiley−McLaren time-of-flight mass spectrometer[52] operating at 100 Hz. At the focus of the mass-spectrometer, a mass-selected ion packet was intersected with laser pulses obtained from a commercial Ti:sapphire laser (Spectra Physics). The fundamental at 1.55 eV was used as a probe pulse. Its third harmonic at 4.66 eV served as the pump pulse and was generated by frequency doubling in a BBO (type I) crystal followed by a calcite plate, a half-waveplate, and a second BBO (type I) crystal to mix the fundamental and second harmonic. Pump and probe pulses we delayed with respect to each other using a motorized delay stage. The time-resolution in the interaction region was ∼100 fs. Upon irradiation of the ion packet, the ejected photoelectrons were collected and imaged by a perpendicular velocity-map imaging (VMI) arrangement.[53] Photoelectron spectra were extracted from the raw images using onion peeling in polar coordinates.[54] The photoelectron spectrum of I^- was used to calibrate the VMI spectrometer. The spectral resolution was approximately ∼5% of the electron kinetic energy, eKE.

The pump light at 4.66 eV is sufficiently high in energy to cause significant noise from photons striking the VMI electrodes. To minimize this, we coated the electrodes with platinum, which has a work function of ∼4.6 eV.[55] The reduction of noise is approximately an order of magnitude at $h\nu$ = 4.66 eV. Additionally, photoelectron images were collected both in the presence and absence of ions (by closing the ion trap) at ∼1 Hz and actively subtracted. This removes the background photoelectron noise contribution from the image and also leads to larger ion signal levels. The latter arises because the loading rate of the trap is too low to fill the trap completely before it is emptied at 100 Hz. Hence, when allowed to accumulate in the ions off cycle, there are many more ions to be extracted from the trap.

RESULTS AND ANALYSIS

Figure 1 shows two pump−probe photoelectron spectra at delays of t = −200 and 0 fs. Because the probe photon energy ($h\nu_{pr}$ = 1.55 eV) is well below any excited states and the detachment threshold for $[ATP-H_2]^{2-}$, the t = −200 fs photoelectron spectrum is identical with the single-photon spectrum that we have acquired at $h\nu_{pu}$ = 4.66 eV. The intense feature centered at eKE = 0.55 eV has been assigned to tunneling emission through the RCB following excitation to the $^1\pi\pi^*$ states.[13] When the pump and probe pulses overlap in time (t = 0 fs), the feature at eKE = 0.55 eV is depleted, and a new feature is seen at higher eKE that extends to eKE ∼ 2 eV.

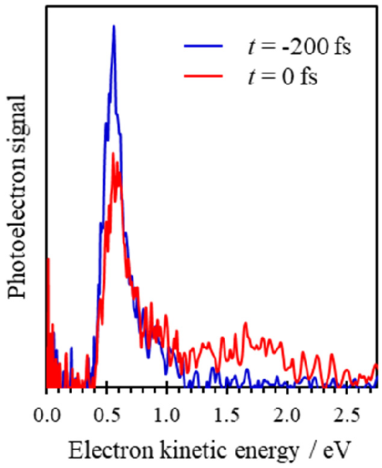

Figure 1. Time-resolved photoelectron spectra of $[ATP-H_2]^{2-}$ taken at t = −200 fs (blue) and 0 fs (red).

Figure 2 shows a selection of the time-resolved photoelectron spectra of $[ATP-H_2]^{2-}$ in the 200 ≤ t ≤ +300 fs range, where each spectrum has had an average of the spectra with t ≤ −200 fs subtracted to show only the time-resolved spectral changes. Additionally, to remove high-frequency noise in the spectra, a moving average (10-point) has been applied to the photoelectron spectra. Figure 2 shows three distinct features that evolve as a function of pump−probe delay; these have been highlighted in Figure 2 as shaded regions. The peak at eKE = 0.55 eV shows a negative signal that arises from the depletion seen in the photoelectron spectra shown in Figure 1. This depletion signal recovers rapidly and has essentially recovered fully by ∼300 fs. At higher energy, there is a positive signal that decays as a function of pump−probe delay, but also appears to shift toward lower eKE. Shifts in eKE can arise from changing Franck−Condon factors associated with vibrational wavepacket dynamics along an excited state potential energy surface and/or from changes in electronic state following a nonadiabatic transition.

The dynamics were analyzed using two approaches. First, the integrated photoelectron signal over three spectral windows in Figure 2 were taken and are shown in Figure 3. Also shown is the total integrated signal. The spectral windows 0.45 < eKE < 0.60 eV, 0.60 < eKE < 1.50 eV, and 1.50 < eKE < 2.10 eV are representative of the dynamics associated with the depletion, the red-shifted positive feature, and the high eKE feature, respectively. These data clearly show that the high eKE

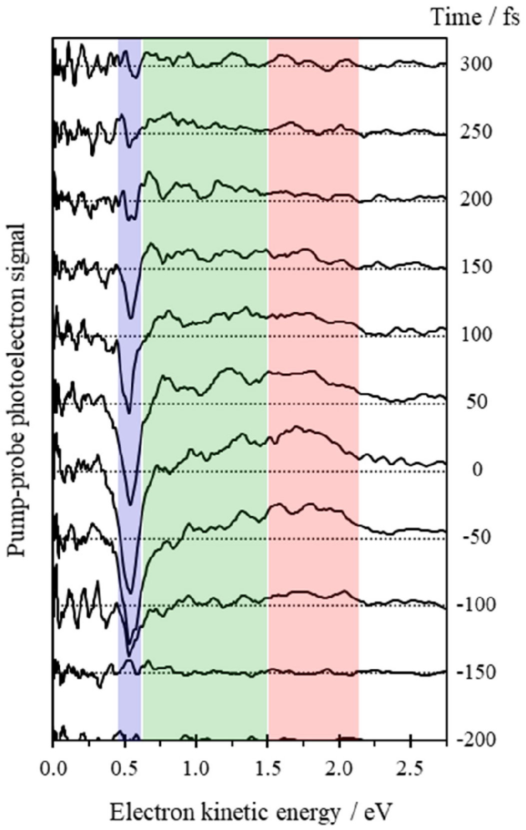

Figure 2. Time-resolved photoelectron spectra of $[\text{ATP}{-}\text{H}_2]^{2-}$ taken from −200 to +300 fs and plotted in terms of eKE. An average of the spectra at $t \leq -200$ fs was used for background subtraction.

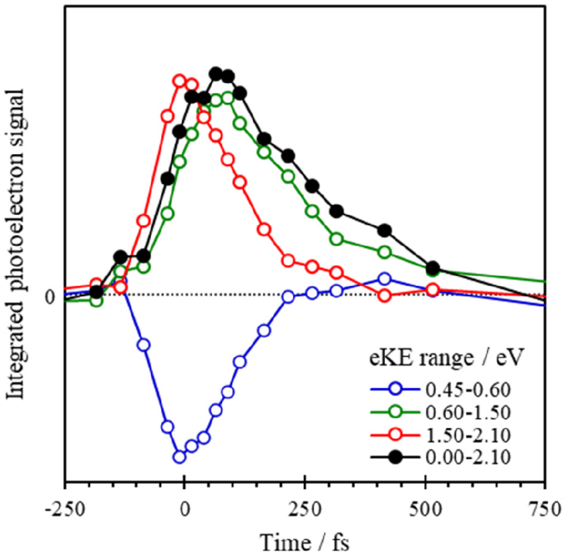

Figure 3. Integrated photoelectron signal plotted as a function of time over four different energy ranges.

feature is associated with depletion of the peak at 0.55 eV and that there is a second feature that appears and decays in the 0.6 < eKE < 1.5 eV spectral range. We can approximate that the fastest component at high eKE (which is concerted with the depletion recovery) occurs on a time scale similar to, or lower than, the cross-correlation between pump and probe pulses, i.e., <100 fs. The intermediate signal decays to a value of $1/e$ at ~300 fs. The key limitation with the analysis shown in Figure 3 is that there is significant spectral overlap between the differing features such that it is difficult to assess the overall spectral shape of the individual contributions.

As a second analysis method, a global fit to the time-resolved data was performed. The global fit has the form $f(\text{eKE}, t) = \sum_i g(t) \otimes c_i(\text{eKE}) \exp(-t/\tau_i)$, where $c_i(\text{eKE})$ represent photoelectron spectra that are associated with specific decays with lifetime τ_i (so-called decay-associated spectra). These are convoluted with the instrument response function, $g(t)$ (the cross-correlation of pump and probe pulses, which is assumed to be a Gaussian function with full-width at half-maximum of 100 fs). The minimum number of decays required to fit the data was two. In other words, the data are best represented by a 3-state model 1 → 2 → 3, in which 1 and 2 are observable and 3 is some final state that cannot be probed by the current experiment.

Figure 4 shows that the photoelectron spectra associated with decays τ_1 and τ_2, where $\tau_1 = 54 \pm 50$ fs and $\tau_2 = 211 \pm 100$ fs. The first is within the time-resolution of the experiment and so should be taken as $\tau_1 < 100$ fs. The kinetics are consistent with those estimated from Figure 3. The τ_1-associated spectrum has positive signal at 1.2 < eKE < 2.3 eV and negative signal between 0.4 < eKE < 1.2 eV. A positive signal corresponds to the signal decaying with a lifetime of τ_1, while a negative signal indicates the population growing with the same lifetime. The τ_2-associated spectrum simply decays, as the final state is not observable.

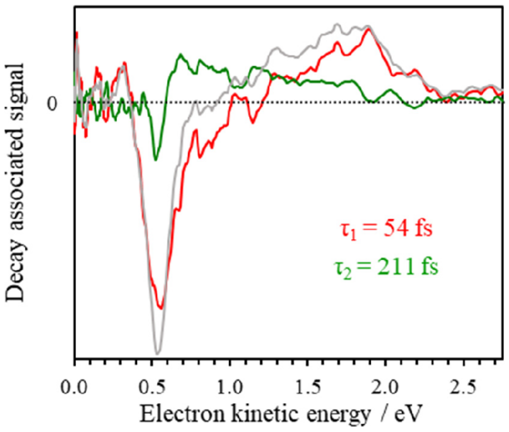

Figure 4. Decay-associated spectra obtained from a global fit to the time-resolved photoelectron spectra, a selection of which was shown in Figure 3. Red and green lines represent the spectra associated with τ_1 and τ_2, respectively. The gray line is the sum of both decay associated spectra and represents the time-resolved photoelectron spectrum arising from the initially excited state.

Inspection of the τ_1-associated spectrum shows that the negative peak at eKE = 0.55 eV and a positive peak with a maximum around eKE ~ 1.9 eV. However, there is also a negative signal in the range 0.6 < eKE < 1.2 eV. This overlaps with the τ_2-associated spectrum, showing that some signal in the 1.2 < eKE < 2.3 eV range leads to the τ_2-associated spectrum (the other fraction leads to the recovery of the bleach at 0.55 eV). For a three-state model, the photoelectron spectrum associated with the initial excited state can be obtained by the sum of the τ_1- and τ_2-associated spectra.[56] This spectrum is also included in Figure 4.

■ DISCUSSION

Two-photon resonance-enhanced photoelectron spectroscopy has previously shown the electron affinity of $[\text{ATP}-\text{H}_2]^-$ to be ADE ∼ 4.1 eV.[13] Hence, excitation at $h\nu_{\text{pu}}$ = 4.66 eV is above the adiabatic energy of $[\text{ATP}-\text{H}_2]^{2-}$. This is consistent with the pump−probe spectrum in Figures 1 and 2 that shows the photoelectron extends to eKE ∼ 2.1 eV. However, even though it is above the adiabatic energy, the excitation energy does not overcome the RCB. Hence, electron emission following one-photon excitation at $h\nu_{\text{pu}}$ = 4.66 eV requires the tunneling of an electron through this RCB. The initial excitation is resonant with the bright $^1\pi\pi^*$ states on adenine, and it is this population that tunnels through the RCB.[13] At $t = 0$, some population of the $^1\pi\pi^*$ states on adenine that would otherwise have tunneled has now been projected higher in energy by $h\nu_{\text{pr}}$ = 1.55 eV. Hence, a depletion is observed in the peak at eKE = 0.55 eV and a new feature is seen at higher eKE. As the total energy is above the RCB ($h\nu_{\text{pu}} + h\nu_{\text{pr}}$ > ADE + RCB), this photoelectron feature is associated with direct detachment from the $^1\pi\pi^*$ states on adenine. The observed dynamics in the high eKE feature in Figure 3 is thus a reflection the population in the $^1\pi\pi^*$ states and its temporal evolution. Note that the monoanion, $[\text{ATP}-\text{H}_2]^-$, has a large electron affinity and cannot be probed by $h\nu_{\text{pr}}$. The overall dynamics are shown schematically in Figure 5.

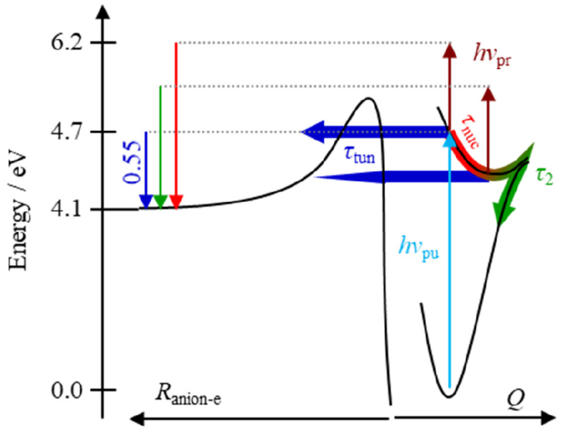

Figure 5. Schematic representation of the dynamics of $[\text{ATP}-\text{H}_2]^{2-}$ following excitation at 4.66 eV and probing at $h\nu_{\text{pr}}$ = 1.55 eV. The lifetimes relate to the decays obtained from the global fit, with $\tau_1^{-1} = \tau_{\text{tun}}^{-1} + \tau_{\text{nuc}}^{-1}$.

The kinetics of the feature at eKE = 0.55 eV are mirrored by those of the feature at high eKE. This is most clearly demonstrated in Figure 4, where the decay associated spectrum of the initial process has both positive and negative components that should be interpreted as the high eKE peak that decays with τ_1 < 100 fs also leads to recovery of the peak at 0.55 eV with the same time constant. This comes about because, with increasing delay of $h\nu_{\text{pr}}$, more population has tunneled from the $^1\pi\pi^*$ states to form $[\text{ATP}-\text{H}_2]^-$. Hence, the recovery dynamics of the peak at eKE = 0.55 eV is a measure of tunneling. However, it is clear from Figure 3 that not all of the initially excited $^1\pi\pi^*$ state population decays by autodetachment; otherwise, the total integrated positive and negative transient signals should cancel.[57,58] This population can be identified in the τ_1-decay associated spectrum in Figure 4 by the negative signal between 0.8 < eKE < 1.3 eV, which shows that some population from the initially excited $^1\pi\pi^*$ states produces the photoelectron signal in this range. This range coincides with the τ_2-associated spectrum and thus shows that population flows from the initial $^1\pi\pi^*$ states (with τ_1 < 100 fs) to an intermediate that has a photoelectron spectrum given by the τ_2-associated spectrum (shown schematically in Figure 5). The fact that not all population decays by tunneling through the RCB is consistent with the conclusions of Cercola et al.,[34] who clearly showed that photofragments were generated following excitation at 4.66 eV. Photofragmentation is most likely a ground state process, and hence, we can associate the τ_2 decay dynamics with internal conversion from the intermediate to the ground state. The intermediate does not decay by tunneling through the RCB, as this would have resulted in a negative signal associated with such dynamics. A small negative contribution can be seen in the τ_2-associated spectrum in Figure 4, suggesting that perhaps a small fraction of the population can still tunnel. We suspect that this appears due to inaccuracies in the global fitting procedure, because Figure 3 does not show a similar negative signal. Nevertheless, if this signal was real, then it only amounts to 10% of the observable intermediate population. Note also that the spectral shape of this transient suggests that we are probably not probing all the population of the intermediate and that some signal is likely cut off by an RCB at lower eKE, as can be seen at eKE = 0.55 eV in the τ_2-associated spectrum. In order to observe a larger portion of the intermediate, we have attempted to repeat the experiments with $h\nu_{\text{pr}}$ = 3.10 eV, but these experiments were unsuccessful. Hence, we conclude that the majority (i.e., >90%) of the intermediate state population decays by internal conversion to the ground electronic state.

The τ_2-associated spectrum is that of the intermediate produced (Figure 5). To assign the nature of the intermediate, we consider two likely processes. First, the initially populated vibrational wavepacket moves on the $^1\pi\pi^*$ surface away from the Franck−Condon region to this transient state. Second, initial motion on the $^1\pi\pi^*$ surface can lead to internal conversion to a nearby $^1\text{n}\pi^*$ state through a conical intersection. The role and the relative position of the optically dark $^1\text{n}\pi^*$ state has been extensively debated for nucleobases and nucleotides.[12,59,60] We have previously calculated that the $^1\text{n}\pi^*$ state lies about 0.3 eV lower in energy than the $^1\pi\pi^*$ state in $[\text{ATP}-\text{H}_2]^{2-}$. For the case of deprotonated deoxyadenosine monophosphate (dAMP^-), the two states are very close in energy.[12] However, it should be noted that the relative energies depend sensitively on the level of theory used. The $^1\text{n}\pi^*$ state could also decrease in energy in proximity of a conical intersection, as happens in the case of isolated Ade and 9-methyladenine (9-Me-Ade).[12,61] Finally, the relative energies between the $^1\pi\pi^*$ and $^1\text{n}\pi^*$ states differs in differing environments: in aqueous solution, the $^1\text{n}\pi^*$ state increase in energy for Ade, 9-Me-Ade and dAMP^-.[62−64]

The decay mechanism of $[\text{ATP}-\text{H}_2]^{2-}$ bears close similarities with that of dAMP^-. The time-resolved photoelectron spectroscopy of dAMP^-, excited at 4.66 eV and probed at 3.10 eV, could similarly be fitted with a 3-state model with lifetimes of τ_1 ∼ 30 fs and τ_2 = 290 fs.[12] These values are similar to those observed here, where τ_1 is less than the cross-correlation and τ_2 = 210 fs. However, the most striking similarities are between the decay-associated spectra. The τ_1-associated spectrum has a similar overall spectral shape peaking at high eKE as seen in Figure 4, while obviously no tunneling takes place in dAMP$^-$ and therefore no negative peak at 0.55 eV was observed, although some negative signal was seen indicating that the initial population decays into an intermediate. The τ_2-associated spectrum of the intermediate of dAMP$^-$ is also similar in $[ATP-H_2]^{2-}$. This offers some evidence that the same intermediate is formed in both cases and that the decay from this intermediate is similar. For dAMP$^-$, evidence could be given to support that the intermediate seen corresponds to nuclear motion on the $^1\pi\pi^*$ state, without any involvement of the optically dark $^1n\pi^*$ state.[12] Given the overall similarity of the observed dynamics between dAMP$^-$ and $[ATP-H_2]^{2-}$, we suggest that the intermediate in Figures 3 and 4 also corresponds to a different geometry of the $^1\pi\pi^*$ state. Note that in the study on dAMP$^-$, similarities between it and 9Me-Ade were drawn so that we conclude that the dynamics are in fact very similar to those of just the nucleobase.

Note that the observed τ_1 dynamics arise from competing dynamics: decay by tunneling (τ_{tun}) and decay by nuclear motion on the $^1\pi\pi^*$ states (τ_{nuc}), as shown in Figure 5. The τ_1 lifetime is thence defined by $\tau_1^{-1} = \tau_{tun}^{-1} + \tau_{nuc}^{-1}$. Unfortunately, we cannot independently determine τ_{tun} and τ_{nuc}.

It is perhaps surprising that there are such clear similarities in the dynamics between dAMP$^-$ and $[ATP-H_2]^{2-}$ (and 9Me-Ade). The negative charge has a clear effect on the energies of the π molecular orbitals of Ade relative to the ionization energies, which decrease from 8.26 eV for Ade to 5.65 eV for dAMP$^-$ to 4.1 eV for $[ATP-H_2]^{2-}$. Nevertheless, the excited $^1\pi\pi^*$ states appear at approximately the same excitation energy, and their dynamics—which one might envisage being very sensitive to any external factors such as nearby negative charges—are very similar. Hence, while the energies of the π molecular orbitals have changed substantially relative to the ionization energy, the relative energies between the π and π^* orbitals on the Ade nucleobase appear to not have changed significantly.

CONCLUSIONS

The excited state dynamics following excitation at 4.66 eV of the isolated doubly deprotonated dianion of ATP, $[ATP-H_2]^{2-}$, has been probed using time-resolved photoelectron spectroscopy. The initially excited $^1\pi\pi^*$ state population undergoes decay with a fraction of the population decaying by electron tunneling through the repulsive Coulomb barrier (RCB), while another fraction decays by nuclear motion on the $^1\pi\pi^*$ state, which leads to a discernible intermediate, that subsequently decays on a ~ 200 fs time scale by internal conversion to the ground electronic state. A global analysis reveals that the dynamics of $[ATP-H_2]^{2-}$ are similar to the dynamics observed in dAMP$^-$, where the intermediate was assigned to population on the $^1\pi\pi^*$ state surface that has moved away from the Franck−Condon region. This population can no longer tunnel through the RCB of $[ATP-H_2]^{2-}$ and decays to its ground electronic state. This excess energy then leads to fragmentation as has been observed in the photofragmentation action spectra reported by Cercola et al.[34] In a drive to understand ever larger and more complex systems, such as oligonucleotides and DNA fragments, these data offer an important glimpse into the role of electron tunneling in these systems.

AUTHOR INFORMATION

Corresponding Author

Jan R. R. Verlet − *Department of Chemistry, Durham University, DH1 3LE Durham, U.K.*; orcid.org/0000-0002-9480-432X; Email: j.r.r.verlet@durham.ac.uk

Authors

Maria Elena Castellani − *Department of Chemistry, Durham University, DH1 3LE Durham, U.K.*

Davide Avagliano − *Institute of Theoretical Chemistry, Faculty of Chemistry, University of Vienna, 1090 Vienna, Austria*

Complete contact information is available at:
https://pubs.acs.org/10.1021/acs.jpca.1c01646

Notes

The authors declare no competing financial interest.

ACKNOWLEDGMENTS

J.RR.V. is grateful to Dan Neumark for the fun and productive times in the Berkeley bunkers and for his continued support over the years. This work was supported by funding from the European Union's Horizon 2020 research and innovation program under the Marie Skłodowska-Curie Grant Agreement No. 765266 (LightDyNAmics).

REFERENCES

(1) Alberts, B. *Molecular biology of the cell*, 5th ed.; Garland Science: New York, 2008.

(2) Steenken, S. Purine bases, nucleosides, and nucleotides: aqueous solution redox chemistry and transformation reactions of their radical cations and e- and OH adducts. *Chem. Rev.* **1989**, *89* (3), 503−520.

(3) Burrows, C. J.; Muller, J. G. Oxidative nucleobase modifications leading to strand scission. *Chem. Rev.* **1998**, *98* (3), 1109−1151.

(4) Middleton, C. T.; de La Harpe, K.; Su, C.; Law, Y. K.; Crespo-Hernández, C. E.; Kohler, B. DNA Excited-State Dynamics: From Single Bases to the Double Helix. *Annu. Rev. Phys. Chem.* **2009**, *60* (1), 217−239.

(5) Crespo-Hernández, C. E.; Cohen, B.; Hare, P. M.; Kohler, B. Ultrafast Excited-State Dynamics in Nucleic Acids. *Chem. Rev.* **2004**, *104* (4), 1977−2020.

(6) de Vries, M. S.; Hobza, P. Gas-phase spectroscopy of biomolecular building blocks. *Annu. Rev. Phys. Chem.* **2007**, *58*, 585−612.

(7) Stavros, V. G.; Verlet, J. R. R. Gas-Phase Femtosecond Particle Spectroscopy: A Bottom-Up Approach to Nucleotide Dynamics. *Annu. Rev. Phys. Chem.* **2016**, *67* (1), 211−232.

(8) Satzger, H.; Townsend, D.; Zgierski, M. Z.; Patchkovskii, S.; Ullrich, S.; Stolow, A. Primary processes underlying the photostability of isolated DNA bases: Adenine. *Proc. Natl. Acad. Sci. U. S. A.* **2006**, *103* (27), 10196−10201.

(9) Bisgaard, C. Z.; Satzger, H.; Ullrich, S.; Stolow, A. Excited-State Dynamics of Isolated DNA Bases: A Case Study of Adenine. *ChemPhysChem* **2009**, *10* (1), 101−110.

(10) Wells, K. L.; Hadden, D. J.; Nix, M. G. D.; Stavros, V. G. Competing $\pi\sigma^*$ States in the Photodissociation of Adenine. *J. Phys. Chem. Lett.* **2010**, *1* (6), 993−996.

(11) Mai, S.; Richter, M.; Marquetand, P.; González, L. Excitation of Nucleobases from a Computational Perspective II: Dynamics. In *Photoinduced Phenomena in Nucleic Acids I: Nucleobases in the Gas Phase and in Solvents*; Barbatti, M., Borin, A. C., Ullrich, S., Eds.; Springer International Publishing: Cham, Switzerland, 2015; pp 99−153.

(12) Chatterley, A. S.; West, C. W.; Roberts, G. M.; Stavros, V. G.; Verlet, J. R. R. Mapping the Ultrafast Dynamics of Adenine onto Its

Nucleotide and Oligonucleotides by Time-Resolved Photoelectron Imaging. *J. Phys. Chem. Lett.* **2014**, *5* (5), 843−848.

(13) Castellani, M. E.; Avagliano, D.; González, L.; Verlet, J. R. R. Site-Specific Photo-oxidation of the Isolated Adenosine-5′-triphosphate Dianion Determined by Photoelectron Imaging. *J. Phys. Chem. Lett.* **2020**, *11* (19), 8195−8201.

(14) Chatterley, A. S.; Johns, A. S.; Stavros, V. G.; Verlet, J. R. R. Base-Specific Ionization of Deprotonated Nucleotides by Resonance Enhanced Two-Photon Detachment. *J. Phys. Chem. A* **2013**, *117* (25), 5299−5305.

(15) Yang, X.; Wang, X.-B.; Vorpagel, E. R.; Wang, L.-S. Direct experimental observation of the low ionization potentials of guanine in free oligonucleotides by using photoelectron spectroscopy. *Proc. Natl. Acad. Sci. U. S. A.* **2004**, *101* (51), 17588−17592.

(16) Wang, X.-B.; Ding, C.-F.; Wang, L.-S. Photodetachment Spectroscopy of a Doubly Charged Anion: Direct Observation of the Repulsive Coulomb Barrier. *Phys. Rev. Lett.* **1998**, *81*, 3351−3354.

(17) Simons, J. Molecular Anions. *J. Phys. Chem. A* **2008**, *112* (29), 6401−6511.

(18) Dreuw, A.; Cederbaum, L. S. Multiply Charged Anions in the Gas Phase. *Chem. Rev.* **2002**, *102* (1), 181−200.

(19) Verlet, J. R. R.; Horke, D. A.; Chatterley, A. S. Excited states of multiply-charged anions probed by photoelectron imaging: riding the repulsive Coulomb barrier. *Phys. Chem. Chem. Phys.* **2014**, *16* (29), 15043−15052.

(20) Scheller, M. K.; Compton, R. N.; Cederbaum, L. S. Gas-Phase Multiply Charged Anions. *Science* **1995**, *270* (5239), 1160−1166.

(21) Wang, L.-S.; Wang, X.-B. Probing Free Multiply Charged Anions Using Photodetachment Photoelectron Spectroscopy. *J. Phys. Chem. A* **2000**, *104* (10), 1978−1990.

(22) Wang, X.-B.; Wang, L.-S. Observation of negative electron-binding energy in a molecule. *Nature* **1999**, *400* (6741), 245−248.

(23) Wang, X.-B.; Woo, H.-K.; Huang, X.; Kappes, M. M.; Wang, L.-S. Direct Experimental Probe of the On-Site Coulomb Repulsion in the Doubly Charged Fullerene Anion C_{70}^{2-}. *Phys. Rev. Lett.* **2006**, *96* (14), 143002.

(24) Dau, P. D.; Liu, H.-T.; Yang, J.-P.; Winghart, M.-O.; Wolf, T. J. A.; Unterreiner, A.-N.; Weis, P.; Miao, Y.-R.; Ning, C.-G.; Kappes, M. M.; Wang, L.-S. Resonant tunneling through the repulsive Coulomb barrier of a quadruply charged molecular anion. *Phys. Rev. A: At., Mol., Opt. Phys.* **2012**, *85* (6), 064503.

(25) Horke, D. A.; Chatterley, A. S.; Verlet, J. R. Effect of internal energy on the repulsive Coulomb barrier of polyanions. *Phys. Rev. Lett.* **2012**, *108* (8), 083003.

(26) Horke, D. A.; Chatterley, A. S.; Verlet, J. R. R. Femtosecond Photoelectron Imaging of Aligned Polyanions: Probing Molecular Dynamics through the Electron−Anion Coulomb Repulsion. *J. Phys. Chem. Lett.* **2012**, *3* (7), 834−838.

(27) Horke, D. A.; Chatterley, A. S.; Verlet, J. R. R. Influence of the repulsive Coulomb barrier on photoelectron spectra and angular distributions in a resonantly excited dianion. *J. Chem. Phys.* **2013**, *139* (8), 084302.

(28) Gabelica, V.; Tabarin, T.; Antoine, R.; Rosu, F.; Compagnon, I.; Broyer, M.; De Pauw, E.; Dugourd, P. Electron photodetachment dissociation of DNA polyanions in a quadrupole ion trap mass spectrometer. *Anal. Chem.* **2006**, *78* (18), 6564−72.

(29) Gabelica, V.; Rosu, F.; Tabarin, T.; Kinet, C.; Antoine, R.; Broyer, M.; De Pauw, E.; Dugourd, P. Base-dependent electron photodetachment from negatively charged DNA strands upon 260-nm laser irradiation. *J. Am. Chem. Soc.* **2007**, *129* (15), 4706−13.

(30) Rosu, F.; Gabelica, V.; De Pauw, E.; Antoine, R.; Broyer, M.; Dugourd, P. UV spectroscopy of DNA duplex and quadruplex structures in the gas phase. *J. Phys. Chem. A* **2012**, *116* (22), 5383−91.

(31) Schinle, F.; Crider, P. E.; Vonderach, M.; Weis, P.; Hampe, O.; Kappes, M. M. Spectroscopic and theoretical investigations of adenosine 5′-diphosphate and adenosine 5′-triphosphate dianions in the gas phase. *Phys. Chem. Chem. Phys.* **2013**, *15* (18), 6640−50.

(32) Burke, R. M.; Dessent, C. E. H. Effect of Cation Complexation on the Structure of a Conformationally Flexible Multiply Charged Anion: Stabilization of Excess Charge in the Na+·Adenosine 5′-Triphosphate Dianion Ion-Pair Complex. *J. Phys. Chem. A* **2009**, *113* (12), 2683−2692.

(33) Burke, R. M.; Pearce, J. K.; Boxford, W. E.; Bruckmann, A.; Dessent, C. E. H. Stabilization of Excess Charge in Isolated Adenosine 5′-Triphosphate and Adenosine 5′-Diphosphate Multiply and Singly Charged Anions. *J. Phys. Chem. A* **2005**, *109* (43), 9775−9785.

(34) Cercola, R.; Matthews, E.; Dessent, C. E. H. Photoexcitation of Adenosine 5′-Triphosphate Anions in Vacuo: Probing the Influence of Charge State on the UV Photophysics of Adenine. *J. Phys. Chem. B* **2017**, *121* (22), 5553−5561.

(35) Vonderach, M.; Ehrler, O. T.; Matheis, K.; Weis, P.; Kappes, M. M. Isomer-Selected Photoelectron Spectroscopy of Isolated DNA Oligonucleotides: Phosphate and Nucleobase Deprotonation at High Negative Charge States. *J. Am. Chem. Soc.* **2012**, *134* (18), 7830−7841.

(36) Weber, J. M.; Ioffe, I. N.; Berndt, K. M.; Löffler, D.; Friedrich, J.; Ehrler, O. T.; Danell, A. S.; Parks, J. H.; Kappes, M. M. Photoelectron Spectroscopy of Isolated Multiply Negatively Charged Oligonucleotides. *J. Am. Chem. Soc.* **2004**, *126* (27), 8585−8589.

(37) Daly, S.; Rosu, F.; Gabelica, V. Mass-resolved electronic circular dichroism ion spectroscopy. *Science* **2020**, *368* (6498), 1465−1468.

(38) Ullrich, S.; Schultz, T.; Zgierski, M. Z.; Stolow, A. Direct Observation of Electronic Relaxation Dynamics in Adenine via Time-Resolved Photoelectron Spectroscopy. *J. Am. Chem. Soc.* **2004**, *126* (8), 2262−2263.

(39) Chatterley, A. S.; West, C. W.; Stavros, V. G.; Verlet, J. R. R. Time-resolved photoelectron imaging of the isolated deprotonated nucleotides. *Chem. Sci.* **2014**, *5* (10), 3963−3975.

(40) Canuel, C.; Mons, M.; Piuzzi, F.; Tardivel, B.; Dimicoli, I.; Elhanine, M. Excited states dynamics of DNA and RNA bases: characterization of a stepwise deactivation pathway in the gas phase. *J. Chem. Phys.* **2005**, *122* (7), 074316.

(41) Kang, H.; Lee, K. T.; Jung, B.; Ko, Y. J.; Kim, S. K. Intrinsic lifetimes of the excited state of DNA and RNA bases. *J. Am. Chem. Soc.* **2002**, *124* (44), 12958−9.

(42) Nix, M. G. D.; Devine, A. L.; Cronin, B.; Ashfold, M. N. R. Ultraviolet photolysis of adenine: Dissociation via the $\pi 1\sigma^*$ state. *J. Chem. Phys.* **2007**, *126* (12), 124312.

(43) Kleinermanns, K.; Nachtigallová, D.; de Vries, M. S. Excited state dynamics of DNA bases. *Int. Rev. Phys. Chem.* **2013**, *32* (2), 308−342.

(44) Serrano-Andrés, L.; Merchán, M.; Borin, A. C. Adenine and 2-aminopurine: paradigms of modern theoretical photochemistry. *Proc. Natl. Acad. Sci. U. S. A.* **2006**, *103* (23), 8691−8696.

(45) Barbatti, M.; Aquino, A. J. A.; Szymczak, J. J.; Nachtigallová, D.; Hobza, P.; Lischka, H. Relaxation mechanisms of UV-photoexcited DNA and RNA nucleobases. *Proc. Natl. Acad. Sci. U. S. A.* **2010**, *107* (50), 21453−21458.

(46) Barbatti, M.; Lischka, H. Nonadiabatic Deactivation of 9H-Adenine: A Comprehensive Picture Based on Mixed Quantum−Classical Dynamics. *J. Am. Chem. Soc.* **2008**, *130* (21), 6831−6839.

(47) Barbatti, M.; Lan, Z.; Crespo-Otero, R.; Szymczak, J. J.; Lischka, H.; Thiel, W. Critical appraisal of excited state nonadiabatic dynamics simulations of 9H-adenine. *J. Chem. Phys.* **2012**, *137* (22), 22A503.

(48) Serrano-Andrés, L.; Merchán, M. Are the five natural DNA/RNA base monomers a good choice from natural selection?: A photochemical perspective. *J. Photochem. Photobiol., C* **2009**, *10* (1), 21−32.

(49) Improta, R.; Santoro, F.; Blancafort, L. Quantum Mechanical Studies on the Photophysics and the Photochemistry of Nucleic Acids and Nucleobases. *Chem. Rev.* **2016**, *116* (6), 3540−3593.

(50) Lecointre, J.; Roberts, G. M.; Horke, D. A.; Verlet, J. R. R. Ultrafast Relaxation Dynamics Observed Through Time-Resolved Photoelectron Angular Distributions. *J. Phys. Chem. A* **2010**, *114* (42), 11216−11224.

(51) Stanley, L. H.; Anstöter, C. S.; Verlet, J. R. R. Resonances of the anthracenyl anion probed by frequency-resolved photoelectron

imaging of collision-induced dissociated anthracene carboxylic acid. *Chem. Sci.* **2017**, *8* (4), 3054−3061.

(52) Wiley, W. C.; McLaren, I. H. Time-of-Flight Mass Spectrometer with Improved Resolution. *Rev. Sci. Instrum.* **1955**, *26* (12), 1150−1157.

(53) Horke, D. A.; Roberts, G. M.; Lecointre, J.; Verlet, J. R. R. Velocity-map imaging at low extraction fields. *Rev. Sci. Instrum.* **2012**, *83* (6), 063101.

(54) Roberts, G. M.; Nixon, J. L.; Lecointre, J.; Wrede, E.; Verlet, J. R. R. Toward real-time charged-particle image reconstruction using polar onion-peeling. *Rev. Sci. Instrum.* **2009**, *80* (5), 053104.

(55) Fingerman, S. CRC handbook of chemistry and physics; a ready-reference book of chemical and physical data, 87th ed. *Sci-Tech News* **2007**, *61* (1), 38−38.

(56) Mooney, C. R. S.; Horke, D. A.; Chatterley, A. S.; Simperler, A.; Fielding, H. H.; Verlet, J. R. R. Taking the green fluorescence out of the protein: dynamics of the isolated GFP chromophore anion. *Chem. Sci.* **2013**, *4* (3), 921−927.

(57) Horke, D. A.; Li, Q.; Blancafort, L.; Verlet, J. R. R. Ultrafast above-threshold dynamics of the radical anion of a prototypical quinone electron-acceptor. *Nat. Chem.* **2013**, *5* (8), 711−717.

(58) Anstöter, C. S.; Bull, J. N.; Verlet, J. R. R. Ultrafast dynamics of temporary anions probed through the prism of photodetachment. *Int. Rev. Phys. Chem.* **2016**, *35* (4), 509−538.

(59) Gustavsson, T.; Sharonov, A.; Onidas, D.; Markovitsi, D. Adenine, deoxyadenosine and deoxyadenosine 5′-monophosphate studied by femtosecond fluorescence upconversion spectroscopy. *Chem. Phys. Lett.* **2002**, *356* (1), 49−54.

(60) Markovitsi, D. UV-induced DNA Damage: The Role of Electronic Excited States. *Photochem. Photobiol.* **2016**, *92* (1), 45−51.

(61) Picconi, D.; Avila Ferrer, F. J.; Improta, R.; Lami, A.; Santoro, F. Quantum-classical effective-modes dynamics of the $\pi\pi^* \rightarrow n\pi^*$ decay in 9H-adenine. A quadratic vibronic coupling model. *Faraday Discuss.* **2013**, *163* (0), 223−242.

(62) Gustavsson, T.; Sarkar, N.; Vayá, I.; Jiménez, M. C.; Markovitsi, D.; Improta, R. A joint experimental/theoretical study of the ultrafast excited state deactivation of deoxyadenosine and 9-methyladenine in water and acetonitrile. *Photochem. Photobiol. Sci.* **2013**, *12* (8), 1375−1386.

(63) Improta, R.; Barone, V. The excited states of adenine and thymine nucleoside and nucleotide in aqueous solution: a comparative study by time-dependent DFT calculations. *Theor. Chem. Acc.* **2008**, *120* (4), 491−497.

(64) Santoro, F.; Improta, R.; Fahleson, T.; Kauczor, J.; Norman, P.; Coriani, S. Relative Stability of the La and Lb Excited States in Adenine and Guanine: Direct Evidence from TD-DFT Calculations of MCD Spectra. *J. Phys. Chem. Lett.* **2014**, *5* (11), 1806−1811.